

Jet Propagation and Mach-Cone Formation in (3+1)-dimensional Ideal Hydrodynamics

Dissertation
zur Erlangung des Doktorgrades
der Naturwissenschaften

vorgelegt beim Fachbereich Physik
der Johann Wolfgang Goethe–Universität
in Frankfurt am Main

von
Barbara Betz
aus Hanau am Main

Frankfurt am Main 2009
(D30)

vom Fachbereich Physik der Johann Wolfgang Goethe–Universität
in Frankfurt am Main als Dissertation angenommen

Dekan Prof. Dr. Dirk H. Rischke

Gutachter Prof. Dr. Dirk H. Rischke, Prof. Dr. Horst Stöcker

Datum der Disputation 13. Oktober 2009

Nicht [die] Kunst und Wissenschaft allein,
Geduld will bei dem Werke sein.

Faust I, Hexenküche, 1808

Johann Wolfgang von Goethe (1749-1832)

Übersicht

Diese Arbeit untersucht Jet-Medium-Wechselwirkungen in einem Quark-Gluon-Plasma mittels eines hydrodynamischen Modells. Ein solches Quark-Gluon-Plasma repräsentiert eine Frühphase unseres Universums und kann in Schwerionenkollisionen erzeugt werden. Seine Eigenschaften sind Gegenstand der aktuellen Forschung. Da der Vergleich von Meßdaten und Modellrechnungen nahelegt, dass sich das Quark-Gluon-Plasma wie eine nahezu ideale Flüssigkeit verhält, läßt sich das bei einer Schwerionenkollision gebildete Medium mittels hydrodynamischer Simulationen beschreiben. Eine der in diesem Zusammenhang grundlegenden Fragestellungen ist, ob energiereiche Teilchen (sogenannte Jets), die zu Beginn einer Kollision erzeugt werden und das Medium durchqueren, zur Bildung eines Machkegels führen. Dieser kann theoretisch immer erwartet werden, wenn sich ein Jet mit Überschallgeschwindigkeit relativ zum Medium bewegt. Die gemessene Winkelverteilung der aus der Kollision hervorgehenden und in den Detektoren gemessenen Teilchen sollte dann eine charakteristische Struktur aufweisen, aus der man auf direktem Wege Rückschlüsse auf die Zustandsgleichung des Mediums, im Besonderen auf seine Schallgeschwindigkeit, ziehen kann. Es werden unterschiedliche Szenarien eines Jetenergieverlustes betrachtet, dessen exakte Form und der ihm zugrundeliegenden Wechselwirkungen unbekannt sind. Dazu werden verschiedene Quellterme untersucht, die eine solche Wechselwirkung des Jets mit dem Medium repräsentieren und die Abgabe von Energie und Impuls an das Medium beschreiben. Dabei werden sowohl Mechanismen einer schwachen Wechselwirkung (basierend auf Rechnungen der perturbativen Quantenchromodynamik, pQCD) als auch einer starken Wechselwirkung (welche anhand der sogenannten “Anti-de-Sitter/Conformal Field Theory”-Korrespondenz, AdS/CFT, ermittelt wird) behandelt. Obwohl diese in unterschiedlichen Winkelverteilungen resultieren und somit (für Einzeljetereignisse) eine Unterscheidung der zugrundeliegenden Prozesse ermöglichen könnten, zeigt sich, dass die für die gemessenen Teilchenspektren charakteristische Struktur durch die Überlagerung verschiedener Jettrajektorien beschrieben werden kann. Eine solche Struktur läßt sich nicht direkt mit der Zustandsgleichung in Verbindung bringen. In diesem Zusammenhang werden die Auswirkungen eines starken Flusses diskutiert, der sich bei nahezu allen betrachteten Jetenergieverlustszenarien entlang der Trajektorie des Jets bildet. Darüber hinaus werden die Transportgleichungen der dissipativen Hydrodynamik diskutiert, welche die Grundlage einer numerischen Berechnung von viskosen Effekten innerhalb eines Quark-Gluon-Plasmas bilden.

Zusammenfassung

Einleitung

Von jeher beschäftigte Menschen die Frage nach dem Ursprung des Lebens, dem Beginn des Universums und dem Aufbau der Materie. Letzterer wird durch das sogenannte Standardmodell [1, 2] beschrieben, das die Elementarteilchen und deren Wechselwirkungen zusammenfasst. Eine Vielzahl der uns heute umgebenden Materie (wie Protonen und Neutronen, aus denen beispielsweise die Atomkerne aufgebaut sind) setzt sich aus Quarks zusammen, die durch Gluonen miteinander wechselwirken.

Diese (starke) Wechselwirkung wird durch die Quantenchromodynamik (QCD) beschrieben, welche eine Besonderheit aufweist, die als “asymptotische Freiheit” [3, 4] bezeichnet wird: Für hohe Temperaturen und/oder Dichten nimmt die Stärke der Wechselwirkung zwischen den Quarks und Gluonen ab, so dass sich diese wie nahezu freie Teilchen verhalten und eine eigene Phase, das Quark-Gluon-Plasma [5, 6, 7], bilden.

Eine solche heiße und dichte Phase existierte wahrscheinlich kurz nach dem Urknall, bevor im Prozeß der Ausdehnung und Abkühlung des Universums die Quarks und Gluonen zu Teilchen rekombinierten. Man nimmt an, dass das Quark-Gluon-Plasma heutzutage im Inneren von dichten Neutronensternen vorhanden ist.

Bereits in den 1960er Jahren wurde die Möglichkeit diskutiert, Materie experimentell unter extremen Bedingungen zu untersuchen [8]. Daraus entwickelte sich einer der spannendsten Forschungsbereiche der modernen Physik.

Hochenergetische, relativistische Schwerionenkollisionen eröffnen die einzigartige Möglichkeit, sehr heiße und dichte Materie im Labor zu erzeugen. Dabei geht es nicht nur um den eindeutigen Nachweis des Quark-Gluon-Plasmas, der die Theorie der Quantenchromodynamik und somit das Standardmodell bestätigen würde, sondern auch darum, die Eigenschaften jener Phase mit experimentellen Beobachtungen in Verbindung zu bringen.

Obwohl die Erzeugung eines Quark-Gluon-Plasmas sowohl bei Messungen am Super Proton Synchrotron (SPS, CERN) als auch am Relativistic Heavy Ion Collider (RHIC, Brookhaven National Laboratory) offiziell erklärt wurde [9, 10, 11, 12, 13], bleiben seine Eigenschaften weiterhin umstritten, da ein solch experimentell erzeugtes Quark-Gluon-Plasma nur für sehr kurze Zeit existiert. In naher Zukunft werden große Beschleunigeranlagen wie der Large Hadron Collider (LHC, CERN) und die Facility for Antiproton and Ion Research (FAIR, GSI) Materie bei noch höheren Energien bzw. Dichten analysieren.

Eines der herausragenden Ergebnisse des RHIC-Programms war der Nachweis, dass sich das erzeugte Medium annähernd wie eine ideale Flüssigkeit verhält [10, 11, 12, 13, 14]. Damit scheint es gerechtfertigt, hydrodynamische Modelle zur Beschreibung des in einer Schwerionenkollision gebildeten Mediums zu verwenden, dessen Eigenschaften sich anhand verschiedener Proben (Sonden) ermitteln lassen.

Man nimmt an, dass zu Beginn der Kollision energiereiche Teilchen, die sog. harten Sonden, gebildet werden, welche das sich ausbildende Plasma durchqueren. Dabei induzieren sie Teilchenschauer, die Jets genannt werden, und geben Energie sowie Impuls an das Medium ab.

Durch die Wechselwirkungen des Jets mit dem Medium erhofft man sich Rückschlüsse auf das Medium ziehen zu können. Unter anderem geht man davon aus, dass ein sich mit Überschallgeschwindigkeit relativ zum Plasma bewegendes Jet die Bildung eines Machkegels hervorruft, welcher wiederum eine charakteristische Struktur in der Winkelverteilung der durch die Kollision gebildeten Teilchen bewirkt. Da diese Struktur direkt mit der Schallgeschwindigkeit des Mediums in Verbindung gebracht werden kann, erwartet man, anhand entsprechender Messungen nähere Informationen über die Zustandsgleichung des Quark-Gluon-Plasmas ableiten zu können.

Diese Arbeit untersucht die Propagation von Jets in einem hydrodynamischen Medium für unterschiedliche Szenarien der Energieabgabe, wobei sowohl starke als auch schwache Wechselwirkungen zwischen Jet und Medium betrachtet werden. Es zeigt sich, dass die resultierenden Winkelverteilungen verschiedenen Einflüssen der Kollision unterworfen sind.

Theoretischer Hintergrund

Hydrodynamik

Die Beschreibung der dynamischen Prozesse von Schwerionenkollisionen mit Hilfe von hydrodynamischen Modellen hat eine fast 30-jährige Tradition, da die Zustandsgleichung eine der wenigen essentiell benötigten Informationen darstellt und man somit leicht Eigenschaften verschiedener Medien (mit unterschiedlichen Zustandsgleichungen) überprüfen kann. Allerdings muss zunächst ein Anfangszustand festgelegt werden, der jedoch mit erheblichen theoretischen Unsicherheiten verbunden ist. Es werden sowohl geometrische Ansätze (wie das Glauber-Modell, das in der folgenden Betrachtung für die Beschreibung des sich expandierenden Mediums angewendet wird) als auch Plasmainstabilitäts-Modelle oder das sogenannte *Colour-Glass Condensate* verwendet.

Relativistische Hydrodynamik bedeutet die (lokale) Erhaltung von Energie und Impuls (repräsentiert durch den Energie-Impuls-Tensor $T^{\mu\nu}$) sowie der Ladung (bzw. Baryonenzahl, ausgedrückt durch die Ladungsdichte N)

$$\partial_\mu T^{\mu\nu} = 0, \quad \partial_\mu N^\mu = 0. \quad (1)$$

Falls sich die Materie im lokalen thermodynamischen Gleichgewicht befindet, lassen sich der Energie-Impuls-Tensor und die erhaltene Ladung durch

$$T^{\mu\nu} = (\varepsilon + p)u^\mu u^\nu - pg^{\mu\nu}, \quad N^\mu = nu^\mu \quad (2)$$

ausdrücken und hängen nur von der Energiedichte ε , dem Druck p , der Ladungsdichte n , der Vierergeschwindigkeit des Mediums u^μ und dem metrischen Tensor $g^{\mu\nu} = \text{diag}(+, -, -, -)$ ab, wobei sich alle Größen auf das Ruhesystem des Mediums beziehen. Um dieses System der Bewegungsgleichungen zu schließen, benötigt man eine Zustandsgleichung der Form

$$p = p(\varepsilon, n). \quad (3)$$

Anhand dieser Gleichungen wird die Dynamik der Kollision eindeutig aus dem Anfangszustand bestimmt. Hydrodynamik stellt somit eine direkte Verbindung zwischen der Zustandsgleichung und dem expandierenden Medium dar, die sich auch im emittierten Teilchenspektrum manifestiert.

Bei numerischen Simulationen werden die Erhaltungsgleichungen allerdings meist ins Laborsystem transformiert und in diskretisierter Version mit unterschiedlichen Algorithmen gelöst. Einer davon ist SHASTA (SHarp And Smooth Transport Algorithm), der sich besonders gut zur Beschreibung von Stoßwellenphänomenen eignet, zu deren Klasse auch die Machkegel gehören, und der im Folgenden Verwendung findet.

Hydrodynamische Simulationen bestimmen die zeitliche Entwicklung von Feldern wie dem Temperatur- oder Geschwindigkeitsfeld. Um das Resultat einer solchen hydrodynamischen Rechnung mit experimentellen Daten vergleichen zu können, benötigt es eine Beschreibung zur Umwandlung der Flüssigkeit in Teilchen. Somit muss die hydrodynamische Konfiguration in ein Emissionsspektrum übersetzt werden, wobei die Erhaltung beispielsweise der Energie, des Impulses und der Teilchenzahl (sowie aller anderen Quantenzahlen) garantiert sein muss.

Ein häufig verwendeter Ansatz ist der sogenannte Cooper-Frye Ausfrierprozeß [129]. Zunächst wird anhand eines bestimmten Kriteriums (wie etwa einer kritischen Zeit oder einer kritischen Temperatur T_c) der Ausfrierpunkt auf einer Hyperfläche Σ der Raum-Zeit bestimmt. Mit einer thermischen Verteilungsfunktion f , welche die Teilchenweltlinien zählt, die durch Σ hindurchtreten, kann das Emissionsspektrum über

$$E \frac{dN}{d^3p} = \int_{\Sigma} d\Sigma_\mu p^\mu f(u \cdot p/T) \quad (4)$$

bestimmt werden. Allerdings bedeutet diese Methode, dass das Flüssigkeitsfeld instantan in freie Teilchen umgewandelt wird. Da jedoch die Viskosität während der letzten Entwicklungsstufen des sich expandierenden Medium zunimmt, führt diese direkte Umwandlung möglicherweise zu unphysikalischen Artefakten. Sie ist trotzdem eine anerkannte Methode, da die Entkopplungszeiten für die Flüssigkeit und somit für die Umwandlung in Teilchen unbekannt sind.

Viskosität

Wie oben bereits erwähnt, verhält sich das in einer Schwerionenkollision am RHIC gebildete Medium wie eine nahezu ideale Flüssigkeit. Während ideale Hydrodynamik einen kontinuierlichen Anstieg der Anisotropien in der Winkelverteilung (dem sogenannten Elliptischen Fluß) mit zunehmendem Transversalimpuls (p_T) der erzeugten Teilchen vorhersagen, flachen die gemessenen Werte bei ungefähr

$p_T \approx 1.5 - 2$ GeV ab, was auf viskose Effekte zurückgeführt werden konnte. Da diese Anisotropien in peripheren (d.h. nicht-zentralen Stößen) und für geringere Kollisionsenergien stärker ausgeprägt sind, müssen sie in realistischen Simulationen mit einbezogen werden.

In diesem Fall führt die Tensorzerlegung des Energie-Impulstensors $T^{\mu\nu}$ und der Ladung N auf

$$T^{\mu\nu} = \varepsilon u^\mu u^\nu - (p + \Pi) \Delta^{\mu\nu} + q^\mu u^\nu + q^\nu u^\mu + \pi^{\mu\nu}, \quad N^\mu = n u^\mu + V^\mu, \quad (5)$$

wobei Π den isotropen viskosen Druck (*bulk pressure*), q^μ den Wärmefluß, $\pi^{\mu\nu}$ den Schertensor und V^μ den Diffusionsstrom bezeichnen. $\Delta^{\mu\nu} = g^{\mu\nu} - u^\mu u^\nu$ beschreibt eine Projektion auf einen 3-dimensionalen Unterraum, orthogonal zu u^μ . Mit Hilfe dieser Ausdrücke werden erstmals ausgehend von der Boltzmann Gleichung für ein verdünntes Gas

$$k^\mu \partial_\mu f(k, x) = C[f], \quad (6)$$

wobei C den Kollisionsterm und k^μ den Impuls beschreibt, die Transportgleichungen bis zur zweiten Ordnung in den auftretenden Gradienten für den isotropen viskosen Druck, den Wärmefluß und den Schertensor abgeleitet. Diese sind von grundlegender Bedeutung für jede numerische Simulation viskoser Hydrodynamik.

Jet-Energieverlust und Hydrodynamik

Aufgrund von Energie- und Impulserhaltung sind die in der Frühphase einer Schwerionenkollision gebildeten Jets eigentlich ein System bestehend aus zwei Jets (Di-Jet), die sich in entgegengesetzte Richtung bewegen. Man nimmt an, dass sich solche Di-Jets vorwiegend am Rande des Mediums bilden und einer der beiden Jets (der sogenannte Trigger-Jet) das Medium ohne weitere Wechselwirkung verlassen kann, während der andere (der assoziierte oder *away-side* Jet) die während der Kollision entstandene Materie durchquert und dabei entlang seines Weges Energie und Impuls an das Medium abgibt.

Eine Messung [88] beweist, dass sich der mittlere Impuls der emittierten Teilchen auf der Seite des Mediums, das der Jet durchquert hat, zumindest für nicht allzu periphere Kollisionen dem Wert für ein Medium im thermischen Gleichgewicht annähert. Deshalb dürfte die vom Jet in das Medium deponierte Energie schnell thermalisieren, weshalb man die vom Jet hervorgerufene Störung hydrodynamisch beschreiben kann.

Dazu wird ein Quellterm J^ν in das System von Energie- und Impulserhaltungsgleichungen eingebaut,

$$\partial_\mu T^{\mu\nu} = J^\nu, \quad (7)$$

so dass die zeitliche Entwicklung des vom Jet durchdrungenen Mediums bestimmt werden kann. Allerdings ist dieser Quellterm, J^μ , nicht der Quellterm des Jets, sondern das Residuum an Energie und Impuls, das der Jet an das Medium abgibt. Die Ableitung eines Quellterms, welcher die Wechselwirkung des Jets mit dem Medium korrekt wiedergibt, ist Gegenstand der aktuellen Forschung, wobei sowohl eine schwache Wechselwirkung (die mittels perturbativer Quantenchromodynamik, pQCD, beschrieben werden kann) als auch eine starke Wechselwirkung (welche

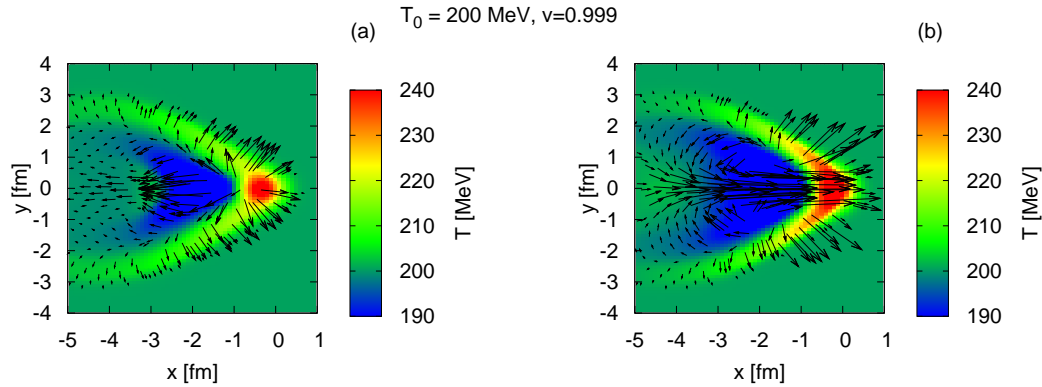


Abbildung 1: Temperatur- und Geschwindigkeitsprofil (Pfeile) im Fall einer reinen Energieabgabe (links) und für ein Szenario mit Energie- und Impulsabgabe (rechts) für einen Jet, der das Medium mit einer konstanten Geschwindigkeit nahe der Lichtgeschwindigkeit durchschlägt.

im Rahmen der Anti-de-Sitter/Conformal Field Theory-Korrespondenz, AdS/CFT, formuliert ist) zugrundegelegt wird. Neben diesen beiden Arten der Jet-Medium-Wechselwirkung wird zudem noch ein schematischer Quellterm betrachtet, der die Abgabe von Energie und Impuls entlang einer Trajektorie durch das Medium beschreibt.

Aus dem gewonnenen Teilchenspektrum werden jeweils Winkelkorrelationen bestimmt, die den Relativwinkel zwischen Trigger- und einem assoziierten Teilchen beschreiben. Ein solches Spektrum sollte im Fall der Ausbildung eines Machkegels zwei Maxima auf der dem Triggerteilchen gegenüberliegenden Seite (der Away-side) aufweisen.

Ergebnisse

Das statische Medium

Zunächst wird ein statisches Medium für verschiedene Szenarien der Energie- und Impulsabgabe betrachtet. Da die exakte Form eines entsprechenden Quellterms, der die Jet-Medium-Wechselwirkung im Quark-Gluon-Plasma beschreibt, unbekannt ist, wird hierbei sowohl auf die Möglichkeit des reinen Energieverlustes (welcher unwahrscheinlich ist, jedoch nicht ausgeschlossen werden kann) als auch des gleich starken Energie- und Impulsübertrages eingegangen.

Es zeigt sich, dass in beiden Fällen eine kegelartige Struktur ausgebildet wird, wie der Abbildung 1 zu entnehmen ist. Wird jedoch nicht nur Energie, sondern auch Impuls an das Medium abgegeben, so entsteht ein starker Fluß entlang der Trajektorie des Jets, den man als *Diffusion Wake* (Diffusionswelle) bezeichnet.

Erfolgt der Ausfrierprozeß, d.h. die Umwandlung der Flüssigkeitsfelder in Teilchen, gemäß der Cooper-Frye Formel [vgl. Gl. (4)], so führt dieser starke Fluß zur Aus-

prägung eines Maximums auf der *Away-side*. Für den Prozeß der reinen Energieabgabe hingegen tritt eine Zweipeak-Struktur auf wie sie im Fall der Ausprägung eines Machkegels zu erwarten ist und in den aus experimentellen Daten gewonnenen (und veröffentlichten) Winkelverteilungen auftritt. Diese Ergebnisse stimmen mit früheren Untersuchungen [83] unter Verwendung linearisierter Hydrodynamik überein. Inwieweit sie allerdings auf ein expandierendes Medium übertragen werden können, läßt sich erst nach einer Betrachtung eines solchen Systems sagen (siehe unten). Auf die Bedeutung der *Diffusion Wake* wird im Folgenden noch mehrfach eingegangen.

Darüber hinaus konnte gezeigt werden, dass diese Ergebnisse unabhängig davon sind, ob der Impuls longitudinal oder transversal zur Jetrichtung abgegeben wird und ob dieser Jet im Medium thermalisiert wird (also stoppt) oder durch das Medium durchschlägt. Hierbei wurde die Rückreaktion des Mediums bei Abbremsung eines Jets durch ein einfaches Bethe–Bloch-Modell beschrieben, welches zur Ausprägung eines sogenannten *Bragg-Peaks* führt, also eines Maximums der Energie- und Impulsabgabe kurz vor dem Endpunkt der Jettrajektorie.

Teilchenkorrelationen in pQCD und AdS/CFT

Bei dem oben betrachteten Quellterm handelt es sich um eine schematische Beschreibung eines Jetenergie- und Impulsverlustes. Es wurden jedoch auch Jet-Medium-Wechselwirkungen sowohl im Rahmen der perturbativen Quantenchromodynamik (pQCD) [199] als auch unter Anwendung der Anti-de-Sitter/Conformal Field Theory-Korrespondenz (AdS/CFT) abgeleitet [233] und untersucht [231]. Diese beiden vollkommen unabhängigen Ansätze beziehen sich auf eine schwache bzw. starke Wechselwirkung.

In der vorliegenden Arbeit konnte durch Vergleich der resultierenden Winkelkorrelationen gezeigt werden, dass die experimentelle Bestimmung einer Zweiteilchenkorrelation für einzelne, identifizierte, schwere Quarks am RHIC oder LHC die Möglichkeit bieten könnte, eine Aussage über die Stärke der Wechselwirkung zu machen, da die berechneten Winkelverteilungen, wie man Abbildung 2 entnehmen kann, unterschiedliche Strukturen aufweisen.

Hierzu wurde der pQCD-Quellterm in die hydrodynamische Simulation eingebaut und das Ergebnis einer AdS/CFT-Rechnung gegenübergestellt (siehe Abbildung 2). Man sieht deutlich, dass für den pQCD-Quellterm ein Maximum in der dem Trigger-Jet entgegengesetzten Richtung auftritt, während die mittels AdS/CFT erhaltenen Korrelationen eine Doppelpeak-Struktur aufweist, welche jedoch nicht auf die Ausbildung eines Machkegels zurückgeführt werden kann, da für einen solchen Machkegel, im Gegensatz zu den erhaltenen Resultaten, die Lage der Maxima von der Geschwindigkeit des Jets abhängt.

Stattdessen führt ein starker Transversalimpuls in der sogenannten *Neck region*, einem Bereich nahe dem Jet, zur Ausprägung dieser Doppelpeak-Struktur. Obwohl in beiden Fällen sowohl eine Machkegel-artige Struktur als auch eine *Diffusion Wake* auftritt, wird die Winkelkorrelation letztendlich eindeutig von dieser *Neck region* dominiert.

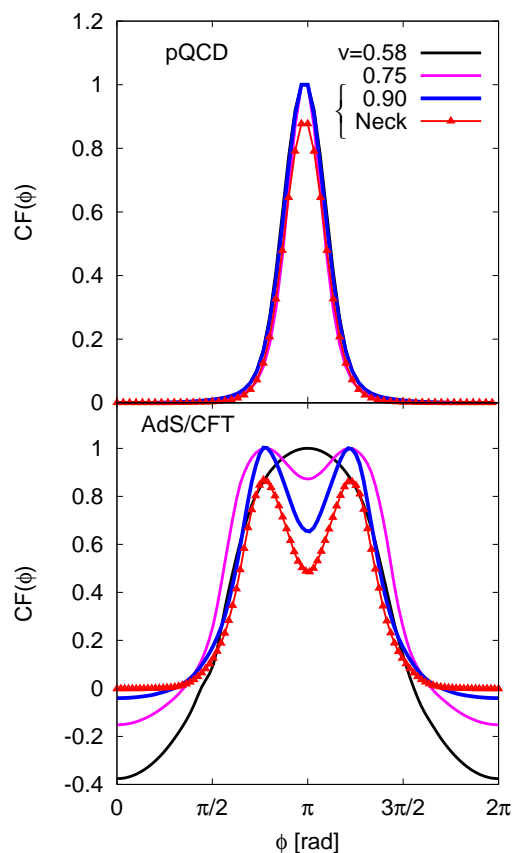


Abbildung 2: Normierte Winkelkorrelationen nach Hintergrundsubtraktion, erhalten gemäß dem Cooper-Frye Ausfrierprozeß für einen Quellterm der pQCD (oben) und der AdS/CFT (unten) für $p_T \sim 3.14$ GeV, verschwindende Rapiditäten ($y = 0$) und verschiedene Geschwindigkeiten des Jets. Die rote Linie mit Dreiecken repräsentiert den Beitrag der sog. *Neck region* für einen Jet mit $v = 0.9$ c.

Das expandierende Medium

Die realistische Beschreibung einer Schwerionenkollision erfordert natürlich ein expandierendes Medium. Zwar ist es unwahrscheinlich (wenn auch nicht unmöglich), dass während eines sogenannten *Events* (also einer Kollision) mehrere Jets gleichzeitig die bei dem Stoß gebildete Materie durchqueren, die experimentell ermittelten Zweiteilchenkorrelationen werden jedoch in jedem Fall über mehrere *Events* gemittelt. Somit werden unterschiedliche Jettrajektorien in Betracht gezogen.

Wie sich herausstellt (vgl. Abbildung 3), führen die Einzelbeiträge verschiedener Jettrajektorien (siehe Abbildung 3 unten) zu einer Substruktur auf der *Away-side* (gestrichelte Linien in den oberen Abbildungen), welche entweder zu einem breiten Maximum oder einer ursprünglich durch die Bildung eines Machkegels erwarteten Doppelpeak-Struktur führen.

Dies legt die Schlußfolgerung nahe, dass die experimentell beobachtete Struktur

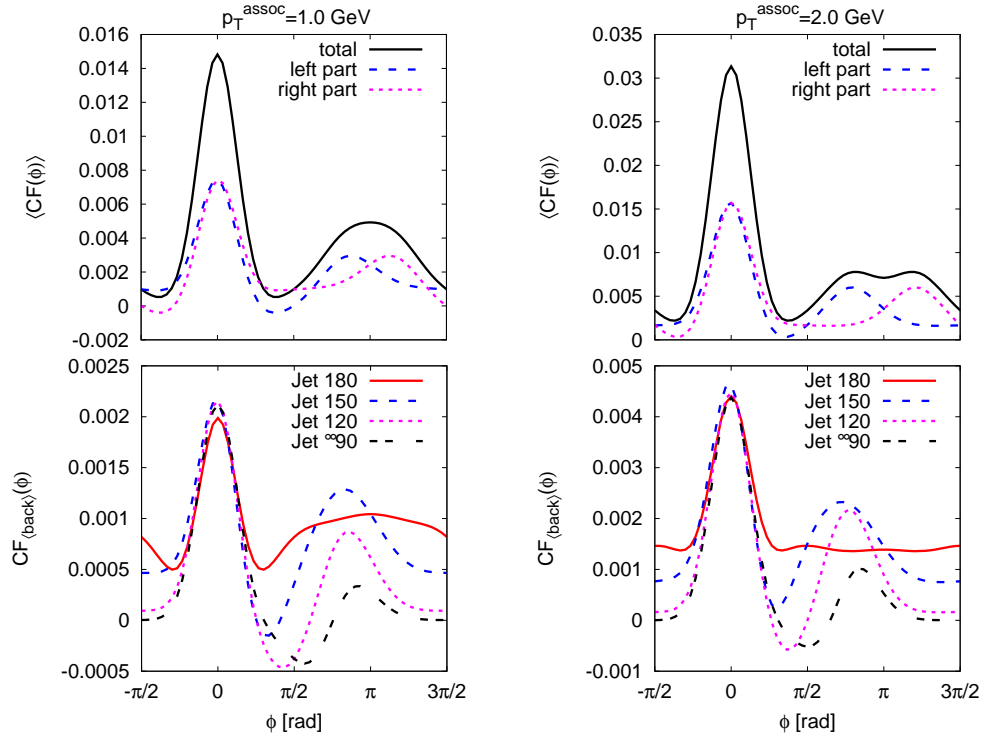


Abbildung 3: Normierte und über verschiedene Jettrajektorien gemittelte Zweiteilchenkorrelationen nach einem Cooper-Frye Ausfrierprozeß (durchgezogene schwarze Linie) für einen Jet, der insgesamt 5 GeV an Energie und Impuls an das Medium abgibt, wobei für die assoziierten Teilchen ein Transversalimpuls von $p_T^{\text{assoc}} = 1$ GeV (links) und $p_T^{\text{assoc}} = 2$ GeV (rechts) angenommen wird. Die gestrichelten Linien (blau und violett) repräsentieren dabei die gemittelten Beiträge von verschiedenen Jets, unterschieden durch den Azimuthalwinkel ihres Anfangspunktes. Die Beiträge für vier verschiedene Jettrajektoren, deren Mittelung die blau gestrichelte Linie ergibt, sind im unteren Teil der Abbildung dargestellt. Dabei repräsentiert 'Jet 180' denjenigen Jet, der das Medium mittig durchquert.

durch einen Mittelungsprozeß verschiedener abgelenkter Jets entsteht und somit nicht direkt mit der Zustandsgleichung in Verbindung gebracht werden kann.

Es muss allerdings erwähnt werden, dass dies die Bildung eines Machkegels in Schwerionenkollisionen nicht ausschließt, jedoch dürfte dessen Emissionswinkel erst durch Untersuchung von Einzeljet-Events möglich werden.

Es konnte außerdem gezeigt werden, dass die Wechselwirkung zwischen radialem und durch die Bewegung des Jets hervorgerufenem Fluß zu einer Reduzierung der *Diffusion Wake* und einer Krümmung des (Mach-)Kegels führen kann, wie es in einer früheren Arbeit aus theoretischen Überlegungen abgeleitet wurde [170]. Der Einfluß der *Diffusion Wake* auf das resultierende Teilchenspektrum bleibt jedoch erhalten, hängt aber von der Weglänge des Jets und somit von der Relativbewegung zwischen Jet und Medium ab. Wie man Abbildung 3 entnehmen kann, haben jedoch die nicht-zentralen Jets einen großen Einfluß auf die resultierende Struktur, wobei dieser vom Betrag und von der zugrundegelegten Energie- und Im-

pulsverluste abhängt, deren Bestimmung somit, besonders in Abhängigkeit der abgegebenen Energie und der Geschwindigkeit des Jets, notwendig ist.

Durch eine Vergleichsrechnung, die wie im statischen Fall einen reinen Energieverlust beschreibt, konnte gezeigt werden, dass dieses Jetenergieverlustszenario im Gegensatz zum statischen Fall (siehe oben) nicht zu einer experimentell beobachteten Doppelpeak-Struktur führt und somit im Widerspruch zu den experimentellen Ergebnissen steht.

Schlußfolgerungen

Die Struktur der experimentell gewonnenen Winkelverteilungen läßt sich durch die Bewegung von Jets durch ein hydrodynamisches Medium beschreiben. Allerdings muss dabei über verschiedene Jettrajektorien gemittelt und die Wechselwirkung mit einem expandierenden Medium berücksichtigt werden. Somit ist es von fundamentaler Bedeutung, die Wechselwirkung zwischen Jet und Medium mit nicht-linearer Hydrodynamik zu untersuchen. Der Einfluß verschiedener Effekte wie der der *Diffusion Wake* oder der sog. *Neck region* kann jedoch nur durch die Analyse eines statischen Mediums bestimmt werden.

Somit ist es nicht möglich, aus den bisher bestimmten Winkelverteilungen eindeutig auf die Emissionswinkel und somit auf die (gemittelte) Zustandsgleichung des in einer Schwerionenkollision entstandenen Mediums zu schließen.

Dazu müßte man, wie es in naher Zukunft am RHIC und LHC möglich sein dürfte, die Winkelverteilung für einzelne (energiereiche) Jets extrahieren. Die kürzlich veröffentlichten Daten [77, 79] über die Veränderung des Kegelwinkels mit der Reaktionsebene versprechen allerdings bereits weitere Einsichten in die Phänomenologie der Machkegel in Schwerionenkollisionen, wenngleich neue Untersuchungen [295, 296], die eine Rekonstruktion des Jets umfassen, aufzeigen, dass die der Jet-Medium-Wechselwirkung zugrundeliegenden Prozesse weiterer Untersuchungen bedürfen. Für den Vergleich der experimentell gemessenen Daten mit hydrodynamischen Simulationen ist eine solche Jetrekonstruktion unerlässlich, da im letzteren Fall per Definition ein bzw. mehrere Jets vorliegen.

Zudem bleibt das Verfahren der experimentellen Hintergrundsubtraktion und somit die Frage zu klären, ob bzw. wie stark die Bewegung des Jets Einfluß auf den Gesamtfluß des Mediums hat. Dieses kann und sollte mittels hydrodynamischer Untersuchungen analysiert werden.

Um die Beschreibung der Jet-Medium-Wechselwirkungen möglichst genau an die realistischen Gegebenheiten anzupassen, ist es weiterhin notwendig, longitudinale Expansion, nicht-zentrale Stöße und verschiedene Zustandsgleichungen zu betrachten. Außerdem könnte der Ausfrierprozeß bzw. die nach der Entstehung der Teilchen zwischen diesen auftretenden Wechselwirkungen noch Einfluß auf die Winkelverteilungen haben.

Allgemein gesehen bedarf es noch eines detaillierteren Verständnisses des Quellterms, dessen Bedeutung auch für die durch die verschiedenen Experimente (RHIC, LHC und FAIR) abgedeckten Energiebereiche ermittelt werden muss.

Abstract

This thesis investigates the jet-medium interactions in a Quark-Gluon Plasma using a hydrodynamical model. Such a Quark-Gluon Plasma represents a very early stage of our universe and is assumed to be created in heavy-ion collisions. Its properties are subject of current research. Since the comparison of measured data to model calculations suggests that the Quark-Gluon Plasma behaves like a nearly perfect liquid, the medium created in a heavy-ion collision can be described applying hydrodynamical simulations. One of the crucial questions in this context is if highly energetic particles (so-called jets), which are produced at the beginning of the collision and traverse the formed medium, may lead to the creation of a Mach cone. Such a Mach cone is always expected to develop if a jet moves with a velocity larger than the speed of sound relative to the medium. In that case, the measured angular particle distributions are supposed to exhibit a characteristic structure allowing for direct conclusions about the Equation of State and in particular about the speed of sound of the medium. Several different scenarios of jet energy loss are examined (the exact form of which is not known from first principles) and different mechanisms of energy and momentum loss are analyzed, ranging from weak interactions (based on calculations from perturbative Quantum Chromodynamics, pQCD) to strong interactions (formulated using the Anti-de-Sitter/Conformal Field Theory Correspondence, AdS/CFT). Though they result in different angular particle correlations which could in principle allow to distinguish the underlying processes (if it becomes possible to analyze single-jet events), it is shown that the characteristic structure observed in experimental data can be obtained due to the different contributions of several possible jet trajectories through an expanding medium. Such a structure cannot directly be connected to the Equation of State. In this context, the impact of a strong flow created behind the jet is examined which is common to almost all jet deposition scenarios. Besides that, the transport equations for dissipative hydrodynamics are discussed which are fundamental for any numerical computation of viscous effects in a Quark-Gluon Plasma.

Table of Contents

I	Quark-Gluon Plasma and Heavy-Ion Collisions – an overview	1
1	Introduction	3
1.1	The Standard Model of Elementary Particle Physics	5
1.2	The Phase Diagram of QCD	6
1.3	Probing the QGP: Ultra-relativistic Heavy-Ion Collisions	10
1.4	The Signatures of QGP	11
2	The Experimental Search for the QGP	15
2.1	Collective Effects	17
2.2	Hard Probes	18
2.2.1	One-particle correlations	19
2.2.2	Two-particle correlations	20
2.2.3	Three-particle correlations	25
2.3	Correlations in Pseudorapidity: The Near-side Ridge	26
II	Hydrodynamics and Jet Energy Loss	27
3	Ideal Hydrodynamics	29
3.1	The Hydrodynamical Equations of Motion	30
3.2	Numerical Solutions for the Equations of Motion	31
3.3	Transformation between the Laboratory Frame and the Local Rest Frame	32
3.4	The SHASTA	32
3.5	Initial Conditions	33
3.6	The Equation of State	36
3.7	The Freeze-out	36
3.7.1	The Hypersurface	37
3.7.2	Isochronous Freeze-out	38
3.7.3	Isothermal Freeze-out	39
3.7.4	Bulk Flow Freeze-out	40
4	Viscous Hydrodynamics	41
4.1	Tensor Decomposition of N^μ and $T^{\mu\nu}$	41
4.2	The Eckart and Landau Frames	43
4.3	The Fluid Dynamical Equations of Motion	43
4.4	The Navier–Stokes Approximation	44

4.5	A Phenomenological Derivation	45
4.6	Scales in Fluid Dynamics	46
4.7	The Knudsen Number	46
4.8	Transport Equations of Dissipative Quantities To Second Order in the Knudsen Number	47
4.9	The Shear Viscosity over Entropy Ratio	49
5	Shock Wave Phenomena	51
5.1	Mach cones	52
5.2	The Influence of Radial Flow	54
6	Jet-Energy Loss	57
6.1	In-medium Energy Loss	57
6.2	Mechanisms of Jet Energy Loss from QCD	59
6.3	First Studies of Jet-Energy Transfer to the Medium	61
6.4	Jet Energy Loss in Hydrodynamics	64
6.5	A pQCD Source Term	65
7	From String to Field Theory: The AdS/CFT Correspondence	69
7.1	Hard Probes in AdS/CFT	70
7.2	Shear Viscosity from the AdS/CFT Correspondence	72
7.3	Comparison of AdS/CFT to Hydrodynamics	73
7.4	Mach-Cone-like Correlations in AdS/CFT	74
7.5	The No-Go Theorem	78
III	Jet Propagation and Mach-Cone Formation	81
8	The Diffusion Wake	83
8.1	Punch-Through Jets in a Static Medium	85
8.2	Stopped Jets in a Static Medium	88
9	Polarization Probes of Vorticity	95
9.1	Hyperon Polarization	95
9.2	Initial Conditions and Reaction-Plane Polarization	98
9.3	Hydrodynamic Evolution, Polarization, and Jets	104
9.4	Mean-Free Path and Polarization	105
10	Di-Jet Correlations in pQCD vs. AdS/CFT	109
10.1	The Stress Zones	111
10.2	The pQCD Source Term	113
10.3	Freeze-out Procedures	115
10.4	Freeze-out Results in pQCD	117
10.5	Freeze-out Results in AdS/CFT	119
11	Conical Correlations in an Expanding Medium	123
11.1	Two-Particle Correlations in an Expanding Medium	127

IV Jets in Heavy-Ion Collisions: Conclusions and Outlook	133
Appendices	139
A The Evolution of the Universe	141
B Glauber Model	143
C The EoS for an Ideal Gas	147
D A Microscopic Derivation of Relativistic Fluid Dynamics	149
D.1 The Boltzmann Equation	149
D.2 Ideal Hydrodynamics from Kinetic Theory	151
D.3 Viscous Hydrodynamics from Kinetic Theory	151
D.3.1 Transport Equations in the Eckart Frame	154
D.3.2 The Tsumura-Kunihiro-Ohnishi Matching Condition . . .	159
D.3.3 Transport Equations in the Landau Frame	159
D.3.4 The Israel–Stewart Equations	160
E Energy and Momentum Deposition in the Bethe–Bloch Formalism	163
F Joule Heating	165
G Isochronous and Isothermal Freeze-out	167
H Distortion of Conical Structures due to Background Flow	171
References	173
Acknowledgements	189

List of Figures

1.1	Comparison of different measurements of the coupling constant α_s as a function of the transferred momentum to QCD model calculations.	6
1.2	The energy density (scaled by T^4) as a function of temperature from lattice QCD calculations.	7
1.3	A schematic phase diagram of QCD matter in the (T, μ) -plane. . .	8
1.4	Geometry of a heavy-ion collision.	9
1.5	Sequences of a heavy-ion collision.	10
2.1	Elliptic flow (v_2) for measured PHOBOS data vs. a viscous hydrodynamical calculation.	17
2.2	Leading-order differential cross sections for p+p collisions at SPS, RHIC, and LHC energies.	18
2.3	Measured $R_{AA}(p_T)$ in central Au+Au collisions at RHIC.	19
2.4	Schematic picture for the formation and propagation of a jet. . . .	20
2.5	Two-particle correlation functions for a trigger particle of $4 < p_T^{\text{trig}} < 6$ GeV and associated particles with different p_T	21
2.6	The $\Delta\phi$ distribution for various trigger and (increasing) partner p_T of p+p and 0 – 20% central Au+Au collisions.	22
2.7	Two-particle correlations for various centrality regions of Au+Au collisions and the reaction plane dependence of the per trigger yield.	23
2.8	Measured two-particle correlation and background contributions leading to a background-subtracted pattern, applying the ZYAM method.	24
2.9	Background subtracted three-particle correlations for a 30 – 50% central Au+Au collision at top RHIC energies.	25
2.10	Distribution of correlated hadron pairs as a function of $\Delta\phi$ and $\Delta\eta$, leading to the so-called Ridge phenomenon.	26
3.1	Schematic picture of the temporal evolution of a system formed in a heavy-ion collision according to the Landau and Bjorken model.	34
3.2	Schematic representation of a heavy-ion collision considering a scenario with and without the creation of a QGP.	37
3.3	A schematic picture of the space-time distribution of an isochronous and isothermal hypersurface.	38

5.1	The evolution of a shock wave.	52
5.2	The interference pattern of spherical waves leading to the formation of a Mach cone.	53
5.3	The change in the Mach angle as a function of the background flow.	55
5.4	Sketch of the deformation of Mach cones in an expanding medium.	55
6.1	The stopping power, i.e., the energy loss per unit length dE/dx , for muons in copper.	58
6.2	Collisional (elastic) and radiative energy loss of light quarks as well as light and heavy quarks passing through a medium produced in central Au+Au collisions at RHIC.	59
6.3	R_{AA} measured for central Au+Au collisions at $\sqrt{s_{NN}} = 200$ GeV compared to model calculations for varying values of the \hat{q} parameter.	60
6.4	Nuclear modification factor for high- p_T pions in central and semi-central Au+Au collisions at RHIC, compared to AMY, HT and ASW energy loss calculations.	61
6.5	Azimuthal particle distributions for non-isentropic and isentropic excitations.	62
6.6	Mean transverse momentum of associated hadrons for different trigger- p_T 's as a function of centrality.	64
6.7	Perturbed energy and momentum densities for a gluon moving with a velocity of $u = 0.99955$ along the positive z -axis of a QCD medium with $\eta/s = 0.13$	65
6.8	Perturbed momentum density for different values of the shear viscosity to entropy ratio η/s	66
6.9	Schematic representation of the different regions associated with a jet event.	67
7.1	A schematic picture of a moving quark using the AdS/CFT correspondence.	71
7.2	The fractional energy density perturbation and the field of the local Knudsen number for the disturbance caused by a heavy quark jet using the AdS/CFT correspondence.	73
7.3	Energy and momentum (Poynting vector) distribution calculated for a jet moving with $v = 0.75$ using the AdS/CFT correspondence.	74
7.4	The Poynting vector distribution calculated from the gauge/string duality.	75
7.5	The relative energy-density perturbation due to a heavy quark propagating with $v = 0.9$ through an $\mathcal{N} = 4$ Super-Yang-Mills (SYM) plasma.	76
7.6	Background-subtracted, azimuthal angular distribution for massless particles at mid-rapidity obtained from an isochronous Cooper-Frye freeze-out for the temperature and velocity fields obtained from the AdS/CFT string-drag model.	77

8.1	Temperature pattern and flow velocity profile for a pure energy deposition as well as an energy and momentum deposition scenario in a static medium.	85
8.2	Normalized angular distribution created by a punch-through jet at mid-rapidity with a fixed energy loss and different momentum loss rates as well as for a jet moving at different velocities associated with a pure energy deposition scenario.	86
8.3	Temperature pattern and flow velocity profile assuming a constant energy loss rate for full transverse momentum deposition and longitudinal as well as transverse momentum deposition. Additionally, the corresponding normalized angular distributions are shown.	87
8.4	The jet velocity $v_{\text{jet}}(t)$ and energy-deposition rate $dE(t)/dt$ as a function of time for a jet decelerating according to the Bethe–Bloch formula.	89
8.5	Temperature pattern and flow-velocity profile after a hydrodynamical evolution of $t = 4.5$ fm, $t = 6.5$ fm, and $t = 8.5$ fm for a jet that decelerates according to the Bethe–Bloch formula and stops after $\Delta x = 4.5$ fm for a vanishing-momentum loss rate as well as energy and momentum loss.	90
8.6	The normalized angular distribution generated by a decelerating jet at mid-rapidity that stops after $\Delta x = 4.5$ fm for a hydrodynamical evolution of $t = 4.5$ fm, $t = 6.5$ fm, and $t = 8.5$ fm.	91
8.7	Decomposition of a jet event into the regions of head, neck, diffusion wake, and Mach cone, applying a Cooper–Frey freeze-out at $p_T = 5$ GeV for a jet depositing energy and momentum, and stopping according to the Bethe–Bloch formalism.	92
9.1	The magnitude of polarization in x , y and z -direction (P_x , P_y , and P_z) from the $\Lambda^0 \rightarrow p + \pi^-$ decay as a function of the Λ^0 transverse momentum.	96
9.2	Definition of production and reaction plane.	97
9.3	Schematic illustration of non-central heavy-ion collisions. Partons produced in the overlap region carry global angular momentum along the $(-y)$ -axis, opposite to the reaction plane.	99
9.4	Initial densities in the Brodsky–Gunion–Kuhn model as well as the firestreak model.	100
9.5	Initial shear in the Brodsky–Gunion–Kuhn model as well as the firestreak model.	102
9.6	Ratio of Brodsky–Gunion–Kuhn to firestreak predictions as a function of \sqrt{s} and σ_η , the correlation length between space-time and flow rapidity.	103
9.7	Vorticity generated by a fast jet traversing the system in the positive x -direction.	104
10.1	The fractional-energy density perturbation due to a heavy quark with $v = 0.9$ in a QCD plasma of temperature $T_0 = 200$ MeV. . .	111

10.2	A magnified view of the near “neck” zone shows the relative local-energy density perturbation $\Delta\varepsilon/\varepsilon_0$ and fluid-flow directions induced by a heavy supersonic quark jet moving with $v = 0.9$	116
10.3	The (normalized) momentum-weighted bulk-flow angular distribution as a function of polar angle with respect to the away-side jet comparing pQCD and AdS/CFT calculations.	118
10.4	Normalized (and background subtracted) azimuthal away-side jet associated correlation after a Cooper–Frye freeze-out for pQCD and AdS/CFT calculations.	119
10.5	The (normalized) momentum weighted bulk-flow angular distribution and the normalized (and background-subtracted) azimuthal away-side jet-associated correlation after a Cooper–Frye freeze-out using the pQCD source term for $\alpha_s \approx 0.5$	121
11.1	Schematic representation of different jet paths assuming that surface emission is the dominant effect in heavy-ion collisions. . . .	125
11.2	Jet energy deposition as a function of time for jets depositing 5 GeV and 10 GeV along different trajectories.	126
11.3	The temperature pattern of four different jets with varying origins at the moment of freeze-out.	127
11.4	The normalized, background-subtracted and path-averaged azimuthal two-particle correlation after performing an isochronous Cooper–Frye freeze-out for jets depositing 5 GeV of energy and momentum and $p_T^{\text{assoc}} = 1$ GeV as well as $p_T^{\text{assoc}} = 2$ GeV.	129
11.5	The normalized, background-subtracted and path-averaged azimuthal two-particle correlation after performing an isochronous CF freeze-out for jets depositing 10 GeV of energy and momentum and $p_T^{\text{assoc}} = 1$ GeV as well as $p_T^{\text{assoc}} = 2$ GeV.	130
11.6	The normalized, background-subtracted and path-averaged azimuthal two-particle correlation after performing an isochronous CF freeze-out for jets depositing and energy of 5 GeV and assuming a vanishing momentum loss rate for $p_T^{\text{assoc}} = 1$ GeV and $p_T^{\text{assoc}} = 2$ GeV.	131
A.1	The evolution of the universe.	141
B.1	Schematic representation of the Glauber Model geometry.	143
B.2	The correlation between the number of participating nucleons in a heavy-ion collision, their cross section and the impact parameter b , defining the centrality classes.	144
G.1	The freeze-out hypersurface for a jet moving through the middle of the medium and for a non-central jet.	167
G.2	Background subtracted and normalized azimuthal particle correlations obtained from an isochronous and an isothermal Cooper–Frye freeze-out for $p_T = 1$ GeV and $p_T = 2$ GeV.	168

G.3	Background subtracted and normalized azimuthal particle correlations obtained from an isochronous and an isothermal Cooper–Frye freeze-out for $p_T = 1$ GeV and $p_T = 2$ GeV after convolution with a trigger jet.	168
H.1	The temperature pattern of three different jets depositing energy and momentum along trajectories for varying angles w.r.t. the x -axis at the moment of freeze-out.	172

Part I

Quark-Gluon Plasma and Heavy-Ion Collisions – an overview

Chapter 1

Introduction

One of the common features to all civilizations is the development of (philosophical) models about the beginning of the universe, the origin of life and the description of matter. However, testing these paradigms was always (and is) a demanding problem and just at the beginning of the last century, it became possible to prove the existence of various types of (short-living) particles.

Based on those findings, the *standard model* was developed which goes back to the work of Glashow, Weinberg, and Salam [1, 2] and characterizes the electroweak as well as strong interactions, but does not include gravity. Thus, the standard model is not a complete theory of all fundamental interactions.

Quantum Chromodynamics (QCD), the theory of strong interactions, is part of the standard model and exhibits a characteristic property, named “asymptotic freedom” [3, 4]: For high temperatures and/or densities, the strength of the interaction between the fundamental particles of QCD (the quarks and gluons) decreases, allowing them to behave as nearly free particles and to form a particular state of matter, the *Quark-Gluon Plasma* (QGP) [5, 6, 7].

Such extreme conditions probably existed shortly after the Big Bang at the very hot and early stages of the evolution of the universe before in the process of expansion and cooling quarks and gluons recombined into compound, color-neutral particles, the hadrons. It is assumed that nowadays the QGP is present in the cold, but dense inner core of neutron stars.

The idea to experimentally study matter under extreme conditions goes back to the 1960’s [8] (which was even before QCD was introduced). Today, one of the most exciting and challenging research programs is to probe the QGP. Relativistic high-energy heavy-ion collisions offer the unique possibility to study matter experimentally under extreme conditions in the laboratory. A formidable problem is to conclusively identify QGP production and to relate its properties to experimental observables. An unambiguous evidence of the QGP implies a proof of QCD and thus of the standard model.

Both, the Super Proton Synchrotron (SPS) program at CERN¹ [9] and the Relativistic Heavy Ion Collider (RHIC) program at BNL² [10, 11, 12, 13] have announced success in detection of the QGP. However, its fundamental properties are still dis-

¹European Organization for Nuclear Research close to Geneva, the acronym is derived from its former french name Conseil Européen pour la Recherche Nucléaire.

²Brookhaven National Laboratory, Long Island, USA.

cussed vividly which is due to the fact that the lifetime of such an experimentally created QGP is extremely short, making its detection highly challenging. In the near future, large accelerator facilities, the Large Hadron Collider (LHC) at CERN and Facility of Antiproton and Ion Research (FAIR) at GSI³, will examine further the matter created in heavy-ion collisions, promising deeper insights into fundamental interactions of matter.

One of the major results of the RHIC program was to show that the medium created during the collision behaves like a fluid [10, 11, 12, 13, 14]. Thus, it seems justified to use hydrodynamic models for the description of the matter formed during a heavy-ion collision [15, 16, 17]. Moreover, the fluid-like behaviour points to having created a new state of matter since normal hadronic matter is very viscous [18].

There exist different methods to probe the matter created in a heavy-ion collision. One of those are the so-called *hard probes* which are partons produced at an early stage of the evolution with a large transverse momentum (p_T) that penetrate the system formed, inducing showers of particles (*jets*) and depositing energy in the medium. The interaction of jets with the medium, which significantly affects the properties of the jets, are assumed to allow for conclusions about medium properties. Amongst other things, a hard- p_T jet travelling through the medium supersonically is supposed to create a *Mach cone* with an enhanced particle emission into the distinct Mach cone angle. Since this angle is connected to the speed of sound of the medium, it could provide a constraint on the average speed of sound of the strongly coupled QGP (sQGP) [19].

In this work, we investigate the propagation of a jet through a medium using (3+1)-dimensional ideal hydrodynamics. First, we consider different energy-loss mechanisms in a static medium and determine the azimuthal particle correlations to see if a conical structure has formed and if differences between various energy- and momentum-loss scenarios can be determined. Then, for comparison to experimental data, we study an expanding medium and discuss the importance of the convolution of different jets produced by experiment for the azimuthal particle correlations.

The thesis is organized as follows: In the first part, we give an overview about the properties of matter, present possible signatures of the QGP, and introduce important experimental findings. Part II then focuses on the hydrodynamical prescription of heavy-ion collisions. Having obtained a qualitative understanding of the system's evolution, we introduce the different energy- and momentum-loss mechanisms. The results of our simulations are presented in part III for the static as well as the expanding medium. After a subsequent discussion, the thesis concludes with a summary and an outlook in part IV.

³GSI Helmholtz Centre for Heavy Ion Research GmbH in Darmstadt, Germany. The acronym is also derived from its former name of Gesellschaft für Schwerionenforschung.

1.1 The Standard Model of Elementary Particle Physics

The standard model of elementary particle physics [1, 2] describes the elementary particles, *quarks* and *leptons*⁴, and their interactions mediated by the corresponding gauge bosons⁵. There exist six different quarks (*up*, *down*, *charm*, *strange*, *top*, *bottom*) and six different leptons (*electron*, *muon*, *tauon*, *electron-neutrino*, *muon-neutrino*, *tauon-neutrino*) as well as four gauge bosons (*graviton*⁶, Z^0/W^\pm bosons, *photon*, *gluons*).

Quarks and leptons, just like their antiparticles, can be combined to three doublets due to their mass as seen in table 1.1. Each gauge boson mediates (again sorted by increasing strength, see table 1.2) either gravitation, weak, electromagnetic, or strong interaction. All fermions have an antiparticle with opposite electromagnetic and color charge, but same mass and spin.

Leptons carry an electromagnetic as well as a weak charge, while quarks additionally have a so-called color charge that is a quantum number associated with a local SU(3) symmetry. This color charge couples to a gluon, the gauge boson of the strong interactions, which carries color charge itself. Thus, QCD is a non-Abelian gauge symmetry. In Abelian theories, like Quantum Electrodynamics (QED), the gauge bosons (i.e., the photons) do not carry (electric) charge.

Below energy densities of $\sim 1 \text{ GeV/fm}^3$ quarks, in contrast to leptons, are always confined in color-neutral *hadrons* (for a brief history of the formation of particles during the evolution of the universe see appendix A). Those are particles consisting either of quark-antiquark pairs (*mesons*) or three quarks or antiquarks (*baryons*). If two quarks get separated in space, the gluon field between them forms a narrow

⁴Quarks and leptons are fermions, i.e., spin 1/2-particles.

⁵Gauge bosons are spin 1-particles.

⁶Though gravitation is not incorporated into the standard model, it is commonly also mentioned in this context.

particle			charge
e	μ	τ	-1
ν_e	ν_μ	ν_τ	0
u	c	t	+1/3
d	s	b	-2/3

Table 1.1

Building blocks of matter in the standard model. Matter consists of fermions that can be classified into three families of equal electric charge, but different masses. The mass increases from the left to the right.

gravitation	weak	electromagnetic	strong
graviton	Z^0, W^\pm	γ	g

Table 1.2

The gauge bosons of the standard model, mediating the four fundamental interactions.

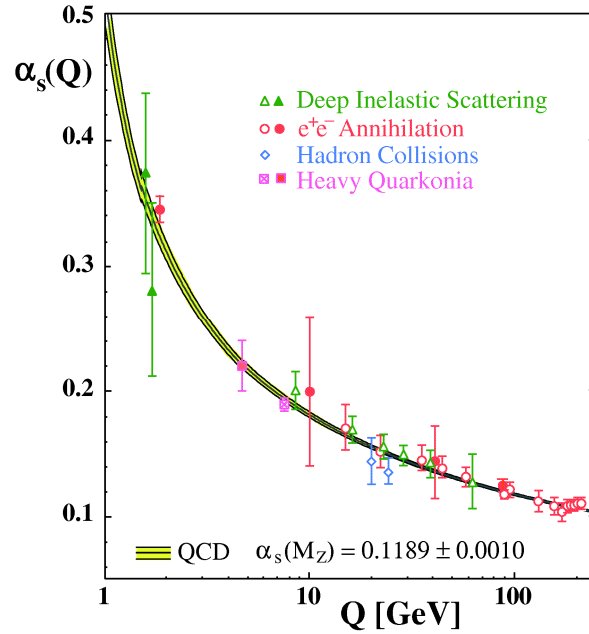


Figure 1.1

Comparison of different measurements of the coupling constant α_s as a function of the transferred momentum to QCD model calculations [21].

tube (string) and the potential between the quarks increases with distance [20],

$$V(r) = -\frac{4}{3} \frac{\alpha_s(Q^2)}{r} + kr, \quad (1.1)$$

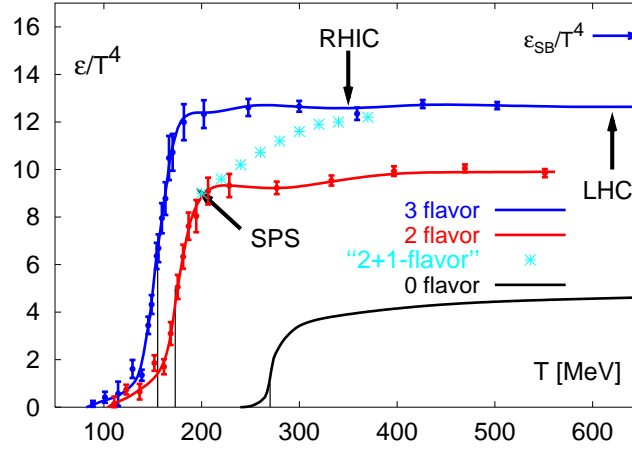
where α_s is the running coupling constant. At a certain distance, the energy becomes sufficiently large to create quark-antiquark pairs and thus other hadrons. This concept of color neutrality is called *color confinement* and is one of the two most prominent features of QCD. The other one is the above mentioned *asymptotic freedom*.

Both are due to the fact that the strength of the interaction between quarks and gluons becomes weaker as the exchanged momentum Q^2 increases or, equivalently, the distance decreases, as can be seen from Fig. 1.1. The decrease in the coupling constant for *hard* processes (i.e., for large transferred momentum) allows not only for the creation of a QGP, but also to describe the related processes perturbatively, i.e., to low order in the coupling constant.

1.2 The Phase Diagram of QCD

As discussed in the previous section, strongly interacting matter can occur in different phases. A phase describes a state of a thermally equilibrated system that is characterized by a certain set of macroscopic observables.

With a change in at least one of those thermodynamic variables, the system undergoes a *phase transition*. Phase transitions are characterized by the nature of change

**Figure 1.2**

The energy density (scaled by T^4) as a function of temperature from lattice QCD calculations, taken from [22], for various numbers of quark species. The figure includes the estimated temperatures reached at SPS, RHIC, and LHC.

of the relevant thermodynamic variable(s) and are commonly classified into phase transitions of *first order*, *second order*, and *cross-over*.

In general, there is an n th order phase transition if the $(n - 1)$ th derivative of a thermodynamic variable (like the energy density or the number density) is discontinuous. While a first-order transition always implies the existence of a *mixed phase*, a second order phase transition does not exhibit a mixed phase.

If the characteristic observables change rapidly, but without showing a (mathematical) discontinuity, the transition is called a *cross-over* and the actual transition between the phases cannot exactly be specified. A common structure in phase diagrams is that the line of a first-order phase transition ends in a critical end point of second order. Beyond that critical point, the transition becomes a cross-over.

Lattice QCD calculations [23, 24, 25, 26, 27, 28] (see Fig. 1.2) indicate a rapid increase of the energy density around $T \approx 160 - 170$ MeV. Since energy density, like pressure or entropy density, is proportional to the number of degrees of freedom, this behaviour can be understood as a phase transition between confined and deconfined states. The lattice QCD calculation shown in Fig. 1.2 is performed for a vanishing baryo-chemical potential, $\mu_B = 0$.

The QCD phase diagram (see Fig. 1.3) is obtained by plotting the relevant degrees of freedom for strongly interacting matter. Commonly, these degrees of freedom are studied as a function of temperature T and quark chemical potential μ which is associated with the net-quark number. Thus, for a vanishing quark chemical potential, an equal number of quarks and antiquarks is present in the system. Consequently, a positive quark chemical potential implies an excess of quarks over antiquarks. Therefore, a large value of μ is equivalent to a large net quark density ρ . Since quarks carry baryon number ($B = 1/3$), an equivalent measure to characterize the density is the baryochemical potential μ_B which is just scaled by a factor of 3 as compared to the quark chemical potential $\mu_B = 3\mu$.

Nuclear matter at its ground state has a temperature of $T \simeq 0$ MeV and a baryon

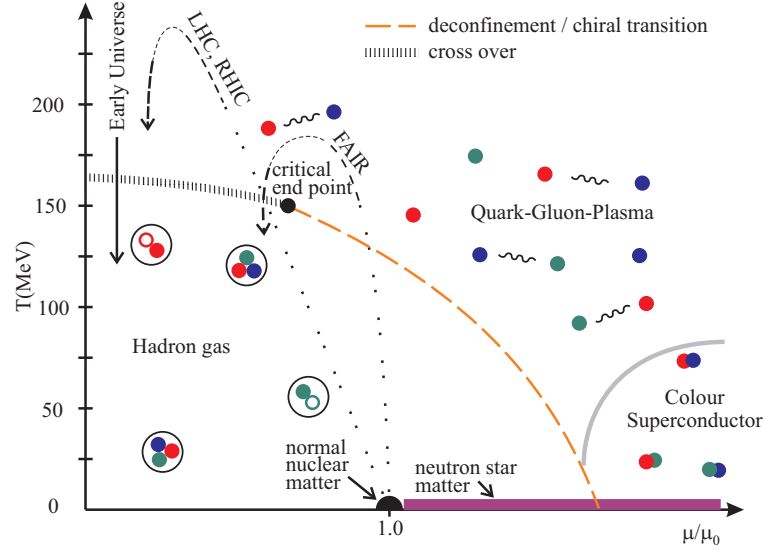


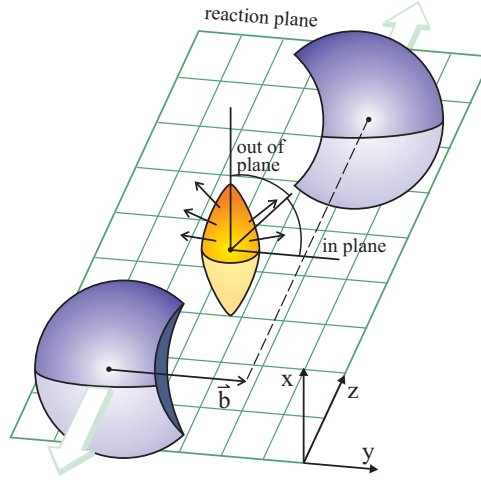
Figure 1.3

A schematic phase diagram of QCD matter in the (T, μ) -plane. The solid black line represents the chemical freeze-out, while the dashed orange line illustrates the chiral/deconfinement transition. Both end at the critical point which is connected to the $\mu = 0$ axis by a cross-over around $T \approx 170$ MeV. The ground state of nuclear matter is at $T = 0$ MeV and $\mu = \mu_0$. For high chemical potential and low temperature, there exists a phase of color superconductivity. The dashed black lines indicate the estimated properties of the medium created by various experiments.

density of $\rho \simeq 0.16 \text{ fm}^{-3}$ which corresponds to a quark chemical potential of $\mu_0 = 308 \text{ MeV}$ [29]. For low temperatures and small values of the quark chemical potential, strongly interacting matter forms a hadron gas. At sufficiently high temperature and/or chemical potential, hadrons strongly overlap, creating an extended region of deconfined quark-gluon matter, the QGP [5, 6, 7]. The phase transition is presumed to be of first order, ending in a critical point of second order, the location of which is not yet determined exactly. Predictions vary widely [23, 24, 25, 26, 27], but some lattice calculations [28], extended to the region of non-zero baryo-chemical potential, predict the critical end point to occur around $T \approx 160 \text{ MeV}$ and $\mu \approx 260 \text{ MeV}$ which would be a region accessible to heavy-ion collisions.

For cool and dense quark matter another phase transition is proposed. Due to the attractive interaction between quarks the formation of another ground state is expected. This phase is commonly referred to as color-superconducting [29, 30] and seems to contain a variety of additional phases [31].

At high temperatures, the nature of the QGP is not yet fully explored. There, the QGP is most probably not an ideal gas of non-interacting quarks and gluons [32], but behaves like a strongly coupled plasma (*strongly coupled QGP*, sQGP) corresponding to an ideal fluid, a concept that is supported by RHIC data [9, 10, 11, 12, 13, 14, 15, 16].

**Figure 1.4**

Geometry of a heavy-ion collision. The two nuclei move along the beam axis (z -axis) with an impact parameter b , determining the reaction plane. The corresponding definitions of in-plane and out-of-plane are also displayed.

For massless quarks, the QCD Lagrangian⁷ is chirally symmetric, i.e., invariant under a $U(N_f)_{rl}$ transformation of the right- and left-handed components of the quark spinors

$$\mathcal{L}(\psi_r, \psi_l) = \mathcal{L}(U_r \psi_r, U_l \psi_l). \quad (1.2)$$

Since spontaneous symmetry breaking is supposed to vanish for high temperatures and the mass of the deconfined quarks⁸ ($m_{u,d} \approx 10$ MeV), breaking the symmetry explicitly, is negligible small, chiral symmetry is supposed to be restored in the QGP [33]. However, the chiral phase transition might not coincide with the deconfinement phase transition.

Our knowledge about the phase diagram of QCD is currently limited to the region of the ground state of nuclear matter. The exploration of the other parts, including the verification of phase transitions, the confirmation of the critical point as well as the characterization of the QGP and hadronic matter are subject of current research. Two regions of the QCD phase diagram were or are realized in nature under extreme conditions: At vanishing quark chemical potential and large temperature, the QGP existed to our knowledge within the first microseconds of the universe [34], while dense and cool quark matter might exist (today) in the inner core of compact stars.

One feasible method to probe the phase diagram of QCD is to study the collisions of heavy nuclei at ultra-relativistic energies which offer the possibility to artificially create matter under extreme conditions. Different collision energies enable us to test various regions of the phase diagram. While the large-energy runs (at

⁷The QCD Lagrangian is given by $\mathcal{L} = \bar{\psi}(i\gamma^\mu D_\mu - m)\psi - 1/4 F_a^{\mu\nu} F_{\mu\nu}^a$, where ψ ($\bar{\psi}$) denotes the spinor (adjoint spinor) of the quark field, m the quark mass, D_μ the covariant derivative and $F_a^{\mu\nu}$ the field-strength tensor.

⁸Bound quarks are described by the so-called *constituent quarks* with a large effective mass of $m \approx m_{\text{nucleon}}/3$ that is mainly caused by the interaction of the gluons.

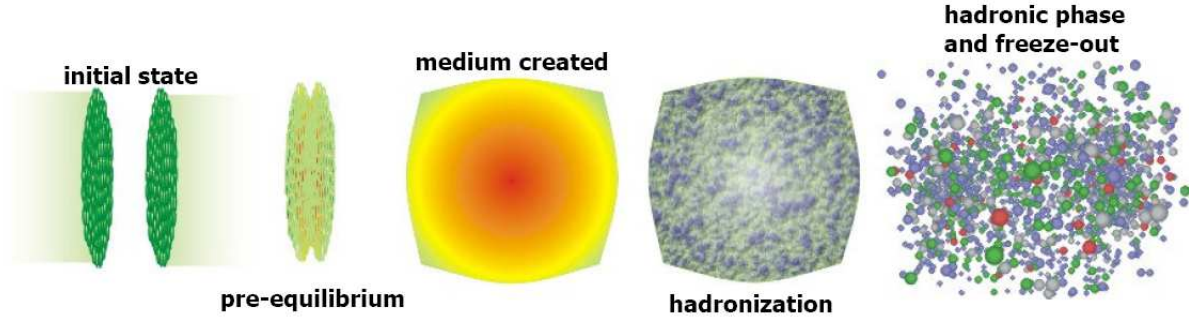


Figure 1.5

Sequence of a heavy-ion collision, from Ref. [35]. The incoming nuclei are Lorentz-contracted since they are accelerated to ultra-relativistic velocities (initial state). At the beginning of the collision, a non-equilibrated phase (pre-equilibrium) is created that develops into a thermalized and expanding fireball. During the cooling, hadrons are formed again (hadronization) which interact until the system is too dilute (hadronic phase and freeze-out).

RHIC and LHC) explore the region around $\mu \sim 0$, the lower-energy runs at RHIC and GSI (FAIR) are dedicated to the search for the critical end point. Moreover, the experimentally collected data allow to draw conclusions about the properties of matter.

1.3 Probing the QGP: Ultra-relativistic Heavy-Ion Collisions

Though it is assumed that already the collision of two nuclei at a centre-of-mass energy larger than $\sqrt{s_{NN}} \approx 8$ GeV leads to such a strong compression of matter that colour charges are deconfined, the experimental proof that such a QGP is really created in a heavy-ion collision is extremely challenging since a deconfined phase is supposed to exist only for a very short time of roughly $\Delta t \leq 10 \text{ fm}/c \sim 3 \cdot 10^{-23} \text{ s}$, depending on the collision energy.

The description of such a collision is based on the assumption that ions are composed of nucleons. Due to the fact that these ions are accelerated to ultra-relativistic velocities, they are Lorentz-contracted, approaching each other along the *beam axis* (which is normally taken to be the z -axis, see Fig. 1.4) with an offset that is called the *impact parameter* b .

This impact parameter (or more precisely the direction of the strongest momentum gradient) and the direction of the beam axis determine the so-called *reaction plane*. For $b > 0 \text{ fm}$, some of the nucleons do not participate in the collision. They are called *spectators* and leave the reaction zone immediately, in contrast to the *participants* of the reaction.

A snapshot of the subsequent collision (which is here assumed to be central, i.e., $b = 0 \text{ fm}$) is shown in Fig. 1.5. After the impact, in the early phase of the collision, the matter is strongly compressed, indicating a *pre-equilibrium* state. When compression is completed, a phase with extremely high temperatures and densities is created. The system is supposed to be able to equilibrate, developing a *fire-*

ball which expands and cools rapidly. As soon as the temperature drops below the phase transition to the deconfined phase, hadrons are formed again (*hadronization*). Subsequent interactions of those hadrons (in the hadronic phase) will be both elastic and inelastic until *chemical freeze-out* is reached where *inelastic collisions* terminate. The expanding system becomes more and more dilute so that finally, at the *kinetic freeze-out*, all further interactions have ceased. The created hadrons which might be subject to decay will finally reach the detectors.

However, hadrons are always created in a heavy-ion collision, independent of QGP formation. Thus, the only way to prove the existence of a QGP experimentally, via a heavy-ion collision, is to analyze the particle distributions at the end of the collision and to compare them to theoretical predictions assuming the creation of a deconfined phase. Therefore, it is extremely important to identify robust criteria to distinguish a QGP from a hot and dense hadron gas.

Since the system of coordinates (as shown in Fig. 1.4) is usually defined such that the beam axis is aligned with the z -direction, the momentum \vec{p} of a particle can easily be split into a longitudinal (p_L) and a transversal (p_T) component (w.r.t. the beam axis), indicated by the angle θ

$$p_L = p \cdot \cos \theta = p_z, \quad (1.3)$$

$$p_T = p \cdot \sin \theta = \sqrt{p_x^2 + p_y^2}. \quad (1.4)$$

In contrast to the transverse momentum, the longitudinal component (p_L) is not invariant under Lorentz transformations. Therefore, the *rapidity* is introduced, which describes the velocity of a particle p_L/E in longitudinal direction,

$$y = \operatorname{artanh} \left(\frac{p_L}{E} \right) = \frac{1}{2} \ln \left(\frac{E + p_L}{E - p_L} \right), \quad (1.5)$$

implying the relations⁹

$$E = m_T \cdot \cosh y, \quad p_L = m_T \cdot \sinh y, \quad (1.6)$$

where $m_T = \sqrt{m_0^2 + p_T^2}$ denotes the transverse mass of the particle. If it is not possible to identify the mass of a particle, the *pseudorapidity*,

$$\eta = -\ln \left[\tan \left(\frac{\vartheta}{2} \right) \right] = \frac{1}{2} \ln \left(\frac{p + p_L}{p - p_L} \right), \quad (1.7)$$

is used instead, with ϑ being the emission angle w.r.t. the beam axis. In the ultra-relativistic case ($E \approx p \gg m_0$), rapidity and pseudorapidity become equal.

1.4 The Signatures of QGP

Certainly, one of the main challenges of heavy-ion collision experiments is the identification of the QGP phase. However, since the early stages of the evolution are not directly accessible, (unique) signatures are needed, some of which are:

⁹Additionally, it also implies $\cosh y = \gamma_L$ and $\sinh y = \gamma_L v_L$ with $\gamma_L = 1/\sqrt{1 - v_L^2}$.

- **Global observables**

The rapidity distribution of particles dN/dy and transverse energy dE_T/dy allow for the determination of temperature, entropy, and energy density of the system created in a heavy-ion collision. These observables need to be compared to model calculations, e.g. lattice QCD calculations [24, 25, 26, 28], in order to investigate if the system may have reached the QGP phase.

- **Early thermalization and flow**

Though it is not clear from first principles that a QGP phase should be in thermodynamic equilibrium, it could be shown that hydrodynamical models, which are based on the assumption of (local) thermodynamic equilibrium, can describe flow observables quite well (as will be discussed in detail in the following chapter) [15, 16]. These flow characteristics imply that the interaction of the medium constituents are strong enough to translate density gradients into pressure and thus to convert spatial into momentum anisotropies. This collective behaviour has to result from the early stages of the collision since the spatial anisotropy (in contrast to momentum anisotropy) reduces with the expansion of the system. Moreover, the collective behaviour is supposed to change when the system undergoes a phase transition [36].

- **Photon and dilepton measurements**

Photons and dileptons do not interact strongly. Thus, they leave the medium without being influenced by the expanding fireball, carrying information about the initial state. Thermal photons may serve as a thermometer, while the reconstruction of the spectral density of vector mesons (like the ρ -meson) could indicate the restoration of chiral symmetry. In general, such a restoration should lead to the disappearance of the mass splitting between hadronic states of opposite parity [37].

- **Hard probes, jet quenching and Mach cones**

The interaction of particles with high transverse momenta, created at the early stages of the collision, with the medium they traverse (leading either to quenching effects or the formation of a signal that is interpreted to be due to the formation of a Mach cone) has recently attracted a lot of interest and is the main topic of this thesis. It will be discussed in detail in the following chapters.

- **Strangeness Enhancement**

Since the production of an $s\bar{s}$ -pair is more likely in a deconfined phase (where thermal production of $s\bar{s}$ -pairs, having a threshold of ~ 300 MeV, is supposed to set in), more s -quarks should be present in the QGP phase, leading to an enhancement in the formation of multi-strange baryons [38] which was found experimentally [39].

- **The J/ψ -meson**

Originally, it was assumed that the production of J/ψ (which is a bound $c\bar{c}$ -state) is suppressed in the QGP phase since color screening prevents $c\bar{c}$ binding [40]. Indeed, it was found that the J/ψ melts in the QGP phase,

implying rapid production and subsequent destruction. However, lattice calculations indicate that the J/ψ may survive at temperatures larger than the transition temperature to the QGP and, due to the creation of many c -quarks at large (LHC) energies, its yield may even be enhanced at very high collision energies [41].

- **Fluctuations and correlations**

Fluctuations are sensitive to the underlying degrees of freedom. Thus, the fluctuations of conserved quantities like charge, energy, or transverse momentum, could provide a signal of the QGP [42]. These effects should be very strong in the vicinity of the critical point. Likewise, the correlation of charges and their associated anti-charges seen in late-stage hadronization may indicate a deconfined phase [43].

Chapter 2

The Experimental Search for the QGP

The possibility to accelerate and collide ions was already discussed in the late 1960's [8]. After systematic studies with heavy ions at the BEVALAC¹ and the AGS², the hunt for the QGP started with the collision of lead ions at the SPS³ at CERN. Seven experiments (like NA49 and NA45/CERES), all being fixed target experiments, participated in the SPS project. The SIS⁴ program at GSI followed and its experiments, like HADES⁵, provide (up until today) information about hadron properties in a hot and dense environment.

The development of experimental tools culminated in the first heavy-ion collider, RHIC at BNL, which was commissioned in the year 2000. It has a circumference of 3.8 km and is composed of two independent rings. Unlike fixed target experiments, the kinetic energy of the accelerated particles is available in the center-of-mass frame. Its four experiments BRAHMS, PHENIX, PHOBOS, and STAR⁶ are dedicated to heavy-ion physics. While RHIC operates around $\mu \approx 0$ MeV, other experiments e.g. at the SPS, probe regions with nonzero quark chemical potentials, but lower temperatures.

In the near future, the LHC (with a circumference of 27 km) at CERN is expected to commence operation. The primary target of its experiments ATLAS, CMS, and LHCb⁷ is the search for the Higgs boson⁸ in proton+proton (p+p) collisions. The ALICE⁹ experiment however, is primarily dedicated to heavy-ion physics.

¹The BEVATRON (**B**illions of **eV** **S**ynchro**t**ron) was coupled to the SuperHILAC (**S**uper **H**eavy-**I**on **L**inear **A**ccelerator), and subsequently named BEVALAC. It is located at the Lawrence Berkeley National Laboratory (LBNL), Berkely, USA.

²Alternating Gradient Synchrotron, BNL, USA.

³Super Proton Synchrotron, CERN, Switzerland.

⁴SchwerIonenSynchrotron, GSI, Germany.

⁵High Acceptance Di-Electron Spectrometer.

⁶Broad **R**ange **H**adron **M**agnetic **S**pectrometers **E**xperiment (BRAHMS), **P**ioneering **H**igh **E**nergy **N**uclear **I**nteractions **E**Xperiment (PHENIX), and **S**olenoidal **T**racker **A**t **R**HIC (STAR).

⁷**A** Toroidal **L**H**C** **A**pparatus (ATLAS), **C**ompact **M**uon **S**olenoid (CMS), and **L**H**C** **b**eauty (LHCb).

⁸The Higgs boson is a massive, scalar elementary exchange particle, predicted by the standard model.

⁹**A** **L**arge **I**on **C**ollider **E**xperiment.

Accelerator	Beam	Max. Energies	Period
Bevalac, LBNL	Au	< 2 AGeV	1984 – 1993
AGS, BNL	Si / Au	14.5 / 11.5 AGeV	1986 – 1994
SPS, CERN	S / Pb	200 / 158 AGeV	1986 – 2002
SIS, GSI	Au	2 AGeV	1992 –
RHIC, BNL	Au	$\sqrt{s_{NN}} = 130 / 200$ GeV	2000 –
LHC, CERN	Pb	$\sqrt{s_{NN}} = 5500$ GeV	2009 –
FAIR, GSI	Au	$\sqrt{s_{NN}} = 5\text{--}10$ GeV	2015 –

Table 2.1

Review of accelerators, their maximal energies, and commission periods that were pioneering in the sector of heavy-ion collisions.

The energy regions (see table 2.1) covered by the planned FAIR Facility is understood to be adequate to probe highly compressed baryonic matter, the deconfinement phase transition, and the critical point.

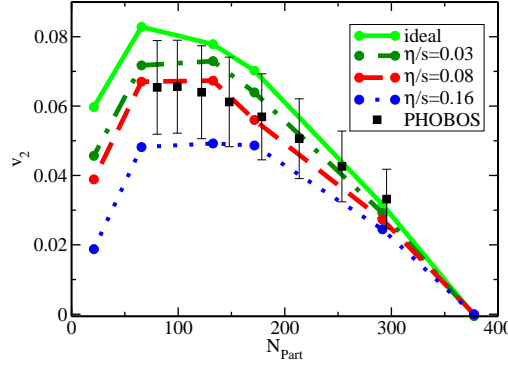
The first phase of the RHIC program has become a great success since the results obtained by the four experiments, summarized in a series of so-called white papers [10, 11, 12, 13], are in remarkable agreement with each other. RHIC offered the unique possibility to study p+p, d+Au and Au+Au at identical center-of-mass energies¹⁰ from 19.6 to 200 GeV for different collision geometries using the same detectors. The main observations can be summarized as follows:

- Fast thermalization, indicated by strong momentum anisotropies (elliptic flow),
- Low viscosity of the produced medium, suggesting that it behaves like a “nearly ideal fluid”,
- Jet Quenching, implying a large energy loss of partons and the creation of a dense and opaque system,
- Strong suppression of high- p_T heavy-flavour mesons, stressing a large energy loss of the heavy c and b quarks,
- Direct photon emission at high transverse momenta confirms the scaling behaviour of hard processes,
- Charmonium suppression similar to the one observed at lower SPS energies.

These results are consistent with models describing the creation of a new state of thermalized matter, exhibiting an almost ideal hydrodynamic behaviour. However, they do not provide evidence that the QGP has been formed and leave a lot of open questions especially concerning the properties of the created medium.

This thesis is based on the idea of coupling two of the major experimental findings (the almost ideal hydrodynamic behaviour of the phase created and the energy deposition of hard particles) to study jet-medium interactions and to identify matter properties if possible.

¹⁰The Mandelstam variable s is the sum of the 4-momenta of the scattering particles (before the interaction), $s = (p_1^\mu + p_2^\mu)^2$. In the centre-of-mass system, the total energy of the reaction is given in terms of $\sqrt{s_{NN}}$.

**Figure 2.1**

Elliptic flow (v_2) from measured PHOBOS data [47] for charged particles in Au+Au collisions at a center-of-mass energy of $\sqrt{s_{NN}} = 200$ MeV compared to a hydrodynamical calculation [16] for various ratios of shear viscosity to entropy density, η/s .

2.1 Collective Effects

The medium created in a heavy-ion collision at RHIC energies features a strong collective behaviour which causes the system to behave like a fluid. For non-central collisions, the initial reaction zone reveals an elliptic shape (see Fig. 1.4). If the interactions between the plasma components are sufficiently strong, the resulting flow will follow the density gradients which are stronger along the short side of the reaction zone. Thus, the initial spatial density profile becomes an azimuthal momentum anisotropy of the emitted particles that can be quantified by the Fourier coefficients of the particle distribution [44]

$$\frac{dN}{p_T dp_T dy d\phi} = \frac{1}{2\pi} \frac{dN}{p_T dp_T dy} \left[1 + 2 \sum_{n=1}^{\infty} v_n(p_T, y, b) \cos(n\phi) \right]. \quad (2.1)$$

The second coefficient v_2 , commonly named *elliptic flow*, accounts for the largest contribution. Anisotropies arising from the hydrodynamical flow are the prominent indicator of fast thermalization in heavy-ion collisions since they require a medium in local thermodynamic equilibrium. Appropriate models implicitly assume that the equilibration time is roughly 1 fm [45, 46]. It was demonstrated [16] (see Fig. 2.1) that the elliptic flow which characterizes the eccentricity of the system can be described by a medium possessing a small amount of viscosity. Ideal fluid calculations lead to an overprediction of the data for peripheral collisions, but still show a decent agreement for central reactions [15, 16].

This success of describing the momentum anisotropies which are assumed to be conserved from the early stages of the collision using hydrodynamical models lead to the conclusion that the medium created at RHIC and thus the medium that was formed at the very early stages of our universe behaves like a fluid. This is normally regarded as one of the most important results from RHIC.

However, these hydrodynamical calculations strongly depend on the initial conditions and in general fail to describe the elliptic flow for charged hadrons away from mid-rapidity. In Ref. [48] it was argued that the observed collective behaviour

might not require local thermodynamical equilibration. An isotropic momentum distribution of the medium constituents could be sufficient to obtain the measured data. Indeed, even such a fast isotropization would point towards a strongly coupled QGP.

2.2 Hard Probes

Among all available observables in high-energy nucleus-nucleus collisions, particles with a large transverse momentum ($p_T \gtrsim 2$ GeV) are assumed to be a very useful probe to study the hot and dense phase created in the reaction. Such *hard probes* are produced at the very early stages of the collision ($t \sim 0.1$ fm) in the hard scattering of partons (quarks, antiquarks or gluons) with large momentum transfer Q^2 . Subsequent collision and radiation processes (which can be described using hard QCD processes [49, 50, 51]) induce showers of particles, so-called *jets*, that propagate through the system formed.

In contrast to direct photons that should escape the medium unaffectedly, the created jets will further interact with the medium, resulting in an energy loss of the jet from which fundamental information about the jet characteristics (like its energy and mass) and plasma properties can be deduced. Of course it is preferable to reconstruct single jets. However, at RHIC individual jet reconstruction is very difficult due to the large background contribution. At LHC energies, different cross sections are anticipated (see Fig. 2.2) and since hard jets with $p_T > 50$ GeV will become accessible, full jet reconstruction will be possible in the next years.

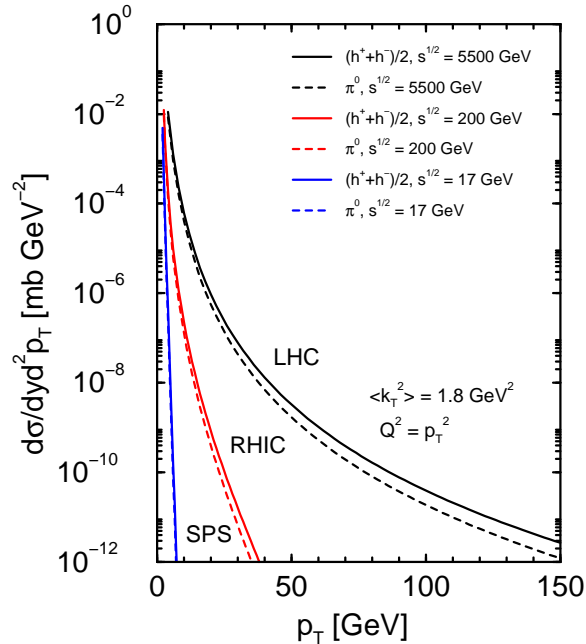
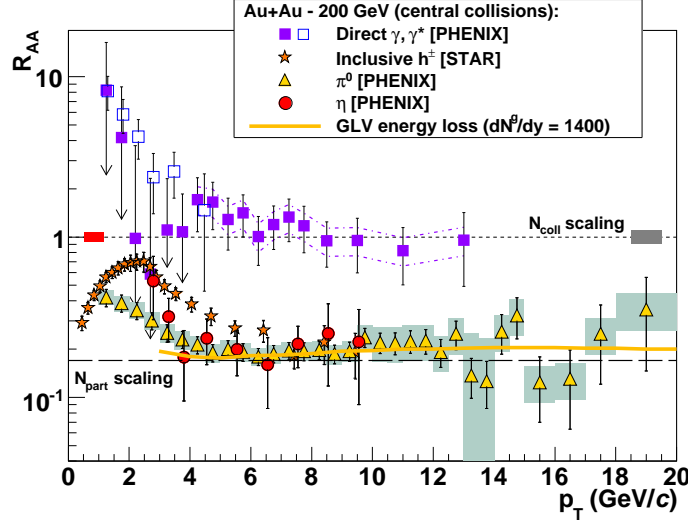


Figure 2.2

Differential cross section, calculated to leading order (LO) from pQCD, for inclusive neutral pion and charged hadron production at mid-rapidity in p+p reactions at SPS, RHIC, and LHC energies [52].

**Figure 2.3**

$R_{AA}(p_T)$ measured in central Au+Au collisions at $\sqrt{s_{NN}} = 200$ GeV, taken from [55], for direct photons [56], π^0 [57], η mesons [58], and charged hadrons [59, 60], compared to theoretical predictions for parton energy loss in a dense medium with $dN^g/dy = 1400$ (yellow curve) [61, 62].

The pattern of particles produced in a heavy-ion collision is examined using particle correlations which characterize the jet-medium effects. Several different methods including one, two, and three particles have been established within the recent years and will be discussed in the following.

2.2.1 One-particle correlations

Direct information about thermodynamic and transport properties can be deduced from one-particle correlations. They are usually studied applying the nuclear modification factor

$$R_{AA} = \frac{d^2 N_{AA}/dp_T dy}{T_{AA} d\sigma_{NN}/dp_T dy}, \quad (2.2)$$

which is the ratio of the number of particles produced in a nucleus-nucleus (A+A) collision to the yield in a p+p collision, scaled by the number of binary collisions, for a certain transverse momentum p_T and rapidity y . $T_{AA} = \langle N_{coll} \rangle / \sigma_{NN}$ is the nuclear overlap function and σ_{NN} the nucleon-nucleon cross section. Thus, this measure is based on the assumption that the production of high- p_T particles scales with the number of binary collisions in p+p reactions.

If a jet traverses the medium created without being affected, the nuclear modification factor will be equal to one. However, initial state effects like the Cronin effect¹¹ [53, 54] might result in an enhancement for low p_T with $R_{AA} > 1$, while energy loss induced by jet-medium interactions lead to a suppression and $R_{AA} < 1$. The nuclear modification factor is usually taken as the experimental measure to

¹¹The Cronin effect leads to a p_T -broadening and is often attributed to multiple soft parton scattering.

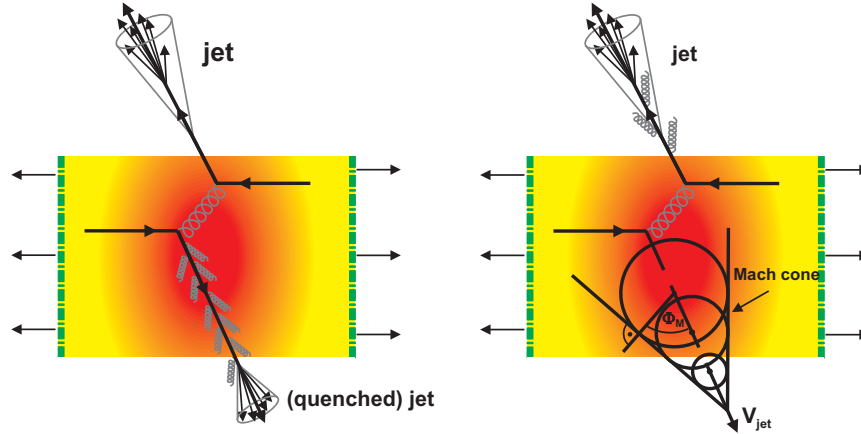


Figure 2.4

Formation and propagation of a jet, leading either to a quenched jet (left panel) or the creation of a Mach cone by the interference of sound waves (right panel) according to Ref. [55].

determine the amount of energy lost by a hard particle.

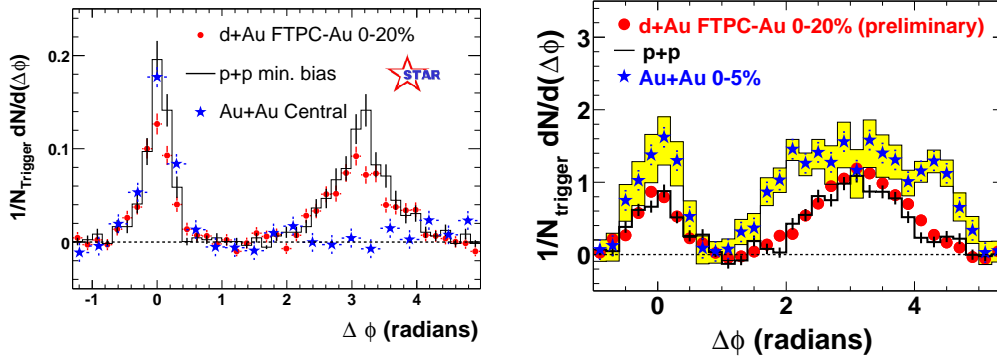
Figure 2.3 compiles the measured $R_{AA}(p_T)$ for various hadron species and for direct photons in central Au+Au collisions at $\sqrt{s_{NN}} = 200$ GeV. Above $p_T \sim 5$ GeV, direct photons [56] are in perfect agreement with the binary collision scaling, while π^0 [57], η [58], and charged hadrons [59, 60] (dominated by π^\pm) show a common factor of ~ 5 suppression. The fact that $R_{AA} \approx 0.2$ irrespective of the nature of the finally produced hadrons is consistent with a scenario where the energy loss of the parent parton takes place prior to its fragmentation into hadrons. The suppression factor is close to the so-called participant scaling which assumes a strong quenching limit where only hadrons formed close to the surface of the medium can reach the detector without any further modification [63].

2.2.2 Two-particle correlations

Due to energy conservation, jets are always produced back-to-back, i.e., separated by an angle of π in the azimuthal plane. One of these partons, the *trigger particle*, is assumed to leave the expanding fireball without any further interaction while its partner parton, the *associated particle*, traverses the medium depositing energy and momentum (see Fig. 2.4).

Two-particle correlations are determined on a statistical basis by selecting high- p_T trigger particles and measuring the azimuthal ($\Delta\phi = \phi - \phi_{\text{trig}}$) distributions of associated hadrons relative to the trigger. A p_T -range for the trigger and the associated particles has to be defined, taking into account that the hard partons leaving the medium unaffected exhibit a larger momentum than those ones propagating through the medium.

The fact that a jet, moving through dense matter and depositing its energy, eventually disappears is called *jet quenching*. This effect was predicted theoretically [64, 65, 66] and found experimentally at RHIC [10, 11, 12, 13, 67, 68]. As the left panel of Fig. 2.5 reveals, the trigger-side peak (the so-called *near-side*) is the same

**Figure 2.5**

Two-particle correlation functions for a trigger particle of $4 < p_T^{\text{trig}} < 6$ GeV and associated particles with (left panel) $p_T^{\text{assoc}} > 2$ GeV [67] and (right panel) $0.15 < p_T^{\text{assoc}} < 4$ GeV [69] for p+p, d+Au, and central Au+Au collisions.

for p+p, d+Au and Au+Au collisions, but the correlations in the opposite direction of the trigger jet (the *away-side*) shows a vanishing yield for central Au+Au collisions, demonstrating that the corresponding away-side jet is quenched.

This observation is considered as a proof that in an Au+Au collision, in contrast to p+p and d+Au reactions, a dense and opaque system is formed, indicating the creation of a QGP.

Since energy and momentum always have to be conserved, the “missing” fragments of the away-side (quenched) parton are either shifted to lower energies and/or scattered into a broadened angular distribution. Both, softening and broadening, are seen in the data when the p_T of the away-side associated hadrons is lowered [see right panel of Fig. 2.5 and also e.g. panel (c) of Fig. 2.6]. A double or even triple-peaked structure arises. However, the main characteristic of the angular distribution is the “dip” on the away-side around $\Delta\phi = \pi$, accompanied by the two neighbouring local maxima at $\Delta\phi \approx \pi \pm (1.1 - 1.4)$. Such a structure is interpreted as a signal of the creation of a Mach cone (see section 5.1) due to the preferential emission of energy from the quenched parton into a definite angle with respect to the jet axis.

Fig. 2.6 displays the correlations for two different trigger- p_T ranges ($3 < p_T < 4$ GeV and $5 < p_T < 10$ GeV) for increasing p_T of the associated hadrons. The decreasing away-side yield for larger p_T^{assoc} and the distortion of the double peak is clearly visible. Moreover, for hard trigger and associated particles [see panel (h) of Fig. 2.6], an away-side peak around $\Delta\phi = \pi$ is formed again, providing a di-jet signal and thus pointing towards highly-energetic partner particles that punch through the medium created (*punch-through jets*) [70, 71].

The structure of the away-side was examined intensively. A study of the centrality dependence (see left panel of Fig. 2.7) [72, 73] reveals that for centralities up to 40% a clear double-peaked structure occurs on the away-side while for more peripheral collisions an away-side peak around $\Delta\phi = \pi$ appears again, suggesting that the developing structure depends on the path length of the jet through the medium.

The comparison of different collision energies, from SPS $\sqrt{s_{NN}} = 17.2$ GeV to

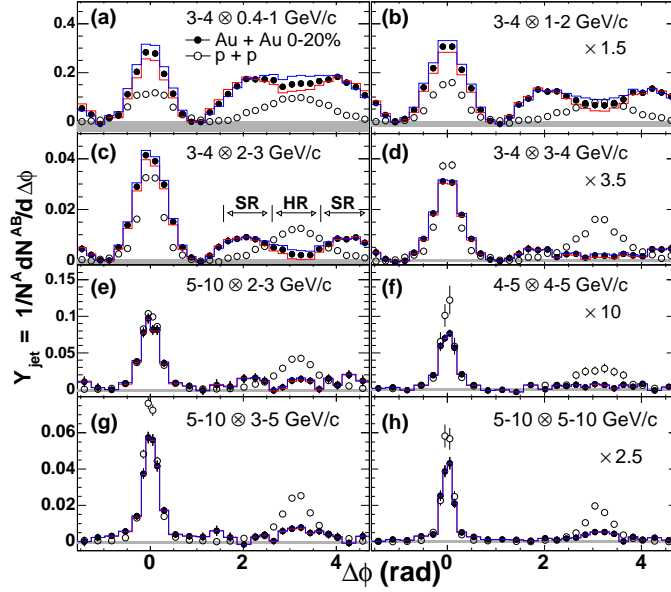


Figure 2.6

The $\Delta\phi$ distributions for various trigger and (increasing) partner p_T of p+p and (0 – 20%) central Au+Au collisions. The solid histograms and shaded bands indicate the uncertainties regarding background subtraction [70].

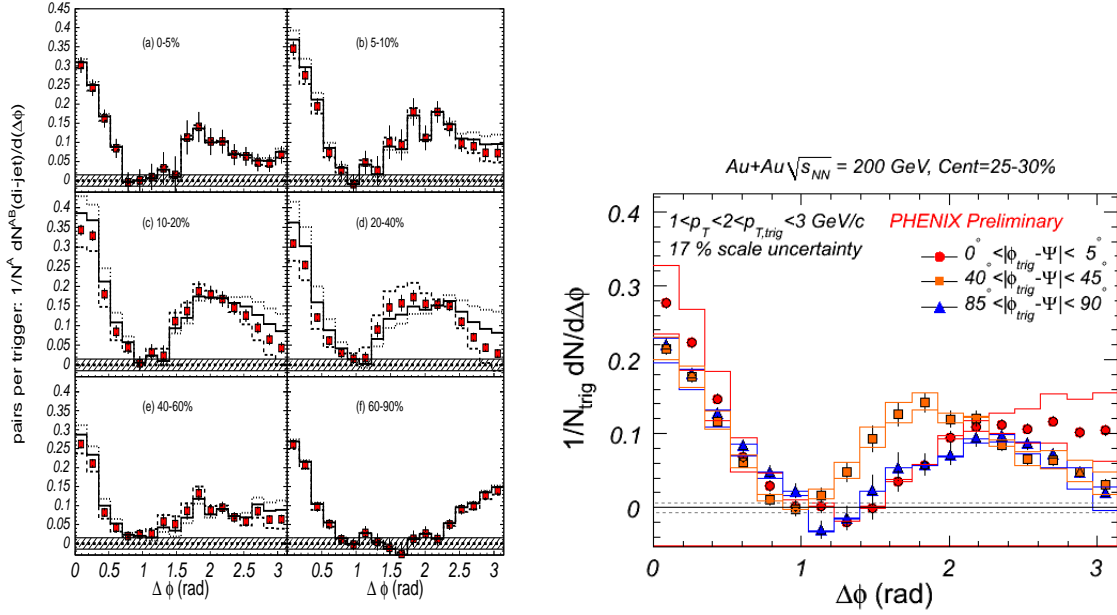
top RHIC energies of $\sqrt{s_{NN}} = 200$ GeV [74, 75] showed that the double-peaked structure gets more pronounced for larger energies. However, still a plateau-like shape with a slight peak around $\Delta\phi = 2$ rad is visible [75, 76].

Recently, the reaction plane dependence of the two-particle correlation was investigated [77, 78, 79] (see right panel of Fig. 2.7). For this purpose, different angles of a trigger particle with respect to the reaction plane were chosen for a certain centrality of 25 – 30% and the corresponding two-particle correlations were determined to examine the influence of different geometries like the path length of the quenched jet. As can be seen from the right panel of Fig. 2.7, the near-side jet contribution is nearly the same for all correlations, but the away-side reveals a plateau *in-plane* (i.e., for a small angle with respect to the reaction plane), while *out-of-plane* (thus for large angles with respect to the reaction plane) a clear double-peaked structure occurs. The most interesting feature is that for an angle of $40 < |\phi_{\text{trig}} - \psi| < 45^\circ$ between trigger jet ϕ_{trig} and reaction plane ψ , the peak on the away-side is shifted to smaller values in $\Delta\phi$.

Several explanations for the observation of the double-peaked structure have been discussed:

- **Large Angle Gluon Radiation**

This medium-induced gluon bremsstrahlung [80, 81] is generated if a (color) charged particle, i.e., a quark, is accelerated or decelerated. The emitted gluons have a continuous spectrum in energy due to the fact that the acceleration process itself may vary and thus the emitted gluons exhibit different energies/wavelengths. However, since a quark cannot deposit more energy into the medium than it got through the acceleration/deceleration, the energy

**Figure 2.7**

(Left panel) Two-particle correlations for a trigger particle with $2.5 < p_T < 4.0$ GeV and associated particles with $1.0 < p_T < 2.5$ GeV for various centrality regions of Au+Au collisions at $\sqrt{s_{NN}} = 200$ GeV [73]. (Right panel) Reaction plane dependence of the per trigger yield in 25 – 30% Au+Au collisions at $\sqrt{s_{NN}} = 200$ GeV for trigger particles with $1.0 < p_T < 2.0$ GeV and associated particles of $2.0 < p_T < 3.0$ GeV [78, 79].

spectrum is cut at the upper end. Assuming that the gluon emission only takes places in the direction of the away-side jet ("large angle" [81]), the gluon radiation causes a deviation of the jet from being back-to-back.

- **Deflected Jets**

The strong interaction of the jet traversing through the medium might cause a deflection of the jet: In non-central collisions the interaction region of the two colliding nuclei has a large eccentricity. Due to this eccentricity, a jet might be carried away with the expanding medium and therefore leave its predetermined direction of propagation.

- **Mach cone**

If the away-side parton propagates with a velocity v_{jet} larger than the speed of sound c_s of the medium, it is supposed to re-distribute its energy to lower- p_T particles, leading to quenched parton correlations for high- p_T . This re-distributed energy might excite sound waves (like a stone sliding through water) which interfere, forming a Mach cone (see right panel of Fig. 2.4) with an enhanced particle emission into the distinct Mach cone angle (ϕ_M) [82, 83]. This thesis addresses the question if a jet propagating through a hydrodynamical medium, resembling the hot and dense phase created within a heavy-ion collision, can lead to Mach cone formation and if such a Mach

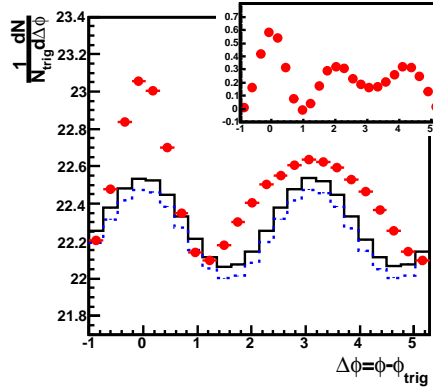


Figure 2.8

Measured two-particle correlation (raw data, points) and background from flow modulation (elliptic flow, solid line) as well as scaled according to ZYAM (dashed line) [90]. The upper small insert shows the two-particle correlation after background subtraction.

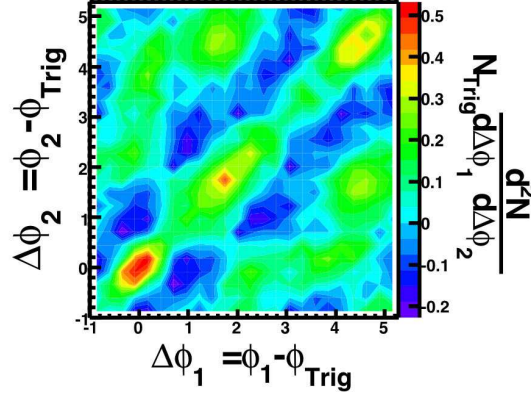
cone will result in a measurable signal. Thus, the main discussion of a Mach-cone contribution will follow in the course of the subsequent chapters. For a detailed discussion of Mach cones see chapter 5.

- **Čerenkov Gluon Radiation**

Čerenkov gluon radiation¹² leads to the formation of a cone similar to a Mach cone [84]. However, as shown in Refs. [85, 86], there is a strong dependence of the Čerenkov angle [$\cos \Theta_c = 1/n(p)$, where n is the index of reflection] on the momentum p of the emitted particle. This angle vanishes quickly for larger momenta. Thus, a distinct experimental signature of Čerenkov gluon radiation is a strong momentum dependence of the cone angle for soft particles and a disappearance of the cone-like structure for associated particles with large p_T . As can be seen from Fig. 2.6, the position of the peaks within the away-side do not change strongly with the p_T of the associated particle. Therefore, it is very unlikely that the observed double-peaked structure results from Čerenkov Gluon Radiation. A Mach cone however, is independent of the momentum of the emitted particles.

One of the crucial problems in the context of two-particle correlations is the treatment of the background which has to be subtracted. Experimentally, combinatorial background contributions and the superimposed effects of collective azimuthal modulations (the elliptic flow) are taken care of with different techniques [73, 87, 88]. The most common method applied to experimental data [89] is to subtract the elliptic flow represented by the v_2 parameter in Eq. (2.1). This method (ZYAM) is discussed controversially since it is not clear from first principles if the flow is independent of the jet transit. The acronym ZYAM (Zero Yield At Minimum) is

¹²Čerenkov radiation is electromagnetic radiation that is emitted when a charged particle passes through an insulator at a speed greater than the speed of light in that medium. It is named after the Russian scientist Pavel Alekseyevich Čerokov. Since higher frequencies (and thus shorter wavelengths) are more intense, the observed radiation is blue. It is often used for particle identification.

**Figure 2.9**

Background subtracted three-particle correlations for a 30 – 50% central $Au + Au$ collision at top RHIC energies [94].

chosen because the elliptic flow is adjusted to the measured particle correlation in such a way that the subtraction leads to a vanishing yield at a certain, freely chosen minimum between near-side and away-side. However, since the elliptic flow contribution might be much weaker, it is not clear at all that the emerging minimum, which can even be shifted by this method, will lead to a vanishing yield. Moreover, as can be seen from Fig. 2.8, even a measured broad away-side peak might result after background subtraction, applying the ZYAM method, in a double-peaked structure. In other words, if the hydrodynamical flow changes due to a jet, the particle correlations obtained from experimental measurements should be revised and might lead to a different interpretation of the ongoing processes. A theoretical proof for the applicability for ZYAM is still missing.

2.2.3 Three-particle correlations

Two-particle correlations could not clarify the origin of the double-peaked structure on the away-side. In particular, since they include a sampling over many different events, it cannot be distinguished if the peaks result from randomly deflected jets or if due to the formation of a Mach cone two particles are produced on the away-side and emitted into a distinct direction. Thus, for a further exploration, three-particle correlations were introduced [91, 92, 93]. Again, high- p_T trigger particles are chosen on a statistical basis, but for this analysis, the azimuthal angle of two associated particles ($\Delta\phi_1 = \phi_1 - \phi_{\text{trig}}$ and $\Delta\phi_2 = \phi_2 - \phi_{\text{trig}}$) are determined and plotted against each other (see Fig. 2.9).

Randomly deflected jets will lead to a smeared peak around the diagonal axis over a wide range in $\Delta\phi_1$ and $\Delta\phi_2$, resulting from the fact that two particles within a deflected jet will be redirected into the same direction. On the other hand, if a Mach cone is formed, two particles will be produced due to the distinct emission into the Mach-cone angle and thus by measuring the relative angle between the trigger particle and its associated hadrons (considering the possible interchange of $\Delta\phi_1$ and $\Delta\phi_2$ due to symmetry), four distinct peaks are expected [91].

The measurement reveals (cf. Fig. 2.9) that the resulting shape is a superposition

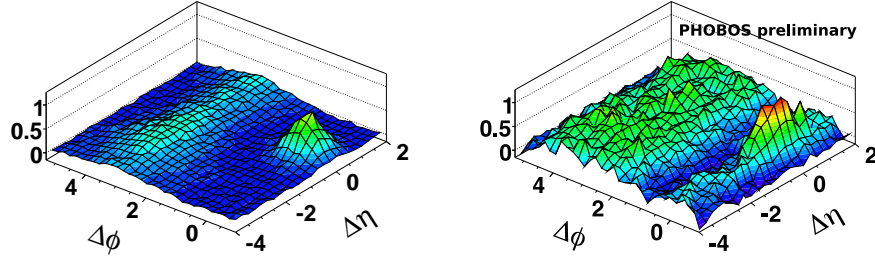


Figure 2.10

Distribution of correlated hadron pairs as a function of $\Delta\phi$ and $\Delta\eta$ for a trigger particle with $p_T > 2.5$ GeV in p+p (PYTHIA simulation, left panel) and 0 – 30% Au+Au collisions [95].

of deflected jets and Mach-cone contributions. However, since four distinct peaks occur on the away-side, the experimentally determined three-particle correlations seem to favour the Mach-cone ansatz.

2.3 Correlations in Pseudorapidity: The Near-side Ridge

The *ridge* is a long-ranged structure in $\Delta\eta$ on the near-side. While the near-side jet in p+p collisions (see left panel of Fig. 2.10) displays a clear peak at $(\Delta\eta, \Delta\phi) \approx (0, 0)$, as expected from jet fragmentation, the near-side jet in heavy-ion collisions features a peak at the same location, but is elongated over a wide range in pseudorapidity (see right panel of Fig. 2.10) [70, 95, 96, 97].

The existence of such a long-ranged correlation on the near-side is not understood since by construction the trigger parton is the one least affected by the medium. Investigations of this structure ensured that its properties like the particle composition, p_T -slope, and intra-particle correlations are very similar to the soft underlying events of the collision [77]. Thus, the ridge seems to be formed by bulk matter and not from jet fragments. Many different models for explaining the ridge phenomena have been discussed, including plasma instabilities [98], glasma flux-tubes [99], and modifications of the two- and three-particle correlations due to radial flow [100].

Part II

**Hydrodynamics and Jet Energy
Loss**

Chapter 3

Ideal Hydrodynamics

It is a long-standing tradition in heavy-ion physics to model the dynamical evolution of heavy-ion collisions using fluid dynamics [101, 102, 103, 104], mainly because the only essential information needed is the Equation of State (EoS) of the matter considered, allowing for straightforward studies of nuclear matter properties like the phase transition to the QGP.

Once an initial condition is specified, the Equations of Motion (EoM) uniquely determine the dynamics of the collision. Thus, a detailed knowledge of the microscopic processes on the parton level is not needed, in contrast to cascade models like UrQMD (Ultrarelativistic Quantum Molecular Dynamics) [105] or BAMPS (Boltzmann Approach of MultiParton Scatterings) [106].

The basic requirement for the applicability of hydrodynamics is that the system has to be in (local) thermodynamic equilibrium. This condition is fulfilled if the mean free path λ of a particle is small compared to the length scale over which the fluid-dynamical variables vary. In that case, local equilibrium can develop due to the scattering of particles.

Around 20 years ago, it was already shown that collective effects at the BEVALAC experiment, like the sideward deflection of matter in the reaction plane [named *side-splash* or *bounce-off*, the coefficient v_1 of Eq. (2.1)], and azimuthal deflections out of the reaction plane [*squeeze-out*, the coefficient v_2 of Eq. (2.1)], can be described using hydrodynamical models [107]. However, the great success of the fluid-dynamical model came with the RHIC experiment. As already discussed in section 2.1, the collective flow effects measured at RHIC, in particular the elliptic flow (v_2), were described by hydrodynamics on a quantitative level [16].

While the application of ideal hydrodynamics already leads to qualitative and sometimes even quantitative agreement with the measured data [15], it is important to include viscous effects to check whether their impact is really small. Indeed, the matter created in heavy-ion collisions appears to be a “nearly perfect liquid”, characterized by a small amount of viscosity [16].

In a heavy-ion collision, the equilibration time is estimated to be roughly 1 fm. Afterwards, the system can be described using thermodynamical field quantities like the temperature $T(t, \vec{x})$, the four-velocities $u_\mu(t, \vec{x})$, and the chemical potentials $\mu_i(t, \vec{x})$. The temporal evolution of these variables is determined by the hydrodynamical Equations of Motion until the system is so dilute that the fluid constituents decouple and can be regarded as free particles, a transition called freeze-out (see

section 1.3). Therefore, hydrodynamical models can be applied to the expansion stage of heavy-ion collisions. However, they require a proper choice of the initial conditions and the freeze-out procedure.

3.1 The Hydrodynamical Equations of Motion

Relativistic hydrodynamics implies the (local) conservation of energy-momentum (represented by the energy-momentum tensor $T^{\mu\nu}$) and of conserved charge currents like (net) baryon number or (net) strangeness (described by N_i^μ) [108]. For n currents, this leads to the hydrodynamical Equations of Motion

$$\partial_\mu T^{\mu\nu} = 0, \quad \mu, \nu = 0, \dots, 3; \quad (3.1)$$

$$\partial_\mu N_i^\mu = 0, \quad i = 1, \dots, n. \quad (3.2)$$

They form a system of $4 + n$ conservation equations for the energy, the three components of the momentum, and the n currents of the system. In general, however, these equations have $10 + 4n$ independent variables, the ten independent components of the symmetric energy-momentum tensor $T^{\mu\nu}$ and four components of each current N_i . Thus, the system of fluid-dynamical equations is not closed and cannot be solved in complete generality.

Additional assumptions are needed to close this set of equations. The simplest approximation is to consider an ideal gas in local thermodynamical equilibrium. From kinetic theory, the energy-momentum tensor and (net) charge currents are [109]

$$T^{\mu\nu}(x) = \frac{g}{(2\pi)^3} \int \frac{d^3\vec{k}}{E} k^\mu k^\nu [n(E) + \bar{n}(E)], \quad (3.3)$$

$$N_i^\mu(x) = \frac{g}{(2\pi)^3} q_i \int \frac{d^3\vec{k}}{E} k^\mu [n(E) - \bar{n}(E)], \quad (3.4)$$

where g counts the particle's degrees of freedom like spin and colour, $E = \sqrt{\vec{k}^2 + m^2}$ describes the on-shell energy of particles with rest mass m , and $n(E)$ [$\bar{n}(E)$] denotes the Fermi–Dirac and Bose–Einstein distributions for particles (and antiparticles)

$$n(E) = \frac{1}{\exp\{[E - \sum_i \mu_i(x)]/T(x)\} \pm 1}, \quad (3.5)$$

$$\bar{n}(E) = \frac{1}{\exp\{[E + \sum_i \mu_i(x)]/T(x)\} \pm 1}. \quad (3.6)$$

Here, $\mu_i(x)$ and $T(x)$ are the local chemical potentials and temperatures.

Defining the *local rest frame* [LRF, a frame where $u^\mu = (1, \vec{0})$], the (net) charge density (of type i)

$$n_i = g q_i \int \frac{d^3\vec{k}}{(2\pi)^3} [n(E) - \bar{n}(E)], \quad (3.7)$$

the ideal gas energy density

$$\varepsilon = g \int \frac{d^3\vec{k}}{(2\pi)^3} E [n(E) + \bar{n}(E)], \quad (3.8)$$

and the ideal gas pressure

$$p = g \int \frac{d^3 \vec{k}}{(2\pi)^3} \frac{\vec{k}^2}{3E} [n(E) + \bar{n}(E)], \quad (3.9)$$

equations (3.3) and (3.4) can be rewritten, resulting in the energy-momentum tensor and conserved current for an ideal gas,

$$T^{\mu\nu} = (\varepsilon + p)u^\mu u^\nu - pg^{\mu\nu}, \quad (3.10)$$

$$N_i^\mu = n_i u^\mu. \quad (3.11)$$

Here, u^μ is the fluid four-velocity, $u^\mu = \gamma(1, \vec{v})$ with $\gamma = (1 - v^2)^{-1/2}$, and $g^{\mu\nu} = \text{diag}(+, -, -, -)$ is the metric tensor. Now, the $4 + n$ Equations of Motion contain only $5 + n$ unknown functions for the energy density ε , the pressure p , the three components of the 4-velocity u^μ and the n conserved currents. To close the system an EoS for the fluid has to be specified

$$p = p(\varepsilon, n_i). \quad (3.12)$$

The EoS is the only place where information about the nature of the fluid constituents and their macroscopic interactions enters. Though an EoS is normally computed for a system in (local) thermodynamic equilibrium, its explicit form is completely unrestricted, allowing e.g. the inclusion of phase transitions. Thus, the ideal-fluid approximation derived above allows to consider a wider class of systems than just an ideal gas in (local) thermodynamic equilibrium.

3.2 Numerical Solutions for the Equations of Motion

For numerical applications, it is convenient to write the conservation equations using calculational (i.e. laboratory) frame quantities. For the sake of simplicity, we restrict to the case of one conserved charge until the end of this chapter. Defining

$$E \equiv T^{00} = (\varepsilon + p)\gamma^2 - p, \quad (3.13)$$

$$\vec{M} \equiv T^{0i} = (\varepsilon + p)\gamma^2 \vec{v}, \quad (3.14)$$

$$R \equiv N^0 = n\gamma, \quad (3.15)$$

where E is the energy density, \vec{M} the 3-momentum and R the charge density, the conservation equations (3.1) and (3.2) take the form

$$\frac{\partial E}{\partial t} + \vec{\nabla} \cdot (E\vec{v}) = -\vec{\nabla} \cdot (p\vec{v}), \quad (3.16)$$

$$\frac{\partial \vec{M}}{\partial t} + \vec{\nabla} \cdot (\vec{M}\vec{v}) = -\vec{\nabla} p, \quad (3.17)$$

$$\frac{\partial R}{\partial t} + \vec{\nabla} \cdot (R\vec{v}) = 0. \quad (3.18)$$

This set of equations can be solved numerically. However, E , \vec{M} , and R are values in the laboratory frame. While in the non-relativistic limit there is no difference between n and R or ε and E and the momentum density of the fluid can be simply related to the fluid velocity, the LRF quantities ε , n , and \vec{v} have to be extracted

from the laboratory frame values of E , \vec{M} , and R in the relativistic case that has to be employed for the description of heavy-ion collisions. Such a transformation requires the knowledge of the EoS, $p(\varepsilon, n)$, and the velocity \vec{v} of the local rest frame.

3.3 Transformation between the Laboratory Frame and the Local Rest Frame

The transformation between the laboratory frame (that is chosen for numerical applications) and the LRF is in principle explicitly given by equations (3.13) – (3.15). However, this implies a root-finding algorithm for a system of 5 equations that are nonlinear, since the pressure p is a function of ε and n . This would be very time-consuming in a numerical application. Therefore, the complexity of the transformation problem is reduced as follows [110].

The fundamental observation is that \vec{M} and \vec{v} are parallel. This leads via

$$\vec{M} \cdot \vec{v} = |\vec{M}| \cdot |\vec{v}| = (\varepsilon + p)\gamma^2 v^2 = (\varepsilon + p)(\gamma^2 - 1) = E - \varepsilon \quad (3.19)$$

[or alternatively using Eqs. (3.13) – (3.15)] to the expressions

$$\varepsilon = E - |\vec{M}| \cdot |\vec{v}|, \quad n = R/\gamma = R\sqrt{1 - v^2}. \quad (3.20)$$

Moreover, using that

$$|\vec{M}| = (\varepsilon + p)\gamma^2 v = (E + p)v, \quad (3.21)$$

a general expression for the velocity \vec{v} in the LRF can be derived

$$v = \frac{|\vec{M}|}{E + p(\varepsilon, n)}. \quad (3.22)$$

Inserting Eq. (3.20) leads to a fixed point equation for v

$$v = \frac{|\vec{M}|}{E + p(E - |\vec{M}| \cdot |\vec{v}|, R\sqrt{1 - v^2})}. \quad (3.23)$$

Thus, for given E , \vec{M} , and R , the modulus of the fluid velocity can be determined. From that the fluid velocity vector \vec{v} can be reconstructed using $\vec{v} = v\vec{M}/M$. Finally, the expressions of Eq. (3.20) return the energy and charge densities ε and n in the LRF. The pressure p can then be determined using the EoS $p(\varepsilon, n)$.

3.4 The SHASTA

In order to model heavy-ion collisions with ideal fluid dynamics, a discretized version of the five conservation equations (3.16) – (3.18) has to be solved. However, due to the fact that a system of coupled, nonlinear equations is studied, complex algorithms have to be applied. One of those is the SHASTA (SHarp And Smooth Transport Algorithm) [110, 111, 112, 113, 114] that will be used in this thesis.

Another prominent algorithm is the (relativistic) HLLE (Harten–Lax–van Leer–Einfeldt) algorithm, originally proposed in Ref. [115]. Both algorithms are euclidian and explicit, i.e., the local rest frame quantities E , \vec{M} , and R are discretized on a fixed, euclidean grid and are calculated at discrete time steps t_n , involving only quantities from previous time steps t_{n-1} .

The basic idea is to construct the full 3-dimensional solution by solving sequentially three one-dimensional problems, applying the so-called method of *operator splitting*. In general, the numerical algorithm solves equations of the type

$$\partial_t U + \partial_x(Uv + f) = 0, \quad (3.24)$$

where U is one of the quantities E , \vec{M} , or R , and f represents one of the source terms on the r.h.s. of equations (3.16) – (3.18). For a general review, see e.g. Ref. [116].

To smooth over instabilities and oscillations, Boris and Book [111, 112] developed the method of *flux correction* (FCT, Flux Corrected Transport). An antidiffusion term is added to the transport scheme after each timestep.

Since the equations of relativistic hydrodynamics are hyperbolic, they respect the causality requirement. Any algorithm solving the finite difference of a hyperbolic differential equation has to fulfill the Courant–Friedrichs–Lewy criterion [117]

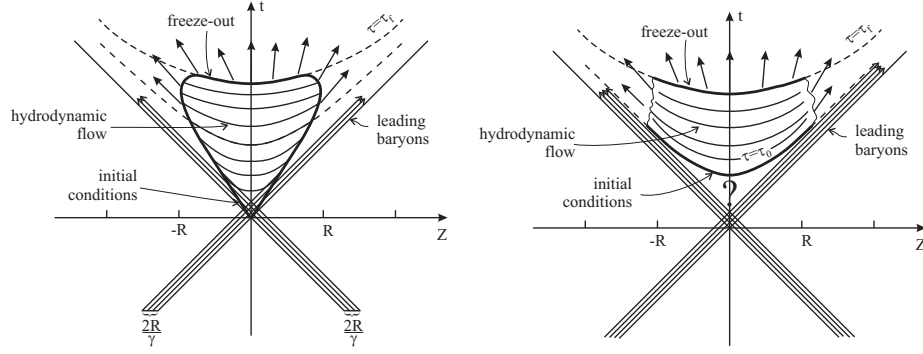
$$\frac{\Delta t}{\Delta x} \equiv \lambda < 1, \quad (3.25)$$

ensuring that matter is transported causally within each time step, $\Delta t = \lambda \Delta x$. Since the algorithm averages the propagated quantities over a cell after each time step, it may happen that due to this process matter is distributed over an acausal spatial distance. This purely numerical phenomenon is called *prediffusion*. Some FCT algorithms like the SHASTA require that $\lambda < 1/2$. It was shown in Refs. [110, 114] that $\lambda = 0.4$ is a convenient choice for the algorithm used in the following.

3.5 Initial Conditions

As mentioned above, the hydrodynamical framework provides a useful tool to study high-energy nuclear collisions. However, the initial conditions are not specified by hydrodynamics and have to be chosen in a proper way, defining the thermodynamic state of matter shortly after the impact. The evolution of the collision in longitudinal direction, normally chosen to be along the z -axis in direction of the beam, is usually described via two idealizations:

- **Landau Model:** Historically, this was the first scenario where fluid dynamics was applied to hadron-hadron collisions [118]. It characterizes low-energy collisions and assumes that the nuclei are completely stopped during the impact, creating a highly excited, baryon-free medium at rest which is immediately thermalized. The EoS of this medium is supposed to have a simple form of $p = c_s^2 \varepsilon$, with the speed of sound $c_s = \text{const}$. Though Lorentz contraction is weak, the initial extension of the medium in longitudinal direction is much smaller than in the transverse plane, resulting in a mainly longitudinal and thus one-dimensional expansion. Experimental

**Figure 3.1**

Schematic picture of the temporal evolution of a system formed in a heavy-ion collision according to the Landau (left panel) and Bjorken model (right panel) [120].

results are in reasonable agreement with the Landau model, however, for unrealistic values of the initial energy.

- Bjorken Model:** It describes the penetration of two nuclei through each other and is therefore applied to collisions with a high center-of-mass energy. Though already investigated earlier [119], it was Bjorken who first applied it to hadron-hadron collisions [64]. After the impact, again due to the limited amount of nuclear stopping power, the baryon charges keep on moving along the light cone, while microscopic processes lead to the creation of hot and dense matter in the collision zone that is assumed to thermalize within a time of τ_0 . In contrast to the Landau model, the collective velocity of this medium is supposed to scale like $v_z = z/t$. However, this condition leads to boost invariance¹: Energy density and pressure are independent of the longitudinal coordinate z if it is compared at the same proper time $\tau = \sqrt{t^2 - z^2}$. Such curves of constant τ describe hyperbola in space-time as can be seen in Fig. 3.1. The disadvantage of this model is that it becomes independent of the rapidity since the EoM are boost-invariant along the beam axis. In Ref. [17] it was shown that at RHIC energies boost-invariant and non-boost-invariant calculations lead to very similar results.

One possibility to determine the initial conditions in the transverse plane is given by the **Glauber Model** [121] which is described in detail in appendix B. It is based on the assumption that in ultra-relativistic heavy-ion collisions the participating partons can be described as colliding particles. Thus, nucleus-nucleus collisions are treated as multiple nucleon-nucleon collisions. Starting from a Woods–Saxon distribution for a nucleus,

$$\rho_A(\vec{x}) = \frac{\rho_0}{1 + \exp[(|\vec{x}| - R_A)/d]}, \quad (3.26)$$

¹Boost invariance describes the invariance of a system under Lorentz boost which is a transformation to a system moving with different velocity.

where $R_A = 6.4$ fm and $d = 0.54$ fm assuming a gold nucleus with mass number $A = 197$, the nuclear thickness function

$$T_A(x, y) = \int_{-\infty}^{+\infty} dz \rho_A(\vec{x}) \quad (3.27)$$

is calculated, describing the part of a nucleus A which is seen by a nucleon that passes through this nucleus. The parameter ρ_0 , indicating the mean density in the nucleus, is chosen to fulfill the condition $\int d^3\vec{x} \rho_A(\vec{x}) = A$. Subsequently, see appendix B, the number density of participating nucleons (n_{WN}), also referred to as wounded nucleons, and the number density of binary collisions (n_{BC}), characterizing the number of inelastic nucleon-nucleon collisions, can be calculated via

$$n_{WN}(x, y, b) = T_A\left(x + \frac{b}{2}, y\right) \left[1 - \left(1 - \frac{\sigma_{NN} T_A\left(x - \frac{b}{2}, y\right)}{A} \right)^A \right] \\ + T_A\left(x - \frac{b}{2}, y\right) \left[1 - \left(1 - \frac{\sigma_{NN} T_A\left(x + \frac{b}{2}, y\right)}{A} \right)^A \right], \quad (3.28)$$

$$n_{BC}(x, y, b) = \sigma_{NN} T_A\left(x + \frac{b}{2}, y\right) T_A\left(x - \frac{b}{2}, y\right), \quad (3.29)$$

where σ_{NN} is the nucleon-nucleon cross section which is assumed to be $\sigma \simeq 40$ mb for a Au+Au collision at $\sqrt{s}_{NN} = 200$ GeV. While the total number of participating nucleons $N_{WN}(b) = \int dx dy n_{WN}(x, y, b)$ can be used to define the centrality class of a collision, Glauber-model initial conditions are characterized by the parametrization [122]

$$\varepsilon(\tau = \tau_0, x, y, b) = \text{const} \times n_{BC}(x, y, b), \quad (3.30)$$

which leads to a reasonable description of experimentally measured multiplicity distributions. The constant is usually chosen to guarantee that the central energy density in the overlap region corresponds to a predefined temperature. As proven e.g. in Refs. [15, 122], this temperature can eventually be employed as a fitting parameter for the multiplicities.

The above expression for the energy density can be used as initial condition for a hydrodynamic simulation of a heavy-ion collision since such a numeric application propagates (as shown in the previous sections) an initial energy and velocity distribution.

When studying jets traversing a hydrodynamical medium in part III, we will first focus on a static medium. However, chapter 11 discusses an expanding system where Glauber-model initial conditions [as defined by Eq. (3.30)] are applied, though any longitudinal flow will be neglected.

However, there are still theoretical uncertainties regarding the Glauber approach and it is discussed if plasma-instability models [123] or a color-glass condensate [124] might be more appropriate to specify the initial stage. The latter one is based on the idea of gluon saturation at high energies and, as shown in Ref. [122], does not seem to require early thermalization in order to describe the elliptic flow of charged hadrons.

3.6 The Equation of State

Once an initial condition is specified, the hydrodynamic evolution is uniquely determined by the Equations of Motion (see section 3.1). However, the essential information needed is the Equation of State (EoS), providing a correlation between the pressure $p(\varepsilon, n_i)$, the energy density ε , and the charge densities n_i of the system.

Several different EoS are used in hydrodynamical applications, since they also offer the possibility to study phase transitions. Thus, some of the applied EoS try to model the phase diagram of QCD (see sec. 1.2) to check its properties.

The simplest EoS is the one for an ideal gas of massless non-interacting massless particles given by

$$p(\varepsilon) = \frac{\varepsilon}{3}, \quad (3.31)$$

which is independent of the charge current. The relation is derived in appendix C. This EoS is certainly an idealization, but appropriate to study the intrinsic characteristics of certain effects – as we are going to do in the course of this thesis. Therefore, the results presented in part III will focus on the ideal gas EoS. In particular, a gas of massless gluons will be considered, for which

$$\varepsilon(T) = \frac{g}{30}\pi^2 T^4 \quad \text{and} \quad g = 2 \cdot 8 = 16. \quad (3.32)$$

Another very common EoS contains a first order phase transition [15, 113]. In Ref. [113], the MIT-Bag Model² [125] specifies the QGP phase and is coupled via Gibbs' conditions for phase equilibrium³ to a hadronic phase described by a modified version of the σ - ω model [126].

Likewise, an EoS characterizing a cross-over transition to a chiral condensate [127] and an EoS based on Lattice QCD calculations [122, 128] were employed to hydrodynamic models.

The EoS defines the speed of sound c_s of the medium studied,

$$c_s^2 = \left. \frac{\partial p}{\partial \varepsilon} \right|_{s/n}. \quad (3.33)$$

For an ideal gas EoS, the speed of sound is $c_s = \sqrt{1/3} \approx 0.577$.

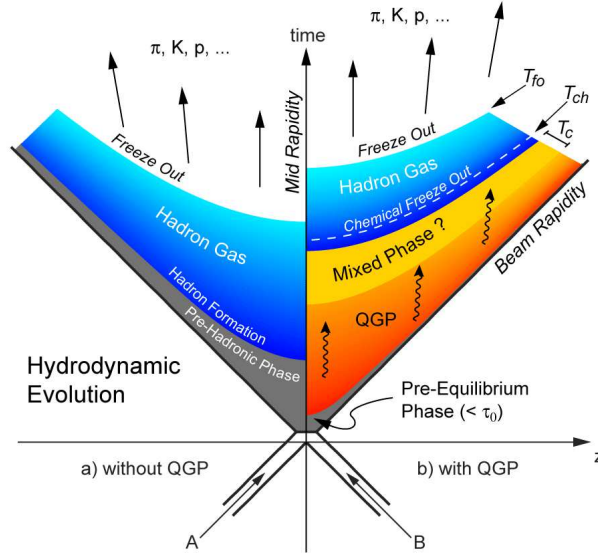
3.7 The Freeze-out

Hydrodynamical calculations provide the temporal evolution of fields, like e.g. the temperature and the velocity (flow) fields. In order to compare the result of such a hydrodynamic evolution to experimentally measured observables, a description for the conversion of the fluid into particles is needed.

Consequently, the hydrodynamical configuration has to be translated into an emission profile, providing the average number of particles from the fluid with a momentum p . A schematic representation of the complete process is given in Fig. 3.2.

²The MIT Bag Model describes a bag in which the quarks are allowed to move around freely.

³Gibbs' conditions for phase equilibrium imply that $p_{\text{had}} = p_{\text{QGP}}$, $T_{\text{had}} = T_{\text{QGP}}$, and $\mu_{\text{had}} = \mu_{\text{QGP}}$.

**Figure 3.2**

Schematic representation of a heavy-ion collision, plotted as a function of t and z , considering a scenario without (left panel) and with (right panel) the creation of a QGP [130].

One of the common approaches used is the **Cooper–Frye** freeze-out [129]. Here, the above mentioned conversion of the fluid into free particles is achieved instantaneously at a critical surface $d\Sigma_\mu$ in space-time (see Fig. 3.3). Applying a thermal distribution function, the emission pattern can be calculated via

$$E \frac{dN}{d^3\vec{p}} = \int_{\Sigma} d\Sigma_\mu p^\mu f(u \cdot p/T), \quad (3.34)$$

where T is the temperature and u^μ the flow at the freeze-out position. Here, f denotes the Boltzmann, Fermi–Dirac or Bose–Einstein distribution. Since

$$\frac{dN}{d^3\vec{p}} = \frac{1}{E} \frac{dN}{p_T dp_T d\varphi dy}, \quad (3.35)$$

with the rapidity y and the azimuthal angle φ , the Cooper–Frye formula can be rewritten to the form usually applied in heavy-ion physics

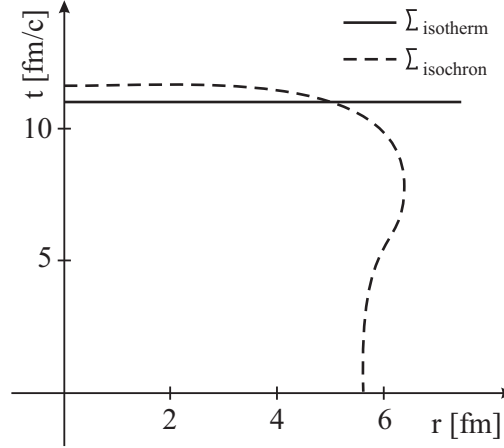
$$\frac{dN}{p_T dp_T d\varphi dy} = \int_{\Sigma} d\Sigma_\mu p^\mu f(u \cdot p/T). \quad (3.36)$$

In the following, we will focus on the Boltzmann distribution

$$f(u \cdot p/T) = \frac{g}{(2\pi)^3} \exp \left[-\frac{u^\mu p_\mu}{T(x)} \right]. \quad (3.37)$$

3.7.1 The Hypersurface

The hypersurface indicates the space-time location for particle emission according to some criterion which is typically chosen to be a certain time or a certain temperature, specifying an *isochronous* or *isothermal* freeze-out, respectively, see Fig.

**Figure 3.3**

A schematic picture of the space-time distribution of an isochronous and isothermal hypersurface.

3.3.

Since the code [114] applied for the hydrodynamical simulations in part III is defined in (t, x, y, z) , we will use Cartesian coordinates below. For the parameterization of a boost-invariant surface, depending on the rapidity, see e.g. Ref. [131].

Thus, the hypersurface is defined as

$$\Sigma^\mu = \Sigma^\mu(t, \vec{x}) = \Sigma^\mu[t(\vec{x}), \vec{x}], \quad (3.38)$$

and the normal vector on such a surface is given by

$$d\Sigma^\mu = \varepsilon^{\mu\nu\lambda\rho} \frac{\partial \Sigma_\nu}{\partial x} \frac{\partial \Sigma_\lambda}{\partial y} \frac{\partial \Sigma_\rho}{\partial z} d^3\vec{x}, \quad (3.39)$$

where $\varepsilon^{\mu\nu\lambda\rho}$ denotes the Levi-Civita tensor

$$\varepsilon^{\mu\nu\lambda\rho} = -\varepsilon_{\mu\nu\lambda\rho} = \begin{pmatrix} 1 & \text{even permutation} \\ -1 & \text{odd permutation} \\ 0 & \text{otherwise} \end{pmatrix}. \quad (3.40)$$

Generally, $d\Sigma^\mu$ can be either space-like ($d\Sigma = g_{\mu\nu} d\Sigma^\mu d\Sigma^\nu < 0$) or time-like ($d\Sigma > 0$).

3.7.2 Isochronous Freeze-out

An isochronous freeze-out describes the particle emission at a certain time $t = \text{const.}$ Therefore, the normal vector of the hypersurface, applying Eq. (3.39), becomes

$$d\Sigma_\mu = (1, \vec{0}) d^3\vec{x} \quad (3.41)$$

which leads to a straight line in the space-time representation shown in Fig. 3.3. The general expression⁴ for the four-momentum of the particle is⁵

$$p^\mu = [m_T \cosh y, \vec{p}_T, m_T \sinh y], \quad (3.42)$$

where $m_T = \sqrt{\vec{p}_T^2 + m^2}$ denotes the transverse mass of the particle. This relation fulfills the condition $p^\mu p_\mu = m^2$. After choosing a transverse momentum distribution, where $\vec{p}_T = p_T(\cos \varphi, \sin \varphi)$, and inserting the Boltzmann distribution Eq. (3.37), the particle emission pattern can be computed via

$$\begin{aligned} \frac{dN}{p_T dp_T d\varphi dy} &= \frac{g}{(2\pi)^3} \int d^3\vec{x} m_T \cosh y \\ &\times \exp \left\{ -\frac{\gamma}{T} \left[m_T \cosh y - p_T v_x \cos \varphi \right. \right. \\ &\quad \left. \left. - p_T v_y \sin \varphi - m_T v_z \sinh y \right] \right\}. \end{aligned} \quad (3.43)$$

3.7.3 Isothermal Freeze-out

The isothermal freeze-out characterizes the decoupling of the fluid if the temperature has fallen below a certain critical temperature T_{FO} . In that case, the normal vector of the hypersurface [see Eq. (3.39)] is

$$d\Sigma_\mu = (1, -\partial_x t, -\partial_y t, -\partial_z t) d^3\vec{x}. \quad (3.44)$$

Thus, for the same assumptions as in the previous section [namely for inserting the four-momentum of Eq. (3.42) and considering a Boltzmann distribution], one obtains

$$\begin{aligned} \frac{dN}{p_T dp_T d\varphi dy} &= \frac{g}{(2\pi)^3} \int d^3\vec{x} \left[m_T \cosh y - (\partial_x t) p_T \cos \varphi \right. \\ &\quad \left. - (\partial_y t) p_T \sin \varphi - (\partial_z t) m_T \sinh y \right] \\ &\times \exp \left\{ -\frac{\gamma}{T} \left[m_T \cosh y - p_T v_x \cos \varphi \right. \right. \\ &\quad \left. \left. - p_T v_y \sin \varphi - m_T v_z \sinh y \right] \right\}. \end{aligned} \quad (3.45)$$

As mentioned above, the Cooper–Frye method implies an instantaneous conversion of the fluid fields into free particles, assuming that the mean-free path immediately changes from zero to infinity. Since viscosity (which assumes a non-zero mean-free path within the fluid) increases during the last stages of the fireball evolution, it is possible that this direct conversion and emission generates considerable unphysical artifacts.

Therefore, hydrodynamical evolutions were coupled to hadronic kinetic models like the UrQMD [105, 127, 132, 133]. The transition between these two models, however, is still done using a Cooper–Frye prescription. Unfortunately, the decoupling time of the fluid is unknown and because of effects like rescattering and

⁴Here the transformations $E = m_T \cosh y$ and $p_z = m_T \sinh y$ are used.

⁵Actually several particles species have to be considered for a correct prescription of the freeze-out leading to various particles with different masses.

coalescence [134, 135] at the late stages of the hadronic evolution one might have to revise the freeze-out prescription.

3.7.4 Bulk Flow Freeze-out

As an alternate freeze-out scheme we will also consider a calorimetric-like observable (called **bulk flow freeze-out**) in part III, describing a polar-angle distribution weighted by the momentum density

$$\begin{aligned} \frac{dS}{d\cos\theta} &= \sum_{cells} |\vec{\mathcal{P}}_c| \delta(\cos\theta - \cos\theta_c) \\ &= \int d^3\mathbf{x} |\vec{M}(t, \vec{x})| \delta\left[\cos\theta - \frac{M_x(t, \vec{x})}{|\vec{M}(t, \vec{x})|}\right] \Big|_{t_f} \end{aligned} \quad (3.46)$$

that was presented in Ref. [136]. Its basic assumption is that all the particles inside a given small subvolume of the fluid will be emitted in the same direction. This quantity differs from the Cooper–Frye freeze-out mainly by the neglect of the thermal smearing at the freeze-out time.

The very strong assumption in this decoupling scheme is that hadrons from each frozen-out cell emerge parallel to the cell total momentum $\mathcal{P}_c^i = d^3\vec{x} T^{0i}(t_f, \vec{x})$. Many other similar purely hydrodynamic measures of bulk flow are possible [82], e.g. weighting by energy or entropy density instead of momentum density. Indeed, an equivalent measure is given by the energy flow distribution [137]

$$\frac{d\mathcal{E}}{d\phi dy} = \int d^3\vec{x} \mathcal{E}(\vec{x}) \delta[\phi - \Phi(\vec{x})] \delta[y - Y(\vec{x})], \quad (3.47)$$

where ϕ denotes the azimuthal angle and y the rapidity. However, we found no qualitative differences when changing the weight function.

Chapter 4

Viscous Hydrodynamics

One of the major successes at RHIC was to show that the medium created during a heavy-ion collision behaves like a “nearly perfect fluid” [10, 11, 12, 13, 14]. This implies that dissipative effects have to be small, but it does not answer the question *how* perfect the “nearly perfect liquid” is, an issue that cannot be answered using ideal hydrodynamics. Therefore, dissipative quantities have to be included into the description of heavy-ion collisions in order to gain a qualitative understanding.

It is necessary to apply viscous hydrodynamics for various realistic initial conditions (which are unfortunately not known explicitly for a heavy-ion collision) to confirm the smallness of the dissipative quantities. Recently [122, 138, 139, 140, 141, 142, 143, 144, 145, 146, 147, 148], theoreticians just began to study those viscous effects systematically and to apply a corresponding description to the collective flow.

4.1 Tensor Decomposition of N^μ and $T^{\mu\nu}$

As already discussed in the previous chapter, relativistic hydrodynamics implies the (local) conservation of energy-momentum and any (net) charge current, Eqs. (3.1) and (3.2). The tensor decomposition of the respective quantities, N^μ and $T^{\mu\nu}$, with respect to an arbitrary, time-like, normalized 4-vector $u^\mu = \gamma(1, \vec{v})$ ($u_\mu u^\mu = 1$) reads

$$N_i^\mu = n_i u^\mu + V_i^\mu, \quad (4.1)$$

$$T^{\mu\nu} = \varepsilon u^\mu u^\nu - (p + \Pi) \Delta^{\mu\nu} + 2q^{(\mu} u^{\nu)} + \pi^{\mu\nu}. \quad (4.2)$$

In the LRF, where $u^\mu = (1, \vec{0})$,

$$n_i \equiv N_i^\mu u_\mu \quad (4.3)$$

is the *net charge density*,

$$V_i^\mu \equiv \Delta_\nu^\mu N_i^\nu \quad (4.4)$$

the *diffusion current*,

$$\varepsilon \equiv u_\mu T^{\mu\nu} u_\nu \quad (4.5)$$

the *energy density*,

$$p + \Pi \equiv -\frac{1}{3}\Delta^{\mu\nu}T_{\mu\nu} \quad (4.6)$$

the sum of the *thermodynamical pressure* p and *bulk viscous pressure* Π ,

$$\Delta^{\mu\nu} = g^{\mu\nu} - u^\mu u^\nu \quad (4.7)$$

denotes the projector onto the 3-space orthogonal to u^μ ,

$$q^\mu \equiv \Delta^{\mu\nu}T_{\nu\lambda}u^\lambda \quad (4.8)$$

is the *heat flux current* and

$$\pi^{\mu\nu} \equiv T^{\langle\mu\nu\rangle} = \left(\Delta_{(\alpha}^{\mu} \Delta_{\beta)}^{\nu} - \frac{1}{3}\Delta^{\mu\nu}\Delta_{\alpha\beta} \right) T^{\alpha\beta} \quad (4.9)$$

the *shear stress tensor*. The notation

$$a^{(\mu\nu)} \equiv \frac{1}{2}(a^{\mu\nu} + a^{\nu\mu}) \quad (4.10)$$

stands for the symmetrization in all Lorentz indices and

$$a^{\langle\mu\nu\rangle} \equiv \left(\Delta_{\alpha}^{(\mu} \Delta_{\beta)}^{\nu} - \frac{1}{3}\Delta^{\mu\nu}\Delta_{\alpha\beta} \right) a^{\alpha\beta} \quad (4.11)$$

represents the symmetrized, traceless spatial projection. By construction,

$$\Delta^{\mu\nu}u_\nu = 0, \quad V^\mu u_\mu = 0, \quad q^\mu u_\mu = 0, \quad \pi^{\mu\nu}u_\mu = \pi^{\mu\nu}u_\nu = \pi^\mu_\mu = 0, \quad (4.12)$$

$$\Delta^{\mu\alpha}\Delta_{\alpha}^{\nu} = \Delta^{\mu\nu}, \quad (4.13)$$

implying that q^μ has only three and $\pi^{\mu\nu}$ only five independent components. Due to the condition for normalization, u^μ also has only three independent components. The space-time derivative decomposes into

$$\partial^\mu a = u^\mu \dot{a} + \nabla^\mu a, \quad (4.14)$$

where $\dot{a} = u_\mu \partial^\mu a$ is the convective (comoving) time derivative and $\nabla^\mu \equiv \Delta^{\mu\nu} \partial_\nu$ the gradient operator. Differentiating $u^\mu u_\mu = 1$ with respect to the space-time coordinates leads to the relation

$$u_\mu \partial_\nu u^\mu = 0. \quad (4.15)$$

Obviously, setting the dissipative quantities bulk viscous flow Π , heat flux current q^μ , shear stress tensor $\pi^{\mu\nu}$, and net charge density V_i^μ to zero

$$\Pi = 0, \quad q^\mu = 0, \quad \pi^{\mu\nu} = 0, \quad V_i^\mu = 0, \quad (4.16)$$

Eqs. (4.1) and (4.2) reduce to the ideal-fluid limit discussed in chapter 3, Eqs. (3.10) and (3.11), describing (local) thermodynamical equilibrium.

4.2 The Eckart and Landau Frames

So far, u^μ is arbitrary, but one can give it a physical meaning. Then, u^μ is a dynamical quantity whose three independent components have to be determined ($u^\mu u_\mu = 0$ is still valid).

- **Eckart (or Particle) frame:**

Here, u^μ is the 4-velocity of the (net) charge flow, i.e., the velocity of charge transport. Thus, u^μ is parallel to the (net) charge current N_i^μ

$$u^\mu = \frac{N_i^\mu}{\sqrt{N_i \cdot N_i}}, \quad (4.17)$$

and the diffusion current vanishes,

$$V_i^\mu = 0. \quad (4.18)$$

- **Landau (or Energy) frame:**

This choice describes u^μ as the 4-velocity of the energy flow. Therefore, u^μ is parallel to the energy flow

$$u^\mu = \frac{T^\mu_\nu u^\nu}{\sqrt{u^\alpha T^\beta_\alpha T_{\beta\gamma} u^\gamma}}, \quad (4.19)$$

and obviously the heat flux current q^μ vanishes,

$$q^\mu = 0. \quad (4.20)$$

Both frames have their advantages. The Eckart frame leads to a simple law for charge conservation, while the Landau frame reduces the complexity of the energy-momentum tensor. However, considering a system without a (net) charge, the 4-velocity in the Eckart frame is not well defined.

4.3 The Fluid Dynamical Equations of Motion

The tensor decomposition of the n (net) charge currents [Eq. (4.1)] and the energy-momentum tensor [Eq. (4.2)] contain $11 + 4n$ unknowns, ε, p, n_i (n Eqs.), Π , the three components of V_i^μ ($3n$ Eqs.), the three components of q^μ , and the five components of $\pi^{\mu\nu}$ ¹.

However, the conservation of the n (net) currents, the energy and the 3-momentum leads to $4 + n$ Equations of Motion. In particular, these are

¹An equivalent way of counting says that for any given 4-velocity u^μ there are the $17 + 5n$ unknowns ε (1 Eq.), p (1 Eq.), n_i (n Eqs.), Π (1 Eq.), V_i^μ ($4n$ Eqs.), q^μ (4 Eqs.) and $\pi^{\mu\nu}$ (10 Eqs.), which are reduced to $11 + 4n$ unknowns by the conditions $q^\mu u_\mu = 0$ (1 Eq.), $\pi^\mu_\mu = 0$ (1 Eq.), $u_\mu \pi^{\mu\nu} = 0$ (4 Eqs.), and $u_\mu V_i^\mu = 0$ (n Eqs.).

- **(Net) charge conservation:**

$$\partial_\mu N_i^\mu = \dot{n}_i + n_i \theta + \partial_\mu V_i^\mu = 0, \quad (4.21)$$

where $\theta = \partial_\mu u^\mu$ is the so-called expansion scalar.

- **Energy conservation:**

$$\begin{aligned} u_\nu \partial_\mu T^{\mu\nu} &= \dot{\varepsilon} + (\varepsilon + p + \Pi) \theta + u_\mu \dot{q}^\mu + \partial_\mu q^\mu - \pi^{\mu\nu} \partial_\nu u_\mu \\ &= 0. \end{aligned} \quad (4.22)$$

- **Momentum conservation (acceleration equation):**

$$\Delta^{\mu\nu} \partial^\lambda T_{\nu\lambda} = 0, \quad (4.23)$$

$$\begin{aligned} (\varepsilon + p) \dot{u}^\mu &= \nabla^\mu (p + \Pi) - \Pi \dot{u}^\mu - \Delta^{\mu\nu} \dot{q}_\nu \\ &\quad - q^\mu \theta - q^\nu \partial_\nu u^\mu - \Delta^{\mu\nu} \partial^\lambda \pi_{\nu\lambda}. \end{aligned} \quad (4.24)$$

Thus, to close the system, one needs additional $7 + 3n$ equations, $6 + 3n$ equations to determine the dissipative quantities Π (one Eq.), q^μ (or V_i^μ , q^μ will be proportional to n_i , thus $3n$ Eqs.), $\pi^{\mu\nu}$ (five Eqs.) and the EoS.

Those equations of dissipative fluid dynamics are either provided by so-called first-order or second-order theories (see below). A first-order theory, like the Navier–Stokes approximation discussed in the next section, expresses the dissipative quantities π , q^μ (or V_i^μ), and $\pi^{\mu\nu}$ in terms of the variables $\varepsilon, p, n_i, u^\mu$, or their gradients. In a second-order theory, those variables are treated as independent dynamical quantities whose evolution is described by transport equations which are differential equations. In the following, we will again restrict to one conserved charge.

4.4 The Navier–Stokes Approximation

In the NS approximation, the dissipative quantities Π , q^μ , $\pi^{\mu\nu}$ are given by

$$\Pi_{\text{NS}} = -\zeta \theta, \quad (4.25)$$

$$q_{\text{NS}}^\mu = \frac{\kappa}{\beta} \frac{n}{\beta(\varepsilon + p)} \nabla^\mu \alpha, \quad (4.26)$$

$$\pi_{\text{NS}}^{\mu\nu} = 2\eta \sigma^{\mu\nu}, \quad (4.27)$$

with the definitions $\beta \equiv 1/T$ and $\alpha \equiv \beta\mu$, where μ is the chemical potential associated with the (net) charge density n . ζ , κ , and η denote the bulk viscosity, thermal conductivity, and shear viscosity coefficients, and $\sigma^{\mu\nu} \equiv \nabla^{<\mu} u^{\nu>}$ is the shear tensor.

While Eq. (4.26) is valid in the Eckart frame, it can easily be adjusted to the Landau frame by applying the transformation $q^\mu \rightarrow -V^\mu(\varepsilon + p)/n$.

Since Π , q^μ (or V^μ), and $\pi^{\mu\nu}$ are only given in terms of the primary variables, one obtains a closed set of Equations of Motion by inserting the above expressions into Eqs. (4.21) – (4.23).

However, these equations will lead to unstable solutions and support acausal propagation of perturbations [149].

A viable candidate for a relativistic formulation of dissipative fluid dynamics, which does not exhibit these problems, is the so-called second-order theory of Israel and Stewart [150] (for a discussion about stable and causal relativistic fluid dynamics see Ref. [151]). In the course of this chapter, we present the full Israel–Stewart equations of relativistic dissipative fluid dynamics as they emerge applying Grad’s 14-moment expansion [152] to the Boltzmann equation and truncating dissipative effects at second order in the gradients.

4.5 A Phenomenological Derivation

One possibility to obtain the fluid-dynamical Equations of Motion for the bulk pressure, the heat flux current, and the shear stress tensor is a phenomenological approach. Here, the derivation shall briefly be introduced, before an alternative (using a derivation applying kinetic theory) is discussed below in detail. It starts from the second law of thermodynamics, the principle of non-decreasing entropy,

$$\partial_\mu S^\mu \geq 0. \quad (4.28)$$

The next step is to find an ansatz for the entropy. In the limit of vanishing Π , q^μ , and $\pi^{\mu\nu}$, the entropy 4-current should reduce to the one of the ideal fluid $S^\mu \rightarrow su^\mu$. Since the only non-vanishing 4-vector that can be formed from the available tensors u^μ , q^μ , and $\pi^{\mu\nu}$ is βq^μ , this leads to

$$S^\mu = su^\mu + \beta q^\mu. \quad (4.29)$$

With the help of this ansatz as well as the conservation equations of (net) charge and energy, one computes that

$$T\partial_\mu S^\mu = (T\beta - 1)\partial_\mu q^\mu + q^\mu(\dot{u}_\mu + T\partial_\mu\beta) + \pi^{\mu\nu}\partial_\mu u_\nu + \Pi\theta \geq 0. \quad (4.30)$$

This inequality can be ensured by choosing the dissipative quantities to agree with the Navier–Stokes equations [Eqs. (4.25) – (4.27)]. Moreover, it results in

$$\partial_\mu S^\mu = \frac{\Pi^2}{\zeta T} - \frac{q^\mu q_\mu}{\kappa T^2} + \frac{\pi^{\mu\nu}\pi_{\mu\nu}}{2\eta T}. \quad (4.31)$$

However, as already mentioned, these equations contain instabilities. A solution is to implement corrections of second order in the dissipative quantities into the entropy current [150, 153],

$$S^\mu = su^\mu + \beta q^\mu + Q^\mu, \quad (4.32)$$

where

$$Q^\mu \equiv \alpha_0 \Pi q^\mu + \alpha_1 \pi^{\mu\nu} q_\nu + u^\mu (\beta_0 \Pi^2 + \beta_1 q^\mu q_\mu + \beta_2 \pi^{\nu\lambda} \pi_{\nu\lambda}). \quad (4.33)$$

Inserting this expression into $\partial_\mu S^\mu \geq 0$ leads to differential equations for Π , q^μ , and $\pi^{\mu\nu}$ which depend on the coefficients ζ , η , κ , α_0 , α_1 , β_0 , β_1 , and β_2 .

However, this phenomenological ansatz (which was explained in detail e.g. by Muronga [154]) does not determine the values of these coefficients.

4.6 Scales in Fluid Dynamics

In order to derive the equations of dissipative fluid dynamics in terms of a gradient expansion, one has to know about the scales in fluid dynamics. In principle, there are three length scales in fluid dynamics, two microscopic scales and one macroscopic scale. The two microscopic scales are the thermal wavelength, $\lambda_{\text{th}} \sim \beta$, and the mean free path, $\ell_{\text{mfp}} \sim (\langle \sigma \rangle n)^{-1}$, where $\langle \sigma \rangle$ is the average cross section. The macroscopic scale, L_{hydro} , is the scale over which the fluid fields (like ε , n , u^μ , ...) vary, i.e., gradients of these fields are typically of order $\partial_\mu \sim L_{\text{hydro}}^{-1}$. Due to the relation $n^{-1/3} \sim \beta \sim \lambda_{\text{th}}$, the thermal wavelength can be interpreted as the interparticle distance. However, the notion of a mean-free path requires the existence of well-defined quasi-particles. Since this quasi-particle concept is no longer valid in strongly coupled theories, these only exhibit two scales, λ_{th} and L_{hydro} .

The ratios of the transport coefficients ζ , κ/β , and η to the entropy density s are solely determined by the ratio of the two microscopic length scales, $\ell_{\text{mfp}}/\lambda_{\text{th}}$. For the proof we use that $\eta \sim (\langle \sigma \rangle \lambda_{\text{th}})^{-1}$ and $n \sim T^3 \sim s$,

$$\frac{\ell_{\text{mfp}}}{\lambda_{\text{th}}} \sim \frac{1}{\langle \sigma \rangle n} \frac{1}{\lambda_{\text{th}}} \sim \frac{1}{\langle \sigma \rangle \lambda_{\text{th}}} \frac{1}{n} \sim \frac{\eta}{s}. \quad (4.34)$$

Similar arguments hold for the other transport coefficients. There exist two limiting cases, the dilute-gas limit, with $\ell_{\text{mfp}}/\lambda_{\text{th}} \sim \eta/s \rightarrow \infty$, and the ideal-fluid limit, where $\ell_{\text{mfp}}/\lambda_{\text{th}} \sim \eta/s \rightarrow 0$. Estimating $\ell_{\text{mfp}} \sim \langle \sigma \rangle^{-1} \lambda_{\text{th}}^3$, the first case corresponds to $\langle \sigma \rangle / \lambda_{\text{th}}^2 \rightarrow 0$, thus, the interaction cross section is much smaller than the area given by the thermal wavelength. In other words, the average distance between collisions is much larger than the interparticle distance, allowing to interpret the dilute-gas limit as a weak-coupling limit. Similarly, the ideal-fluid limit corresponds to $\langle \sigma \rangle / \lambda_{\text{th}}^2 \rightarrow \infty$, describing the somewhat academic case when interactions happen on a scale much smaller than the interparticle distance, defining the limit of infinite coupling. The interactions get so strong that the fluid assumes locally and instantaneously a state of thermodynamical equilibrium.

For any value of η/s [and, analogously, ζ/s and $\kappa/(\beta s)$] between these two limits, the equations of dissipative fluid dynamics may be applied for the description of the system. The situation is particularly interesting for $\ell_{\text{mfp}}/\lambda_{\text{th}} \sim \eta/s \sim 1$ or, equivalently, $\langle \sigma \rangle \sim \lambda_{\text{th}}^2 \sim T^{-2}$. Then, the problem reveals only one microscopic scale λ_{th} , as e.g. in strongly coupled theories.

4.7 The Knudsen Number

The Knudsen number is defined as

$$K \equiv \ell_{\text{mfp}}/L_{\text{hydro}}. \quad (4.35)$$

Since $L_{\text{hydro}}^{-1} \sim \partial_\mu$, an expansion in terms of K is equivalent to a gradient expansion, i.e., an expansion in terms of powers of $\ell_{\text{mfp}} \partial_\mu$ as it is done by using Grad's method [152]. One important conclusion is that the ratios of the dissipative quantities Π , q^μ (or V^μ), and $\pi^{\mu\nu}$, assuming that they do not differ too much from

their Navier–Stokes values, to the energy density are proportional to the Knudsen number. Applying the fundamental relation of thermodynamics, $\varepsilon + p = Ts + \mu n$, to estimate $\beta\varepsilon \sim \lambda_{\text{th}}\varepsilon \sim s$ and employing Eq. (4.25), one can show that

$$\begin{aligned} \frac{\Pi}{\varepsilon} &\sim \frac{\Pi_{\text{NS}}}{\varepsilon} \sim \frac{\zeta\theta}{\varepsilon} \sim \frac{\zeta}{\lambda_{\text{th}}\varepsilon} \lambda_{\text{th}}\theta \sim \frac{\zeta}{s} \frac{\lambda_{\text{th}}}{\ell_{\text{mfp}}} \ell_{\text{mfp}} \partial_{\mu} u^{\mu} \\ &\sim \frac{\zeta}{s} \left(\frac{\ell_{\text{mfp}}}{\lambda_{\text{th}}} \right)^{-1} K |u^{\mu}| \sim K. \end{aligned} \quad (4.36)$$

In the last step, we have employed Eq. (4.34) and the fact that $u^{\mu} \sim 1$. The result is remarkable in the sense that Π/ε is only proportional to K , and independent of the ratio of viscosity to entropy density which drops out on account of Eq. (4.34). Therefore, we can conclude that if the Knudsen number is small, $K \sim \delta \ll 1$, the dissipative quantities are small compared to the primary variables and the system is close to local thermodynamic equilibrium.

Then, the equations of viscous fluid dynamics can be systematically derived in terms of a gradient expansion or, equivalently, in terms of a power series in K or, equivalently because of Eq. (4.36), in terms of powers of dissipative quantities. At zeroth order in K , one obtains the equations of ideal fluid dynamics, at first order in K , one finds the Navier–Stokes equations, and at second order in K , the Israel–Stewart equations emerge.

The independence of the ratio of dissipative quantities to primary variables from the viscosity to entropy density ratio has an important phenomenological consequence. It guarantees that, provided that gradients of the macroscopic fluid fields (and thus K) are sufficiently small, the Navier–Stokes equations [Eqs. (4.25) to (4.27)] are valid and applicable for the description of systems with large η/s , like water at room temperate and atmospheric pressure.

4.8 Transport Equations of Dissipative Quantities To Second Order in the Knudsen Number

To second order in dissipative quantities [or equivalently, because of Eq. (4.36), to second order in the Knudsen number], the relativistic transport equations for the bulk flow Π , the heat flux current q^{μ} , and the shear stress tensor $\pi^{\mu\nu}$, derived from the Boltzmann equation via Grad’s method [152], are given by [155]

$$\begin{aligned} \Pi &= -\zeta\theta - \tau_{\Pi}\dot{\Pi} + \tau_{\Pi q}q_{\mu}\dot{u}^{\mu} - l_{\Pi q}\nabla_{\mu}q^{\mu} - \zeta\hat{\delta}_0\Pi\theta \\ &\quad + \lambda_{\Pi q}q^{\mu}\nabla_{\mu}\alpha + \lambda_{\Pi\pi}\pi_{\mu\nu}\sigma^{\mu\nu}, \end{aligned} \quad (4.37)$$

$$\begin{aligned} q^{\mu} &= \frac{\kappa}{\beta} \frac{n}{\beta(\varepsilon + p)} \nabla^{\mu}\alpha - \tau_q \Delta^{\mu\nu} \dot{q}_{\nu} \\ &\quad - \tau_{q\Pi}\Pi\dot{u}^{\mu} - \tau_{q\pi}\pi^{\mu\nu}\dot{u}_{\nu} + l_{q\Pi}\nabla^{\mu}\Pi - l_{q\pi}\Delta^{\mu\nu}\partial^{\lambda}\pi_{\nu\lambda} + \tau_q\omega^{\mu\nu}q_{\nu} \\ &\quad - \frac{\kappa}{\beta}\hat{\delta}_1 q^{\mu}\theta - \lambda_{qq}\sigma^{\mu\nu}q_{\nu} + \lambda_{q\Pi}\Pi\nabla^{\mu}\alpha + \lambda_{q\pi}\pi^{\mu\nu}\nabla_{\nu}\alpha, \end{aligned} \quad (4.38)$$

$$\begin{aligned} \pi^{\mu\nu} &= 2\eta\sigma^{\mu\nu} - \tau_{\pi}\dot{\pi}^{\langle\mu\nu\rangle} \\ &\quad + 2\tau_{\pi q}q^{\langle\mu}\dot{u}^{\nu\rangle} + 2l_{\pi q}\nabla^{\langle\mu}q^{\nu\rangle} + 4\tau_{\pi}\pi_{\lambda}^{\langle\mu}\omega^{\nu\rangle\lambda} - 2\eta\hat{\delta}_2\theta\pi^{\mu\nu} \\ &\quad - 2\tau_{\pi}\pi_{\lambda}^{\langle\mu}\sigma^{\nu\rangle\lambda} - 2\lambda_{\pi q}q^{\langle\mu}\nabla^{\nu\rangle}\alpha + 2\lambda_{\pi\Pi}\Pi\sigma^{\mu\nu}. \end{aligned} \quad (4.39)$$

For the details of the derivation, see appendix D and Ref. [156]. The expressions for the relaxation times τ_π , τ_q , and τ_π as well as the coefficients $\tau_{\pi q}$, $\ell_{\Pi q}$, $\ell_{q\Pi}$, $\ell_{q\pi}$, $\ell_{\pi q}$, $\lambda_{\Pi q}$, $\lambda_{\Pi\pi}$, λ_{qq} , $\lambda_{q\Pi}$, $\lambda_{q\pi}$, $\lambda_{\pi q}$, $\lambda_{\pi\Pi}$, and $\hat{\delta}_0$, $\hat{\delta}_1$, $\hat{\delta}_2$ will be given in Ref. [156]. They are complicated functions of α and β , divided by tensor coefficients of the second moment of the collision integral.

The form of the transport equations is invariant of the calculational frame (Eckart, Landau, ...), however, the values of the coefficients are frame-dependent, since the physical interpretation of the dissipative quantities varies with the frame. For instance, q^μ denotes the heat flux current in the Eckart frame, while in the Landau frame, $q^\mu \equiv -V^\mu(\varepsilon + p)/n$ is the (negative of the) diffusion current, multiplied by the specific enthalpy. For details see again appendix D.

While the Navier–Stokes equations [Eq. (4.25) – (4.27)] are obtained by neglecting all terms to second order of the Knudsen number (i.e., by considering solely terms to first order in K which are the first terms on the r.h.s.), the so-called simplified Israel–Stewart equations (a term taken from Ref. [157]) emerge by keeping only the first two terms on the r.h.s. of Eqs. (4.37), (4.38), and (4.39). The resulting equations have the simple interpretation that the dissipative quantities Π , q^μ , and $\pi^{\mu\nu}$ relax to their corresponding Navier–Stokes values on time scales of τ_Π , τ_q , and τ_π .

For times $t < \tau_i$ ($i = \Pi, q, \pi$) the dissipative quantities Π , q^μ , $\pi^{\mu\nu}$ are driven towards their Navier–Stokes values. Once they are reasonably close to these, the first terms on the r.h.s. largely cancel against the l.h.s. The further evolution, for times $t > \tau_i$, is then determined by the remaining, second-order terms. Thus, these terms constitute important corrections for times $t > \tau_i$ and should not be neglected.

The third and fourth term in the first line of Eq. (4.37), the second line of Eq. (4.38), and the three first terms in the second line of Eq. (4.39) were also obtained by Israel and Stewart [150], while the remaining second-order terms were missed or neglected. Presumably, Israel and Stewart made the assumption that second-order terms containing θ , $\sigma^{\mu\nu}$, or $\nabla^\mu \alpha$ are even smaller than suggested by power counting in terms of K . Also, the last two terms in the first line of Eq. (4.37), the last three terms of the second line and the first term of the third line of Eq. (4.38) as well as the last three terms of the second line of Eq. (4.39) were obtained by Muronga [144], while the other second-order terms do not appear in that publication. A possible reason is that the corresponding treatment is based on the phenomenological approach to derive the Israel–Stewart equations and terms not generating entropy are absent.

The third line of Eq. (4.37), as well as the last three terms in the third line of Eqs. (4.38) and (4.39) were (with one exception discussed below) neither given by Israel and Stewart [150] nor by Muronga [144], and are thus completely new in the discussion of the transport equations for the dissipative quantities [155].

If we set $\Pi = q^\mu = 0$ in Eq. (4.39), the resulting equation for $\pi^{\mu\nu}$ is identical to that found in Ref. [158]. In particular, the first term in the third line was already obtained in that paper, where it appeared in the form $(\lambda_1/\eta^2) \pi_\lambda^{<\mu} \pi^{\nu>\lambda}$. Using the NS value (4.27) for $\pi^{\nu\lambda}$, which is admissible because we are computing to second order in K , to this order this is identical to $2(\lambda_1/\eta) \pi_\lambda^{<\mu} \sigma^{\nu>\lambda}$. By comparison with Eq. (4.39), we thus get a prediction for the coefficient λ_1 from kinetic theory, $\lambda_1 \equiv \tau_\pi \eta$, in agreement with Ref. [158].

Note, however, that this discussion so far neglects additional terms which arise at second order in K when expanding the second moment of the collision integral. (This was already noted in Ref. [158].) This will change the coefficient of the respective term such that it is no longer equal to τ_π . It will therefore also lead to a different result for λ_1 . In a recent study [159] a complete calculation was performed.

Thus, the treatment discussed above leads to transport equations of the bulk flow Π , heat flux current q^μ , and shear stress tensor $\pi^{\mu\nu}$ to second order in the Knudsen number. It is also applicable to non-conformal systems with non-vanishing (net) charge density. In the future, it will be necessary to work on a generalization of those equations to a system of various particle species [160] as well as on the numerical implementation and application to modelling the dynamics of heavy-ion collisions.

4.9 The Shear Viscosity over Entropy Ratio

One measure for the viscosity of a system is the shear viscosity to entropy ratio, η/s , reflecting the “degree of thermalization” since for low η a large s means that a hot system thermalizes quickly. More than 20 years ago, this ratio was already estimated to be [161]

$$\frac{\eta}{s} \geq \frac{1}{15} = 0.067. \quad (4.40)$$

Since the contribution from shear viscosity to viscous hydrodynamics is larger than from bulk viscosity or thermal conductivity, progress has mainly been made in performing viscous hydrodynamical calculations including the shear terms. From comparing those elliptic flow calculations [122, 162, 163] to experimentally measured data, it was shown that

$$0 < \eta/s \lesssim 0.2. \quad (4.41)$$

Recently [46], a calculation using the parton cascade BAMPS led to $0.08 \leq \eta/s \leq 0.15$.

Chapter 5

Shock Wave Phenomena

Fluid dynamics exhibits a special feature: Shock waves. They are discontinuities and characterize that part of the medium which will subsequently move with a velocity $v_{\text{shock}} \neq v_{\text{medium}}$.

The easiest way to introduce shock waves is by discussing the *Riemann problem* which describes the decay of a discontinuity between two regions of constant flow. It is a well-known problem in fluid dynamics and can be solved analytically in one dimension for an ideal fluid (for a review see e.g. [116]).

The corresponding initial conditions are two different regions, both in thermodynamical equilibrium, that differ by their pressures (see Fig. 5.1). During the following hydrodynamic evolution, a shock wave will develop that travels supersonically ($v_{\text{shock}} > c_s$) into that part of the system with the lower pressure (i.e., to the right in Fig. 5.1), while simultaneously a rarefaction wave moves with a velocity equal to the speed of sound into matter with larger pressure (to the left in Fig. 5.1). During that process, a region of constant pressure evolves behind the shock wave which is called the shock plateau.

Applying the conservation equations of (net) charge, energy, and momentum, it is possible to show that the velocity of the shock front [108, 110, 116]

$$v_{\text{shock}} = \sqrt{\frac{(p_2 - p_1)(\varepsilon_2 + p_1)}{(\varepsilon_1 + p_2)(\varepsilon_2 - \varepsilon_1)}} \quad (5.1)$$

can be determined from the relativistic Rankine–Hugoniot–Taub equation (RHTA) [164]

$$\frac{w_1^2}{\rho_1^2} - \frac{w_2^2}{\rho_2^2} + (p_2 - p_1) \left(\frac{w_1}{\rho_1^2} + \frac{w_2}{\rho_2^2} \right) = 0, \quad (5.2)$$

where $w = \varepsilon + p$ denotes the enthalpy, ρ the particle density, and p_1 (p_2) the pressure in front of (behind) the relativistic shock front so that $p_2 > p_1$.

Theoretically, it was already predicted in the 1970's that shock waves should occur in collisions of heavy nuclei [165] due to the strong compression of the medium. Later on, this phenomenon was observed experimentally [166, 167, 168]. Of course, one of the basic questions is the origin of the discontinuity. The early works [166] investigated the penetration of a smaller nucleus through a larger one. In that case, a region of extremely dense matter is formed (mainly from the remnant

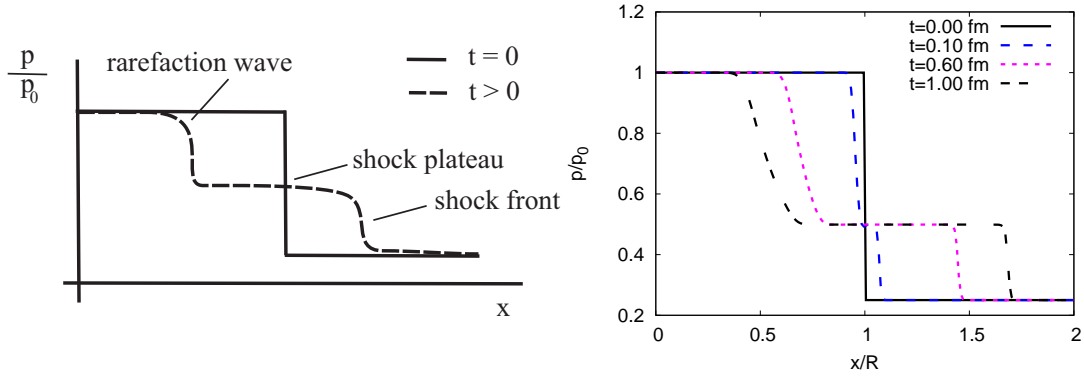


Figure 5.1

The evolution of a discontinuity leading to a shock front as a sketch (left panel) and calculated with a 1-dimensional hydrodynamical algorithm [110].

of the smaller nuclei) which moves in beam direction with a velocity larger than the speed of sound leading to a discontinuity due to the superposition of a large number of infinitesimal sonic perturbations. Such perturbations can superimpose to the characteristic pattern of a Mach cone, which is discussed in the next section. Currently, the penetration of a smaller nucleus through a larger one is investigated for FAIR conditions [169].

It was suggested [82, 83, 170, 171, 172, 173] that such Mach cones could also be created in heavy-ion collisions. As already mentioned in section 2, hard probes formed in the very early stages of the collision can propagate through the medium, acting as perturbations of the medium.

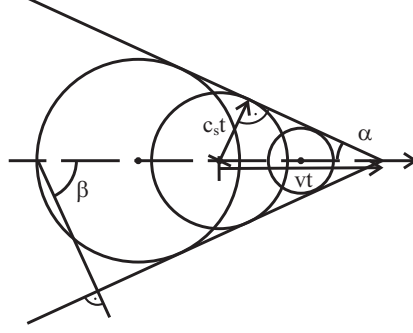
5.1 Mach cones

Sound waves can be created due to a perturbation (like a jet) and propagate through a fluid. If the origin of this perturbation (i.e., the source) does not move, it emits spherical waves which travel (isotropically) with the speed of sound through the medium. For a moving source, however, the spherical waves interfere, leading to a compression zone in the direction of motion as described by the Doppler effect. As soon as the velocity of the source is larger than the speed of sound, the source moves even faster than the emitted sound waves. Thus, as shown in Fig. 5.2, the interference pattern results in a conical compression zone, a discontinuity called **Mach cone**¹. The opening angle of such a Mach cone is given by

$$\sin \alpha = \frac{c_s}{v}, \quad (5.3)$$

(as one can easily deduce from Fig. 5.2 applying simple trigonometric functions) where v denotes the velocity of the source through the medium. If particles are created in the discontinuity, they are mostly emitted perpendicularly to the Mach cone.

¹Ernst Mach (1838–1916) was an Austrian physicist who was a professor in Graz and Prague.

**Figure 5.2**

The interference pattern of spherical waves leading to the formation of a Mach cone. The source emitting sound waves propagates with a velocity larger than the speed of sound through the medium so that a conical discontinuity emerges with an opening angle α . Particles created in this discontinuity are always emitted into an angle $\beta = \pi - \alpha$.

Thus, the emission angle (often also referred to as Mach angle ϕ_M) is $\beta = \phi_M = \pi - \alpha$, and therefore

$$\cos \beta = \frac{c_s}{v}. \quad (5.4)$$

Since Mach cones are discontinuities, they belong to the category of shock waves. If one wants to study Mach cones with a certain numerical algorithm, it has to be first checked that it is possible to describe the propagation of shock waves using this particular application. For the SHASTA, this was done in Ref. [110]. Recently, as demonstrated in Ref. [174], it was shown that it is possible to describe shock waves using the parton cascade BAMPS [106].

The basic idea when applying the concept of Mach cones to high-energy heavy-ion collisions is that a hard- p_T particle, travelling with a velocity v_{jet} (close to the speed of light) through the medium, re-distributes its energy to lower- p_T particles. Thus, it acts as a source in the fluid probably exciting sound waves which interfere and form a Mach cone.

Subsequently, there should be an enhanced particle emission under a distinct Mach-cone angle. If this idea is correct and it is possible to extract the emission angle from the measured particle distributions, it would give direct access to the (averaged) speed of sound of the medium via Eq. (5.4). Then, as suggested in Refs. [82, 83], it might be possible to draw conclusions about the properties of the medium, especially about the speed of sound and to extract information about the EoS.

Assuming that the medium can be described by an ideal gas EoS with $c_s = 1/\sqrt{3} \sim 0.57$, the Mach-cone emission angle is $\beta = \phi_M = 0.96$ rad, which agrees with the measured particle distributions introduced in chapter 2. Therefore, the medium formed in a heavy-ion collision might possibly behave like an ideal gas which thermalizes quickly, allowing for the creation of Mach cones.

Of course, it is tacitly assumed here that the velocity of the jet, which is usually estimated to be close to the speed of light, is constant and known. However, even in that case it is only possible to extract a mean value for the speed of sound. If the medium properties change, e.g. due to a phase transition (as it is expected when the medium cools down), the speed of sound changes (and might actually go to zero in

case of a first-order phase transition), affecting the Mach-cone angle as well. Strictly speaking, Eq. (5.4) only applies for weak, sound-like perturbations. Certainly there is no reason to assume that in physical systems the amplitude of the perturbation is really small. Thus, to calculate the opening angle of a cone that is created due to the pile-up of matter at the head of the jet which creates a shock perturbation, a more general problem has to be addressed. It was shown in Ref. [175] that this problem splits up into

- the oblique-shock-wave problem [108, 176] close to the head of the jet leading to the cone angle that results from the shock wave, taking into account the influence of flow,
- and the Taylor–Maccoll problem [177, 178] behind the shock which calculates the flow of matter along the cone.

The first one determines the opening angle of the cone in the vicinity of the shock to be

$$\sin \phi_M = \frac{\gamma_{cs} c_s}{\gamma_v v}, \quad (5.5)$$

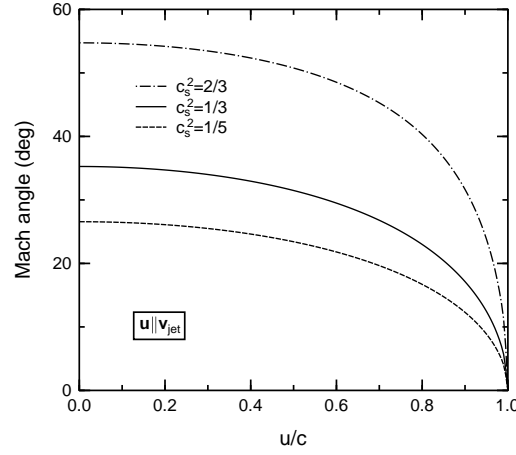
with $\gamma_{cs} = 1/\sqrt{1 - c_s^2}$. Only in the non-relativistic limit, this results in the above Eq. (5.3). Thus, just (far) behind the head of the jet, in the so-called *far zone*, where the perturbations due to the jet are much weaker than close to the head of the jet, Mach-cone angles computed according to Eq. (5.4) are quite well reproduced. As can be seen from the figures of part III, especially slow moving partons create a pile-up of matter leading to a bow shock which changes the opening angle of the Mach cone close to the head of the jet.

It should be mentioned in this context that the creation of a Mach cone is a general phenomenon possible in any plasma. Thus, Ref. [173] discusses the possibility that shock waves and Mach cones might also appear in a plasma formed due to mono-jets that are emitted by radiating mini-black holes which can be produced in large collider facilities like the LHC.

It was already discussed in chapter 2 that conical emission patterns were found in the two- and three-particle correlations measured at RHIC. Nevertheless, it could not be proven that this shape results from the creation of Mach cones (see section 2.2.2). The main issue of this thesis is to test whether hydrodynamic models support the Mach-cone hypothesis. A crucial ingredient is the mechanism of energy and momentum loss by the jet which will be addressed in chapter 6.

5.2 The Influence of Radial Flow

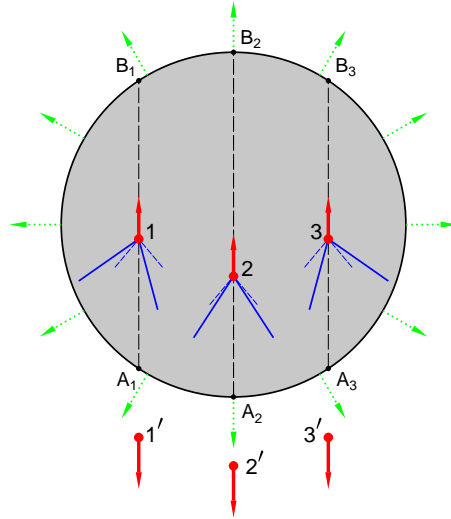
The medium created in a heavy-ion collision, through which the jet propagates probably exciting sound waves, expands rapidly. Consequently, there will be a strong flow (v_{flow}) relative to the velocity of the jet that certainly influences its propagation, the interference pattern of the sound waves, and hence the Mach cone angle. It was shown in Ref. [170] that a background flow parallel to the velocity of the jet ($v_{\text{flow}} || v_{\text{jet}}$) leads to a narrowing of the Mach angle in the center-of-mass frame which has a purely relativistic origin. Fig. 5.3 depicts this change in the

**Figure 5.3**

The change in the Mach angle as a function of the background flow $v_{\text{flow}} = u/c$ for hadronic matter $c_s^2 = 1/5$, an ideal gas $c_s^2 = 1/3$ and a strongly coupled QGP (sQGP) with $c_s^2 = 2/3$ [170].

Mach angle for different flow velocities and various EoS. It illustrates that a larger background flow results in a smaller Mach angle. However, assuming e.g. an ideal gas EoS and estimating the background flow to be of the order of the speed of sound, $c_s \sim 0.57$, the change of the Mach cone angle is rather small.

Obviously, it is very unlikely that a jet propagates collinearly with the flow. If the background flow has a transverse component w.r.t. the velocity of the jet, this

**Figure 5.4**

Sketch of the deformation of Mach cones in an expanding medium (solid lines). The thick arrows denote the trigger jets and the expected Mach-cone angles in a static medium are shown by dashed lines [170].

should cause a deformation of the Mach cone as displayed in Fig. 5.4. Unfortunately, the derivation of a general solution for the deflected Mach cone angle is far from trivial. A qualitative discussion of this effect is given in appendix H.

Moreover, one always has to consider that the experimentally measured particle distributions sample over many events. As can be seen from Fig. 5.4, the radial expansion of the fireball should lead to a broadening of the measured cone angles when averaging over the different possible jet trajectories. However, this effect might get diminished due to the momentum spread of the initial parton distribution (as shown in Fig. 2.4) which leads to a systematic error in determining the relative azimuthal angle $\Delta\phi$.

Nevertheless, it is necessary to investigate the deformation of Mach cones applying full $(3 + 1)$ -dimensional hydrodynamical simulations in order to prove the interaction of jet and background flow and to study its impact on the particle distributions.

Chapter 6

Jet-Energy Loss

A fast moving particle interacts with the medium it traverses, losing energy. In general, the mechanisms by which this energy is lost as well as the amount of energy deposited depends on the particle characteristics and on the matter properties. Considering certain kinds of particles, this provides fundamental information about the medium itself.

Therefore, such jet-medium interactions are significant for the study of a jet moving through a plasma and its impact on the measured particle distributions. In the following, we discuss different mechanisms that were developed to describe the energy, but not the momentum loss of partons within the QGP. Here, we focus on models based on QCD. The next chapter provides a detailed introduction to the approach obtained by the gauge/string duality, the AdS/CFT correspondence, which can also be used to investigate jet energy loss.

The crucial ingredient to study the propagation of jets in heavy-ion collision is the source term describing the energy and momentum that is lost by the hard probes and thermalizes in the medium. Those source terms will be discussed in the subsequent sections.

6.1 In-medium Energy Loss

In the most general case, the total energy loss of a particle moving through a medium is the sum of

- **Collisional energy loss** through elastic scatterings with the medium constituents and
- **Radiative energy loss** via inelastic scatterings in the medium, determined by the corresponding Bremsstrahlung spectrum.

For incoherent scatterings, the total energy loss is given by $\Delta E^{\text{tot}} = N \cdot \Delta E^{\text{1scat}}$, where $N = L/\ell_{\text{mfp}}$ is the opacity¹ with L being the characteristic length of the medium and ℓ_{mfp} the mean-free path. Thus, the energy loss per unit length, also called stopping power, is given by

$$\frac{dE}{dx} \equiv \frac{dE}{dl} = \frac{\langle \Delta E^{\text{1scat}} \rangle}{\ell_{\text{mfp}}} = \frac{\langle \Delta E \rangle}{L}. \quad (6.1)$$

¹The opacity describes the number of scattering centers in a medium of thickness L .

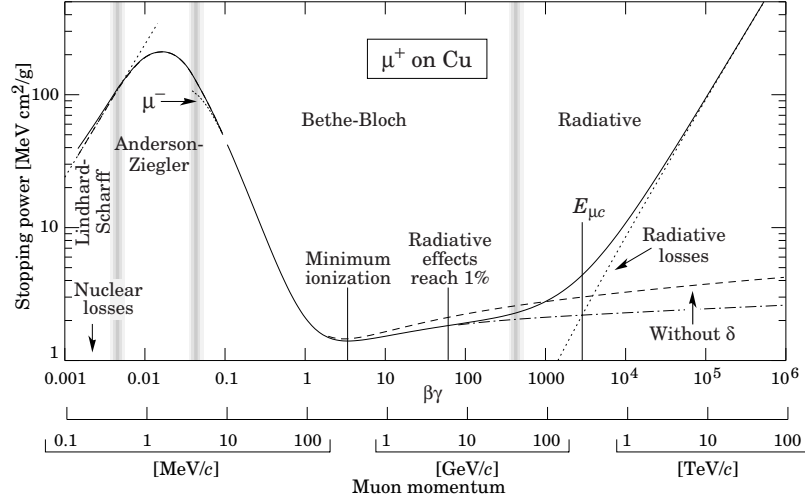


Figure 6.1

The stopping power, i.e., the energy loss per unit length dE/dx , for muons in copper as a function of $\beta\gamma = p/Mc$ [180].

Usually, this quantity is provided with a minus sign demonstrating that the particle has lost energy. Since we will not consider the energy that is lost by the jet in our hydrodynamic simulations, but rather the energy that is given by the jet to the medium, we will assign a positive sign to dE/dx .

The radiative energy loss itself depends on the thickness of the plasma. For a thin medium ($L \ll \ell_{\text{mfp}}$), the traversing particle suffers at most one single scattering. This limit is called the Bethe–Heitler (BH) regime. For thick media ($L \gg \ell_{\text{mfp}}$) however, the multiple scattering reduces the amount of radiation, an effect called Landau–Pomeranchuk–Migdal (LPM) effect².

Moreover, the total amount of radiation emitted from a heavy quark is suppressed at angles smaller than the ratio of the quark mass M to its energy E ($\theta = M/E$). This *dead cone* effect [81] leads to a damping of emission by a factor of m_D^2/M^2 .

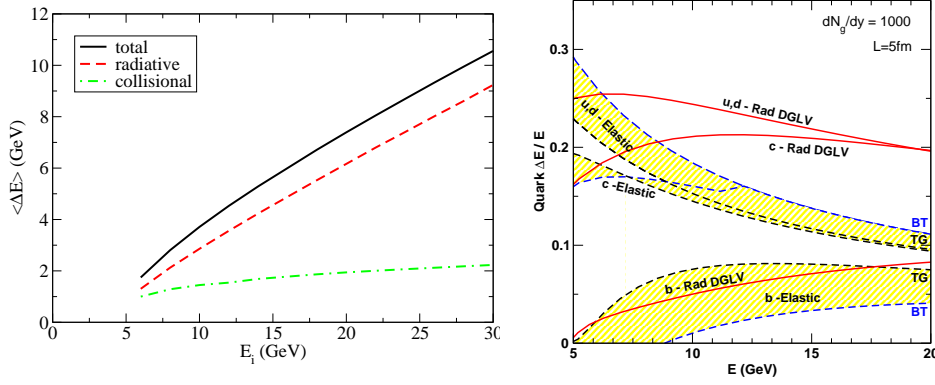
As shown in Fig. 6.1, which displays the energy loss of a muon in copper, the collisional (Bethe–Bloch) energy loss dominates at low energies, while at high energies the radiative loss increases linearly and dominates over the logarithmic growth of the collisional energy loss.

However, this behaviour strongly depends on the properties of the medium as well as on the kinematic region considered. Therefore, it is not possible to universally determine the dominant energy-loss mechanism.

For a long time, it was assumed that the main contribution at high energies results from radiative energy loss. While this appears to be correct for light quarks, a proper prescription of heavy quark energy loss seems to require both, collisional and radiative energy loss [181], see Fig. 6.2.

All medium modifications are often encoded in the *transport coefficient*, the so-

²The LPM effect, originally deduced from photon emission [179], describes the fact that multiple scattering/interaction causes destructive interference which suppresses the radiative spectrum.

**Figure 6.2**

Collisional (elastic) and radiative energy loss of light quarks (left panel) [182] as well as light and heavy quarks (right panel) [181] passing through a medium produced in central Au+Au collisions at RHIC.

called \hat{q} -parameter, characterizing a fundamental quantity of QCD that is defined as the average transverse momentum squared transferred per unit path length,

$$\hat{q} \equiv \frac{\langle Q^2 \rangle}{\ell_{\text{mfp}}} = \frac{m_D^2}{\ell_{\text{mfp}}}, \quad (6.2)$$

where the Debye mass $m_D = gT$ describes the lowest momentum exchange with the medium. The values of this transport coefficient vary for the various approaches reviewed below, $\hat{q} \sim 5 - 25 \text{ GeV}^2/\text{fm}$, exhibiting a large uncertainty when comparing to experimental data [183, 184, 185]. For a comparison of different \hat{q} -parameters to experimental data see Fig. 6.3. Consequently, the TECHQM program [186] has agreed upon a systematic study of the different mechanisms to clarify the ambiguities concerning the various approaches as well as the physical processes during a jet-medium interaction.

The explicit expressions for the collisional and radiative energy loss depend on the nature of the projectile via the colour factor C_R , which is the quadratic Casimir of the respective representation,

$$C_R = \begin{cases} C_F = \frac{N_c^2 - 1}{2N_c} = \frac{4}{3} & \text{fundamental representation for quarks,} \\ C_A = N_c = 3 & \text{adjoint representation for gluons,} \end{cases} \quad (6.3)$$

implying that $C_A/C_F = 9/4$. Therefore, a gluon jet loses roughly twice the energy of a quark jet and exhibits a larger hadron multiplicity.

6.2 Mechanisms of Jet Energy Loss from QCD

Four major phenomenological approaches (often identified with the initials of their authors) have been developed to connect the QCD energy loss calculations with the experimental observables. Those are

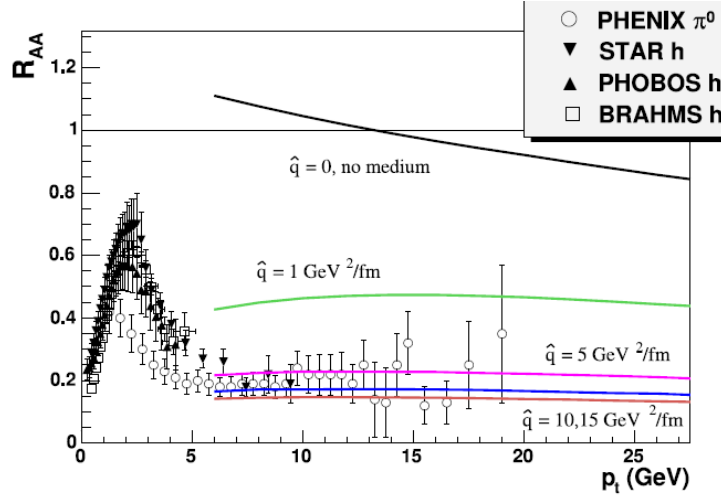


Figure 6.3

R_{AA} measured for central Au+Au collisions at $\sqrt{s_{NN}} = 200$ GeV and compared to model calculations for varying values of the \hat{q} -parameter, based on Ref. [183].

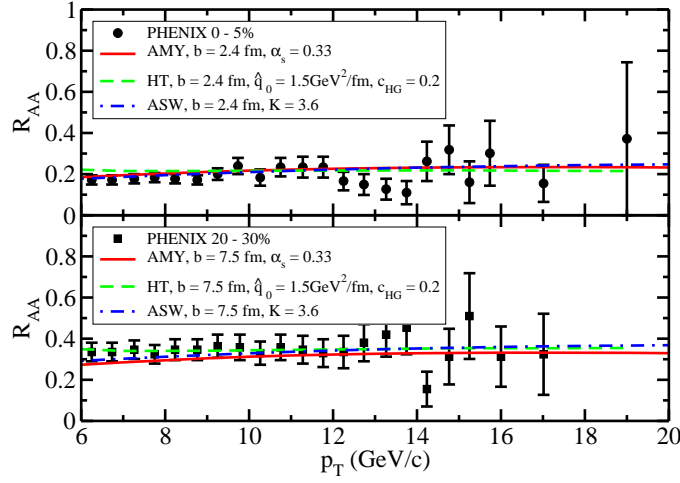
- The **GLV**³ approach [187], nowadays also known as **DGLV**⁴ [188], calculates the parton energy loss in a dense deconfined medium consisting of almost static (i.e. heavy) scattering centers which produce a screened (Yukawa) potential. A single hard radiation spectrum is expanded to account for gluon emission from multiple scatterings via a recursive diagrammatic procedure. This allows to determine the gluon distribution to finite order in opacity.
- The **BDMPS**⁵ scheme [189, 190], similarly established by Zakharov [191] and used in the **ASW**⁶ [192] procedure, calculates the energy loss in a coloured medium for a hard parton interacting with various scattering centers that splits into an outgoing parton as well as a radiated gluon. The propagation of these partons and gluons are expressed using Green's functions which are obtained by path integrals over the fields. Finally, a complex analytical expression for the radiated gluon distribution function is obtained as a function of the transport coefficient \hat{q} .
- The **Higher Twist** (HT) approximation [193, 194] describes the multiple scattering of a parton as power corrections to the leading-twist cross section. These corrections are enhanced by the medium length L and suppressed by the power of the hard scale Q^2 . Originally, this scheme was applied to calculate the medium corrections to the total cross section in nuclear deep-inelastic electron+nucleon scatterings.

³Gyulassy–Levai–Vitev

⁴Djordjevic–Gyulassy–Levai–Vitev

⁵Baier–Dokshitzer–Müller–Peigné–Schiffer

⁶Armesto–Salgado–Wiedemann

**Figure 6.4**

Nuclear modification factor R_{AA} for high- p_T pions in central (upper panel) and semi-central (lower panel) Au+Au collisions at RHIC, compared to AMY, HT and ASW energy loss calculations [197].

- The **AMY**⁷ [195] approach describes the parton energy loss in a hot equilibrated QGP. Multiple scatterings of the partons and their radiated gluons are combined to determine the leading-order gluon radiation rate.

For a detailed review see e.g. Ref. [196]. All four schemes have made successful comparisons to the available data when tuning one distinct model parameter which is the initial gluon density in the GLV approach, the \hat{q} -parameter for the BDMPS/ASW scheme, the initial energy loss in the HT approximation and the temperature in the AMY procedure. However, all approaches are based on certain model assumptions, limiting their scope of application (see Ref. [55, 196]).

The quantitative consistency of the different schemes has been investigated within a 3-dimensional hydrodynamical approach (see Fig. 6.4) [197] using the same space-time evolution. Recently, the nuclear modification factor was also studied using a pQCD-based parton cascade including radiative processes [198].

However, while those energy-loss mechanisms predict the amount of energy lost to the medium, expressed e.g. by the transport coefficient \hat{q} , they do not address the question **how** the energy and momentum deposited by the jet affect the medium. First calculations of a medium response were presented in Ref. [83], applying a schematic source and linearized hydrodynamics as will briefly be reviewed below. A source term expected from a parton moving through the QCD plasma was recently derived by Neufeld et al. [199], see section 6.5.

6.3 First Studies of Jet-Energy Transfer to the Medium

Casalderrey–Solana et al. [83, 171, 200] first examined the problem of **where** the energy of the quenched jets is transferred to. They did not focus on the calculation

⁷Arnold–Moore–Yaffe

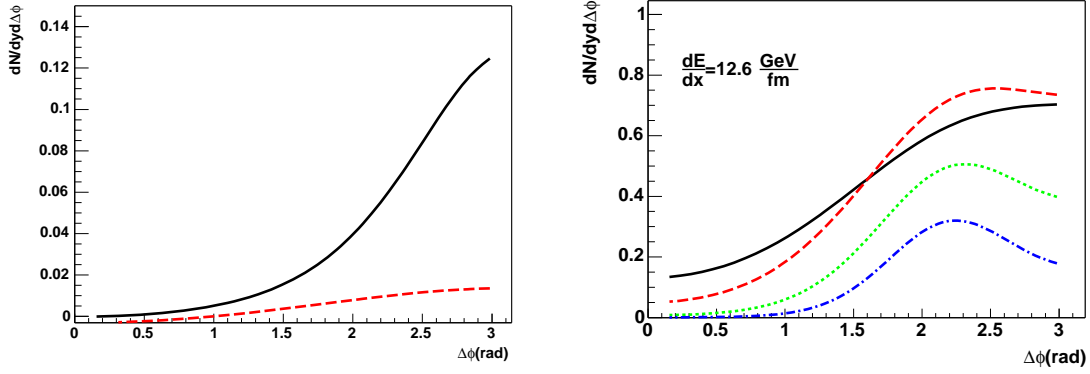


Figure 6.5

Azimuthal particle distributions for non-isentropic (left panel) and isentropic (right panel) excitations [200]. The solid black line in the left panel represents an energy loss of $dE/dx = 12.6$ GeV/fm, while the red dashed line is obtained for $dE/dx = 2$ GeV/fm. In the right panel this energy loss is fixed to $dE/dx = 12.6$ GeV/fm and the different curves represent the various p_T -cuts of $0.2 \leq p_T \leq 1$ (solid black line), $1 \leq p_T \leq 2$ (dashed red line), $2 \leq p_T \leq 3$ (dotted green line) and $3 \leq p_T \leq 4$ (dashed-dotted blue line).

of the amount of energy deposited to the medium, but rather on the evolution of (some) re-distributed energy and momentum.

Their work is based on two major assumptions. First, they consider a di-jet pair that is created back-to-back close to the surface of the medium. While one jet (the trigger jet) escapes, the other one penetrates the plasma. Second, they assume that the energy and momentum density deposited by the jet (into a homogeneous medium at rest) is a small perturbation compared to the total amount of energy stored in the medium which allows to use *linearized hydrodynamics*.

In such a linearized form, the hydrodynamic equations decouple, and with the definition of $\vec{g} = g_L(\vec{k}/k) + \vec{g}_T$ for the momentum density, including the longitudinal (L) and transversal part (T), those equations can be written as

$$\partial_t \varepsilon + ik g_L = 0, \quad (6.4)$$

$$\partial_t g_L + ic_s^2 k \varepsilon + \frac{4}{3} \frac{\eta}{\varepsilon_0 + p_0} k^2 g_L = 0, \quad (6.5)$$

$$\partial_t g_T + \frac{\eta}{\varepsilon_0 + p_0} k^2 g_T = 0. \quad (6.6)$$

Here, c_s denotes the speed of sound and η the viscosity of the medium. Certainly, this ansatz breaks down close to the jet (as will be discussed later in detail), a region that is not describable with this approach.

To address the issue of matter excitation which is unknown in detail since the interaction and thermalization processes of the lost energy are unclear, they studied two different scenarios [83, 171, 200]:

- Local energy and momentum distribution (modelled by Gauss functions) along the path of the jet propagating through the medium (non-isentropic excitation),
- excitation of sound waves due to gradients in the momentum distribution, but vanishing energy deposition (isentropic excitation).

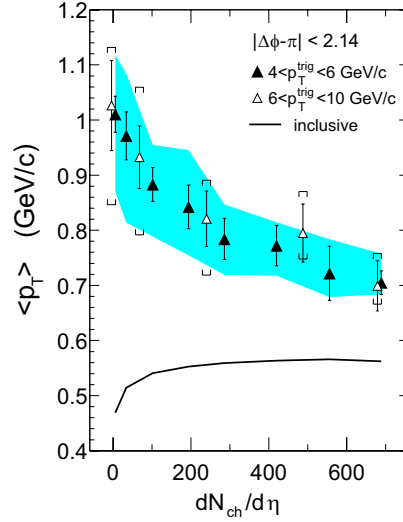
Performing an isochronous Cooper–Frye freeze-out, they obtained the particle distributions of Fig. 6.5. Those figures clearly show that in case of energy and momentum deposition (see left panel of Fig. 6.5), independent of the amount of energy loss (which are displayed for $dE/dx = 2$ GeV/fm and $dE/dx = 12.6$ GeV/fm), a peak occurs in the direction of the jet moving through the plasma (which is located here at $\Delta\phi = \pi$). However, the excitation of sound waves in the second deposition scenario (see right panel of Fig. 6.5) leads to a conical structure as anticipated from an interference pattern of sound waves (see chapter 5, especially Fig. 5.2), though a large dE/dx has to be chosen to observe the effect. Moreover, the peaks obtained on the away-side get more pronounced for larger values of the applied p_T -cuts.

Energy and momentum loss (left panel of Fig. 6.5) do not result in a conical structure. The momentum deposited causes additional “kicks” in direction of the moving jet, forming a strong flow behind the jet [83], named the **diffusion wake**. Given that a Cooper–Frye freeze-out is mainly flow driven, cf. Eq. (3.43), a peak occurs in the direction of jet motion. It has to be stressed that the energy loss described in this scenario leads by itself to the formation of sound waves the interference pattern of which results in a conical structure. However, this structure is not seen in the freeze-out patterns since the flow due to the momentum distribution superimposes and dominates the particle distributions. Thus, the deposition of energy and momentum results in a peak in jet-direction. This is explicitly shown in Figs. 8.1 and 8.2.

The location of the conical peaks in the second scenario (see right panel of Fig. 6.5) is in good agreement with the experimental data (presented in chapter 2) showing away-side peaks at $\pi \pm 1.1$ rad. This suggested to conclude that the second scenario describes the data and reveals some insights into the excitation mechanism. Certainly, one has to keep in mind that the whole approach, though very instructive, is an approximation and it will turn out (as we demonstrate in chapter 11) that the second scenario eventually has to be ruled out.

Beyond the question of energy deposition, the linearized hydrodynamic approximation offers the advantage that the propagation of sound waves can be traced back to Eq. (6.5), while Eq. (6.6) describes the diffusive component. Remarkably, the viscous terms in both equations are of the same order. Thus, dissipative corrections will have about the same effects on both, sound waves and diffusion wake. Therefore, the interplay between both effects does not change in viscous media.

Similar findings about the impact of a jet moving through an expanding medium were shown in Ref. [172, 201, 202]. Chaudhuri and Heinz demonstrated that, using $(2 + 1)$ -dimensional ideal hydrodynamics, the particle correlations obtained from a jet depositing the same amount of energy and momentum, do not lead to a double-peaked structure on the away-side [201]. Renk and Ruppert, however [172], reproduced the measured data when assuming that a certain fraction of energy is transferred into the sound modes while the remaining (smaller amount of) energy is released into the diffusion wake.

**Figure 6.6**

Mean transverse momentum $\langle p_T \rangle$ of associated hadrons for different trigger- p_T 's of $p_T = 4 - 6$ GeV and $p_T = 6 - 10$ GeV as a function of centrality [88].

6.4 Jet Energy Loss in Hydrodynamics

Each parton propagating through a medium, depositing energy (and momentum), acts as a source to the medium. It is not clear from first principles that the energy lost quickly thermalizes and therefore can be incorporated into a hydrodynamic description, as it was done above. However, a measurement [88] proved that the average momentum of particles emitted on the same side as the jet that passes through the medium approaches the value of a thermalized medium with decreasing impact parameter, see Fig. 6.6. Thus, a hydrodynamical prescription seems to be justified and a source term can be added to the equations for energy and momentum conservation [cf. Eq. (3.1)]

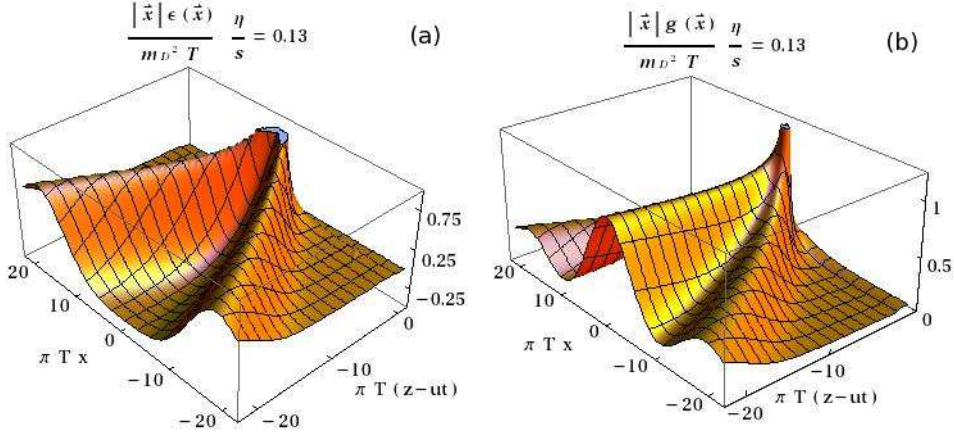
$$\partial_\mu T^{\mu\nu} = J^\nu. \quad (6.7)$$

This source term J^ν is not the source term of the jet, but the residue of energy and momentum given by the jet to the medium. The source term that correctly depicts the interaction of the jet with the QGP is under current investigation using the two completely independent and different approaches of pQCD and AdS/CFT. Both source terms will be introduced below and their impact will be studied in part III. However, before implementing a rather complicated source term into a hydrodynamic algorithm, it might be instructive to first consider a schematic source term that describes the energy and momentum deposition of the jet along a trajectory

$$x^\mu(\tau) = x_0^\mu + u_{\text{jet}}^\mu \tau, \quad (6.8)$$

where x_0^μ denotes the formation point and $u_{\text{jet}}^\mu = (\gamma_{\text{jet}}, \gamma_{\text{jet}} \vec{v}_{\text{jet}})$ the 4-velocity of the jet. Such a source term is given by

$$J^\nu = \int_{\tau_i}^{\tau_f} d\tau \frac{dM^\nu}{d\tau} \delta^{(4)} [x^\mu - x_{\text{jet}}^\mu(\tau)], \quad (6.9)$$

**Figure 6.7**

Perturbed energy (left) and momentum (right) densities for a gluon moving with a velocity of $u = 0.99955$ along the positive z -axis of a QCD medium with $\eta/s = 0.13$ [199].

with the energy and momentum loss rate $dM^\nu/d\tau$, the proper time interval $\tau_f - \tau_i$ associated with the jet evolution and the location of the jet $x_{\text{jet}}(\tau)$. Certainly this source term comprises a significant simplification of the ongoing processes. Nevertheless, as will be demonstrated in part III, it correctly depicts the behaviour of the particle correlations compared to those obtained e.g. from the pQCD source term introduced in the following section.

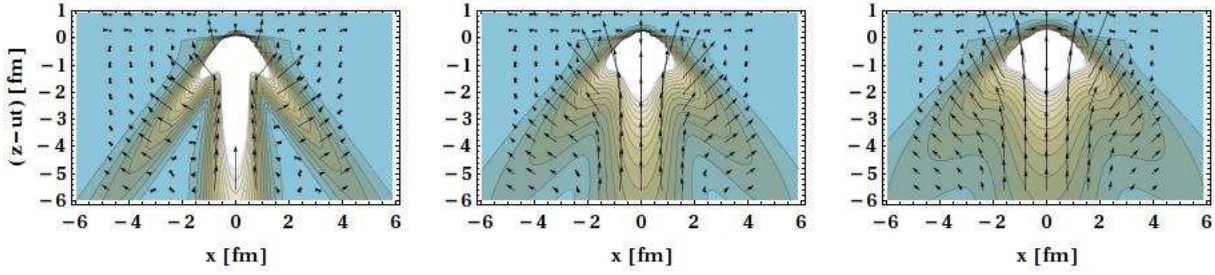
6.5 A pQCD Source Term

The first investigations about the medium response to the passage of a fast parton were based on schematic source terms (see above), mainly representing the moving jet as a δ -function. Recently, Neufeld et al. [199, 203] derived a source term for a supersonic parton popagating through a QCD plasma. Their approach considers the fast parton as a source of an external color field that can be described via perturbative QCD applying a collisionless Boltzmann equation. For a system of partons in an external color field, described by the distribution $f(\vec{x}, \vec{p}, t)$, this Boltzmann equation is defined as [204]

$$\left(\frac{\partial}{\partial t} + \frac{\vec{p}}{E} \cdot \vec{\nabla}_x - \nabla_{pi} D_{ij}(\vec{p}, t) \nabla_{pj} \right) f(\vec{x}, \vec{p}, t) = 0, \quad (6.10)$$

where \vec{p}/E is the velocity of a parton with momentum \vec{p} and energy E . Here, $D_{ij}(\vec{p}, t) = \int_{-\infty}^t dt' F_i(\vec{x}, t) F_j(\vec{x}', t')$ describes the integral over Lorentz forces $F_i(\vec{x}, t) = gQ^a(t) [E_i^a(\vec{x}, t) + (\vec{v} \times \vec{B})_i^a(\vec{x}, t)]$ [$gQ^a(t)$ denotes the charge] on a medium particle caused by the moving parton, acting until a certain time t . These Lorentz forces are considered to lowest order in the coupling constant g .

Since the equations for energy and momentum conservation can be derived from the second moment of the Boltzmann equation $p^\mu \partial_\mu f(\vec{p}, t) = 0$ (see appendix D),

**Figure 6.8**

Perturbed momentum density for different values of the shear viscosity to entropy ratio, $\eta/s = 1/(4\pi), 3/(4\pi), 6/(4\pi)$ [205].

the source term can be defined as

$$J^\nu \equiv \int \frac{d\vec{p}}{(2\pi)^3} p^\nu [\nabla_{pi} D_{ij}(\vec{p}, t) \nabla_{pj} f(\vec{x}, \vec{p}, t)] . \quad (6.11)$$

Omitting dielectric screening and assuming an energy as well as momentum deposition of a parton with constant velocity $\vec{u} = u\vec{e}_z$ at a position $\vec{x} = ut\vec{e}_z$, this source term is evaluated to be [203]

$$J^\nu(\rho, z, t) = [J^0(\rho, z, t), \vec{u}J^0(\rho, z, t) - \vec{J}^v(\rho, z, t)] , \quad (6.12)$$

where $\rho = \sqrt{x^2 + y^2}$ denotes the transverse component and

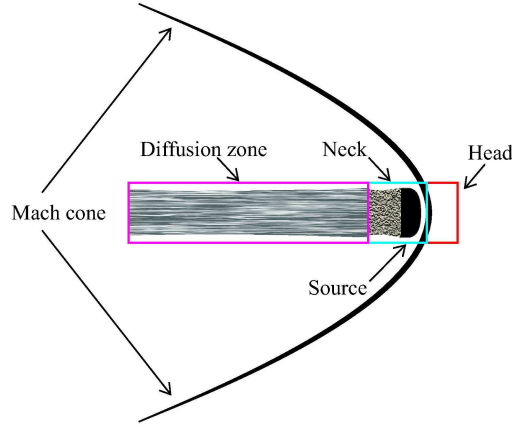
$$J^0(\rho, z, t) = d(\rho, z, t) \gamma u^2 \times \left[1 - \frac{z_-}{z_-^2 + \rho^2} \left(z_- + \frac{\gamma u \rho^2}{\sqrt{\rho^2 + z_-^2 \gamma^2}} \right) \right] , \quad (6.13)$$

$$J^v(\rho, z, t) = (\vec{x} - \vec{u}t) \frac{\alpha_s Q_p^2 m_D^2}{8\pi(z_-^2 + \rho^2)^2} \times \left[\frac{u^4 \rho^4 + (z_-^2 \gamma^2 + \rho^2) (2z_-^2 + (u^2 + 2) \frac{\rho^2}{\gamma^2})}{(z_-^2 \gamma^2 + \rho^2)^2} - \frac{2uz_-}{\gamma \sqrt{z_-^2 \gamma^2 + \rho^2}} \right] , \quad (6.14)$$

with the abbreviation $z_- = (z - ut)$, $\alpha_s = g^2/(4\pi)$, the Casimir operator Q_p [see Eq. (6.3)] and the function $d(\rho, z, t)$

$$d(\rho, z, t) = \frac{\alpha_s Q_p^2 m_D^2}{8\pi[\rho^2 + \gamma^2(z - ut)^2]^{3/2}} . \quad (6.15)$$

It exhibits a singularity at the point of the jet. Thus, an ultraviolet cut-off is needed which was chosen to be $\rho_{\min} = 1/(2\sqrt{E_p T})$ in Ref. [203], where E_p denotes the energy of the fast parton. An infrared cut-off, however, is given by $\rho_{\max} = 1/m_D$. Neufeld et al. [199] applied, as Casalderrey–Solana et al. (cf. section 6.3), linearized hydrodynamics (including viscous terms) to solve Eqs. (6.7). Since the equations decouple in the linearized approach, it allows to separately display the perturbed energy and momentum distributions, excited by a gluon which moves

**Figure 6.9**

Schematic representation of the different regions associated with a jet event.

with a velocity of $u = 0.99955$ along the positive z -axis through a QCD medium (see Fig. 6.7). While the energy density features the shape of a Mach cone, whose intensity is peaked close to the source, the momentum density additionally shows a distinct maximum along the positive z -axis. Plotting the momentum density (see Fig. 6.8), it becomes obvious that this maximum is due to a strong flow created along the trajectory of the jet. Again, like in the scenario studied by Casalderrey–Solana et al. [83] applying a schematic source term, this flow is due to the momentum deposition J^i of the jet. Therefore, the momentum density resulting from the pQCD source term also displays a diffusion wake.

Moreover, Fig. 6.8 illustrates that this diffusion wake gets broader for larger values of the shear viscosity to entropy ratio η/s . Similarly, the intensity of the Mach cone decreases.

Recently, a calculation carried out in the Higher Twist (HT) formalism, including elastic energy loss, for a virtual jet propagating through a medium [206] showed that a Mach-cone structure is formed as well, when plotting the energy-density perturbation.

However, in physical systems the amount of energy and momentum deposited by a propagating jet may be too large to consider them as small perturbations and thus it might not be appropriate to use linearized hydrodynamics. In particular, as Fig. 6.9 reveals, the source itself (which needs a special treatment since it is non-thermalized) as well as the so-called head and neck regions (close to the position of the jet, discussed in detail in the next chapters) are not incorporated in a description applying linearized hydrodynamics. Therefore, something more sophisticated is needed for a correct prescription of the ongoing processes in heavy-ion collisions. In part III, we use a $(3 + 1)$ -dimensional hydrodynamical approach to describe the propagation of a jet through a medium in local thermodynamical equilibrium.

Chapter 7

From String to Field Theory: The AdS/CFT Correspondence

Nature, as presently understood, can be described using quantum field theories like QCD. These theories are able to explain experiments at observable distances. However, it is very likely that at extremely short distances or equivalently at high energies (i.e., at the order of the Planck scale¹) the effect of gravity, which is in general not included in quantum field theories, will become important.

Nevertheless, it is possible to include quantum gravity in a consistent quantum theory by assuming that the fundamental particles are not point-like, but extended objects, *strings* [207].

Depending on their state of oscillation, strings are able to give rise to different kinds of particles and they are able to interact. String theory can only be defined in a certain number of dimensions and geometries. For a flat space, it can only exist in 10 dimensions [208]. Such a 10-dimensional theory describes strings with fermionic excitations and gives rise to a supersymmetric theory. It is a candidate for a quantum theory of gravity [208] since it predicted massless spin 2 particles, gravitons.

Originally, string theory was developed in the 1960's to describe the large number of mesons that were found experimentally at that time, a characteristic feature of the hadron spectrum. It was derived to describe the dynamics of mesons propagating in space-time, but later on it was discovered that the strong interaction is very successfully described by the gauge theory QCD.

QCD exhibits the feature of asymptotic freedom, i.e., its effective coupling constant decreases with increasing energy. At low energies it becomes strongly coupled, so that perturbation theory is no longer valid, complicating any analytic calculations. Lattice gauge theory seems to be the best available tool in this energy range.

It was 'tHooft [209] who suggested that QCD is simpler in the limit of an infinite number of colors, $N_c \rightarrow \infty$. Subsequently, this would allow for an expansion in $1/N_c = 1/3$. Since a diagrammatic expansion of QCD indicates that in the large N_c -limit QCD is a weakly interacting string theory, this $N_c \rightarrow \infty$ limit might connect gauge and string theories.

¹The Planck scale is an energy scale at which gravity becomes strong. It is characterized by the Planck length $l_{\text{Pl}} = 10^{-35}$ m and by the Planck mass $m_{\text{Pl}} = \sqrt{\hbar c/G} \sim 1 \cdot 10^{19}$ GeV/ c^2 which may be defined as the mass for which the Compton wavelength of a particle $\lambda = \hbar/(Mc)$ equals its Schwarzschild radius $r_s = (GM)/c^2$.

Thus, there may be a correspondence between the large N_c -limit of field theories and string theories which is rather general.

In particular, it was shown by Maldacena [210, 211, 212] that there is a correspondence between a supersymmetric $SU(N_c)$ (non-Abelian, i.e., Yang–Mills) conformal field theory² in 4 dimensions ($\mathcal{N} = 4$) which has a constant coupling of $g_{YM}^2/(4\pi) = g_s \sim 1/N_c$ ($\lambda \equiv g_{YM}^2 N_c$, g_s is the string coupling) and a 10-dimensional string theory on the product space $AdS_5 \times S^5$. The (5-dimensional) Anti-de-Sitter space (AdS_5) is the space which characterizes the maximally symmetric solution of Einstein’s equations with negative curvature. In general, the strings are propagating in a curved 10-dimensional background of the form $AdS_5 \times X^5$ where X^5 has to be a compact curved Einstein space. The simplest example is when X^5 is a 5-sphere S^5 [213]. The conjecture is remarkable in a sense that it relates a 10-dimensional theory of gravity to a 4-dimensional theory without gravity, which is defined at the boundary of the AdS_5 space. This is a realization of the so-called *holographic principle*³. For a review, see e.g. Ref. [208]. The advantage of this *AdS/CFT correspondence* is that it offers direct access to the strong-coupling region. Since the gauge theory has a coupling constant of λ , which is connected to the coupling constant of the gravitational theory α'/R^2 (with R being the radius of the AdS space and $\alpha' \sim l_{Pl}^2$) by the relation $\sqrt{\lambda} = R^2/\alpha'$, the conjecture relates either a weakly coupled gauge theory with a strongly coupled string theory or vice versa.

Moreover, nonzero temperatures can be studied by introducing a black-hole horizon. This allows for an extraction of transport coefficients, such as viscosity (discussed below) and heat diffusion. However, there is yet **no** dual for QCD itself and most calculations performed using the AdS/CFT correspondence are only done to leading order in the limit of strong (i.e., infinite) coupling.

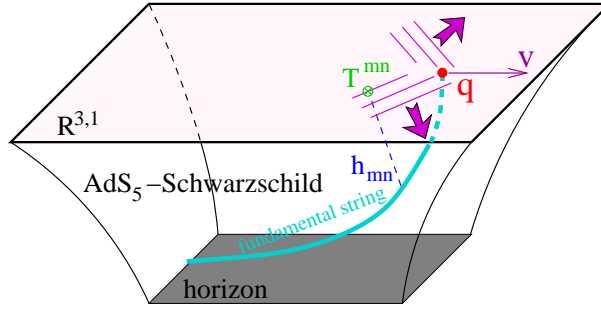
Hence, there is a caveat in applying the AdS/CFT duality to study properties of QCD, especially to describe experimental observables of heavy-ion collisions. One has to be aware of the fact that string theory is compared to a gauge theory with a constant coupling and that the duality for an infinite numbers of colors is already applicable in the case of $N_c = 3$, as in QCD.

7.1 Hard Probes in AdS/CFT

Hard probes are an excellent tool to study the matter created in a heavy-ion collision since their rate of energy and momentum deposition and their interactions with the medium allow for conclusions about the properties of the plasma formed. At weak coupling, the energy loss of both light and heavy quarks can be well described using perturbative QCD (pQCD). However, in the regime of strong coupling, so far no reliable theoretical descriptions are available, but the AdS/CFT correspondence introduced above may offer some guidance.

²Conformal theories are invariant under conformal transformations, i.e., dilatation (scale invariance), inversion and so-called special conformal transformations. QCD is not a conformal invariant theory since there is a scale in the theory, $\Lambda_{QCD} \approx 0.2$ GeV, and its coupling constant is runs.

³In a theory of quantum gravity the holographic principle states that all physics in some volume can be thought of as encoded on the boundary of that region, which should contain at most one degree of freedom per Planck area [208].

**Figure 7.1**

A schematic picture of a moving quark using the AdS/CFT correspondence. A string trails the jet that is moving at the boundary of the 5-dimensional AdS_5 -Schwarzschild space [218].

Usually the investigation of hard probes using AdS/CFT is more complicated for light [214] than for heavy quarks. The problem of a heavy quark moving at a constant speed through a strongly coupled, nonzero temperature $\mathcal{N} = 4$ Super-Yang–Mills (SYM) medium can be analyzed by considering metric fluctuations due to a string hanging down from the boundary of an AdS_5 -Schwarzschild background geometry [215, 217, 218], see Fig. 7.1. Here, it is assumed that the quark has been moving since $t \rightarrow -\infty$, thus it is a steady state solution.

This model is also called the *trailing string*. The heavy quark can be seen as a hard probe if its mass is sufficiently large compared to the temperature of the background. To be precise the mass has to be larger than the typical scale of the medium, thus $M \gg m_D = gT$ for pQCD and $M \gg \sqrt{\lambda}T$ for an $\mathcal{N} = 4$ SYM theory.

Energy and momentum flow down the string at a constant rate, corresponding to the re-distribution of energy along the string. As a consequence of this energy loss, due to the drag (i.e., fluid resistance) force of the plasma, it is necessary to include background electric fields on the brane in order to ensure the constant velocity of the quark. Alternatively, it can be assumed that the quark is infinitely heavy so that it maintains its velocity despite the energy loss. The trailing string provides a source term for the Einstein equations that can be solved to obtain the full energy-momentum tensor in the wake of the jet.

An example of the formidable analytical power of AdS/CFT calculations was given by Yarom in Ref. [219] (see also Ref. [220]). The total energy-momentum tensor describing the near-quark region in the laboratory frame [for cylindrical coordinates $w^\mu = (t, x_1, r, \theta)$ quoted in dimensionless units, thus divided by πT] is determined to be

$$T_{\mu\nu}^Y = P_0 \text{diag}\{3, 1, 1, r^2\} + \xi P_0 \Delta T_{\mu\nu}(x_1, r), \quad (7.1)$$

where $P_0 = N_c^2 \pi^2 T^4 / 8$ is the pressure of the ideal Super-Yang–Mills (SYM) plasma [221] and $\xi = 8\sqrt{\lambda} \gamma / N_c^2$. The explicit form of $\Delta T_{\mu\nu}$ (which scales as $1/x^2$ with the distance x from the quark) is

$$\Delta T_{tt} = \alpha \frac{v \left[r^2(-5 + 13v^2 - 8v^4) + (-5 + 11v^2)x_1^2 \right] x_1}{72 \left[r^2(1 - v^2) + x_1^2 \right]^{5/2}},$$

$$\begin{aligned}
\Delta T_{tx_1} &= -\alpha \frac{v^2 [2x_1^2 + (1-v^2)r^2] x_1}{24 [r^2(1-v^2) + x_1^2]^{5/2}}, \\
\Delta T_{tr} &= -\alpha \frac{(1-v^2)v^2 [11x_1^2 + 8r^2(1-v^2)] r}{72 [r^2(1-v^2) + x_1^2]^{5/2}}, \\
\Delta T_{x_1x_1} &= \alpha \frac{v [r^2(8-13v^2+5v^4) + (11-5v^2)x_1^2] x_1}{72 [r^2(1-v^2) + x_1^2]^{5/2}}, \\
\Delta T_{x_1r} &= \alpha \frac{v(1-v^2) [8r^2(1-v^2) + 11x_1^2] r}{72 [r^2(1-v^2) + x_1^2]^{5/2}}, \\
\Delta T_{rr} &= -\alpha \frac{v(1-v^2) [5r^2(1-v^2) + 8x_1^2] x_1}{72 [r^2(1-v^2) + x_1^2]^{5/2}}, \\
\Delta T_{\theta\theta} &= -\alpha \frac{v(1-v^2)x_1}{9 [r^2(1-v^2) + x_1^2]^{3/2}}, \tag{7.2}
\end{aligned}$$

with $\alpha = \gamma\sqrt{\lambda}T^2$. However, it was assumed throughout the derivation of Eq. (7.1) that the metric disturbances caused by the moving string are small in comparison to the AdS_5 background metric, resulting in the condition that $\xi \Delta T_{\mu\nu} < 1$. Applying this approach to heavy-ion collisions with a proper choice of N_c , λ , and γ [222] leads to a condition about the minimum distance from the quark where the above result is applicable. This energy-momentum tensor is the full non-equilibrium result in the strong-coupling limit and not just a solution of the hydrodynamic equations.

However, it is important to mention that up until now the experimentally measured particle distributions, see chapter 2, are obtained by triggering on **light** quark and gluon jets. Thus, the calculations for heavy quark jets based on AdS/CFT have to be considered as a prediction.

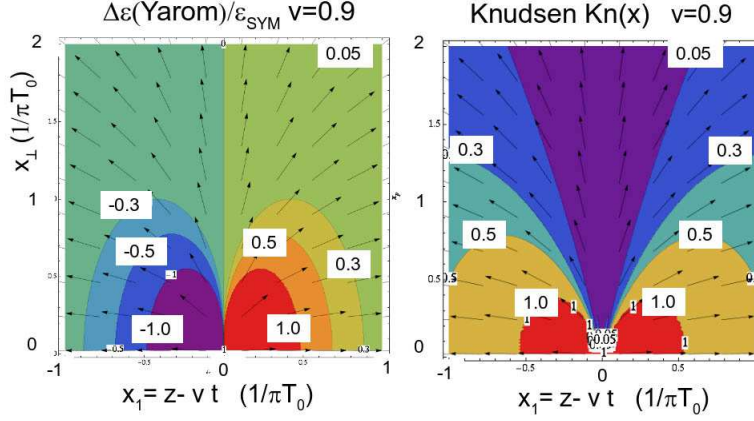
Moreover, an idealized scenario is assumed in that context in which the probe travels through an infinitely extended, spatially uniform plasma. Though this is an approximation, it is always advisable to first investigate an idealized condition. The resulting properties can be included into hydrodynamic models or they can (as will be shown in chapter 10) be compared to pQCD calculations for jet energy loss.

7.2 Shear Viscosity from the AdS/CFT Correspondence

One of the most appealing properties of the AdS/CFT correspondence is that it reflects the hydrodynamic behaviour of field theories. Thus, it was possible to extract the shear viscosity to entropy ratio which was shown to be [223]

$$\frac{\eta}{s} \geq \frac{1}{4\pi}. \tag{7.3}$$

This limit is supposed to be universal for all theories including gravitational duals in the supergravity limit ($N_c \rightarrow \infty$ and $\lambda \equiv g_{YM}^2 N_c \rightarrow \infty$) [224, 225] and implies that a fluid of a given volume and entropy density cannot be a perfect liquid (with vanishing viscosity). It means that in all theories with gravity duals, even in the limit of an infinite coupling, η/s is larger than ~ 0.08 .

**Figure 7.2**

The fractional energy density perturbation (left panel) and the field of the local Knudsen number (right panel) for the disturbance caused by a heavy quark jet as calculated from the total energy-momentum tensor describing the near-quark region using the AdS/CFT correspondence [219], taken from [230].

This result is especially interesting because it was shown by calculations based on pQCD [46] and by comparison of elliptic flow measurements to theoretical predictions [122] that the medium created in a heavy-ion collision can be well described by a fluid with a small η/s ratio (depending on initial conditions, $0 < \eta/s \lesssim 0.2$). This range is clearly consistent with the value of η/s calculated from the AdS/CFT correspondence. It was shown that within Gauss–Bonnet theory higher order derivatives may lead to a shear viscosity to entropy ratio of [226, 227, 228]

$$\frac{\eta}{s} \geq \frac{16}{25} \left(\frac{1}{4\pi} \right) \sim 0.05, \quad (7.4)$$

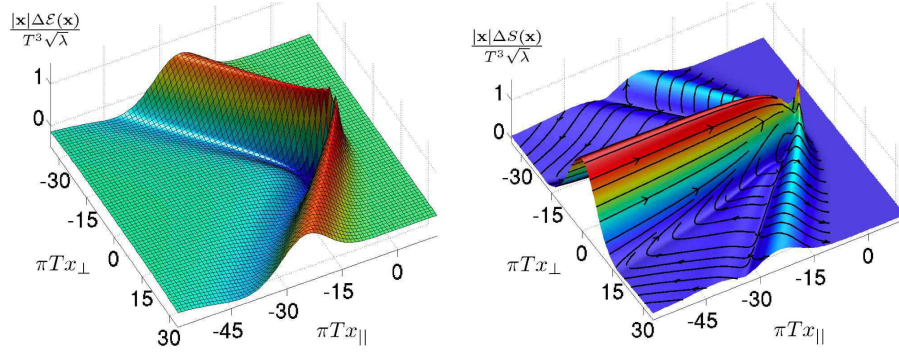
smaller than conjectured by the Kovtun–Starinets–Son viscosity bound.

7.3 Comparison of AdS/CFT to Hydrodynamics

The disturbances in the fluid caused by a moving jet are expected to behave hydrodynamically in the region sufficiently far from the present position of the jet (*far zone*). Close to the jet (in the so-called *near zone*) these disturbances should be large and thus hydrodynamics is supposed to break down.

In fluid dynamics, the Knudsen number K is defined as the ratio between the mean-free path and the characteristic macroscopic length of the system [see Eq. (4.35)]. Hydrodynamics is applicable when $K \ll 1$.

In conformal field theories at nonzero temperatures, the only dimensionful parameter is given by the temperature T and, thus, both the mean-free path and the characteristic length should be proportional to $1/T$. However, the mean-free path is not a well-defined quantity in $\mathcal{N} = 4$ Super–Yang–Mills (SYM) theories for very strong coupling. Nevertheless, one can still establish an effective Knudsen field (that is well defined in the supergravity limit) in terms of the sound attenuation (or

**Figure 7.3**

Energy and momentum (Poynting vector) distribution calculated for a jet moving with $v = 0.75$ using the AdS/CFT correspondence. A Mach cone angle with $\phi_M \sim 50^\circ$ is visible in both patterns, however, a strong flow along the trajectory of the jet (diffusion wake) is also visible in the right plot [232].

absorption) length $\Gamma = 1/3\pi T$ and the Poynting vector⁴ $S^i = T^{0i}$ [229]

$$Kn = \Gamma \left| \frac{\nabla \cdot \vec{S}}{S} \right|. \quad (7.5)$$

As Fig. 7.2 shows, for a jet moving with $v = 0.9$, the region characterized by a large energy perturbation of $\Delta\epsilon/\epsilon_{\text{SYM}} > 0.3$ [computed from the energy-momentum tensor given above, see Eq. (7.1)] corresponds approximately with the locus defined by the local Knudsen number of $Kn \geq 1/3$. Therefore, it was argued in Refs. [230, 231] that for $Kn \geq 1/3$ the system can no longer be described by linearized first-order Navier–Stokes hydrodynamics. A direct comparison of the total energy-momentum tensor describing the near-zone energy-momentum tensor of Ref. [219] [cf. see again Eq. (7.1)] and a first-order Navier–Stokes ansatz showed [229] that a hydrodynamic description of the disturbances caused by the heavy quark is valid down to distances of about $1/T$ from the heavy quark. Later on, we will use the condition for applicability of hydrodynamics ($Kn \leq 1/3$) to analyze AdS/CFT results.

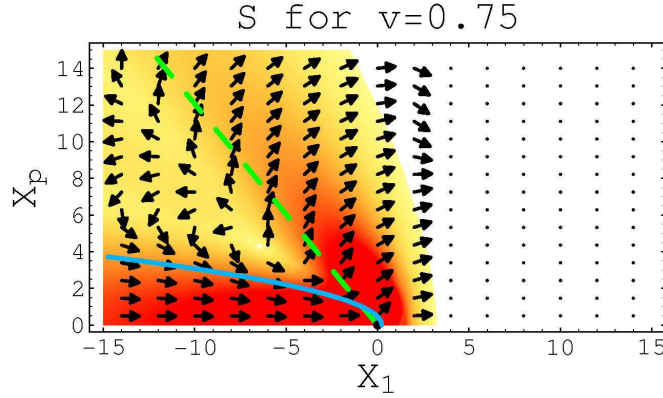
7.4 Mach-Cone-like Correlations in AdS/CFT

The propagation of a supersonic jet through a fluid, associated with energy deposition, is supposed to lead to the creation of Mach cones (see chapter 5). Since, as discussed above, the far zone of the jet can be described using hydrodynamics, the question arises if Mach-cone formation also emerges when calculating the disturbance of the medium due to a jet moving faster than the speed of sound⁵ applying the AdS/CFT correspondence.

In Ref. [232] (see Fig. 7.3), it was demonstrated that using the gauge/string duality, the perturbation of the energy (left panel of Fig. 7.3) and momentum distributions

⁴The Poynting vector represents the energy flux vector of electromagnetic energy.

⁵In $\mathcal{N} = 4$ Super–Yang–Mills (SYM) theory the speed of sound is $c_s = 1/\sqrt{3}$.

**Figure 7.4**

The Poynting vector distribution (the magnitude of $|\vec{S}|$ is color-coded with red indicating a large and white zero magnitude) calculated from the gauge/string duality [233]. The green dashed line indicates the Mach cone while the solid blue line estimates where the diffusion-wake profile reaches half of its maximal value.

(often also referred to as Poynting-vector distribution, right panel of Fig. 7.3) result in a sonic disturbance leading to a shock front with a characteristic opening angle [see Eq. (5.3)] which therefore can be identified with as Mach cone. The same was also shown in Ref. [233], however it was stressed in this publication that a strong flow is created behind the jet which is called the **diffusion wake** (see Fig. 7.4). The impact of this diffusion wake will be discussed in detail in chapter 8.

Those energy and momentum distribution patterns cannot directly be compared to the particle correlations obtained from experiment. Thus, it is necessary to perform a convolution into particles. However, a conical signal based on a hydrodynamic perturbation may be washed out by thermal smearing once the system breaks up into particles. Hence, it might also be possible that a detectable Mach-cone-like signal could come from the region where the linearized hydrodynamical approximation is not valid. It was shown in Ref. [230, 231] that a region close to the location of the jet, the so-called *neck zone* (see the framed area in Fig. 7.5) reveals a strong transverse component that leads to a double-peaked structure in the calculated two-particle distribution (see Fig. 7.6).

The energy-momentum tensor that was used in this investigation and describes both the near and the far-zone was computed by Gubser, Yarum, and Pufu in Ref. [233] for a jet moving with $v = 0.9$, applying the string-drag model. Plotting the energy-density perturbation $\Delta\epsilon/\epsilon_{\text{SYM}}$ (cf. Fig. 7.5), different regions may be introduced:

- The Mach cone, indicated by the dashed magenta line,
- the diffusion zone below that line, characterized by the strong flow along the jet axis (x_1 -axis in Fig. 7.5),
- the neck zone (denoted by the box in Fig. 7.5), specified by the condition that $\Delta\epsilon/\epsilon_{\text{SYM}} > 0.3$,

- the head zone which is an inner region of the neck area⁶, very close to the location of the jet.

In the supergravity limit the energy-momentum tensor can be decomposed accordingly (into the string-drag zones)

$$T^{\mu\nu}(t, \vec{x}) = T_0^{\mu\nu}(t, \vec{x}) + \delta T_{Mach}^{\mu\nu}(t, \vec{x}) + \delta T_{neck}^{\mu\nu}(t, \vec{x}) + \delta T_{Coul}^{\mu\nu}(t, \vec{x}). \quad (7.6)$$

Here, $x_1 = x - vt$ denotes the direction along the (away-side) jet and x_T the transverse coordinate. Then, the Mach part for which the condition $Kn < 1/3$ has to be fulfilled in order to guarantee the applicability of linearized first-order Navier–Stokes hydrodynamics, can be expressed in terms of the local temperature and flow velocity fields through [230]

$$\delta T_{Mach}^{\mu\nu}(x_1, x_\perp) = \frac{3}{4}K \left\{ T^4 \left[\frac{4}{3}u^\mu u^\nu - \frac{1}{3}g^{\mu\nu} + \frac{\eta}{sT} \partial^{(\mu} u^{\nu)} \right] - T_0^{\mu\nu} \right\} \times \theta(1 - 3Kn), \quad (7.7)$$

where $\partial^{(\mu} U^{\nu)}$ is the symmetrized, traceless flow velocity gradient, Kn is the local Knudsen number, $K = (N_c^2 - 1)\pi^2/2$ the Stefan Boltzmann constant for the $\mathcal{N} = 4$ Super–Yang–Mills (SYM) plasma, and $T_0^{\mu\nu}$ the energy-momentum tensor of the (static) background. The theta function defines the far zone where the equilibration happens quickly enough to ensure a hydrodynamical prescription.

This far zone excludes the neck region close to the jet which is a non-equilibrium zone that can be described in $\mathcal{N} = 4$ SYM via [219, 220]

$$\delta T_{neck}^{\mu\nu}(x_1, x_\perp) \approx \theta(3Kn - 1) \frac{\sqrt{\lambda} T_0^2}{x_\perp^2 + \gamma^2 x_1^2} Y^{\mu\nu}(x_1, x_\perp) \quad (7.8)$$

⁶The head zone can also be defined as distinct area following the neck region (see Fig. 6.9).

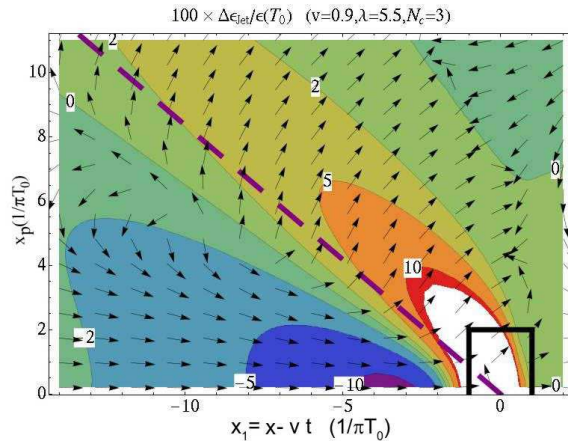
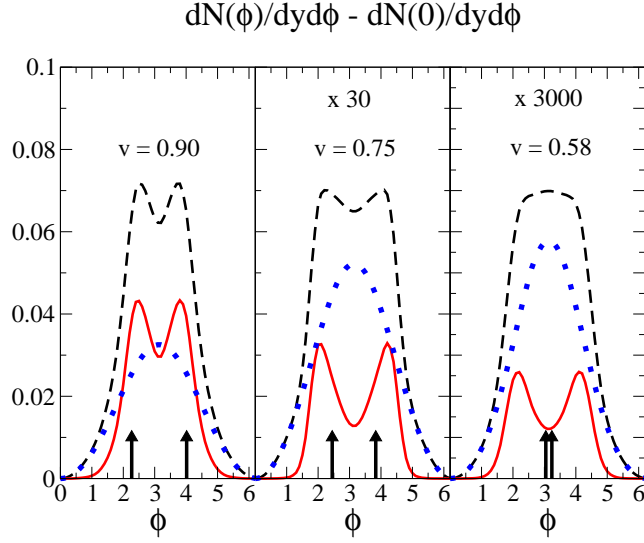


Figure 7.5

The relative energy-density perturbation due to a heavy quark propagating with $v = 0.9$ through an $\mathcal{N} = 4$ Super–Yang–Mills (SYM) plasma with $N_c = 3$ [233]. The arrows indicate the Poynting vector flow (momentum flux) directions and the dashed line denotes the Mach cone with $\cos \phi_M = 1/(\sqrt{3}v)$. The box indicates the neck zone [231].

**Figure 7.6**

Background-subtracted, azimuthal angular distribution for massless particles at mid-rapidity obtained from an isochronous Cooper–Frye freeze-out for the temperature and velocity fields obtained from the AdS/CFT string-drag model [233] for the three different scenarios of $v = 0.9$, $p_T/(\pi T_0) = 4 - 5$, $v = 0.75$, $p_T/(\pi T_0) = 5 - 6$ and $v = 0.58$, $p_T/(\pi T_0) = 6 - 7$. The red curves show the contribution from the neck region, defined by $\Delta\varepsilon/\varepsilon_{\text{SYM}}$, the blue curves result from integrating the far zone (excluding the neck region) and the black line display the total yields. The expected Mach angles are indicated by the arrows [231].

Here, $Y^{\mu\nu}$ is a dimensionless “angular” tensor field, which reduces to the energy-momentum tensor given in Eq. (7.1) at very small distances from the jet.

The head region is that part of the neck zone where the energy-momentum tensor becomes dominated by the contracted Coulomb field of the quark. Thus, as it was shown in Ref. [234], the head can be defined by equating the Coulomb energy density to the near-zone energy density given by Eq. (7.1). Its boundary is approximately given by [231]

$$x_\perp^2 + \gamma^2 x_1^2 = \frac{1}{(\pi T_0)^4} \frac{(2x_\perp^2 + x_1^2)^2}{\gamma^4 x_1^2 (x_\perp^2/2 + \gamma^2 x_1^2)^2}. \quad (7.9)$$

The observable consequences can be investigated by applying a Cooper–Frye hadronization procedure [230, 231] with an isochronous freeze-out as discussed in chapter 3.

This is a very strong model assumption since the freeze-out is applied to the total volume, including the non-equilibrated neck zone (where the Cooper–Frye freeze-out may not be applicable, see also chapter 10) which is roughly the region between $-1 < x_1(\pi T_0) < 1$ and $0 - x_T(\pi T_0) < 2$ (see Fig. 7.5).

The background-subtracted, azimuthal angular distribution for massless particles at mid-rapidity is shown in Fig. 7.6 for three different velocities of the jet and p_T -ranges, $v = 0.9$, $p_T/(\pi T_0) = 4 - 5$, $v = 0.75$, $p_T/(\pi T_0) = 5 - 6$ and $v = 0.58$, $p_T/(\pi T_0) = 6 - 7$. The black lines display the total yield that consists of the contribution from the neck (red line) and from the far region excluding

the neck (blue line). The figure reveals that the double-peaked structure occurring for $v = 0.9$ and $v = 0.75$ is completely due to the (non-equilibrated) neck region that always develops a dip around $\phi = \pi$.

However, this double-peaked structure of the neck region is completely uncorrelated to a Mach cone since the location of the peaks do not follow the expected Mach-cone angles, which are indicated by the arrows in Fig. 7.6 and change with the velocity of the jet. For $v = 0.9$, the two peaks of the neck region incidentally agree with the Mach angle.

Thus, the predictive power of the AdS/CFT string drag model could be tested [230, 231] by looking for conical distributions that deviate from the expected Mach angle for supersonic, but not ultra-relativistic *identified heavy quark jets*.

7.5 The No-Go Theorem

Figure 7.6 reveals that the far zone, which includes the Mach contribution but excludes the neck region, always shows a broad away-side peak instead of an expected double-peaked structure. It can be shown [230, 231], as reviewed below, that this result is universal in the large- N_c limit and independent of the strength of the diffusion wake formed behind the jet.

For associated away-side particles with $p^\mu = (p_T, p_T \cos(\pi - \phi), p_T \sin(\pi - \phi), 0)$ the azimuthal distribution at mid-rapidity is given by [see Eq. (3.36)]

$$\frac{dN}{p_T dp_T d\phi dy} \Big|_{y=0} = \int_{\Sigma} d\Sigma_\mu p^\mu [f(u \cdot p/T) - f_{eq}(E_0/T_0)] , \quad (7.10)$$

where a constant, thermal background f_{eq} is subtracted. In the supergravity approximation of $N_c \rightarrow \infty$, or equivalently for $\Delta T \ll T_0$ and $\vec{p} \cdot \vec{u} \ll T_0$ (both, $\Delta T \sim \sqrt{\lambda}$ and $u \sim \sqrt{\lambda}/N_c^2$ are small, since $\lambda \gg 1$, but $N_c \gg \lambda$), the Boltzmann exponent can be expanded up to corrections of $\mathcal{O}(\lambda/N_c^4)$.

Choosing an isochronous ansatz with $d\Sigma^\mu = x_T dx_T dx_1 d\varphi (1, 0, 0, 0)$ and coordinates of $u^\mu(x_1, x_T) = (u^0, u_1, u_T \sin \varphi, u_T \cos \varphi, 0)$, after integration over φ in we obtain the distribution

$$\begin{aligned} \frac{dN}{p_T dp_T d\phi dy} \Big|_{y=0} &= 2\pi p_T \int_{\Sigma} dx_1 dx_T x_T \\ &\times \left(\exp \left\{ -\frac{p_T}{T} [u_0 - u_1 \cos(\pi - \phi)] \right\} I_0(a_T) - e^{-p_T/T_0} \right) . \end{aligned} \quad (7.11)$$

Here, $a_T = p_T u_\perp \sin(\pi - \phi)/T$ and I_0 denotes the modified Bessel function. However, in the supergravity approximation $a_\perp \ll 1$, and therefore one can expand the Bessel function

$$\lim_{x \rightarrow 0} I_0(x) = 1 + \frac{x^2}{4} + \mathcal{O}(x^4) \quad (7.12)$$

to get an approximate expression for the distribution [231]

$$\frac{dN}{p_T dp_T d\phi dy} \Big|_{y=0} \simeq e^{-p_T/T_0} \frac{2\pi p_T^2}{T_0} \left[\frac{\langle \Delta T \rangle}{T_0} + \langle u_1 \rangle \cos(\pi - \phi) \right] , \quad (7.13)$$

where $\langle \Delta T \rangle = \int_{\Sigma} dx_1 dx_{\perp} x_{\perp} \Delta T$ and $\langle u_1 \rangle = \int_{\Sigma} dx_1 dx_{\perp} x_{\perp} u_1$. Generally speaking, the above equation holds as long as the approximation $p_T/T = p_T/(T_0 + \Delta T) \approx p_T/T_0(1 - \Delta T/T_0)$ is valid. Therefore, in the $N_c \rightarrow \infty$ limit, the associated away-side distribution reveals a broad peak around $\phi = \pi$. A double-peaked structure in the away-side of the jet correlation function can only arise when the approximations made become invalid.

Part III

Jet Propagation and Mach-Cone Formation

In the following chapters, we present our investigations about the propagation of a jet through a strongly-coupled medium, using $(3 + 1)$ -dimensional ideal hydrodynamics. We apply and compare different source terms describing the energy and momentum deposition of a jet as well as its interaction with the QGP, starting with a schematic source term, but also for the two independent approaches of pQCD and AdS/CFT.

While the pQCD scenario is certainly the correct description in the hard-momentum region where jets are produced ($Q \gg T_0$), in the soft part of the process ($Q \sim T_0$) non-perturbative effects, covered by the AdS/CFT approach, may become relevant. Here, the most striking differences will become apparent due to the influence of the neck region as already discussed in chapter 7.

We start with a study on the away-side angular correlations for punch-through and fully stopped jets applying a simple ansatz for the source term. Surprisingly enough, we find that the medium's response as well as the corresponding correlations are largely insensitive to whether the jet punches through or stops inside the medium. The existence of the diffusion wake is shown to be universal to all scenarios where momentum as well as energy is deposited into the medium. In ideal hydrodynamics, this can be readily understood through vorticity conservation which is examined separately in chapter 9.

Though the above mentioned analyses are done for a static medium, chapter 11, which discusses an expanding system, shows that while radial flow may for some jet trajectories diminish the impact of the diffusion wake [235], it still strongly influences the final angular particle distributions. However, the main characteristics of those distributions are due to the different contributions of several possible jet-trajectories through the expanding medium [236, 237] leading to a double-peaked structure which is therefore not directly connected to the emission angles of a Mach cone.

Chapter 8

The Diffusion Wake

In general, a fast moving parton (which could be a light quark/gluon or a heavy quark) will lose a certain amount of its energy and momentum along its path through the medium and consequently decelerate. Thus, the fate of the parton jet strongly depends on its initial energy: if the parton has enough energy it can punch through the medium and fragment in the vacuum (a *punch-through jet*) or it can be severely quenched until it becomes part of the thermal bath (a *stopped jet*). Of course, the amount of initial energy required for the parton to punch through depends on the properties of the medium (a very large energy loss per unit length dE/dx means that most of the jets will be quenched while only a few jets would have enough energy to leave the plasma). In the following, we solve the $(3 + 1)$ -dimensional ideal hydrodynamical equations including source terms (see chapter 6.4) that describe those two scenarios in order to compare the final away-side angular correlations produced by a punch-through and a fully stopped jet in a static medium with a background temperature T_0 .

For simplicity, our medium is considered to be a gas of massless $SU(3)$ gluons for which $p = \varepsilon/3$, where p and ε are the pressure and the energy density, respectively. Two different freeze-out procedures, briefly reviewed below (see also section 3.7), are employed in order to obtain the angular distribution of particles associated with the away-side jet.

We use a simplified Bethe–Bloch model [238] to show that the explosive burst of energy and momentum (known as the Bragg peak [239, 240, 241, 242]) deposited by a fully quenched jet immediately before it thermalizes does not stop the strong flow behind the jet (the diffusion wake) and, thus, the structures on the away-side of angular correlation functions are very similar to those of punch-through jets. This explosive release of energy before complete stopping is a general phenomenon which has been employed, for instance, in applications of particle beams for cancer therapy [243, 244, 245].

In our system of coordinates, the beam axis is aligned with the z -direction and the associated jet moves along the x -direction with velocity $\vec{v} = v \hat{x}$. We take the net baryon density to be identically to zero. Moreover, we omit the near-side correlations associated with the trigger jet and assume that the away-side jet travels through the medium according to a source term that depends on the jet velocity profile which shall be discussed below for the case of punch-through and stopped jets.

The away-side jet is implemented in the beginning of the hydrodynamical evolution at $x = -4.5$ fm, and its motion is followed until it reaches $x = 0$. For a jet moving with a constant velocity v_{jet} this happens at $t_f = 4.5/v_{\text{jet}}$ fm.

In order to obtain the away-side angular correlations, we use the two different methods introduced in section 3.7. Applying the isochronous Cooper–Frye (CF) [129], the fluid velocity $u^\mu(t_f, \vec{x})$ and temperature $T(t_f, \vec{x})$ fields are converted into free particles at a freeze-out surface Σ at constant time t_f . In principle, one has to ensure that energy and momentum are conserved during the freeze-out procedure [104]. However, the associated corrections are zero if the equation of state is the same before and after the freeze-out, as it is assumed in the present considerations. In this case, the momentum distribution for associated (massless) particles $p^\mu = (p_T, p_T \cos(\pi - \phi), p_T \sin(\pi - \phi))$ at mid-rapidity $y = 0$ is computed via

$$\frac{dN_{\text{ass}}}{p_T dp_T dy d\phi} \Big|_{y=0} = \int_{\Sigma} d\Sigma_\mu p^\mu [f_0(u \cdot p/T) - f_{eq}] . \quad (8.1)$$

Here, ϕ is the azimuthal angle between the emitted particle and the trigger, p_T is the transverse momentum, $f_0 = \exp[-u^\mu(t, \vec{x}) p_\mu / T(t, \vec{x})]$ the local Boltzmann equilibrium distribution, and $f_{eq} \equiv f|_{u^\mu=0, T=T_0}$ denotes the isotropic background yield. We checked that our results do not change significantly if we use a Bose–Einstein distribution instead of the Boltzmann distribution. The background temperature is set to $T_0 = 0.2$ GeV.

Following Refs. [83, 171, 231, 246], we define the angular function

$$CF(\phi) = \frac{1}{N_{\text{max}}} \left(\frac{dN_{\text{ass}}(\phi)}{p_T dp_T dy d\phi} - \frac{dN_{\text{ass}}(0)}{p_T dp_T dy d\phi} \right) \Big|_{y=0} , \quad (8.2)$$

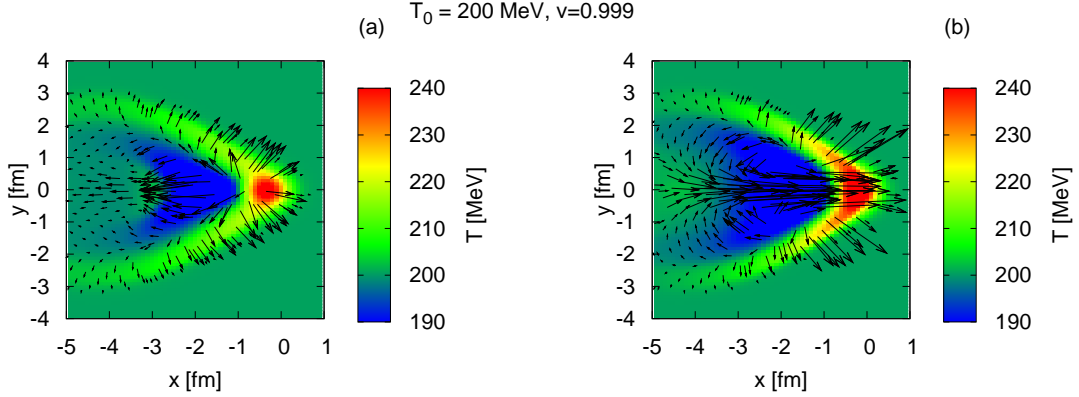
where the constant N_{max} is used to normalize the plots. It is important to mention that in the associated p_T -range of interest a coalescence/recombination hadronization scenario [134, 135, 247, 248, 249] may be more appropriate than CF freeze-out. Since it might well be possible that procedures following the recombination of partons into hadrons influence the final particle distributions, this issue deserves further scrutiny.

The other freeze-out prescription (called bulk-flow freeze-out) was introduced in Ref. [136]. The main assumption behind the bulk-flow freeze-out is that all the particles inside a given small sub-volume of the fluid will be emitted into the same direction as the average local energy flow

$$\frac{d\mathcal{E}}{d\phi dy} = \int d^3\vec{x} \mathcal{E}(\vec{x}) \delta[\phi - \Phi(\vec{x})] \delta[y - Y(\vec{x})] . \quad (8.3)$$

Here, ϕ is again the azimuthal angle between the detected particle and the trigger jet and y is the particle rapidity. Only the $y = 0$ yield is considered. The cells are selected according to their local azimuthal angle $\Phi(\vec{x}) = \arctan[\mathcal{P}_y(\vec{x})/\mathcal{P}_x(\vec{x})]$ and rapidity $Y(\vec{x}) = \text{Artanh}[\mathcal{P}_z(\vec{x})/\mathcal{E}(\vec{x})]$. The local momentum density of the cell is $T^{0i}(\vec{x}) = \mathcal{P}_i(\vec{x})$, while its local energy density in the lab frame is $\mathcal{E}(\vec{x}) = T^{00}(\vec{x})$. The δ -functions are implemented using a Gaussian representation as in Ref. [136].

Due to energy and momentum conservation, this quantity should be conserved after freeze-out. Eq. (8.3) is not restricted to a certain p_T and does not include the thermal smearing that is always present in the CF freeze-out.

**Figure 8.1**

Temperature pattern and flow velocity profile (arrows) after a hydrodynamical evolution of $t = 4.5/v_{\text{jet}}$ fm, assuming (a) an energy loss rate of $dE/dt = 1.5$ GeV/fm for a vanishing momentum loss rate and (b) an energy and momentum loss rate of $dE/dt = dM/dt = 1.5$ GeV/fm for a punch-through jet moving with a constant velocity of $v_{\text{jet}} = 0.999$ along the x -axis through a static background plasma with temperature $T_0 = 200$ MeV. The jet is sitting at the origin of the coordinates at the time of freeze-out [137].

8.1 Punch-Through Jets in a Static Medium

In this section, we consider a jet moving with a uniform velocity of $v_{\text{jet}} = 0.999$ through the medium. The source term is given by [cf. Eq. (6.9)]

$$J^\nu = \int_{\tau_i}^{\tau_f} d\tau \frac{dM^\nu}{d\tau} \delta^{(4)} \left[x^\mu - x_{\text{jet}}^\mu(\tau) \right], \quad (8.4)$$

where $\tau_f - \tau_i$ denotes the proper time interval associated with the jet evolution. We further assume a constant energy and momentum loss rate $dM^\nu/d\tau = (dE/d\tau, d\vec{M}/d\tau)$ along the trajectory of the jet $x_{\text{jet}}^\mu(\tau) = x_0^\mu + u_{\text{jet}}^\mu \tau$.

In non-covariant notation, this source term has the form

$$J^\nu(t, \vec{x}) = \frac{1}{(\sqrt{2\pi}\sigma)^3} \exp \left\{ -\frac{[\vec{x} - \vec{x}_{\text{jet}}(t)]^2}{2\sigma^2} \right\} \left(\frac{dE}{dt}, \frac{d\vec{M}}{dt}, 0, 0 \right), \quad (8.5)$$

where \vec{x}_{jet} describes the location of the jet, \vec{x} is the position on the computational grid, and $\sigma = 0.3$ fm. The system plasma+jet evolves according to Eq. (6.7) until the freeze-out time $t_f = 4.5/v_{\text{jet}}$ fm is reached.

The temperature and flow velocity profiles created by a punch-through jet with a constant energy loss rate of $dE/dt = 1.5$ GeV/fm and vanishing momentum deposition are shown in Fig. 8.1 (a). In Fig. 8.1 (b) the jet has lost the same amount of energy and momentum. One can clearly see that the space-time region close to the jet, where the temperature disturbance is the largest, is bigger than in the pure energy deposition scenario.

The creation of a diffusion wake behind the jet in case of equal energy and momentum deposition is clearly visible, which is indicated by the strong flow observed in

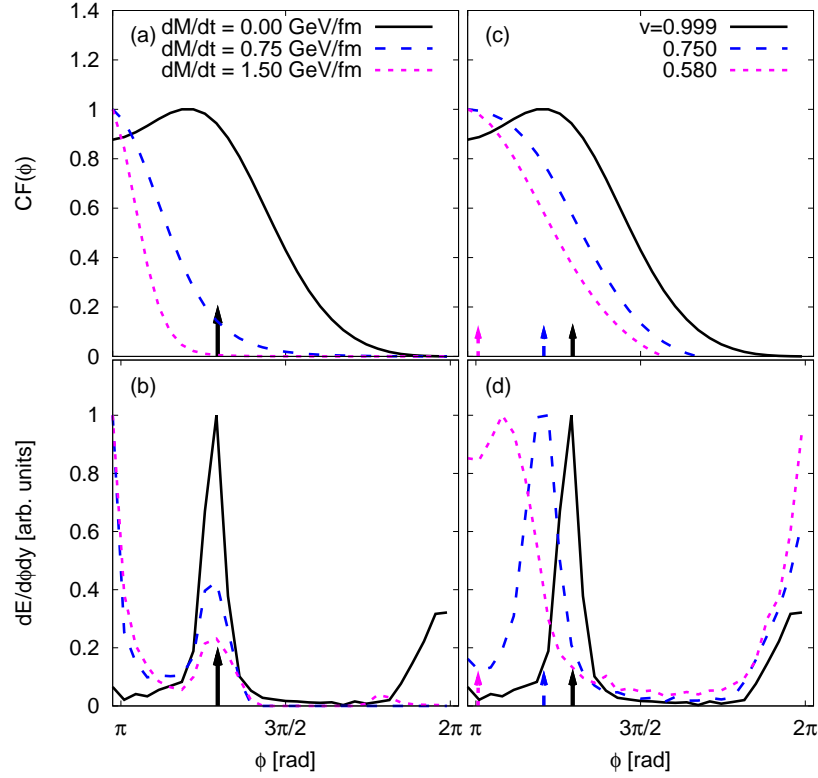


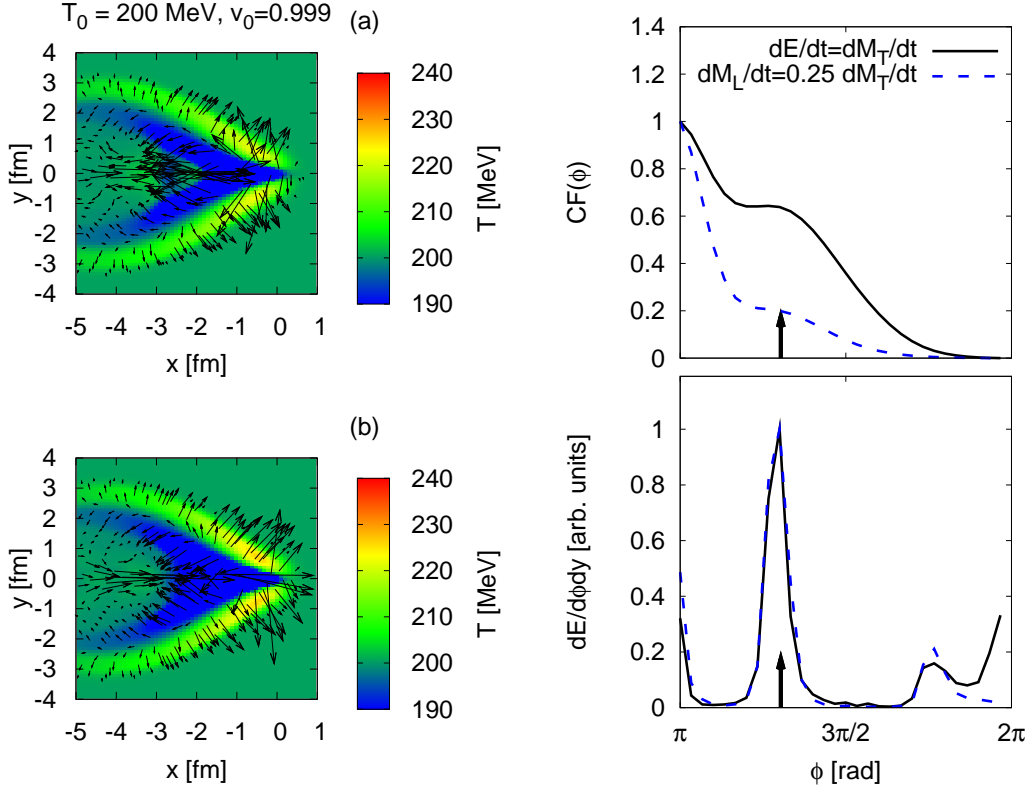
Figure 8.2

The left panels show the normalized angular distribution created by a punch-through jet at mid-rapidity with a fixed energy loss of $dE/dt = 1.5$ GeV/fm and different momentum loss rates. The jet moves at a constant velocity $v_{\text{jet}} = 0.999$ through the medium. The right panels show the angular distributions associated with jets with $dE/dt = 1.5$ GeV/fm and vanishing momentum loss ($dM/dt = 0$). Here, the jets move with different velocities through the medium: $v_{\text{jet}} = 0.999$ (black), $v_{\text{jet}} = 0.75$ (blue), and $v_{\text{jet}} = 0.58$ (magenta). In the upper panels, an isochronous Cooper–Frye freeze-out at $p_T = 5$ GeV is used while in the lower panels we employed the bulk-flow freeze-out procedure [136]. The arrows indicate the angle of the Mach cone as computed via Mach’s law [137].

the forward direction (at $\phi = \pi$).

It is important to mention that, see Fig. 8.2 (a), for the punch-through jet deposition scenario with equal energy and momentum loss one always obtains a peak in the associated jet direction after performing the freeze-out using the two prescriptions described above.

However, the energy-flow distribution in Fig. 8.2 (b) displays an additional small peak at the Mach cone angle indicated by the arrow. This Mach signal cannot be seen in the Cooper–Frye freeze-out because of thermal smearing [83, 136, 231, 246] and the strong influence of the diffusion wake, which leads to the strong peak around $\phi \sim \pi$ in the bulk energy-flow distribution. However, given that the exact form of the source term in the sQGP is unknown, one may want to explore other energy-momentum deposition scenarios where the jet deposits more energy than

**Figure 8.3**

Left panel: Temperature pattern and flow velocity profile (arrows) after a hydrodynamical evolution of $t = 4.5/v_{\text{jet}}$ fm, assuming an energy loss rate of $dE/dt = dM/dt = 1.5$ GeV/fm for (a) full transverse momentum deposition and (b) longitudinal as well as transverse momentum deposition with a ratio of $dM_L/dt = 0.25 dM_T/dt$. Right panel: The normalized angular distribution created by a punch-through jet at mid-rapidity for the two above mentioned transverse momentum deposition scenarios. In the upper panel, an isochronous Cooper–Frye freeze-out at $p_{\perp} = 5$ GeV is used while in the lower panel the bulk-flow freeze-out procedure [136] is employed. The arrows indicate the ideal Mach-cone angle [137].

momentum along its path. While this may seem unlikely, such a situation cannot be ruled out. Thus, for the sake of completeness, we additionally consider in Fig. 8.2 (a) the case where the jet source term is described by a fixed energy loss of $dE/dt = 1.5$ GeV/fm and different momentum loss rates.

In the bulk-flow distribution in Fig. 8.2 (b), one can see that the peak at the Mach-cone angle is more pronounced for smaller momentum loss while the contribution of the diffusion wake (indicated by the peak in forward direction) is reduced. The associated particle distribution from the CF freeze-out in Fig. 8.2 (a) reveals a peak at $\phi \neq \pi$ for pure energy deposition (solid black line), however, the opening angle is shifted to a value smaller than the Mach cone angle due to thermal smearing [246].

In Figs. 8.2 (c,d) we consider $dM/dt = 0$ jets that move through the medium with different velocities $v_{\text{jet}} = 0.999, 0.75$, and 0.58 . In Fig. 8.2 (d) the peak position changes in the bulk-flow distribution according to the expected Mach-cone angles (indicated by the arrows). However, due to the strong bow shock created by a jet moving at a slightly supersonic velocity of $v_{\text{jet}} = 0.58$, there is a strong contribution in the forward direction and the peak position is shifted from the expected value. In the CF freeze-out shown in Fig. 8.2 (c), the peak from the Mach cone can again be seen for the jet moving nearly at the speed of light ($v_{\text{jet}} = 0.999$), but for slower jets thermal smearing again leads to a broad distribution peaked in the direction of the associated jet. It can indeed be shown that those broad distributions can be obtained by modelling the away-side distribution with two Gaussians, the peak locations of which follow Mach's law if the width of the distributions, and thus the thermal smearing, is sufficiently large.

It is apparently surprising that the above mentioned results are independent of whether the momentum deposited by the particle is in the longitudinal (along the motion of the jet) or transversal (perpendicular) direction. Repeating the calculation shown in Fig. 8.1 including transverse momentum deposition

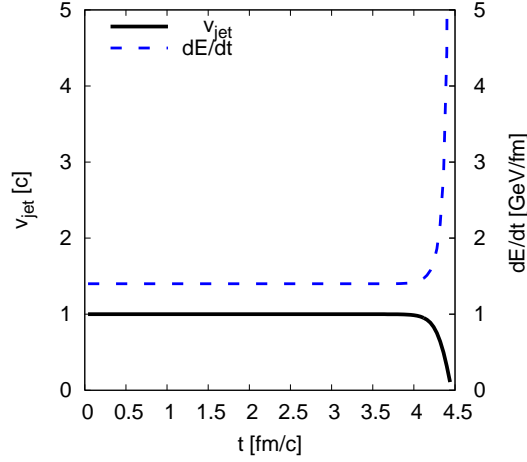
$$J^\nu(t, \vec{x}) \propto \begin{bmatrix} dE/dt \\ dM_L/dt \\ (dM_T/dt) \cos \varphi \\ (dM_T/dt) \sin \varphi \end{bmatrix}, \quad (8.6)$$

where φ is the latitude angle in the $(y-z)$ -plane with respect to the jet motion and the magnitude of $J^\nu(t, \vec{x})$ is the same as Eq. (8.4), shows that transverse momentum deposition will not alter the results presented in this section (see Fig. 8.3). A longitudinal diffusion wake still forms during the fluid evolution stage, and its contribution will still dominate the resulting angular inter-particle correlations though a peak occurs around the expected Mach cone angle in the CF freeze-out.

The reason is that transverse momentum deposition will force the fluid around the jet to expand, and the empty space left will be filled by matter flowing in a way that behaves much like a diffusion wake. In terms of ideal hydrodynamics, this universality of the diffusion wake can be understood in the context of vorticity conservation since momentum deposition, whether transverse or longitudinal, will add vorticity to the system. This vorticity will always end up behaving as a diffusion wake [250]. In the next section, we demonstrate that these results are largely independent of whether the jet is fully quenched or survives as a hard trigger.

8.2 Stopped Jets in a Static Medium

In the previous section we considered a uniformly moving jet that deposited energy and/or momentum in the medium at a constant rate. However, due to its interaction with the plasma, the jet will decelerate and its energy and/or momentum loss will change. Thus, the deceleration roughly represents the response of the medium. In general, a decelerating jet should have a peak in the energy loss rate because the interaction cross section increases as the parton's energy decreases. In other words, when the particle's velocity goes to zero there appears a peak in dE/dx known as

**Figure 8.4**

The jet velocity $v_{\text{jet}}(t)$ (solid black line) and energy deposition rate $dE(t)/dt$ (dashed blue line) according to Eq. (8.9). The initial jet velocity and energy-loss rate are $v_{\text{jet}} = 0.999$ and $a \simeq -1.3607$ GeV/fm, respectively [137].

the Bragg peak [239].

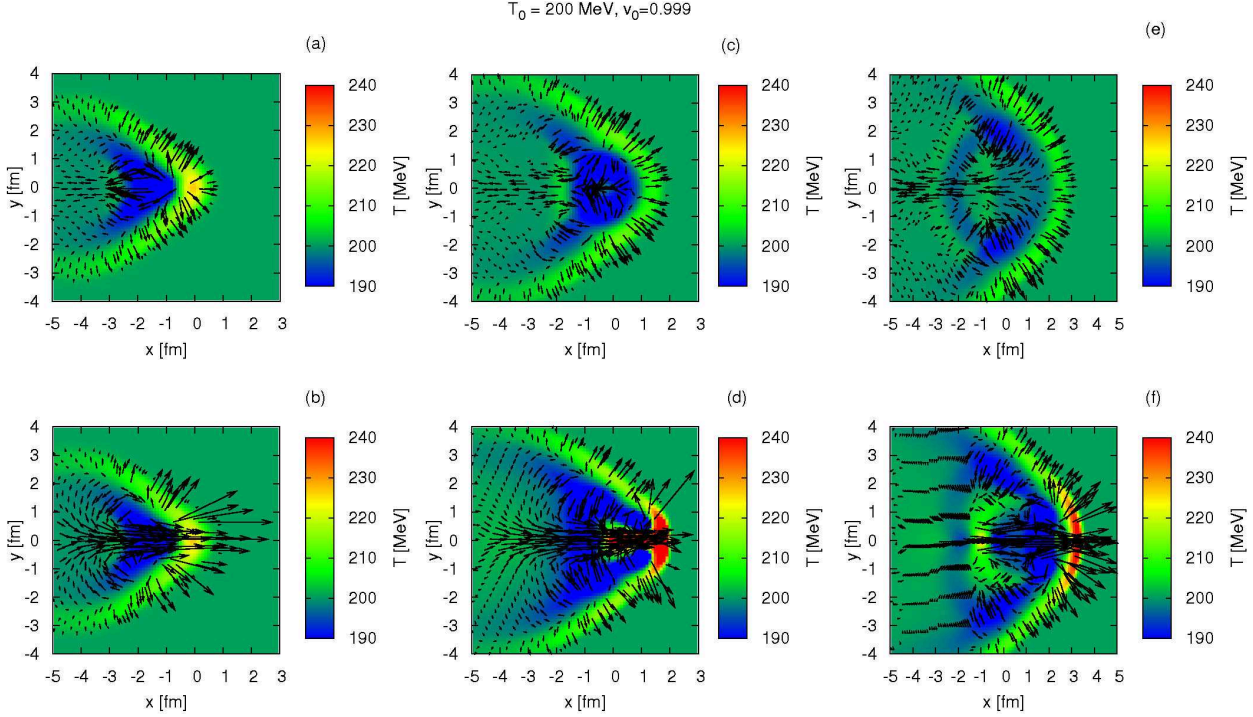
The question to be considered in this section is whether this energy-deposition scenario might be able to somehow stop the diffusion wake and, thus, change the angular distributions shown in Fig. 8.2. The source term in this case is still given by Eq. (8.5) and, according to the Bethe–Bloch formalism [239, 240, 241, 242], one assumes that

$$\frac{dE(t)}{dt} = a \frac{1}{v_{\text{jet}}(t)}, \quad (8.7)$$

which shows that when the jet decelerates the energy loss rate increases and has a peak as $v_{\text{jet}} \rightarrow 0$. Here, dE/dt is the energy lost by the jet, which is the negative of the energy given to the plasma. Using this ansatz for the velocity dependence of the energy-loss rate and the identities $dE/dt = v_{\text{jet}} dM/dt$ and $dM/dy_{\text{jet}} = m \cosh y_{\text{jet}}$ (as well as $v_{\text{jet}} = \tanh y_{\text{jet}}$), one can rewrite Eq. (8.7) as

$$t(y_{\text{jet}}) = \frac{m}{a} \left[\sinh y_{\text{jet}} - \sinh y_0 - \arccos \frac{1}{\cosh y_{\text{jet}}} + \arccos \frac{1}{\cosh y_0} \right], \quad (8.8)$$

where y_0 is the jet's initial rapidity. A detailed derivation of this equation is given in appendix E. The equation above can be used to determine the time-dependent velocity $v_{\text{jet}}(t)$. The initial velocity is taken to be $v_0 = \text{Artanh} y_0 = 0.999$. The mass of the moving parton is assumed to be of the order of the constituent quark mass, $m = 0.3$ GeV. Moreover, the initial energy loss rate $a \simeq -1.3607$ GeV/fm is determined by imposing that the jet stops after $\Delta x = 4.5$ fm (as in the previous section for a jet with $v_{\text{jet}} = 0.999$). Thus, the jet location as well as the energy and momentum deposition can be calculated (see again appendix E) as a function

**Figure 8.5**

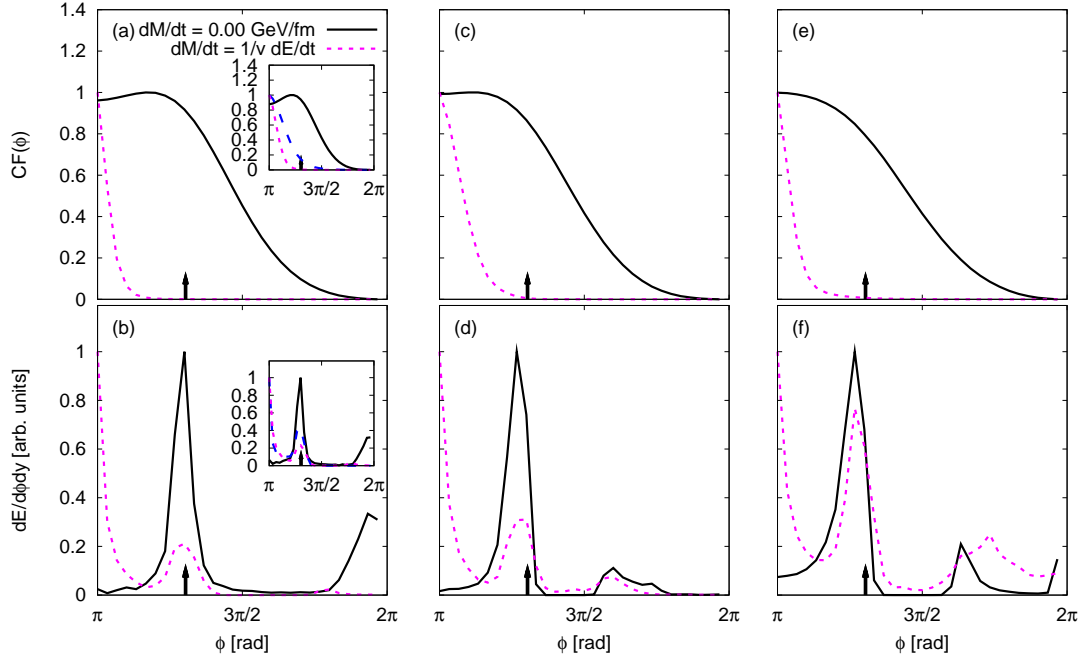
Temperature pattern and flow-velocity profile (arrows) after a hydrodynamical evolution of $t = 4.5$ fm (left panel), $t = 6.5$ fm (middle panel), and $t = 8.5$ fm (right panel) for a jet that decelerates according to the Bethe–Bloch formula and stops after $\Delta x = 4.5$ fm. The jet’s initial velocity is $v_{\text{jet}} = 0.999$. In the upper panel a vanishing momentum-loss rate is assumed while in the lower panel the momentum loss is related to the energy loss by Eq. (8.9) [137].

of time via the following equations

$$\begin{aligned}
 x_{\text{jet}}(t) &= x_{\text{jet}}(0) + \frac{m}{a} \left[(2 - v_{\text{jet}}^2) \gamma_{\text{jet}} - (2 - v_0^2) \gamma_0 \right], \\
 \frac{dE}{dt} &= a \frac{1}{v_{\text{jet}}}, \quad \frac{dM}{dt} = a \frac{1}{v_{\text{jet}}^2},
 \end{aligned} \tag{8.9}$$

which can be used to determine the corresponding source term for the energy-momentum conservation equations. The change of the jet velocity $v_{\text{jet}}(t)$ and energy deposition $dE(t)/dt$ are displayed in Fig. 8.4. The strong increase of energy deposition shortly before the jet is completely stopped corresponds to the well-known Bragg peak [239].

The main difference between the ansatz described here and the Bethe–Bloch equation is that the momentum deposition is longitudinal (parallel to the motion of the jet) rather than transverse (perpendicular to the motion of the jet). According to most pQCD calculations, this is true in the limit of an infinite energy jet [65, 187, 189, 192, 251, 252, 253, 254, 255, 256, 257], but it is expected to break down in the vicinity of the Bragg peak where the jet energy is comparable to the energy of a thermal particle. However, as we demonstrated in the previous section,

**Figure 8.6**

The normalized angular distribution generated by a decelerating jet (cf. also Fig. 8.5) at mid-rapidity is shown (upper panel) according to an isochronous Cooper–Frye freeze-out at $p_T = 5$ GeV for a jet that stops after $\Delta x = 4.5$ fm and a hydrodynamical evolution of $t = 4.5$ fm (left panel), $t = 6.5$ fm (middle panel), and $t = 8.5$ fm (right panel). The corresponding bulk-flow pattern [136] is shown in the lower panel. The solid black line in all plots depicts the pure energy-deposition case while the dashed magenta line corresponds to the energy and momentum deposition scenario given by Eq. (8.9). The arrows indicate the angle of the Mach cone as computed via Mach’s law. The inserts repeat Fig. 8.2 (a) and (b) for comparison [137].

the freeze-out phenomenology is rather insensitive to whether the momentum deposition is transverse or longitudinal.

Fig. 8.5 displays the temperature and flow velocity profiles of a jet that stops after $\Delta x = 4.5$ fm, with an energy loss according to Eq. (8.7) and vanishing momentum deposition (upper panel) as well as an energy and momentum deposition following Eq. (8.9) (lower panel). The left panel shows the hydrodynamical evolution after $t = 4.5$ fm, immediately after the jet is stopped, while in the middle and right panel the evolution is continued until $t = 6.5$ fm and $t = 8.5$ fm, respectively.

Comparing this result to Fig. 8.1 leads to the conclusion that the diffusion wake is present independently of whether the jet is quenched or survives until freeze-out. In the former case, the diffusion wake is only weakly sensitive to the duration of the subsequent evolution of the system.

Within ideal hydrodynamics this can be understood via vorticity conservation. The vorticity-dominated diffusion wake will always be there in the ideal fluid, whether the source of vorticity has been quenched or not. The only way this vorticity can

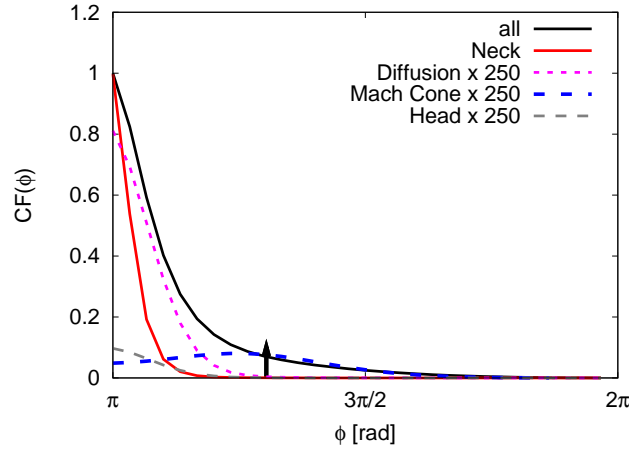


Figure 8.7

Decomposition of a jet event into the regions of head, neck, diffusion wake, and Mach cone, applying a Cooper–Frey freeze-out at $p_T = 5$ GeV for a jet depositing energy and momentum, and stopping according to the Bethe–Bloch formalism. The arrow indicates the expected Mach cone angle for a jet moving with $v_{\text{jet}} = 0.999$.

disappear is via viscous dissipation. While a $(3 + 1)$ -dimensional viscous hydrodynamic calculation is needed to quantify the effects of this dissipation, linearized hydrodynamics predicts that both Mach cones and diffusion wakes are similarly affected [83, 108, 171] as already mentioned in section 6.3.

The angular distribution associated with the decelerating jet (which stops after $\Delta x = 4.5$ fm), shown in Fig. 8.6, is determined according to the two freeze-out prescriptions described above. When the energy and momentum loss rates are determined by Eq. (8.9) (magenta line), both freeze-out procedures display a feature discussed in the previous section for the case of punch-through jets: the formation of a strong diffusion wake which leads to a strong peak in the associated jet direction. The results after the isochronous CF freeze-out are shown in the upper panel of Fig. 8.6. Here (cf. Fig. 8.5), the medium decouples after $t = 4.5$ fm (left panel), $t = 6.5$ fm (middle panel), and $t = 8.5$ fm (right panel). Only the pure energy-deposition scenario produces a peak at an angle close to the Mach angle [see Fig. 8.6 (a)] which is smeared out thermally for larger decoupling times [cf. Fig. 8.6 (b) and (c)]. On the other hand, the bulk-energy-flow freeze-out displayed (lower panel) shows in all cases a peak at the Mach-cone angle. In this case the peak becomes more pronounced when $dM/dt = 0$. While the Mach cone signal increases with the decay time, the signal is still smaller than the forward yield of the diffusion wake.

Clearly it would be interesting to study other models that describe decelerating jets in strongly coupled plasmas. Nevertheless, the simple Bethe–Bloch model used here displays the main qualitative features relevant for the hydrodynamic wake associated with decelerating jets.

So far, we have not yet distinguished different regions of the flow in forward direction behind the jet which we addressed as diffusion wake. However, as already discussed in chapter 7, the jet event can be decomposed into several regions. Since

E_{Mach}	53.9%	M_{Mach}^x	6.5%
$E_{\text{diffusion}}$	-12.3%	$M_{\text{diffusion}}^x$	18.7%
E_{neck}	57.4%	M_{neck}^x	73.7%
E_{head}	1.0%	M_{head}^x	1.0%

Table 8.1

Relative energy and momentum stored in the different regions of a jet event. For details see text.

the physical regimes change close to the jet (expressed by the Knudsen number in chapter 7), is it possible and probably inevitable to consider a neck zone (close to the location of the jet) and a head region (following the neck area), besides a diffusion zone that is characterized as a region where linearized first-order Navier–Stokes hydrodynamics can be applied (see Fig. 6.9).

In the following, we will assume that the transverse expansion of the head, neck, and diffusion zone is $\vec{x}_T < 1$ fm and define that for the present calculations (see e.g. Fig. 8.1) $0.5 < x_{\text{head}} < 1$ fm, $-1.5 < x_{\text{neck}} < 0.5$ fm and $x_{\text{diffusion}} < -1.5$ fm. This decomposition reveals (see Fig. 8.7) that for a jet depositing energy and momentum, and decelerating according to the Bethe–Bloch formalism, the away-side distribution can clearly be attributed to the strong flow behind the jet. Moreover, it shows that the main contribution is actually due to the neck region, while the large p_T -cut results in a strong suppression of the far zone (Mach-cone regions). This means that, as can be seen from the flow-velocity profiles (cf. e.g. Fig. 8.1), a Mach-cone contribution is indeed formed, but it is strongly overwhelmed by the flow along the jet trajectory.

However, even the exclusion of the head and neck zones would not change this result since (see Fig. 8.7) the contribution of the diffusion zone largely overwhelms that one of the Mach region.

It is also possible to calculate the amount of energy and momentum stored in these regions from the hydrodynamic evolution. The neck region (cf. Table 8.1) by far contains the most energy and momentum along the jet trajectory (which is the x -axis). The contribution from the Mach region is large in energy, but small for momentum and the diffusion zone even reveals a negative energy content which is due to the fact that behind the jet there is a region with lower temperature/energy than the background (see again e.g. Fig. 8.1)

Our results confirm previous studies [83, 201, 202] in the sense that a single peak in the away-side of the associated dihadron correlations occurs unless the total amount of momentum loss experienced by the jet is much smaller than the corresponding energy loss. Thus, it is clear that in Ref. [201] the existence of conical flow effects could not be proven since it was assumed that $dM/dx = dE/dx$, while as seen in Refs. [172] the double-peaked structure found by experiment can be reproduced assuming that most of the energy lost excites sound modes which is equivalent to $dM/dx \ll dE/dx$.

We would like to stress that the formation of a diffusion wake (i.e., the strong flow behind the jet) is a generic phenomenon [108] and, thus, its phenomenological consequences must be investigated and cannot simply neglected.

Considering already the above mentioned vorticity conservation, the diffusion wake cannot be an artifact of the calculation.

In the present study, the path lengths of both types of jets were taken to be the same. A different scenario in which the light jets are almost immediately stopped in the medium while the heavy quark jets are still able to punch through may lead to different angular correlations. However, as Fig. 8.7 reveals, the main contribution to the strong flow of the diffusion wake comes from the regions close to the jet and therefore, the diffusion wake is produced on the same time scale as the Mach cone which needs $t \sim 2$ fm to develop.

Nevertheless, one can expect that the strong forward-moving fluid represented by the diffusion wake can be considerably distorted in an expanding medium by the presence of a large radial flow. The interplay between radial flow and away-side conical correlations in an expanding three-dimensional ideal fluid will be presented in chapter 11.

Chapter 9

Polarization Probes of Vorticity

We demonstrated in the previous chapter that the creation of a diffusion wake is universal to all jet-deposition scenarios implying energy and momentum loss [137]. However, as can be seen from the flow-velocity profiles of Figs. 8.1 and 8.5, the formation of such a strong flow behind the jet is connected to the formation of vortex-like structures which also persist due to vorticity conservation after the jet is fully thermalized in the medium, i.e., after energy and momentum deposition have ceased.

Certainly this raises the question if such a conserved structure may have experimentally observable consequences, probably connected to polarization effects¹ (due to spin-orbit coupling) of particles formed in such a jet event.

More than 30 years ago [258], hyperon² polarization was discovered. It was suggested in Refs. [259, 260] that the disappearance of polarization could signal the onset of an isotropized system where locally no reference frame is preferred, a state close to the sQGP (strongly-coupled Quark-Gluon Plasma).

In the following sections, we will describe the sensitivity of polarization to initial conditions, hydrodynamic evolution (including jet events), and mean-free path.

9.1 Hyperon Polarization

The effect of hyperon polarization was first discovered in the channel $p + Be \rightarrow \Lambda^0 + X$, where X is the sum over the unobserved states and the polarization itself was measured through the Λ^0 -decay $\Lambda^0 \rightarrow p + \pi^-$ (see Fig. 9.1). Various models [258, 259, 261, 262] explain the polarization of Λ -particles, which is a (uds)-quark state, based on the assumption that the spin of this particle is determined by the spin of the s -quark. Generally, in the rest frame of the hyperon Y , the angular decay distribution w.r.t. the polarization plane is [258]

$$\frac{dN}{d\theta} = 1 + \alpha_Y P_Y \cos \theta, \quad (9.1)$$

where P_Y is the hyperon polarization, θ the angle between the proton momentum and the Λ -polar axis, and α_Y a hyperon-specific constant that is measured in elementary processes [258]. It has a value of $\alpha_Y = 0.647 \pm 0.013$ for Λ^0 's.

¹Polarization implies the presence of a nonzero expectation value for the particle spin.

²Hyperons are baryons containing at least one s -quark.

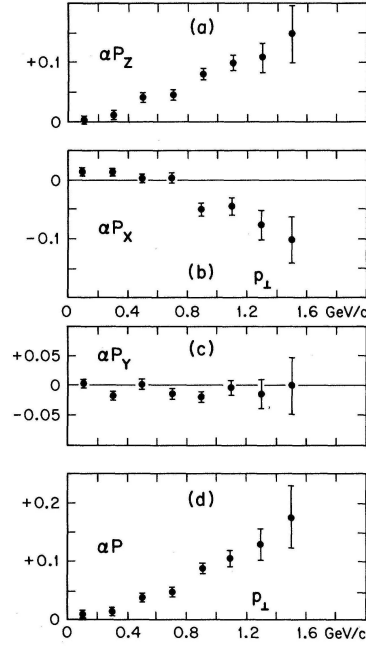


Figure 9.1

The magnitude of polarization in x , y and z -direction (P_x , P_y , and P_z) from the $\Lambda^0 \rightarrow p + \pi^-$ decay as a function of the Λ^0 transverse momentum. Here, the beam direction is chosen to be aligned with the y -axis [258].

Hyperons are polarized perpendicular to the hyperon *production plane* (see right panel of Fig. 9.2) [263]

$$\vec{n} = \frac{\vec{p} \times \vec{p}_H}{|\vec{p} \times \vec{p}_H|}, \quad (9.2)$$

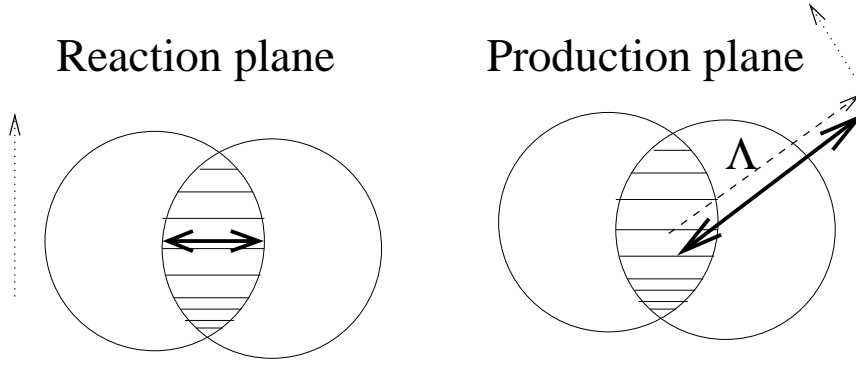
with \vec{p} and \vec{p}_H being the beam and hyperon momenta. This polarization can also be seen from Fig. 9.1 which shows the hyperon polarizations P_x , P_y and P_z in x , y and z -direction. Here, the beam direction was chosen along the y -axis. Thus, the polarization in y -direction vanishes.

The initially generated amount of the *reaction-plane* polarization (see left panel of Fig. 9.2) [263] is given by

$$\langle P_q^R \rangle \sim \int d^2\vec{x}_T \rho(\vec{x}_T) \vec{p} \cdot (\vec{x}_T \times \vec{n}) \sim -\langle p_z x_T \rangle, \quad (9.3)$$

where $\rho(\vec{x}_T) = \int d^3\vec{p} f(\vec{x}_T, \vec{p})$ is the participant transverse density, \vec{x}_T the directions perpendicular to the beam axis, and \vec{n} a unit vector perpendicular to both \vec{x}_T and \vec{p} . This expression strongly depends on the initial density-momentum correlation within the system. Thus, the reaction-plane polarization can be a useful signature for probing the initial conditions of the system created in a heavy-ion collision.

If a specific net $\langle P_Y \rangle \neq 0$ exists for any axis definable event-by-event, it is in principle possible to measure this polarization, using Eq. (9.1), in the observed

**Figure 9.2**

Definition of production and reaction plane. The beam line (traditionally the z -axis) is perpendicular to the sheet. The dotted line, with arrow, indicates the direction of polarization of the produced Λ [250].

spectra of Λ and other hyperon (like Ξ or Ω) decay products. This opens a new avenue to investigate heavy-ion collisions which has been proposed both to determine confined/deconfined regimes [259, 260, 264], and to mark global properties of the event [263, 265, 266, 267].

While a strong transverse polarization of hyperons in the *production plane* (see right panel of Fig. 9.2) is observed in (unpolarized) p+p and p+A collisions [268, 269], a disappearance of this polarization is assumed to be a signal of deconfinement [259, 260]. So far, no such measurement exists at RHIC energies, but a measurement at AGS shows that the transverse polarization is comparable to those of p+A collisions, thus at AGS the signal does not disappear.

It has also been suggested [263] to use hyperon polarization in the *reaction plane* (left panel, Fig. 9.2) to test for the vorticity of matter produced in heavy-ion collisions. The idea is that the initial momentum gradient in non-central collisions should result in a net angular momentum (shear) in this direction which will be transferred to the hyperon spin via spin-orbit coupling. This polarization direction will be called P_Y^R . A similar, though quantitatively different result, can be obtained from a microcanonical ensemble with a net angular momentum [266].

The STAR collaboration measured the reaction-plane polarization [270], reporting results consistent with zero. The above mentioned production-plane polarization measurement is also planned.

In the following, we will present a few general considerations regarding the insights that can be gained from polarization measurements. We examine how the polarization, in both production and reaction plane, is sensitive to initial conditions, hydrodynamic evolution (in particular the vortex structure of a jet event), and mean-free path. We suggest that measuring the polarization in different directions (production, reaction, and jet axis) could provide a way to go beyond model dependence.

While we use the Λ polarization as our signature of choice throughout this chapter, the points made here can easily be generalized to the detection of vector-meson polarization [271] which is also used as a polarization probe in a way very similar to hyperons [265].

9.2 Initial Conditions and Reaction-Plane Polarization

The QCD spin-orbit coupling is capable of transforming the total orbital angular momentum $\langle \vec{x} \times \vec{p} \rangle$ into spin.

For a large system, such as a heavy nucleus, we have to convolute the net polarizing interaction cross section per unit of transverse nuclear surface ($d\Delta\sigma/d^2\vec{x}_T$), calculated in Ref. [263], with the (initial) parton phase-space distributions $f(\vec{x}_T, \vec{p})$ to obtain the net local polarized parton phase-space density $\rho_{P_q^R}$ produced in the first interactions

$$\rho_{P_q^R}(\vec{x}_T, \vec{p}) = \int d^2\vec{x}'_T d^3\vec{p}' f(\vec{x}_T - \vec{x}'_T, \vec{p} - \vec{p}') \frac{d\Delta\sigma}{d^2\vec{x}'_T}(\vec{p}') . \quad (9.4)$$

Here, $f(\vec{x}_T, \vec{p})$ is the local parton distribution of the medium.

Provided that the initial Debye mass and constituent quark mass is small, the quark polarization in the reaction plane

$$\langle P_q^R \rangle = \int d^2\vec{x} d^3\vec{p} \rho_{P_q^R}(\vec{x}, \vec{p}) \quad (9.5)$$

becomes, as demonstrated in Ref. [263] [see also Eq. (9.3)],

$$\langle P_q^R \rangle \sim \int d^2\vec{x}_T \rho(\vec{x}_T) \vec{p} \cdot (\vec{x}_T \times \vec{n}) \sim -\langle p_z x_T \rangle . \quad (9.6)$$

In ultra-relativistic collisions all significant initial momentum goes into the beam (z -) direction.

For non-central collisions with a nonzero impact parameter \vec{b} however, $\langle \vec{p} \times \vec{x}_T \rangle \propto \vec{b} \neq 0$ results in a net polarization.

Thus, the initially generated amount of reaction-plane polarization strongly depends on the initial density-momentum correlation within the system. In other words, the reaction-plane polarization could be a useful signature for probing the initial conditions of the system created in heavy-ion collisions.

According to the Glauber model, the initial density distribution transverse to the beam axis is given by the sum of the participant and target densities ρ_P and ρ_T ,

$$\rho(\vec{x}_T) = [\rho_P(\vec{x}_T) + \rho_T(\vec{x}_T)] \phi(y, \eta) \quad (9.7)$$

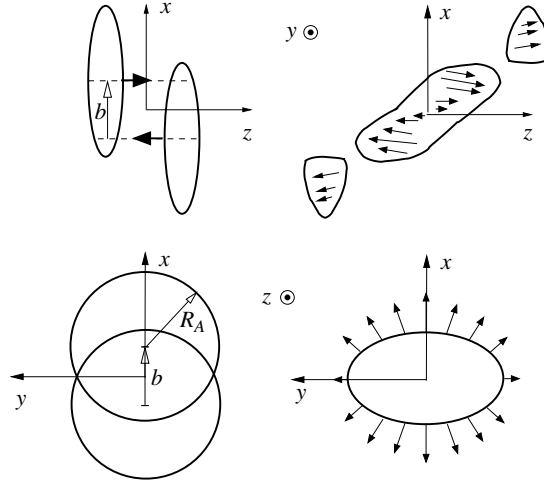
where

$$\rho_{p,T} = T_{P,T} \left(x_T \mp \frac{b}{2} \right) \left\{ 1 - \exp \left[-\sigma_N T_{T,p} \left(x_T \pm \frac{b}{2} \right) \right] \right\} \quad (9.8)$$

and σ_N , $T_{P,T}$ as well as b refer, respectively, to the nucleon-nucleon cross section, the nuclear (projectile and target) density, and the impact parameter.

A crucial model parameter is given by the rapidity which is longitudinally distributed in space-time

$$\eta = \frac{1}{2} \ln \left(\frac{t+z}{t-z} \right) , \quad (9.9)$$

**Figure 9.3**

Schematic illustration of non-central heavy-ion collisions. Partons produced in the overlap region carry global angular momentum along the $(-y)$ -axis, opposite to the reaction plane [263].

and flow rapidity

$$y = \frac{1}{2} \ln \left(\frac{E + p_z}{E - p_z} \right) = \frac{1}{2} \ln \left(\frac{1 + v_z}{1 - v_z} \right), \quad (9.10)$$

which influence the form of $\phi(y, \eta)$. The calculation of the hyperon polarization in the reaction plane [263] depends on an assumption of an initial condition described in Fig. 1 of Ref. [263] (which is reviewed in Fig. 9.3 for convenience). Such an initial condition (generally referred to as the *firestreak model*), is roughly equivalent to two “pancakes”, inhomogeneous in the transverse coordinate \vec{x}_T , sticking together inelastically. Each element of this system then streams in the direction of the local net momentum (Fig. 9.4, right column).

Since projectile and target have opposite momenta in the center-of-mass frame, assuming projectile and target nuclei to be identical, $\phi(y, \eta)$ can be approximated via

$$\phi(y, \eta) \simeq \delta(\eta) \delta[y - y_{cm}(\vec{x}_T)], \quad (9.11)$$

where y_{cm} is the local (in transverse space) longitudinal rapidity, corresponding to the flow velocity v_{cm} . Then, it is possible to rewrite the polarization in the reaction plane for the firestreak model as

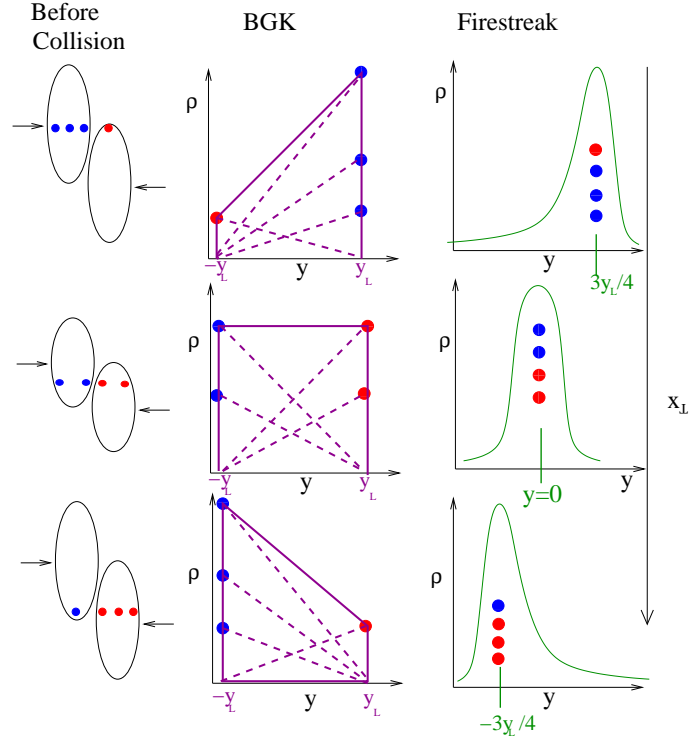
$$\langle p_z x_T \rangle \sim \frac{\sqrt{s}}{c(s) m_N} \langle D_\rho \rangle, \quad (9.12)$$

where

$$\langle D_\rho \rangle = \int d^2 \vec{x}_T \vec{x}_T [\rho_P(\vec{x}_T) - \rho_T(\vec{x}_T)]. \quad (9.13)$$

Here, $c(s)$ is an energy-dependent parameter [263] which can be estimated from final multiplicity using phenomenological formulas [272],

$$c(s) \sim \frac{2y}{N} \frac{dN}{dy} \simeq \frac{1}{1.5} \ln \left(\frac{\sqrt{s}}{1.5 \text{ GeV}} \right) \ln \left(\frac{2\sqrt{s}}{\text{GeV}} \right), \quad (9.14)$$

**Figure 9.4**

Initial densities in the BGK model (left panel) as well as the firestreak model used in Ref. [263] (right panel). In the BGK case, dashed lines represent the rapidity extent of individual nucleons, while solid lines correspond to the cumulative density [250]. For detailed model definitions and further explanations see text.

assuming that all partons receive an equal share of momentum. Since all nuclei have the same \sqrt{s} , $\langle P_q^R \rangle$ should be finite and constant over rapidity.

The physical validity of this firestreak model is compelling at low energies, when the baryon stopping of nuclear matter is large.

At high energies and initial transparencies, however, a more generally accepted ansatz for the initial condition is that the initial partons are produced all throughout the longitudinal flow rapidity spanned between the forward-travelling projectile and the backward-travelling target (middle panel of Fig. 9.4). This approximation is named Brodsky–Gunion–Kuhn (BGK) [273, 274] model.

If participant and target densities are equal, $\rho_P(\vec{x}_T) = \rho_T(\vec{x}_T)$, this ansatz reduces to a boost-invariant initial condition. For a non-central collision, however, such equality will only hold at the midpoint in \vec{x}_T of the collision region. Interpolating linearly in rapidity between participant ρ_P (at $y = y_L$) and target densities ρ_T (at $y = -y_L$), one gets

$$\phi(y, \eta) = (A + yB) \delta(y - \eta), \quad (9.15)$$

with

$$A = \frac{1}{2}, \quad B = \frac{\rho_P(\vec{x}_T) - \rho_T(\vec{x}_T)}{\rho_P(\vec{x}_T) + \rho_T(\vec{x}_T)} \frac{1}{2y_L}, \quad (9.16)$$

which leads to a polarization in the reaction plane for the BGK model

$$\begin{aligned}\langle p_z x_T \rangle &\propto \int dy \sinh(y) \vec{x}_T \rho(\vec{x}_T, y) d\vec{x}_T \\ &\propto \langle D_\rho \rangle [y_L \cosh(y_L) - \sinh(y_L)] .\end{aligned}\quad (9.17)$$

For this initial condition, the axial symmetry of the initial pancakes forces the net polarization to be zero at mid-rapidity.

However, it is also reasonable to assume that the density of matter (in η) flowing with rapidity y is

$$\phi(y, \eta) \sim \exp \left[\frac{-(\eta - y)^2}{2\sigma_\eta^2} \right] , \quad (9.18)$$

where σ_η is a parameter which has to be determined. Applying this distribution instead of the δ -function used above yields, at $\eta = 0$, to another expression for the polarization in the reaction plane for the BGK model

$$\begin{aligned}\langle p_z x_T \rangle \sim & \frac{1}{2\sqrt{2\pi}} \left[B e^{\frac{1}{2}y_L(-2-\frac{y_L}{\sigma_\eta})} \sigma_\eta \times \right. \\ & \left\{ 2 - 2e^{2y_L} + e^{\frac{(\sigma_\eta^2 - y_L)^2}{\sigma_\eta^2}} \sqrt{2\pi} \sigma_\eta \left[-\operatorname{erf} \left(\frac{\sigma_\eta^2 - y_L}{\sqrt{2}\sigma_\eta} \right) \right. \right. \\ & \left. \left. + \operatorname{erf} \left(\frac{\sigma_\eta^2 - y_L}{\sqrt{2}\sigma_\eta} \right) \right] \right\} \right] ,\end{aligned}\quad (9.19)$$

which simplifies at mid-rapidity to

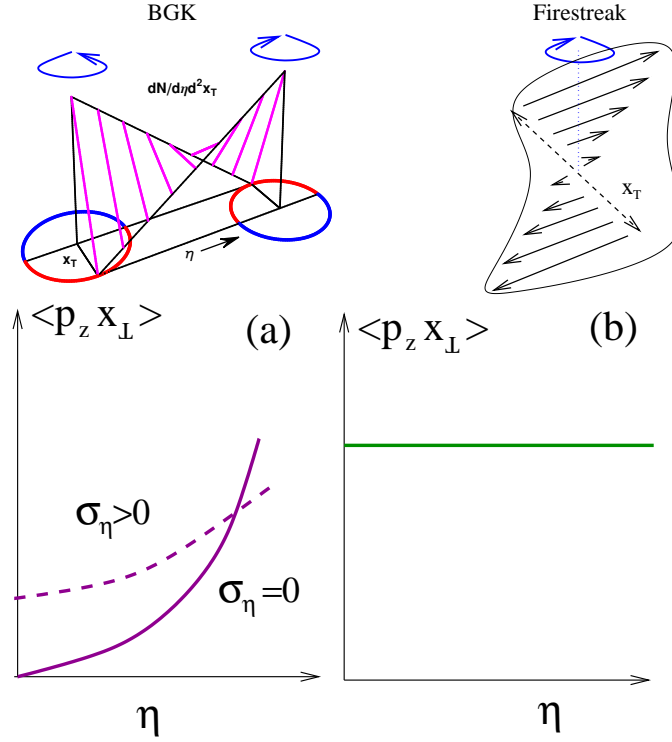
$$\langle p_z x_T \rangle \propto B e^{\sigma_\eta^2/2} \sigma_\eta^2 . \quad (9.20)$$

The rapidity distributions are summarized in Fig. 9.4, and the corresponding shear created is displayed in Fig. 9.5.

Thus, at high (RHIC and LHC) energies we expect that the net polarization around the reaction plane of A+A collisions should vanish at mid-rapidity and re-appear in the target and projectile regions [Fig. 9.5 (a)]. At lower energies, on the other hand, reaction plane Λ or $\bar{\Lambda}$ polarization should be more uniform in rapidity space, and be significantly above zero at mid-rapidity [Fig. 9.5 (b)].

More realistic nuclear geometries should not alter these very basic considerations, although for the BGK case they might considerably slow down the shear rise in rapidity. This is also true for corrections to linear interpolation in rapidity space. Detailed hydrodynamic simulations [16] also reinforce the conclusion that within the boost-invariant limit vorticity is negligible.

Given that the two expressions for the polarization in the reaction plane are known for the firestreak model [see Eq. (9.12)] and the BGK model [see Eq. (9.20)], the measurement of the Λ polarization in the reaction plane could be a valuable tool of investigating the initial longitudinal geometry of the system. At the moment, the longitudinal geometry, and in particular the longitudinal scale variation with energy (i.e., if, how, and at what energy initial conditions change from “firestreak” to “BGK”) is not well understood [275]. This understanding is crucial for both the

**Figure 9.5**

Initial shear in the BGK model (a), as well as the firestreak model used in Ref. [263] (b) [250].

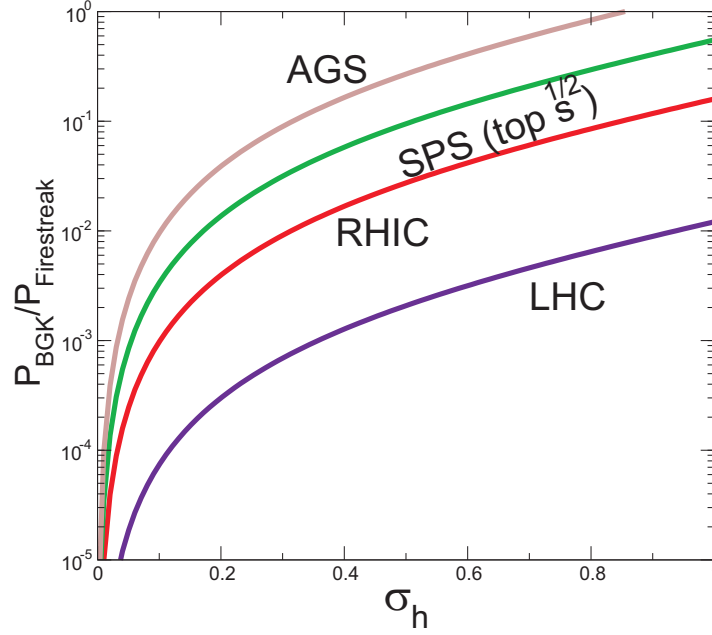
determination of the EoS and the viscosity, since longitudinal geometry is correlated with the initial energy density, and hence to the total lifetime of the system and the time in which flow observables can form [276].

The measurement of the energy and system-size dependence of Λ polarization in the reaction plane at mid-rapidity could be a significant step in qualitatively assessing the perfection of the fluid, and determining at what energy the system enters a fluid-like behaviour.

To investigate the difference between the two above discussed models, it is useful to calculate the ratio

$$\frac{\langle P_q^R \rangle|_{BGK}}{\langle P_q^R \rangle|_{firestreak}} = c(s) \frac{m_N e^{\sigma_\eta^2/2} \sigma_\eta^2}{\sqrt{s}}. \quad (9.21)$$

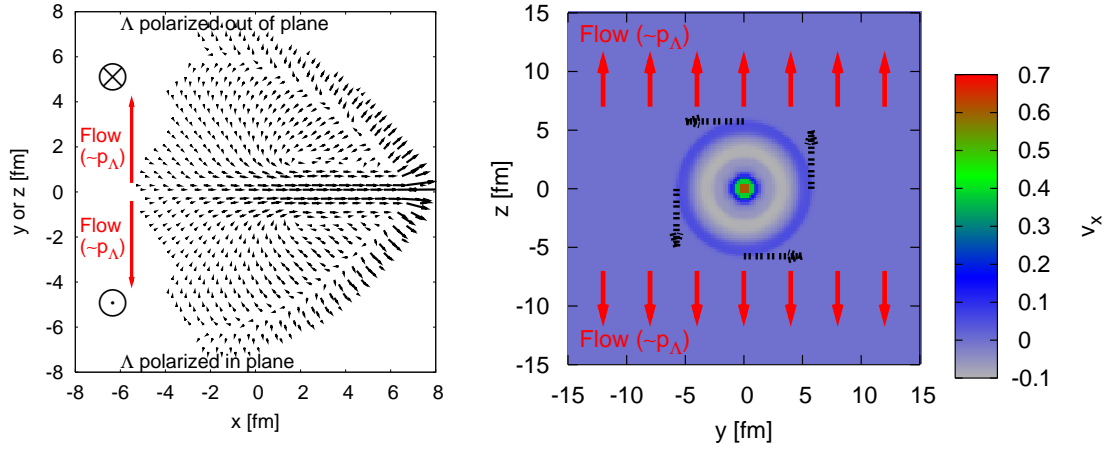
In the limit of $\sigma_\eta \rightarrow 0$ the system has no vorticity and thus, due to spin-orbit coupling, no polarization. While only at very low energies [where Eq. (9.20) and the BGK picture are untenable as approximations] the BGK and firestreak pictures are comparable, vorticity at BGK could still be non-negligible, provided that $\sigma_\eta \sim 1$. It should be stressed that $c(s)$ and σ_η contain very different physics: In Ref. [263], $c(s)$ is interpreted as the number of partons into which the energy of the initial collision is distributed. On the other hand, σ_η depends on the imperfection of “Bjorken” expansion (the correlation between space-time and flow rapidity). These two effects, however, go in the same direction, although $c(s) \sim (\ln \sqrt{s})^2$ is much less

**Figure 9.6**

Ratio of BGK to firestreak predictions as a function of \sqrt{s} and σ_η , the correlation length between space-time and flow rapidity, calculated using Eqs. (9.14) and (9.21) [250].

efficient at diminishing polarization than a small σ_η .

Combining $c(s)$ of Eq. (9.14) with Eq. (9.21), one obtains the ratio between BGK and firestreak expectations, and its dependence on energy and the parameter σ_η . The result is shown in Fig. 9.6, assuming $\sigma_\eta \ll y_L$. This figure should be taken as an illustration for the sensitivity of the polarization measure to the longitudinal structure of the initial condition, rather than as a prediction of the polarization in the two models (as shown in Ref. [267], the small-angle approximation used in Ref. [263] is in any case likely to be inappropriate). As can be seen, the effects of $c(s)$ in the firestreak picture are only at low energies comparable to the effects of a non-negligible σ_η in the BGK picture (where the firestreak picture is thought to work better). At top RHIC energy, even at σ_η of one unit, the BGK polarization should be suppressed with respect to the firestreak expectation with about two orders of magnitude. This grows to several orders of magnitude for LHC energies. Connecting the experimental measurement of the Λ polarization to the initial condition is, however, non-trivial, as this observable is sensitive not just to the initial stage but also to the subsequent evolution of the system, up to the final freeze-out. In the following two sections we will qualitatively discuss the effect the later stages will have on the final observable. We will argue that, while the observable is likely to be modified by the subsequent evolution, a comparison of several kinds of polarization could be useful in obtaining information about initial conditions, the mean-free path and the freeze-out scenario.

**Figure 9.7**

Vorticity generated by a fast jet traversing the system in the positive x -direction. The arrows in the left panel show the momentum density of fluid elements in the (x, y) -plane, while the contour in the right panel displays the x -component of the velocity in the (y, z) -plane. The jet has been travelling for $t = 11.52$ fm through a static medium [279]. The dashed arrows in the right panel indicate the expected direction of polarization of a Λ -particle (out of plane for left panel, tangentially in right panel). If the medium undergoes transverse and longitudinal expansion, the Λ position within the smoke ring is correlated with its mean momentum. Thus, measuring Λ polarization in the plane defined by its momentum and the jet momentum should yield a positive net result [250].

9.3 Hydrodynamic Evolution, Polarization, and Jets

In relativistic hydrodynamics, vorticity works somewhat differently than in the non-relativistic limit [277, 278]. While in non-relativistic ideal hydrodynamics, the conserved circulation is simply defined as $\vec{\nabla} \times \vec{v}$, relativistically the conserved vorticity is

$$\vec{\Omega} = \vec{\nabla} \times w\gamma\vec{v}, \quad (9.22)$$

where w is the enthalpy per particle. In the non-relativistic limit, where $w \simeq m$ and $\gamma = 1$, the usual limit is recovered. In a relativistic fluid with strong pressure and energy-density gradients, on the other hand, vortices can be created and destroyed even in perfectly smooth initial conditions, such as the BGK case described in the previous section.

Since vorticity development is a highly non-linear phenomenon, quantitative details require numerical simulations. Here, we consider the vorticity which develops when a momentum source moving at the speed of light traverses a uniform relativistic fluid. This could be an appropriate description of the thermalized jet-energy loss (see also section 6.3 and chapter 8), if the jet loses energy fast and locally. The calculation is done using a $(3 + 1)$ -dimensional hydrodynamical prescription [114]. The flow vector in the (x, y, z) -coordinate system, where the fluid is at rest (if co-moving with the collective flow), is shown in Fig. 9.7, parallel (left panel) and perpendicular (right panel) to the jet direction.

The simulation shown in Fig. 9.7 is based on a jet energy-loss model that assumes

a high momentum gradient. It is not surprising that a large initial momentum gradient, such as that produced by a jet quickly losing energy, can introduce vorticity into the system.

As shown in the simulation, these vortices are stable enough to last throughout the lifetime of the fluid. Therefore, an interesting polarization measurement is to trigger on jet events and measure Λ polarization (P_{Λ}^J) in the plane perpendicular to the *jet* production plane. Since vorticity in such events exists independently of the global initial conditions, this measurement is sensitive only to the mean-free path and perhaps final-state effects.

Fig. 9.7 also illustrates how such a measurement could be performed: the polarization axis is defined based on the (high- p_T trigger) jet direction. Since vortices above and below the jet move in opposite directions, it would be impossible to detect vorticity via polarization measurements in a *static* medium.

If, however, a smoke ring occurs in a medium undergoing transverse or longitudinal expansion, the flow introduces a correlation between the Λ position within the smoke ring (and hence its polarization) and its average momentum $\langle p_{\Lambda} \rangle$. Measuring the polarization of moderately high momentum but thermal Λ -particles ($\sim 700 MeV$) in the plane defined by the Λ momentum and the jet direction should thus yield a non-zero result.

We therefore propose to measure the polarization P_i^J of jet-associated moderate momentum particles, in the plane defined by the jet direction and the direction of the particle.

The observation of this polarization would be a strong indication of collective behavior, since it signifies jet-induced vorticity.

Unlike production-plane vorticity, jet vorticity does not depend on initial conditions, but should hold for a wide variety of jet energy-loss scenarios, provided the coupling between the system and the jet is strong. It is not at all clear, however, whether in the strongly-coupled regime (rather than the perturbative one, on which the calculations of Ref. [263] are based) vorticity will readily transform into quark polarization. The next section is devoted to this topic.

9.4 Mean-Free Path and Polarization

In a perfect fluid, angular momentum should not go into a *locally* preferred direction, but into vortices where each volume element is locally isotropic in the frame co-moving with the flow.

Such vortices should imprint final observables via longitudinal collective flow (e.g. odd v_n coefficients away from mid-rapidity), but not via polarization since any polarization created would immediately be destroyed by subsequent re-interactions if the equilibration between gain and loss terms happens instantaneously (“a perfect fluid”). In this regime, the equations derived in section 9.2 are no longer tenable because they assume unpolarized incoming particles and a coupling constant small enough for perturbative expansion.

Keeping the first of these assumptions would violate detailed balance³, while the

³Detailed balance means that $P_{ij}q_i = P_{ji}q_j$, i.e., that there is a balance between the states i and j . Here, P_{ij} is the transition probability and q_i the equilibrium probability of being in a state i .

second assumption is probably incompatible with a strong collective behavior. The local isotropy of a perfectly thermalized system was used [259] to suggest that the disappearance of the production-plane polarization observed in elementary collisions could be a signature of deconfinement. A first-order correction becomes necessary if the size of the radius of curvature within the vortex becomes comparable to the mean-free path ℓ_{mfp} . The anisotropy would then be given by the deformation of a volume element of this size. In general, the polarization in any direction i (production, reaction, or jet) can be expressed as ⁴

$$\langle P_q^i \rangle \sim \tanh \left[\vec{\zeta}_i \right] \sim \vec{\zeta}_i \quad (9.23)$$

$$\vec{\zeta}_i = \frac{\ell_{mfp}}{T} \left(\epsilon_{ijk} \frac{d\langle \vec{p}_k \rangle}{d\vec{x}_j} \right), \quad (9.24)$$

where $\langle \vec{p}_j \rangle$ is the local direction of momentum in the laboratory frame and T the temperature. Thus, potentially, the amount of residual polarization which survives a hydrodynamic evolution (whether from initial geometry or from deformation of the system due to jets) is directly connected to the system's mean-free path.

Therefore, determining the polarization rapidity dependence (in any plane, production, reaction, or jet, where it could be expected to be produced) could perhaps ascertain the rapidity domain of the QGP. If a (s)QGP is formed at central rapidity, while the peripheral regions consist of a hadron gas, one should observe a sharp rise in production, reaction- and jet-plane polarization in the peripheral regions.

The problematic aspect of using polarization for such a measurement is that it is sensitive to the late-stage evolution, including hadronization and the interacting hadron gas phase.

As shown in Ref. [280], an unpolarized QGP medium at freeze-out will produce a net production-plane polarization due to hadronic interactions. Similarly, unpolarized p+p and p+A collisions result in net hyperon polarization. While local detailed balance inevitably cancels out such local polarization, the rather large mean-free path of an interacting hadron gas, and the considerable pre-existing flow ensure that any interacting hadron gas phase should be well away from detailed balance, and hence likely to exhibit residual polarization.

It then follows that the absence of a production-plane polarization is not only a strong indication of sQGP formation, but of a “sudden” freeze-out where particles are emitted directly from the QGP phase.

The evidence of quark coalescence even at low momentum [281], together with sudden-freeze-out fits [282, 283], supports further investigation using the polarization observable in any plane (reaction, production, and jet) where the vorticity in the hot phase is expected to be non-zero.

If polarization in *all* directions is consistently measured to be zero, including events with jets and within high rapidity bins, it would provide strong evidence that the mean-free path of the system is negligible, and final-state hadronic interactions are not important enough to impact flow observables. However, a measurement of production plane, but not reaction-plane polarization proves that the initial state of the

⁴Here it is assumed that $\langle P \rangle = [e^{E/T} - e^{-E/T}] / [e^{E/T} + e^{-E/T}] = \tanh E/T \sim E/T$, leading via spin-orbit coupling with a first-order approximation for the spin (that is of the order ℓ_{mfp}) and the local angular momentum density to Eq. (9.24).

system is BGK-like and that the interacting hadron gas phase leaves a significant imprint on soft observables. (The BGK nature of the initial condition can then be further tested by scanning reaction-plane polarization in rapidity.)

An observation of polarization in the jet plane could result in a further estimate of the mean-free path, showing that the jet-degrees of freedom are thermalized and part of the collective medium.

A sudden jump in any of these polarizations at a critical rapidity might signal a sharp increase in the mean-free path, consistent with the picture of a mid-rapidity QGP and a longitudinal hadronic fragmentation region. Analogously, a drop of polarization while scanning in energy and system size could signal the critical parameters required for a transition from a very viscous hadron gas to a strongly interacting quark-gluon liquid.

Thus, motivated by the question if the vortex-like structures produced in a jet event (if momentum loss is sufficiently large) may lead to observable consequences, we discussed the connection of hyperon polarization to initial geometry and microscopic transport properties. However, since the polarization observable can be significantly altered by all stages of the evolution, a quantitative description remains problematic. Nevertheless, the proposed measurements (reaction plane, production plane, and jet plane polarization) might shed some light on several aspects of heavy-ion collisions that are not well understood yet.

In the following, we will again focus on the mechanisms (i.e., the source term) of jet energy and momentum loss by comparing two completely independent and different approaches describing the interaction of the jet with a QGP, pQCD, and AdS/CFT.

Chapter 10

Di-Jet Correlations in pQCD vs. AdS/CFT

As already discussed in part II, the Anti-de-Sitter/Conformal Field Theory (AdS/CFT) correspondence [208, 210, 211, 212] is considered to be a feasible approach for describing a strongly-coupled medium (like possibly the QGP) although QCD, the theory appropriate for characterizing the QGP, is not a conformal field theory. In chapter 7 we reviewed that the propagation of a supersonic heavy quark moving at a constant velocity through a static strongly-coupled $\mathcal{N} = 4$ Supersymmetric Yang–Mills (SYM) background plasma at nonzero temperature T_0 can be formulated using AdS/CFT which provides a detailed energy-momentum (stress) tensor [218, 219, 233]. It features the expected Mach-cone region (commonly named *far zone*) as well as the strong forward-moving diffusion wake (see Fig. 7.4). The far-zone response is well described in the strong-coupling limit of the $\mathcal{N} = 4$ SYM plasma with a “minimal” shear viscosity to entropy density ratio $\eta/s = 1/4\pi$ [which is close to the uncertainty principle limit [161]] [223, 225].

However, we showed in the context of a hydrodynamic prescription (cf. chapter 8 and Ref. [137]) that the strong forward diffusion wake spoils the signature of the Mach cone which would result in a double-peaked structure.

For AdS/CFT, such diffusion wakes were already presented in Refs. [233, 284, 285] and it was demonstrated in Refs. [230, 231] (as reviewed in section 7.5) that in the strict supergravity limit, $N_c \gg 1$, $g_{SYM}^2 \ll 1$ but $\lambda = g_{SYM}^2 N_c \gg 1$, the far-zone wakes have such small amplitudes that they only lead to a single broad peak in the away-side hadronic correlation after a Cooper–Frye (CF) freeze-out of the fluid [129].

The azimuthal correlations of associated hadrons after applying such a CF freeze-out to an AdS/CFT source term calculated in Ref. [233] (shown in Ref. [231], see Fig. 7.6) exhibit, however, an apparent conical signal which does not obey Mach’s law and is due to the non-equilibrium neck zone, introduced in section 7.4. This neck zone is distinguished by a strong transverse flow relative to the jet axis (see Fig. 7.5), inducing the conical correlation that even prevails after a CF thermal broadening at freeze-out.

In section 7.4, based on the considerations of Refs. [229, 230, 231], the neck zone was defined as the region near the heavy quark where the local Knudsen number

is $Kn = \Gamma |\nabla \cdot \vec{M}|/|\vec{M}| > 1/3$ [see Eq. (7.5) and Fig. 7.2], where $M^i(t, x) = T^{0i}(t, x)$ is the momentum flow field of matter and $\Gamma \equiv 4\eta/(3sT_0) \geq 1/(3\pi T_0)$ is the sound attenuation length which is bounded from below for ultra-relativistic systems [161, 223].

In AdS/CFT, this neck region is the field-plasma coupling zone where the stress tensor has a characteristic interference form depending on the coordinates, following $\mathcal{O}(\sqrt{\lambda}T_0^2/R^2)$ [219, 220], with R denoting the distance to the heavy quark in its rest frame. In contrast, the stress in the far zone has the characteristic $\mathcal{O}(T_0^4)$ form. In addition, very near the quark the self-Coulomb field of the heavy quark contributes with a singular stress $\mathcal{O}(\sqrt{\lambda}/R^4)$ [218].

The above strong coupling AdS/CFT results served as a motivation to study whether similar novel near-zone field-plasma dynamical coupling effects also arise in weakly-coupled perturbative Quantum Chromodynamics (pQCD) [136].

In Refs. [199, 203, 205] the heavy quark jet induced stress in a weakly-coupled QGP (wQGP in contrast to sQGP) generated by the passage of a fast parton moving with a constant velocity was computed analytically in the linear-response approximation based on the Asakawa–Bass–Müller (ABM) [204] generalization of chromo-viscous hydrodynamics [286]. The ABM generalization concentrates on the “anomalous diffusion” limit, where the conductivity is dominated by field rather than stochastic dissipative scattering dynamics.

As in the AdS/CFT string-drag model, the generic far-zone Mach and diffusion wakes are also clearly predicted in the pQCD-based ABM formulation [199, 205], exhibiting extremely similar patterns of the energy and momentum-density perturbations as displayed in Fig. 6.7.

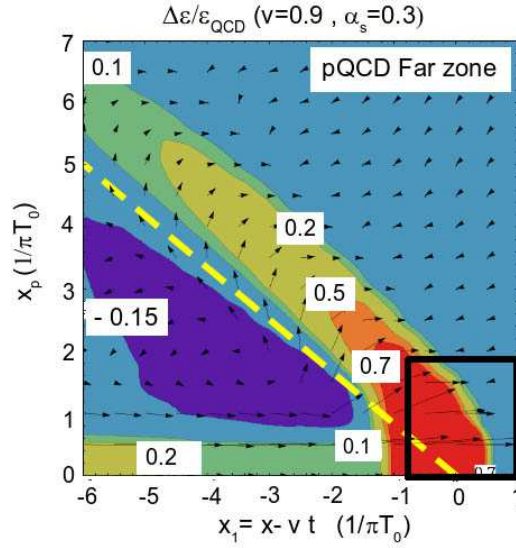
In the following, we compare the azimuthal correlations obtained from AdS/CFT [233] with the ones calculated from pQCD by solving numerically the full non-linear $(3+1)$ -dimensional relativistic hydrodynamic equations using the SHASTA [110], supplemented with the chromo-viscous stress source derived in Refs. [199, 203] and reviewed in section 6.5.

We specialize to the ideal-fluid case of vanishing viscosity to minimize the dissipative broadening of any conical correlations and therefore maximizing the signal-to-noise ratio.

We emphasize that our aim here is not to address the current light quark/gluon jet RHIC correlation data, but to point out the significant differences between weakly and strongly-coupled models concerning the mechanisms of heavy quark energy loss that can be tested experimentally when identified heavy quark (especially bottom quark) jet correlations will become feasible to measure. We limit this study to the most favorable idealized conditions (uniform static plasma coupled to the external Lorentz-contracted color fields). Distortion effects due to evolution in finite expanding plasma geometries will be discussed in the next chapter.

Since the models for the weakly-coupled pQCD and strongly-coupled AdS/CFT prescriptions are shown to predict qualitatively different associated hadron correlations with respect to tagged heavy quark jets [136], we propose that an identified heavy quark jet observable may discriminate between those approaches for the QGP dynamics in ultra-relativistic nuclear collisions at RHIC and LHC energies.

It will be shown that while both models feature similar Mach and diffusion zones (see Fig. 6.9), they differ significantly in the neck region where strong chromo-

**Figure 10.1**

The fractional-energy density perturbation $\Delta\varepsilon/\varepsilon_0 \equiv \varepsilon(x_1, x_p)/\varepsilon_0 - 1$ (in the laboratory frame) due to a heavy quark with $v = 0.9$ in a QCD plasma of temperature $T_0 = 200$ MeV. The induced fluid stress was calculated using $(3 + 1)$ -dimensional hydrodynamics [110] with the anomalous pQCD source of Neufeld [203]. A trigger jet (not shown) moves in the $(-\hat{x})$ -direction. The away-side jet moves in \hat{x} -direction and contours of $\Delta\varepsilon/\varepsilon_0 = -0.15, 0.1, 0.2, 0.5, 0.7$ are labeled in a comoving coordinate system with $x_1 = x - vt$ and the transverse radial coordinate x_p in units of $1/\pi T_0 \approx 0.3$ fm after a total transit time $t = 5\text{fm}/c = 14.4/(\pi T_0)$. The ideal Mach cone for a point source is indicated by the yellow dashed line in the $x_1 - x_p$ plane. See Fig. 10.2 for a zoom of the neck region inside of the black box [136].

fields originating from the heavy quark jet couple to the polarizable plasma. The associated conical correlations from AdS/CFT are dominated (as demonstrated in Ref. [231]) by the jet-induced transverse flow in the neck zone. However, in pQCD, the induced transverse flow in the neck region is too weak to produce conical correlations after a CF freeze-out.

Thus, the observation of conical correlations violating Mach's law would favor the strongly-coupled AdS/CFT string-drag dynamics, while their absence would support weakly-coupled pQCD-based chromo-hydrodynamics.

10.1 The Stress Zones

Jet physics, below some transverse-momentum saturation scale [287], depends on the properties of the medium and allows for testing different models of jet-medium coupling dynamics by studying the detailed angular and rapidity correlations.

In the following, we demonstrate a striking difference between strongly-coupled AdS/CFT and moderate-coupling, multiple-collision pQCD transport models, and study their experimentally measurable consequences.

Ignoring again the near-side associated correlations, the energy-density perturbation for a jet described by the pQCD source term [199, 203] (see section 6.5) clearly

exhibits the Mach-cone region and diffusion wake (including the neck zone) as already discussed in the context of the schematic source term of chapter 8. For the corresponding plot with the AdS/CFT source of Ref. [233], see Fig. 7.5.

The energy-momentum (stress) tensor induced by the away-side heavy quark jet in both pQCD and AdS/CFT can be conveniently decomposed, as introduced in section 7.4 [see Eq. (7.6)] into four separate contributions [229, 230, 231] and is repeated here for convenience

$$T^{\mu\nu}(t, \vec{x}) = T_0^{\mu\nu}(t, \vec{x}) + \delta T_{Mach}^{\mu\nu}(t, \vec{x}) + \delta T_{neck}^{\mu\nu}(t, \vec{x}) + \delta T_{Coul}^{\mu\nu}(t, \vec{x}). \quad (10.1)$$

The static isotropic background stress tensor is assumed to be $T_0^{\mu\nu} = \text{diag}(\varepsilon, p, p, p)$, where $\varepsilon = KT_0^4$ is the background energy density of a gas of massless $SU(3)$ gluons with $K_{QCD} = 8\pi^2/15$ (which we use for the hydrodynamical calculations applying the pQCD source term) whereas for $SU(N_c)$ SYM $K_{SYM} = 3\pi^2(N_c^2 - 1)/8$. In both cases, $\varepsilon = 3p$ and the background temperature is T_0 .

The Coulomb contribution to the energy-momentum tensor $\delta T_{Coul}^{\mu\nu}(t, x)$ arises from the near-zone Lorentz-contracted Coulomb field that remains attached to the heavy quark since we consider only moderate but supersonic velocities $c_s \leq v \leq 0.9$. We can therefore neglect radiative energy loss that dominates in the ultrarelativistic case. The bare comoving Coulomb self-field stress has the singular form $\delta T_{Coul}^{\mu\nu} \propto 1/R^4$ in the quark rest frame.

In both pQCD and AdS/CFT cases we subtract this vacuum self-field stress as in Refs. [233, 284]. In other words, the zero-temperature contribution to the in-medium stress tensor is always subtracted. While in AdS/CFT the form of the Coulomb tensor is known exactly [218], in pQCD this contribution can only be calculated perturbatively. The leading-order expression for the chromo-fields produced by the source in pQCD, in the limit where the dielectric functions are set to unity, displays the same Lienard–Wiechert behavior as in AdS/CFT.

The far-zone “Mach” part of the stress can be expressed in terms of the local temperature $T(t, \vec{x})$ and fluid flow velocity fields $u^\mu(t, \vec{x})$ through the first-order Navier–Stokes stress form, given by Eq. (7.7)

$$\begin{aligned} \delta T_{Mach}(x_1, x_\perp) &= \frac{3}{4}K \left\{ T^4 \left[\frac{4}{3}u^\mu u^\nu - \frac{1}{3}g^{\mu\nu} + \frac{\eta}{sT} \partial^{(\mu} u^{\nu)} \right] - T_0^{\mu\nu} \right\} \\ &\quad \times \theta(1 - 3Kn), \end{aligned} \quad (10.2)$$

The theta function in this equation defines the “far zone” that includes the Mach and diffusion linearized hydrodynamic sound waves. In the far zone, the equilibration rate is over three times the local stress gradient scale, and first-order Navier–Stokes dissipative hydrodynamics provides an adequate formulation of the evolution in that zone.

In AdS/CFT, the hydrodynamic description was shown to be valid down to distances of roughly $3/(\pi T)$ [229] (see also [232] for an analysis of the far zone).

Within a thermal Compton wavelength of the heavy quark the near neck zone is in general a non-equilibrium region strongly influenced by the coupling of the heavy quark’s bare classical Coulomb field to the polarizable plasma.

10.2 The pQCD Source Term

We use the nonlocal pQCD source term, $\mathcal{J}^\nu(x)$, derived in Ref. [203], to drive the perfect fluid response of a pQCD fluid assuming $\eta = 0$ in order to maximize any pQCD transport-induced azimuthal conical signature. Nonzero viscosity, of course, washes out some of the induced correlations as shown in Ref. [205].

However, our main finding below is that even in this perfect $\eta = 0$ hydrodynamic limit the pQCD induced correlations are too weak to generate conical correlations after freeze-out.

Thus, we consider only the $\eta/s = 0$ limit of the full anomalous chromo-viscous equations derived in Refs. [204] and retain the anomalous diffusion-stress Neufeld source [203]. We can rewrite Eqs. (6.2) – (6.11) of Ref. [204] in the more familiar covariant Joule heating¹ form (for details of this analogy see appendix F)

$$\partial_\mu T^{\mu\nu} = \mathcal{J}^\nu = F^{\nu\alpha a} J_\alpha^a = (F^{\nu\alpha a} \sigma_{\alpha\beta\gamma} * F^{\beta\gamma a}), \quad (10.3)$$

where $F^{\mu\nu a}(t, x)$ is the external Yang–Mills field tensor and

$$J^a(t, x) = \int \frac{d^4 k}{(2\pi)^4} e^{ik^\mu x_\mu} J^a(k) \quad (10.4)$$

is the color current that is related via Ohm’s law to $F^{\mu\nu a}(k)$ through the (diagonal in color) conductivity rank-three tensor $\sigma_{\mu\alpha\beta}(k)$. The $*$ denotes a convolution² over the nonlocal non-static conductive dynamical response of the polarizable plasma.

The covariant generalization of Neufeld’s source is most easily understood through its Fourier decomposition,

$$J_\nu^a(k) = \sigma_{\nu\mu\alpha}(k) F^{\mu\alpha a}(k), \quad (10.5)$$

with the color conductivity expressed as in Refs. [288, 289, 290]

$$\sigma_{\mu\alpha\beta}(k) = ig^2 \int d^4 p \frac{p_\mu p_\alpha \partial_\beta^p}{p^\sigma k_\sigma + i p^\sigma u_\sigma / \tau^*} f_0(p), \quad (10.6)$$

where $f_0(p) = 2(N_c^2 - 1) G(p)$ is the effective plasma equilibrium distribution with $G(p) = (2\pi^3)^{-1} \theta(p_0) \delta(p^2) / (e^{p_0/T} - 1)$. Here, u^μ is the 4-velocity of the plasma as in Eq. (10.2).

For an isotropic plasma $u^\beta \sigma_{\mu\alpha\beta}(k) = -\sigma_{\mu\alpha}(k)$. In the long-wavelength limit, $u_\beta \sigma^{\mu\alpha\beta}(k \rightarrow 0) = -\tau^* m_D^2 g^{\mu\alpha} / 3$, where $m_D^2 = g^2 T^2$ is the Debye screening mass for a non-interacting plasma of massless $SU(3)$ gluons in thermal equilibrium.

The relaxation or decoherence time τ^* in Eq. (10.6) has the general form noted in Ref. [204]

$$\frac{1}{\tau^*} = \frac{1}{\tau_p} + \frac{1}{\tau_c} + \frac{1}{\tau_{an}}, \quad (10.7)$$

¹Joule heating is the process by which the passage of an electric current through a conductor releases heat.

² $\sigma_{\alpha\beta\gamma} * F^{\beta\gamma a} = J_\alpha^a(t, x) = \int d^4 k / (2\pi)^4 e^{ik^\mu x_\mu} \sigma_{\alpha\mu\nu}(k) F^{\mu\nu a}(k)$.

with the collisional momentum-relaxation time [161, 286]

$$\tau_p \propto \left[\alpha_s^2 T \ln \left(\frac{1}{\alpha_s} \right) \right]^{-1}, \quad (10.8)$$

the color-diffusion time defined in Ref. [288]

$$\tau_c = \left[\alpha_s N_c T \ln \left(\frac{1}{g} \right) \right]^{-1}, \quad (10.9)$$

and the anomalous strong electric and magnetic field relaxation time derived in Eq. (6.42) of Ref. [204]

$$\tau_{an} \propto \left(m_D \sqrt{\frac{\eta |\vec{\nabla} \cdot \vec{U}|}{T_s}} \right)^{-1}. \quad (10.10)$$

We note that this expression can be written in terms of the local Knudsen number $Kn = \Gamma_s/L$ used in Eq. (10.2)

$$\tau_{an} \propto \frac{1}{gT} \frac{1}{\sqrt{Kn(t, x)}}, \quad (10.11)$$

with L being a characteristic stress gradient scale. However, because of $\eta \propto \tau^* sT$, Eq. (10.11) is really an implicit equation for τ_{an} .

Combining these relations and taking into account the uncertainty-principle constraint [161] that bounds $\tau^* \gtrsim 1/(3T)$ for an ultra-relativistic (conformal) plasma, we have

$$\frac{1}{\tau^*} \propto T \left(a_1 g^4 \ln g^{-1} + a_2 g^2 \ln g^{-1} + a_3 g \sqrt{Kn} \right) \lesssim 3T, \quad (10.12)$$

where a_1, a_2, a_3 are numerical factors. In the near zone close to the quark, Kn becomes large, and τ_{an} can be the dominant contribution to the relaxation time τ^* in the presence of strong classical field gradients.

There is a subtle point in the application of Eq. (10.12) to our heavy quark jet problem. In order to neglect viscous dissipation in the pQCD response, the relaxation rate must be very large compared to the characteristic gradient scale. Hence, in the far zone at least the imaginary part of the conductivity denominator in Eq. (10.6) must be large and dominant. However, in the neck region the field gradients become very large and the relevant wave numbers of the hydrodynamic response, $K \gg 3T$, exceed the uncertainty-limited equilibration rate. Since we only need to consider the conductivity in the asymptotic large K limit in the near zone, it becomes possible to neglect the $\sim i3T$ maximal relaxation rate in the energy denominator and to formally set $1/\tau^* \rightarrow 0^+$ - as if the coupling were parametrically small [which is assumed in Eqs. (53) – (56) of Ref. [203]].

Only in this high-frequency, high-wave number limit, relevant for the neck zone physics, the color conductivity is computable as in Ref. [203].

The neglect of dissipation in the neck zone maximizes the acceleration of the plasma partons, which can subsequently generate transverse collective plasma flow relative to the jet axis. We have to check numerically whether this maximum transfer of field energy-momentum from the field to the plasma is sufficiently anisotropic to generate a conical correlation of the associated hadron fragments.

10.3 Freeze-out Procedures

As mentioned previously, we consider here only the idealized static medium to maximize the plasma response signal. Distortion effects due to e.g. transverse expansion, while important for phenomenological comparisons to heavy-ion data, however obscure the fundamental differences between weakly and strongly-coupled dynamics that is our focus here. Given the large theoretical systematic uncertainty inherent in any phenomenological model of non-perturbative hadronization, we consider two simple limits for modeling the fluid decoupling and freeze-out.

In one often used limit, the fluid cells are frozen-out via the CF prescription on an isochronous hypersurface. This scheme takes into account maximal thermal broadening effects. In the opposite limit, we assume an isochronous sudden breakup or shattering of fluid cells conserving only energy and momentum and avoiding hadronization altogether as described in detail in section 3.7 and is shortly reviewed below for convenience. The difference between the two schemes provides a measure of the systematic theoretical uncertainty associated with the unsolved problem of hadronization.

In the CF method, the conversion of the fluid into free particles is achieved instantaneously at a critical surface $d\Sigma_\mu$ [129]. If we assume such a freeze-out scheme, the particle distributions and correlations can be obtained from the flow velocity field $u^\mu(t, \vec{x})$ and temperature profile $T(t, \vec{x})$.

For associated (massless) particles with $p^\mu = (p_T, p_T \cos(\pi - \phi), p_T \sin(\pi - \phi), 0)$ the momentum distribution at mid rapidity $y = 0$ is [cf. Eq. (3.36)]

$$\frac{dN}{p_T dp_T dy d\phi} \Big|_{y=0} = \int_\Sigma d\Sigma_\mu p^\mu [f_0(u^\mu, p^\mu, T) - f_{eq}] , \quad (10.13)$$

where $f_0 = \exp[-u^\mu p_\mu / T(t, x)]$ is a local Boltzmann equilibrium distribution. No viscous corrections to Eq. (10.13) are included since we are working here in the perfect-fluid limit with $\eta = 0$. We subtract the isotropic background yield via $f_{eq} \equiv f|_{u^\mu=0, T=T_0}$. Moreover, we follow Refs. [83, 231, 246] and perform an isochronous freeze-out where $d\Sigma^\mu = d^3\vec{x} (1, 0, 0, 0)$.

We remark that the absence of well-defined quasi-particle states in AdS/CFT plasmas at large 't Hooft coupling indicates that CF can, at best give a qualitative idea of the observable hadron-level angular correlations [229, 230, 231]. Moreover, even in the pQCD quasiparticle limit, CF freeze-out remains a strong model assumption. In the pQCD case, in the associated p_T -range of interest a coalescence/recombination hadronization scenario [134, 248] may be more appropriate. However, we expect similar CF thermal broadening effects if coalescence hadronization is assumed and full three-momentum conservation is taken into account.

As an alternate freeze-out scheme we consider a calorimetric-like observable given by the momentum density weighted polar angle distribution relative to the jet axis:

$$\begin{aligned} \frac{dS}{d \cos \theta} &= \sum_{cells} |\vec{P}_c| \delta(\cos \theta - \cos \theta_c) \\ &= \int d^3\vec{x} |\vec{M}(t, \vec{x})| \delta \left[\cos \theta - \frac{M_x(t, \vec{x})}{|\vec{M}(t, \vec{x})|} \right] \Big|_{t_f} . \end{aligned} \quad (10.14)$$

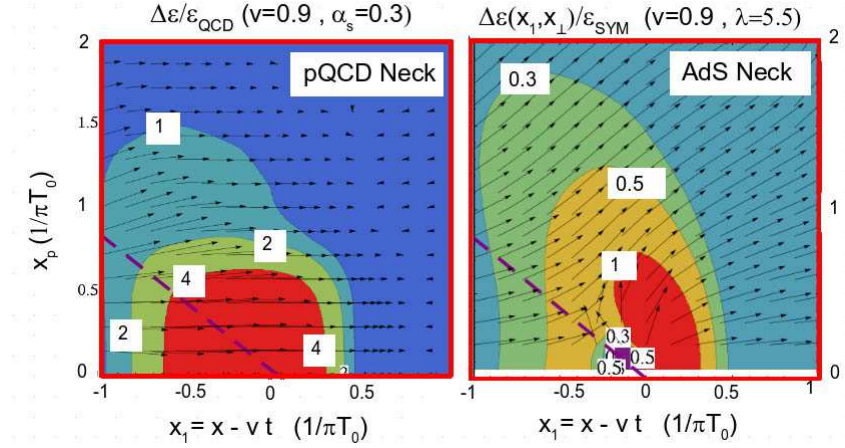


Figure 10.2

A magnified view of the near “neck” zone shows the relative local-energy density perturbation $\Delta\epsilon/\epsilon_0$ and fluid-flow directions induced by a heavy supersonic quark jet moving with $v = 0.9$. As in Fig. 10.1, the pQCD contours were computed using $(3 + 1)$ -dimensional hydrodynamics [110], including the source term from Ref. [203] (left panel). The AdS/CFT neck zone [229, 230, 231] (right panel) uses numerical tables from [233]. The purple dashed line indicates the ideal far-zone point-source shock angle. The heavy quark is at the origin of these comoving coordinates. The arrows indicate both direction and relative magnitude of the fluid flow velocity. The numbers in the plot label the contours of constant $\Delta\epsilon/\epsilon_0$. Note that $\Delta\epsilon/\epsilon_0$ is larger in pQCD but that the transverse flow generated near the quark is much stronger in the AdS/CFT model [136].

This quantity differs from CF mainly by the neglect of the thermal smearing at the freeze-out time, and thus it maximally amplifies the angular anisotropy of the associated hadrons. The very strong assumption in this decoupling scheme is that hadrons from each frozen-out cell emerge parallel to the total momentum of the cell $\mathcal{P}_c^i = d^3\vec{x} T^{0i}(t_f, \vec{x})$. Here $\theta = \pi - \theta_{trigger}$ is the polar angle with respect to the away-side heavy quark jet.

Many other similar purely hydrodynamic measures of bulk flow are possible [82], e.g. weighted by entropy instead of momentum density. However, we found no qualitative differences when the weight function is changed. We used a narrow Gaussian approximation to the Dirac delta in Eq. (10.14) with a $\Delta \cos \theta = 0.05$ width and checked that the results did not change significantly if the width was varied by 50%.

Our intention is not to decide which hadronization scheme is preferred but to apply these two commonly used measures to help quantify the observable differences between two very different approaches to jet-plasma interactions (pQCD x AdS/CFT).

The CF freeze-out employed here and in Refs. [83, 231, 246] is especially questionable in the non-equilibrium neck region but provides a rough estimate of intrinsic thermal smearing about the local hydrodynamic flow.

In Fig. 10.2 we show the relative local energy disturbance and flow profile in the neck region created by a $v = 0.9$ jet in both pQCD and AdS/CFT. The relative transverse flow in the neck zone in AdS/CFT is significantly larger than in pQCD

and as we show below this is reflected in the final angular correlations from that region in both hadronization schemes.

10.4 Freeze-out Results in pQCD

The initial away-side heavy quark jet is assumed to start at $t = 0$ and $x_1 = -4.5$ fm. The freeze-out is done when the heavy quark reaches the origin of the coordinates at time $t_f = 4.5/v$ fm. This provides a rough description of the case in which a uniformly moving heavy quark punches through the medium after passing through 4.5 fm of plasma.

The numerical output of the SHASTA code is the temperature and fluid flow velocity fields $T(t, \vec{x})$ and $\vec{u}(t, \vec{x})$. The hydrodynamic equations were solved in the presence of the source term $\mathcal{J}^\mu(t, \vec{x})$ computed analytically in Ref. [203] in the limit where the dielectric functions that describe the medium's response to the color fields created by the heavy quark were set to unity. The effects from medium screening on \mathcal{J}^μ were studied in detail there. In our numerical calculations we used $x_{pmax} = 1/m_D$ as an infrared cutoff while the minimum lattice spacing naturally provided an ultraviolet cutoff. The background temperature was set to $T_0 = 0.2$ GeV and we assumed $\alpha_s = g^2/(4\pi) = 1/\pi$ in our calculations involving the pQCD source.

The results for the bulk flow according to Eq. (10.14) in pQCD are shown in the upper panel in Fig. 10.3. The curves are normalized in such a way that the largest contributions are set to unity. For all velocities studied here, the pQCD bulk energy-flow distribution has a large forward-moving component in the direction of the jet. In the far zone, this forward-moving energy flow corresponds to the diffusion wake studied in Refs. [83, 137]. The red curve with triangles in the upper panel of Fig. 10.3 corresponds to the yield solely from the neck region for $v = 0.9$. The very small dip at small $\theta = 0$ is mostly due to the weak pQCD neck zone but most of the momentum flow from both neck and diffusion zones is directed around the jet axis.

The relatively small transverse-energy flow in the neck region is evident on the left panel of Fig. 10.2 in contrast to the much larger transverse flow predicted via AdS in that near zone. The Mach cone emphasized in Refs. [199, 205] is also clearly seen but its amplitude relative to the mostly forward diffusion zone plus neck contribution is much smaller than in the AdS/CFT case. The weak Mach peak roughly follows Mach's law as v approaches c_s .

In Fig. 10.4, our CF freeze-out results for the associated away-side azimuthal distribution for $v = 0.58, 0.75, 0.9$ at mid-rapidity and $p_T = 5\pi T_0 \sim 3.14$ GeV light hadrons are shown. The pQCD case, computed from the hydrodynamical evolution, is shown in the upper panel. We again define the angular function

$$CF(\phi) = \frac{1}{N_{max}} \left[\frac{dN(\phi)}{p_T dp_T dy d\phi} \right] \Big|_{y=0}, \quad (10.15)$$

where N_{max} is a constant used to normalize the plots (this function is not positive-definite). The pQCD angular distribution shows only a sharp peak at $\phi = \pi$ for all velocities.

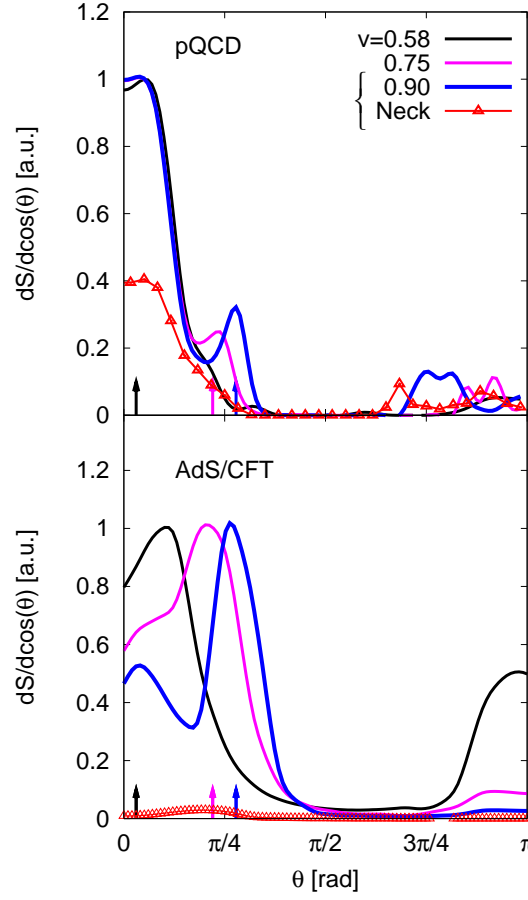
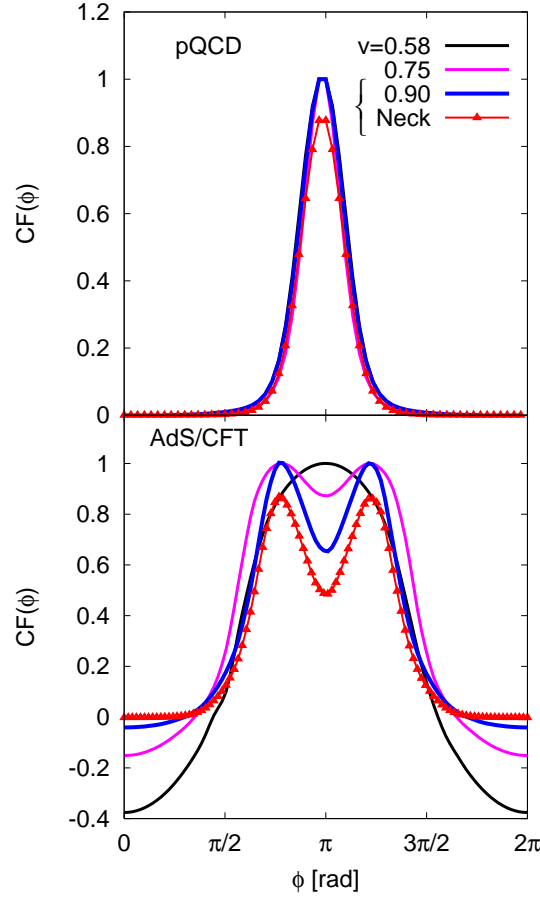


Figure 10.3

The (normalized) momentum-weighted bulk-flow angular distribution as a function of polar angle with respect to the away-side jet is shown for $v = 0.58$ (black), $v = 0.75$ (magenta), and $v = 0.90$ (blue) comparing pQCD anomalous chromo-hydrodynamics to the AdS/CFT string-drag model [215, 233]. The red line with triangles represents the neck contribution for a jet with $v = 0.9$ and the arrows indicate the location of the ideal Mach-cone angle given by $\cos \theta_M = c_s/v$, where $c_s = 1/\sqrt{3}$ [136].

The red curve with triangles denotes the contribution from the pQCD neck region for $v = 0.9$. The different peaks found in the bulk-flow analysis of the pQCD data shown in the upper panel in Fig. 10.3 do not survive CF freeze-out. It was checked that no other structures appear if we either double p_T to 5 GeV or increase α_s to 0.5 (see below). We conclude that the strong forward-moving diffusion zone as well as the mostly forward bow shock neck zone dominate the away-side peak and that the thermal broadened Mach correlations are too weak in pQCD to contribute to the final angular correlations.

**Figure 10.4**

Normalized (and background subtracted) azimuthal away-side jet associated correlation after a Cooper–Frye freeze-out $CF(\phi)$ for pQCD (top) and AdS/CFT from [230, 231] (bottom). Here $CF(\phi)$ is evaluated at $p_T = 5\pi T_0 \sim 3.14$ GeV and $y = 0$. The black line is for $v = 0.58$, the magenta line for $v = 0.75$, and for the blue line $v = 0.9$. The red line with triangles represents the neck contribution for a jet with $v = 0.9$ [136].

10.5 Freeze-out Results in AdS/CFT

We used the same setup employed in Ref. [229, 230, 231] to perform the CF freeze-out of the $\mathcal{N} = 4$ SYM AdS/CFT data computed by Gubser, Pufu, and Yarom in Ref. [233]. They calculated the energy-momentum disturbances caused by the heavy quark, which in this steady-state solution was created at $t \rightarrow -\infty$ and has been moving through the infinitely extended $\mathcal{N} = 4$ SYM static background plasma since then. The freeze-out is computed when the heavy quark reaches the origin of the coordinates. The mass of the heavy quark M in the AdS/CFT calculations is such that $M/T_0 \gg \sqrt{\lambda}$, which allows us to neglect the fluctuations of the string [215, 216].

At $N_c = 3$ the simplifications due to the supergravity approximation are not strictly valid but it is of interest to extrapolate the numerical solutions to study its phenomenological applications. We choose the plasma volume to be the forward light-cone that begins at $x_1 = -4.5$ fm and has a transverse size of $x_p < 4.5$ fm at $T_0 = 0.2$ GeV (our background-subtracted results do not change when larger volumes were used). This choice implies that we assumed the same background temperature for both pQCD and AdS/CFT.

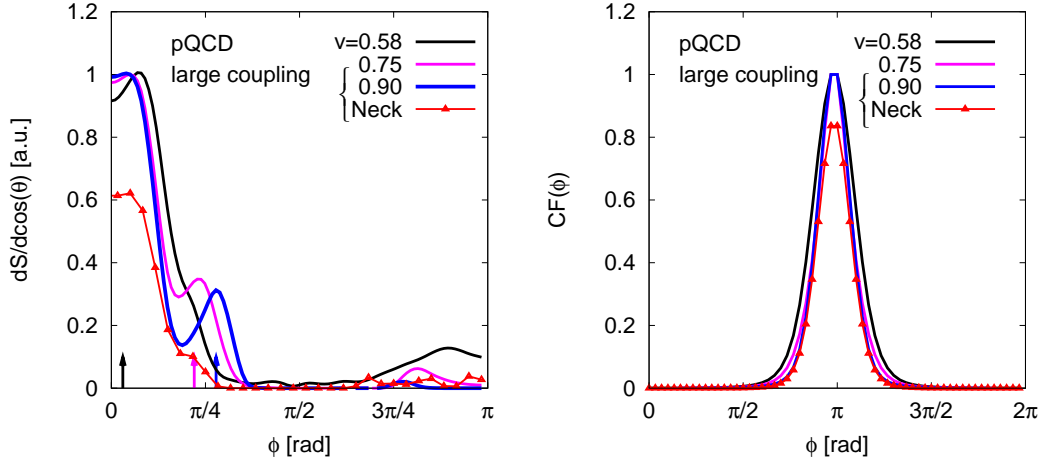
The mapping between the physical quantities in $\mathcal{N} = 4$ SYM and QCD is a highly non-trivial open problem (see, for instance, the discussion in Ref. [291]). We therefore again use CF and bulk-momentum flow as two extreme limits to gauge possible systematic uncertainties.

The (normalized) bulk-momentum flow associated with the AdS/CFT data, computed using Eq. (10.14), is shown in the lower panel of Fig. 10.3. It demonstrates that in AdS/CFT there are more cells pointing into a direction close to the Mach-cone angle than in the forward direction (diffusion zone) when $v = 0.9$ and $v = 0.75$, unlike in the pQCD case displayed in the upper panel. However, when $v = 0.58$, the finite angle from the Mach cone is overwhelmed by the strong bow shock formed in front of the quark, which itself leads to a small conical dip not at the ideal Mach angle (black arrow).

The red line with triangles in the bottom panel of Fig. 10.3 shows that the relative magnitude of the contribution from the neck region to the final bulk-flow result in AdS/CFT is much smaller than in pQCD. However, the small amplitude peak in the AdS/CFT neck curve is located at a much larger angle than the corresponding peak in the pQCD neck, as one would expect from the transverse flow shown Fig. 10.2. Moreover, one can see that a peak in the direction of the trigger particle can be found for all the velocities studied here. This peak represents the backward flow that is always present due to vortex-like structures created by the jet as discussed in detail in Ref. [250] and chapter 9.

Our results for the CF freeze-out of the AdS/CFT solution for $v = 0.58, 0.75, 0.9$ at mid-rapidity and $p_T = 5\pi T_0 \sim 3.14$ GeV are shown in the lower panel in Fig. 10.4. A double-peak structure can be seen for $v = 0.9$ and $v = 0.75$. However, the peaks in the AdS/CFT correlation functions do not obey Mach's law. The reason is that these correlations come from the neck region with a strong transversal non-Mach flow [229, 230, 231]. This is explicitly shown by the red curve with triangles that represents the neck contribution for a jet with $v = 0.9$ as in Fig. 10.3. For $v = 0.58$, the resulting flow is not strong enough to lead to non-trivial angular correlations. The negative yield present in the CF curves for $v = 0.58$ and $v = 0.75$ results from the presence of the vortices discussed above and in chapter 9.

In general [229, 230, 231], the weak sound waves produced by a jet do not lead to a cone-like signal independently of the detailed flow and interference patterns because thermal smearing washes out the signal. Formally, if linearized hydrodynamics applies and in the low-momentum limit ($\vec{u} \cdot \vec{p} \ll T$), the associated hadron away-side distribution is only a very broad peak about $\phi = \pi$ regardless of the detailed combination of Mach wakes, diffusion wakes, or vortex circulation [83, 229, 230, 231, 250]. This result involving CF freeze-out can only be circumvented either in regions with high flow velocities and large gradients as in the neck zone [229, 230, 231], or by increasing p_T to unrealistically high values [83, 246].

**Figure 10.5**

The (normalized) momentum weighted bulk-flow angular distribution (left panel) and the normalized (and background-subtracted) azimuthal away-side jet-associated correlation after a CF freeze-out (right panel) using the pQCD source term for $\alpha_s \approx 0.5$ (in contrast to the previous plots with $\alpha_s = 1/\pi$) for $v = 0.58$ (black), $v = 0.75$ (magenta), and $v = 0.9$ (blue). The red line with triangles represents the neck contribution for a jet with $v = 0.9$. The $CF(\phi)$ is evaluated at $p_T = 5\pi T_0 \sim 3.14$ GeV.

One of the main differences between the two freeze-out procedures employed above (in both AdS/CFT and pQCD) concerns the relative magnitude of the contribution from the neck region to the final angular correlations: the neck region is much more important in CF than in the bulk-flow measure computed via Eq. (10.14). This is due to the exponential factor in CF, which largely amplifies the contribution from the small region close to the jet where the disturbances caused by the heavy quark become relevant.

We checked, as already mentioned previously, that the result is independent of α_s (see Fig. 10.5) by setting the coupling constant to $g = 2.5$, or equivalently $\alpha_s = 0.5$. Since it is known [292] that $\alpha_s = 1/2$ is the critical coupling for charged bosons (in a α_s/r potential), it can be considered as critical pQCD case. Summarizing, we showed that the angular correlations obtained after an isochronous Cooper–Frye (CF) freeze-out of the wake induced by punch-through heavy quark jets (in a static medium) in the Neufeld *et al.* pQCD model of anomalous chromoviscous hydrodynamics do not display a conical structure. This should be compared to the conical-like structures seen after CF freeze-out of the strongly-coupled AdS/CFT string-drag model which, however, are unrelated to Mach’s law and result from a strong flow in the transverse direction that is absent for the pQCD source term (see Fig. 10.2).

Unlike AdS/CFT, the conical flow from the associated non-equilibrium neck zone in pQCD (see the red region in the left panel of Fig. 10.2) and the red curve in Fig. 10.3) is too weak to survive CF freeze-out. In both cases, the actual Mach wakes do not appear after standard CF freeze-out. Mach-like peaks are only observable

in the sudden shattering freeze-out scenario described in Eq. (10.14) in both pQCD and AdS/CFT, in which thermal broadening is entirely neglected.

The neck region (in both pQCD and AdS/CFT) gives the largest contribution to the total yield in CF freeze-out while its contribution in the other extreme case involving the bulk-flow hadronization is not as relevant. This indicates that the magnitude of the neck's contribution to the final angular correlations is still strongly model-dependent. Nevertheless, our results suggest that conical but non-Mach law correlations are much more likely to appear in AdS/CFT than in pQCD.

We therefore propose that the measurement of the jet velocity dependence of the associated away-side correlations with identified heavy quark triggers at RHIC and LHC might provide important constraints on possible pQCD versus AdS/CFT dynamical non-Abelian field-plasma (chromo-viscous) coupling models.

The isochronous hypersurface we used is needed in order to compare AdS/CFT to pQCD since AdS/CFT heavy quark solutions have only been computed so far in a static medium. For realistic simulations that can be compared to data, effects from the medium's longitudinal, transverse, and elliptic flow must be taken into account which will be discussed in the next chapter.

Chapter 11

Conical Correlations in an Expanding Medium

The investigations discussed in the previous chapters focused on the prescription of jet energy and momentum loss by reducing the problem to the most simple case of a static background. This simplification allowed to elaborate detailed reactions of the medium to the jet deposition, like the formation of the diffusion wake (see chapter 8). Moreover, a pQCD source term could be compared to a jet scenario using AdS/CFT (see chapter 10) since the latter prescription always considers an infinite, static, and homogeneous background.

However, the real experimental situation is different in two ways. First, the medium created in a heavy-ion collision expands rapidly. Thus, even assuming that the system equilibrates very quickly [9, 10, 11, 12, 13, 46], i.e., behaves like a “perfect fluid” [15, 16], and a Mach cone is formed, the elliptic and radial expansion will interact with the flow profile created by the jet and cause a distortion of this Mach cone as predicted in Ref. [170]. Hence, Mach cones are sensitive to the background flow. This is a qualitative model-independent effect.

Second, it turned out [10, 11, 12, 13] that the number of observed jets at RHIC is by an order of magnitude lower than expected (also pointing into the direction that the matter created is an opaque, high-density medium where jets quickly thermalize). This means that it is unlikely, but not impossible to have more than one jet in a single event which by itself might lead to new effects [293]. However, the crucial point is that the experimentally determined two- and three-particle correlations (see chapter 2) consider many different events and thus different jet trajectories through the medium. Due to the interaction with radial flow, these jet paths may result in different contributions to the azimuthal correlations. Those patterns show that (the issue of background subtraction is discussed controversially) a two-peaked structure appears on the away-side which is interpreted in a way that a Mach cone is formed during the process of the collision, completely neglecting the multi-event situation.

Therefore, as already discussed by Chaudhuri [236, 237], many different possible paths of a jet through the medium have to be taken into account.

As demonstrated in Refs. [83, 137, 230, 231, 246], two factors strongly go against a conical correlation even in a perfect fluid. The thermal broadening intrinsic to

a Cooper–Frye freeze-out results to first order in p_T/T (see the No-Go Theorem of section 7.5) in a broad away-side peak. Also, the diffusion wake formed (if the momentum deposition is larger than a certain threshold [137, 246]) contributes to one away-side peak opposite to the trigger-jet direction, generally overwhelming any conical signal (see chapter 8).

Nevertheless, while the conclusive detection of Mach cones would provide evidence for the perfect-fluid behavior, the opposite is not the case though it implies that the double-peaked structure cannot directly be compared to the EoS.

As already mentioned above, the expansion of a system created in a heavy-ion collision certainly influences any kind of jet-deposition scenario. It was suggested that the diffusion-wake contribution can be reduced by radial flow [235], and it was shown that longitudinal flow may cause a broadening of the away-side peaks [202]. Thus, for a realistic simulation, all those effects have to be considered.

In the following, we study an expanding medium with Glauber initial conditions [121] (see appendix B), corresponding to a Au -nucleus with $r = 6.4$ fm. We focus on radial flow only, i.e., the medium we investigate is elongated over the whole grid, forming a cylinder expanding in radial direction. Moreover, we only consider most central collisions with an impact parameter of $b = 0$ fm (thus neglecting any elliptic flow contribution), and assume that the maximum temperature of the medium is 200 MeV.

Like in previous chapters, we solve the ideal hydrodynamic equations applying an ideal gas EoS for massless gluons. We choose the following ansatz for the energy and momentum deposition of the jet [cf. Eq. (8.4)]

$$J^\nu = \int_{\tau_i}^{\tau_f} d\tau \frac{dM^\nu}{d\tau} \bigg|_0 \left[\frac{T(t, \vec{x})}{T_{\max}} \right]^3 \delta^{(4)} \left[x^\mu - x_{\text{jet}}^\mu(\tau) \right], \quad (11.1)$$

with the proper-time interval of the jet evolution $\tau_f - \tau_i$, the energy and momentum loss rate $dM^\nu/d\tau = (dE/d\tau, d\vec{M}/d\tau)$, the location of the jet x_{jet} , and $\sigma = 0.3$ fm. In non-covariant notation, this source term reads

$$\begin{aligned} J^\nu(t, \vec{x}) &= \frac{1}{(\sqrt{2\pi} \sigma)^3} \exp \left\{ -\frac{[\vec{x} - \vec{x}_{\text{jet}}(t)]^2}{2\sigma^2} \right\} \\ &\times \left(\frac{dE}{dt} \bigg|_0, \frac{d\vec{M}}{dt} \bigg|_0, 0, 0 \right) \left[\frac{T(t, \vec{x})}{T_{\max}} \right]^3, \end{aligned} \quad (11.2)$$

where we use $dE/dt_0 = 1$ GeV/fm and $dM/dt_0 = 1/v dE/dt_0$. Like in chapter 8 and Refs. [137, 246], we study both jet energy and momentum loss as well as pure energy loss in the context of an expanding medium to investigate the impact of the (radial) expansion and thus the significance of linearized hydrodynamical approaches as used in Refs. [83, 199].

Since we are using a dynamical background, the source term, unlike in Eqs. (8.4) and (8.5), scales with the temperature, based on the assumption that the source is proportional to the density of colored particles. Additionally, a temperature cut is applied to ensure that no deposition takes place outside the medium, i.e., below a temperature of $T_c = 130$ MeV. In Ref. [137] it was shown that the azimuthal correlations obtained after freeze-out do not change significantly when jets decelerate during their propagation according to the Bethe–Bloch formalism, creating a

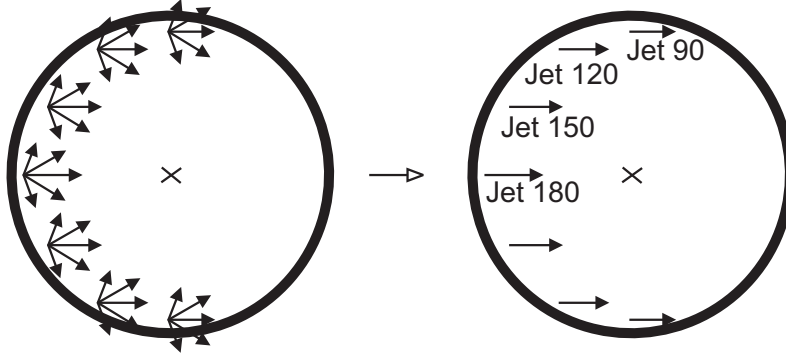


Figure 11.1

Schematic representation of different jet paths assuming that surface emission is the dominant effect in heavy-ion collisions. The right panel shows the reduction of paths due to reasons of symmetry for a medium with vanishing impact parameter, $b = 0$ fm. Those jet trajectories will be studied below.

Bragg peak. Given that we are interested in the modifications of such correlations due to an expanding background, we may therefore simplify to the study of jets propagating with a constant velocity.

However, each parton moving through a medium will eventually be thermalized after the deposition of all its initial energy. Since jets are always created back-to-back, this energy is equal to the one of the trigger jet.

Below, we consider a 5 GeV and a 10 GeV trigger parton which corresponds to trigger- p_T 's of $p_T^{\text{trig}} = 3.5$ and 7.5 GeV assuming that a fragmenting jet creates particles with $\sim 70\%$ of its energy, allowing for an easier comparison to experimental data (see e.g. Fig. 2.6).

Experiment can only trigger on the jet direction, but not on the origin of the jets formed. Thus, one has to consider different starting points for the jet (see Fig. 11.1). Due to reasons of symmetry (cf. Fig. 11.1), the number of paths that need be studied in most central collisions reduces drastically. The jet itself is always taken to propagate along a certain direction, here the positive x -axis, but its origin is varied according to

$$x = r \cos \phi, \quad y = r \sin \phi, \quad (11.3)$$

where $r = 5$ fm is chosen which is close to the surface of the medium. We assume that surface emission is the dominant effect of jet events in heavy-ion collisions, i.e., we suppose that jets are mainly created close to the surface of the the expanding medium (see Fig. 11.1). Here, we consider $\phi = 90, 120, 150, 180, 210, 240, 270$ degrees. According to azimuthal symmetry, the results for $\phi = 210, 240, 270$ degrees are obtained by reflecting the corresponding data for $\phi = 90, 120, 150$ degrees.

As can be seen from Fig. 11.2, the energy and thus the momentum deposition is not constant, but varies because of the temperature dependence in Eq. (11.1) with the jet path. For the 5 GeV jet, the cut for depositing the total amount of energy is clearly visible for the most central jets (see e.g. solid red line in Fig. 11.2). Of course, it is a strong model assumption that $dE/dt|_0$ and $dM/dt|_0$ are the same for a 5 and a 10 GeV jet.

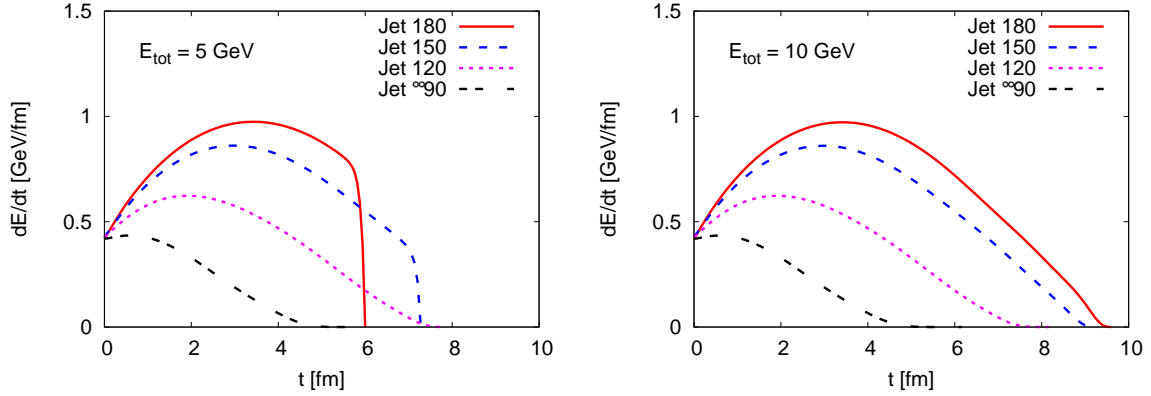


Figure 11.2

Jet energy deposition as a function of time for jets depositing 5 GeV (left panel) and 10 GeV (right panel) along the different trajectories introduced in Fig. 11.1. For the 5 GeV jet, the cut in the total amount of deposited energy is clearly visible for the most central jets.

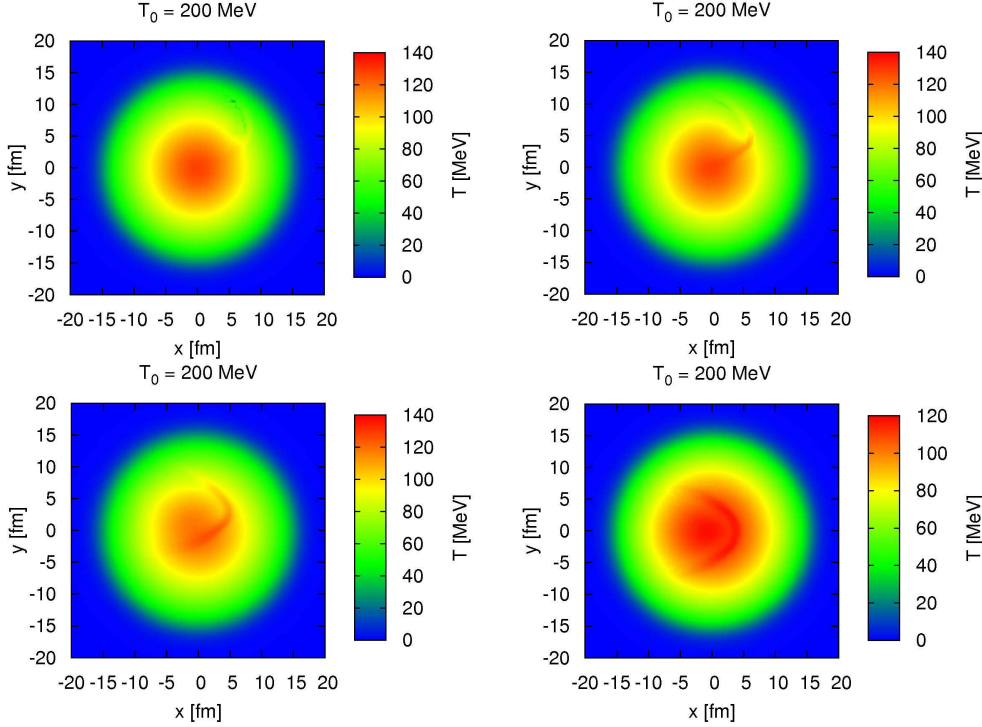
There is a qualitative difference between a 5 GeV and a 10 GeV jet. The 5 GeV jet will stop around the middle of the medium. Thus, it will mainly move against the background flow. A 10 GeV jet, on the contrary, will cross the middle of the medium and be thermalized before it reaches the opposite surface. Therefore, it also propagates a larger distance parallel to the flow.

The temperature pattern of four different jets (Jet 90, Jet 120, Jet 150, and Jet 180 according to Fig. 11.1) at the moment of freeze-out, i.e., when the temperature of all cells has fallen below $T_c = 130$ MeV, are shown in Fig. 11.3. The background flow leads to a distortion of the conical structure, resulting in different contributions to the away-side correlations as will be discussed below in detail.

A crucial aspect of hydrodynamical applications to heavy-ion collisions is the conversion of the fluid into particles, the freeze-out (see e.g. section 3.7). While an isochronous freeze-out, which means that the conversion appears at a certain time t_f , can be an adequate prescription for a static medium, this assumption might not be reasonable for an expanding medium. Nevertheless, it should be mentioned that the “blast wave” model [294] which is based on the isochronous freeze-out reproduces experimental results quite well.

In appendix G we show that the space-time distribution of temperature is severely deformed by the jet. This can be seen by plotting the isothermal hypersurface, i.e., the space-time profile of the fluid cells falling below a certain critical temperature (that was chosen to be $T_c = 130$ MeV in the present study, see Fig. G.1). Moreover, (cf. Figs. G.2 and G.3), we demonstrate that the particle distributions obtained for a jet passing through the middle of the medium (Jet 180 in Fig. 11.1) obtained via an isochronous and an isothermal CF freeze-out are very similar.

This suggests that an isochronous prescription, though a strong model assumption, does not severely alter the results as compared to an isothermal freeze-out. Such an isochronous CF conversion is used below, performed when all cells are below the critical temperature of $T_c = 130$ MeV, for both the jet+medium and, independently, the background simulations.

**Figure 11.3**

The temperature pattern of four different jets (Jet 90 upper left panel, Jet 120 upper right panel, Jet 150 lower left panel, and Jet 180 lower right panel) with varying origins is shown at the moment of freeze-out, i.e., when the temperature of all cells has fallen below $T_c = 130$ MeV. The distortion of the conical structure is clearly visible which produces different contributions to the away-side correlations displayed below.

11.1 Two-Particle Correlations in an Expanding Medium

One major difference between the experimental situation and the hydrodynamical calculation proposed above is that the trajectory of the jet is known by definition in the latter case. However, it is possible to simulate the experimental procedure by convoluting the CF freeze-out results, which only consider the away-side jets, with a function representing the near-side jet

$$f(\phi^*) = \frac{1}{\sqrt{2\pi\sigma^2}} \exp\left(\frac{-\phi^*}{2\sigma^2}\right), \quad (11.4)$$

(here $\sigma = 0.4$ fm), resulting in a two-particle correlation

$$\frac{dN_{\text{con}}}{p_T dp_T dy d\phi} = Af(\phi) + \int_0^{2\pi} d\phi^* \frac{dN(\phi - \phi^*)}{p_T dp_T dy d\phi} f(\phi^*), \quad (11.5)$$

where A is an arbitrary amplitude chosen to adjust the heights of the near-side jet. This signal is then background-subtracted and normalized via

$$CF(\phi) = \frac{1}{\int_0^{2\pi} N_{\text{back}}(\phi) d\phi} \left[\frac{dN_{\text{con}}(\phi)}{p_T dp_T dy d\phi} - \frac{dN_{\text{back}}(\phi)}{p_T dp_T dy d\phi} \right]. \quad (11.6)$$

The different jet paths are implemented by averaging

$$\frac{d\langle N \rangle}{p_T dp_T dy d\phi} = \frac{1}{N_{\text{paths}}} \sum_{i_{\text{paths}}=1}^{N_{\text{paths}}} \frac{dN^i}{p_T dp_T dy d\phi}, \quad (11.7)$$

leading to the definition of the *averaged* two-particle correlation

$$\langle CF(\phi) \rangle = \frac{1}{\int_0^{2\pi} \langle N_{\text{back}}(\phi) \rangle d\phi} \left[\frac{d\langle N_{\text{con}} \rangle(\phi)}{p_T dp_T dy d\phi} - \frac{d\langle N_{\text{back}} \rangle(\phi)}{p_T dp_T dy d\phi} \right]. \quad (11.8)$$

In order to present the contribution of the different paths, we will also depict

$$CF_{\langle \text{back} \rangle}(\phi) = \frac{1}{\int_0^{2\pi} \langle N_{\text{back}}(\phi) \rangle d\phi} \left[\frac{dN_{\text{con}}(\phi)}{p_T dp_T dy d\phi} - \frac{d\langle N_{\text{back}} \rangle(\phi)}{p_T dp_T dy d\phi} \right]. \quad (11.9)$$

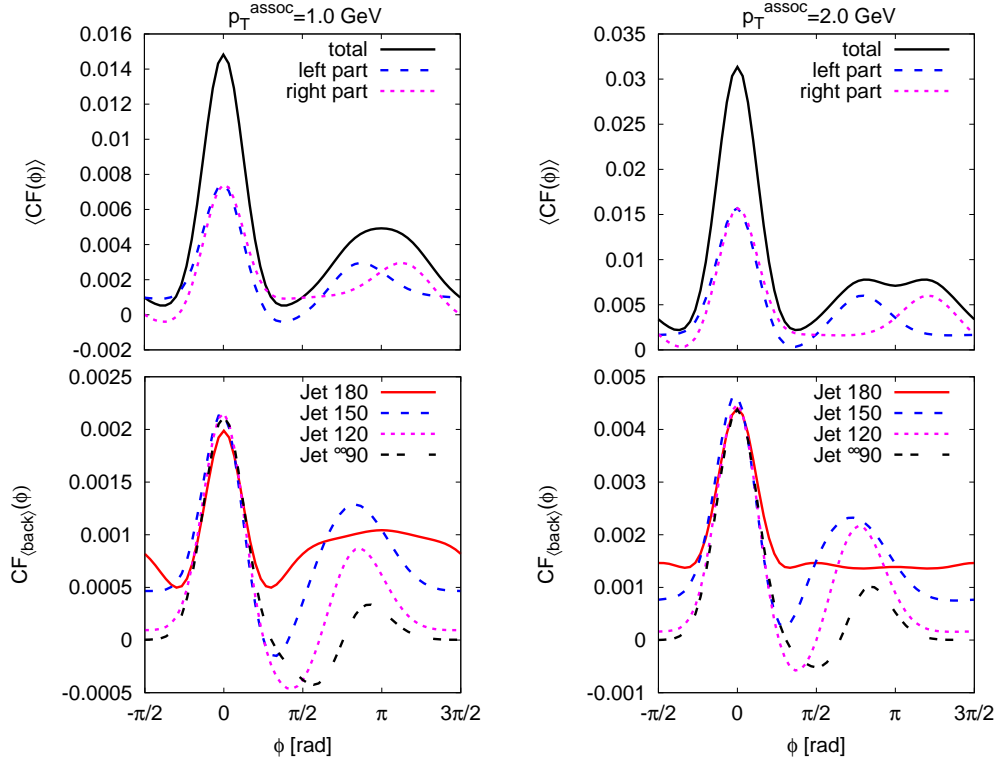
The results show that for a 5 GeV jet, corresponding to a trigger- p_T of 3.5 GeV, the normalized, background-subtracted, and path-averaged CF signal (see solid black line in the upper panel of Fig. 11.4) displays a broad away-side peak for $p_T^{\text{assoc}} = 1$ GeV (left panel of Fig. 11.4), while a double-peaked structure occurs for $p_T^{\text{assoc}} = 2$ GeV. The reason is that the contribution of the different paths (given in the lower panel of Fig. 11.4 for the paths in the upper half of the medium, named according to Fig. 11.1), add up to a peak in the left part of the away-side (see blue dashed line in the upper panel of Fig. 11.4), while the contributions of the paths in the lower half of the medium (which are not shown here in detail) produce a peak in the right part of the away-side (see magenta dashed line in the upper panel of Fig. 11.4).

Depending on the gap between those peaks on the away-side, the different contributions result either in a broad away-side peak (like for $p_T^{\text{assoc}} = 1$ GeV) or a double-peaked structure (as for $p_T^{\text{assoc}} = 2$ GeV).

It is important to notice that the main contributions to the peaks in the left and right part of the away-side come from jets not propagating through the middle of the medium (see lower panel of Fig. 11.4).

Though these simulations do not completely agree with experimental data [comparing with Fig. 2.6 the cases studied above would roughly correspond to part (b) and (c)], they are qualitatively similar. For a $p_T^{\text{trig}} = 3.5$ GeV, the double-peaked structure on the away-side gets more pronounced with larger p_T^{assoc} . However, the yield is different since experimentally the number of jets decreases with increasing transverse momentum.

Considering now a 10 GeV jet (see Fig. 11.5), describing a $p_T^{\text{trig}} = 7.5$ GeV [which can approximately be compared to part (e) of Fig. 2.6], the resulting shape is still the same. There is a broad away-side peak for $p_T^{\text{assoc}} = 1$ GeV and a double-peaked structure for $p_T^{\text{assoc}} = 2$ GeV. However, since the energy and momentum deposition continued for later times (see Fig. 11.2), the jet reaches that part of the medium where the background flow is parallel to its trajectory. Thus, there is again a strong impact of the diffusion wake as can be seen from the solid red line in the lower panel of Fig. 11.5 which represents the jet propagating through the middle of the medium. Compared to the 5 GeV jet, which stops about the center of the medium (see solid red line in the lower panel of Fig. 11.4), the diffusion wake contribution is enhanced, resulting in a broader away-side peak for $p_T^{\text{assoc}} = 1$ GeV

**Figure 11.4**

The normalized, background-subtracted and path-averaged azimuthal two-particle correlation after performing an isochronous CF freeze-out (solid black line) for 5 GeV jets depositing energy and momentum for $p_T^{\text{assoc}} = 1$ GeV (left panel) and $p_T^{\text{assoc}} = 2$ GeV (right panel). The dashed blue and magenta lines in the upper panels represent the averaged contributions from the different jet paths in the upper and lower half of the medium (cf. Fig. 11.1), respectively. The lower panel displays the contribution from the different jet trajectories in the upper half of the medium.

and a smaller dip for $p_T^{\text{assoc}} = 2$ GeV. This strengthens the conclusion that a conical signal can be obtained by averaging over different jet paths.

References [83, 137] showed that, considering a source term with a vanishing momentum-deposition rate in a static medium, a conical signal arises from a CF freeze-out. However, since the deposition of energy and momentum does *not* yield a double-peaked structure on the away-side for a static medium, but rather a peak in the opposite trigger-jet direction [83, 137], the question arises if this result may allow for conclusions about the properties of the source term.

Fig. 11.6 demonstrates that pure jet energy loss in an expanding medium does *not* lead to a double-peaked structure on the away-side for the normalized, background-subtracted and path-averaged azimuthal correlation, neither for $p_T^{\text{assoc}} = 1$ GeV nor for $p_T^{\text{assoc}} = 2$ GeV (though there is a plateau region for $p_T^{\text{assoc}} = 2$ GeV). No peaks occur on the away-side of a jet traversing the middle of the medium (solid red line in the lower panel of Fig. 11.6). However, there appear small peaks around $\phi \sim \pi/2$ and $\phi \sim 3\pi/2$ for a $p_T^{\text{assoc}} = 1$ GeV, consistent with the prediction of Ref. [170] that the emission angle increases with increasing background flow (see

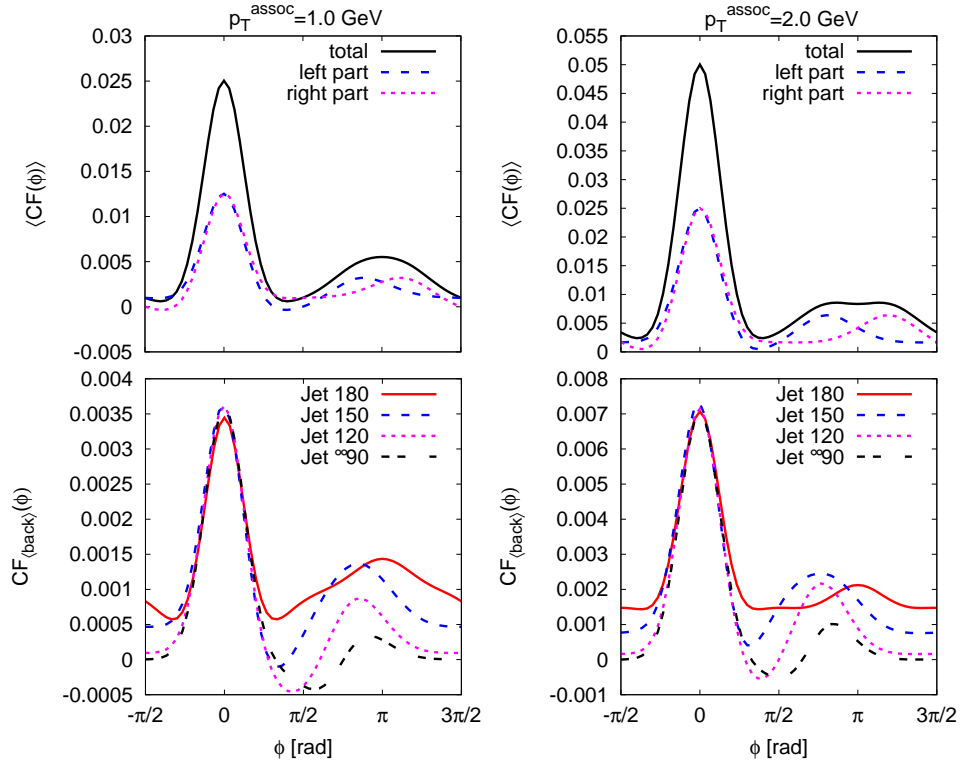


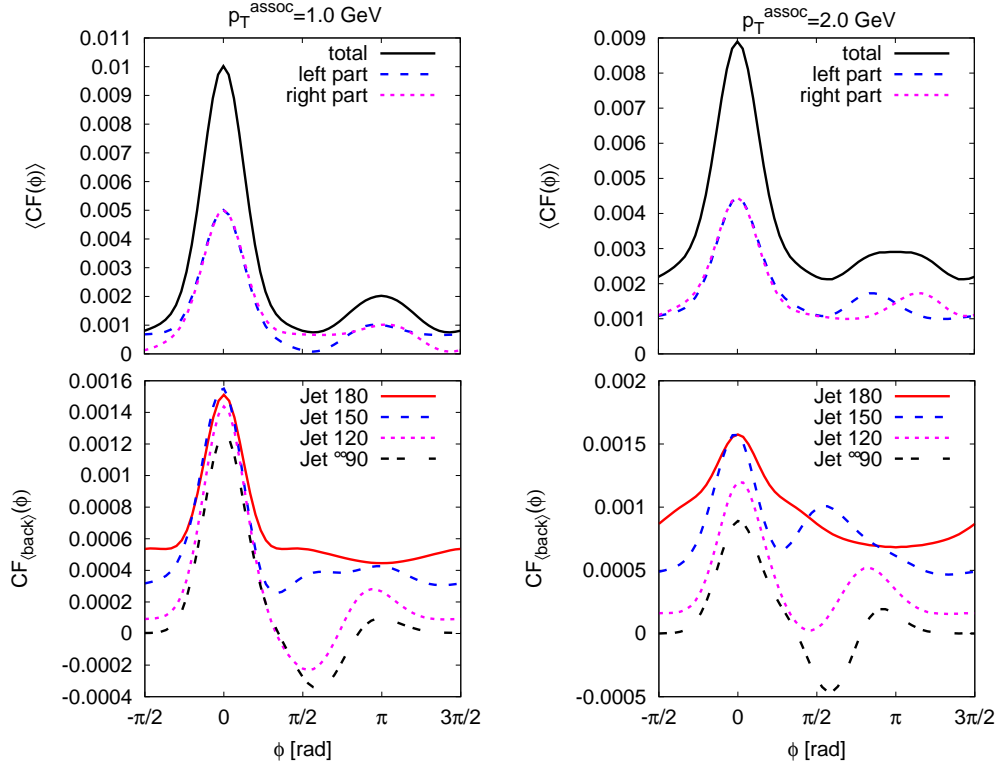
Figure 11.5

The normalized, background-subtracted and path-averaged azimuthal two-particle correlation after performing an isochronous CF freeze-out (solid black line) for 10 GeV jets depositing energy and momentum for $p_T^{\text{assoc}} = 1 \text{ GeV}$ (left panel) and $p_T^{\text{assoc}} = 2 \text{ GeV}$ (right panel). The dashed blue and magenta lines in the upper panels represent the averaged contributions from the different jet paths in the upper and lower half of the medium (cf. Fig. 11.1), respectively. The lower panel displays the contribution from the different jet trajectories in the upper half of the medium. The impact of the diffusion wake is clearly visible for the jet 180 in the lower panel.

also Fig. 5.3¹). Thus, there is a clear difference between a static and an expanding medium. Nevertheless, it is also necessary to study the propagation of a jet through a uniform background since otherwise various effects (like e.g. the impact of the diffusion wake) cannot be understood.

In conclusion, we have shown using a full $(3+1)$ -dimensional ideal hydrodynamic prescription that a double-peaked away-side structure can be formed by averaging over different contributions of several possible jet trajectories through an expanding medium, as already discussed in Refs. [202, 235, 236]. Therefore, it seems natural to conclude that this shape, interpreted as a conical signal, does not result from a “true” Mach cone, but is actually generated by a superposition of distorted wakes. Clearly, the emission angle of such a structure is not connected to the EoS. We verified that the interplay between radial flow and diffusion wake may lead to an

¹It is important to mention here that Satarov et al. predicted a decreasing opening angle of the Mach cone with increasing background flow (parallel or anti-parallel to the trajectory of the jet). Clearly, such a decreasing opening angle results in an increasing emission angle.

**Figure 11.6**

The normalized, background-subtracted and path-averaged azimuthal two-particle correlation after performing an isochronous CF freeze-out (solid black line) for 5 GeV jets assuming a vanishing momentum loss rate for $p_T^{\text{assoc}} = 1 \text{ GeV}$ (left panel) and $p_T^{\text{assoc}} = 2 \text{ GeV}$ (right panel). The dashed blue and magenta lines in the upper panels represent the averaged contributions from the different jet paths in the upper and lower half of the medium (cf. Fig. 11.1), respectively. The lower panel displays the contribution from the different jet trajectories in the upper half of the medium. The Jet 180 in the lower panel exhibits large emission angles.

annihilation of the latter as long as the jet trajectory is opposite to the background flow (see Fig. 11.4), as suggested in Ref. [235]. Nevertheless, the contribution of this diffusion wake, which depends on the path length of the jet, may strongly influence the final azimuthal distributions obtained after freeze-out from averaging over different possible jet trajectories (see Fig. 11.5).

However, the main contribution to the away-side correlation is due to jets that do not propagate through the middle of the medium, depending on the jet energy and momentum loss rate as well as the amount of deposited energy (see e.g. the lower left panel of Fig. 11.4). Obviously, it is necessary to determine the jet energy and momentum loss rates as well as their variance in time depending on the initial energy and velocity of the jet.

These results do not exclude Mach-cone formation in heavy-ion collision. As already proven in Ref. [137] (see chapter 8, in particular Fig. 8.1), a conical shape occurs in all jet-deposition scenarios including energy loss, leading to a constructive interference of the outward-moving sound waves, but the signal is usually too

weak to survive a CF freeze-out scenario [136, 137, 231]. Due to the interaction with radial flow, it might still be possible to observe a Mach-cone signal in single-jet events.

Moreover, these findings are not in contradiction to the measured three-particle correlations. As Fig. 2.9 shows, such pattern exhibits a peak along the diagonal axis, supposed to arise from deflected jets, as well as four off-diagonal peaks on the away-side, presumably resulting from a Mach-cone contribution. Such a structure may indeed be due to the different contributions of the various jet trajectories considered.

We also demonstrated that for the present study (at least for very central jets) an isochronous and an isothermal CF freeze-out prescription (see appendix G) leads to very similar azimuthal particle correlations. Furthermore, we elaborated the difference between a static and an expanding medium by showing that a jet deposition scenario assuming a vanishing momentum-loss rate, which results in a conical signal in a uniform background, does not lead to a conical structure in an expanding medium for low values of p_T^{assoc} (see Fig. 11.6) and is therefore not in accordance with experiment [70] (see Fig. 2.6). Thus, it is not possible to directly extrapolate from a static to an expanding medium and non-linear hydrodynamics is fundamental for quantitative studies of jets in a medium.

In addition, we could verify the predictions by Satarov et al. [170] that a background flow antiparallel to the jet direction leads to larger emission angles of a Mach cone, see Fig. 11.6. For a general, though qualitative, discussion of the distortion effects in an expanding medium see appendix H.

The effects of longitudinal expansion as well as finite impact parameter remain to be considered. Moreover, a different freeze-out prescription (like coalescence [135]) might alter the azimuthal correlations. The recent observation of cone-angle variation with respect to the reaction plane (see right panel of Fig. 2.7 and [77, 78, 79]), which has to be checked applying hydrodynamical prescriptions, raises the prospect that the phenomenology of generating conical signals in heavy-ion collisions could be tested soon. However, the novel results concerning the two-particle correlations obtained from full jet reconstructions [295, 296] reveal that the propagation of a jet through a medium that can be described by hydrodynamics deserves further scrutiny and is far from being resolved yet.

Part IV

Jets in Heavy-Ion Collisions: Conclusions and Outlook

Non-trivial things are the
sum of trivial things.

(Unknown)

The main topic of this thesis was to investigate the jet-medium interactions in a Quark-Gluon Plasma (QGP) that is assumed to be created in heavy-ion collisions and to behave like a “nearly perfect fluid”. For this purpose, we studied the propagation of a fast particle, the so-called jet, through a medium (which can be described by hydrodynamics) using a $(3 + 1)$ -dimensional ideal hydrodynamic algorithm.

The basic question was if the propagation of such a jet leads to the creation of a Mach cone and if the disturbance caused by this Mach cone is large enough to be seen in the final particle distributions that are measured by experiment. Such a result would not only confirm fast thermalization, it would also allow to study the Equation of State (EoS) of the medium formed in a heavy-ion collision (which is supposed to resemble the one created shortly after the Big Bang), since the (particle) emission angles caused by the Mach cone are directly related to the speed of sound of the medium.

After giving a general overview about the basic properties and the phase diagram of Quantum Chromodynamics (QCD), which can properly be tested by heavy-ion collisions, we described the evolution of such a heavy-ion collision and discussed different probes for the QGP. Then, we reviewed the particle correlations measured by experiment. Motivated by the fact that jets are produced back-to-back, two-particle correlations were introduced considering the relative azimuthal angle between two particles. One of these particles, the trigger jet, is assumed to leave the expanding fireball without any further interaction while the associated particle on the away-side, traverses the medium depositing energy and momentum. Such (published) two-particle correlations obtained from experimental data exhibit a clear double-peaked structure on the away-side which is suggested to be caused by the creation of a Mach cone. However, other explanations are also possible and were discussed briefly.

In part II, we introduced the concept of ideal hydrodynamics and its applicability to heavy-ion collisions, starting from a (proper) choice of the initial conditions, via the numerical solution for the Equations of Motion, to the conversion of the fluid fields of temperature and velocities into particles, the so-called freeze-out.

Moreover, we discussed the importance and the effects of viscosity in heavy-ion collisions and deduced the viscous transport equations (for the bulk viscous pres-

sure, the heat flux current, and the shear stress tensor) from kinetic theory. Those equations are the basis for any numerical treatment of viscous hydrodynamics, a prescription that is important to gain a quantitative understanding of the underlying processes in heavy-ion collisions.

Subsequently, we discussed shock-wave phenomena in general, reviewed the predictions concerning the influence of an expanding background on the formation of Mach cones, and outlined different jet energy-loss mechanisms ranging from theories based on weak interactions (as described by perturbative QCD, pQCD) to strong interactions (which can be formulated using the Anti-de-Sitter/Conformal Field Theory correspondence, AdS/CFT). A basic introduction to the latter prescription is given in a separate chapter. Additionally, we also summarized previous studies of jet-energy transfer to the medium using the linearized hydrodynamical approach.

The results of our numerical simulations were summarized in part III. Here, we distinguished a static and an expanding medium and considered different energy and momentum-loss scenarios for a source term schematically characterizing the deposition along the trajectory of the jet as well as another one derived from pQCD. The latter source term is also directly compared to results obtained from a jet propagation described within the framework of AdS/CFT.

One of the basic results is the creation of a strong flow (named the *diffusion wake*) behind the jet common to all different scenarios studied in a static medium if the momentum deposition is larger than a certain threshold. The particle yield coming from this strong forward-moving diffusion wake always overwhelms the weak Mach-cone signal after freeze-out and leads to one single peak on the away-side which is not in agreement with the shape of the published two-particle correlations obtained by experiment.

This peak is found for the schematic as well as for the pQCD source term, but not when evaluating a jet event applying the AdS/CFT correspondence. In that case, the impact of the transverse flow from the so-called neck region (which is an area close to the head of the jet) lead to a double-peaked structure in the final particle correlations that is unrelated to a Mach-cone signal, providing different freeze-out patterns for pQCD and AdS/CFT. Thus, the measurement of identified heavy quark jets at RHIC and LHC might provide an important constraint on possible jet-medium coupling dynamics.

Moreover, we showed that the medium's response and the corresponding away-side angular correlations are largely insensitive to whether the jet punches through or stops inside the medium. We described the backreaction of the medium for the fully stopped jet by a simple Bethe–Bloch-like model which causes an explosive burst of energy and momentum (Bragg peak) close to the end of the jet's evolution through the medium. The resulting correlations are also independent of whether the momentum deposition is longitudinal (as generic to pQCD energy loss models) or transverse.

The universal existence of the diffusion wake in all scenarios where energy as well as momentum is deposited into the medium can readily be understood in ideal hydrodynamics through vorticity conservation. We discussed experimentally observable consequences of such a conserved structure, probably connected to polarization effects of hadrons (like hyperons or vector mesons). Since polarization is

sensitive to initial conditions, hydrodynamic evolution, and mean-free path, corresponding measurements might shed some light on several aspects of heavy-ion collisions that are not well understood yet.

Certainly a realistic description of a heavy-ion collision requires an expanding background. We demonstrated that the interaction of the radial and jet flow may lead to the reduction of the diffusion wake and to a deflection of the Mach cone as predicted in an earlier work. The strength of the diffusion-wake contribution clearly depends on the path length of the jet.

However, the correlation patterns obtained from experiment consider several jet events. We showed that a conical signal can be created by averaging over different possible jet paths. Therefore, it seems natural to conclude that the experimentally observed shape does not result from a “true” Mach cone, but is actually generated by a superposition of distorted wakes. Clearly, the emission angle of such a structure is not related to the EoS.

We illustrated that the diffusion wake nevertheless strongly influences the structure of the final particle correlations obtained from averaging over possible jet trajectories. Depending on the energy and momentum-loss rate as well as on the amount of deposited energy, the main contribution to the away-side correlation may be due to non-central jets. Consequently, it is necessary to determine the jet energy and momentum-loss rates as well as their variance in time depending on the initial energy and velocity of the jet.

Additionally, we elaborated a clear difference between a static and an expanding background. While an energy-loss scenario assuming a vanishing momentum-loss rate results in a conical signal for a uniform background, such a structure is not obtained in an expanding medium which is in disagreement with the experimental data. Thus, it is fundamental to apply non-linear hydrodynamics for quantitative studies of jets in a medium.

The results discussed above are not in contradiction to the measured three-particle correlations that display a distinct emission pattern if Mach cones are produced since these correlations also show a contribution from deflected jets which might be due to the non-central jets mentioned before.

Therefore, an unambiguous proof of a Mach cone which can be related to the EoS requires the investigation of single-jet events (as it should become possible at LHC) for different trajectories through the medium.

The recent observation of cone-angle variation with respect to the reaction plane, which has to be analyzed using a full hydrodynamical prescription, promises further insight into the phenomenology of generating conical interference patterns in heavy-ion collisions. Novel results, however, obtained from full jet reconstruction reveal that the jet-medium interactions deserve further scrutiny both from the experimental and from the theoretical side. For a comparison to hydrodynamic simulations, full jet reconstruction will be essential.

Apparently, the effects of longitudinal expansion, nonzero impact parameter, and phase transitions (connected to a change in the speed of sound of the medium) remain to be considered.

It will also be important to test the experimental procedure of background subtraction. The common method applied is to subtract the elliptic flow arising from angular anisotropies of the expanding system. Since it is not clear from first princi-

ples that the flow is independent of the jet transit, this method (ZYAM) is discussed controversially.

Moreover, different freeze-out prescriptions as well as the interaction of the created hadrons (like coalescence or resonance decays) might alter the azimuthal correlations and need to be examined.

To advance this research area, a more detailed understanding of the source for the hard probes is needed, ranging from weak interactions (as described by pQCD) to strong interactions (formulated by the AdS/CFT correspondence). It is necessary to develop a detailed space-time energy-loss model, considering all different contributions (i.e., radiative and collisional energy loss) to high order in opacity. By coupling quantum transport to hydrodynamics, it will be possible to further investigate the jet-medium interactions for the different energy regions supported by the various experiments like RHIC, LHC, and FAIR.

Appendices

Appendix A

The Evolution of the Universe

About 13.7 billion years ago a hot and dense phase was formed out of a singularity, the so-called *Big Bang*, where quarks, antiquarks, and gluons could move around as free particles. This state of matter is usually called the Quark-Gluon Plasma (QGP). Due to the high pressure gradients, expansion and cooling set in and below a certain critical value of the energy density ($\varepsilon_{\text{crit}} \approx 1 \text{ GeV/fm}^3$), quarks and gluons combined into color-neutral objects, the *hadrons*, a process being called confinement.

Subsequently, the unstable hadrons decayed so that mainly protons as well as neutrons accumulated. Around 1 s after the Big Bang, the main fraction of the building blocks of matter were already formed. Later, heavy elements emerged from fusion processes and supernova explosions.

After the temperature had fallen below $T \approx 3000 \text{ K}$, neutral atoms were gener-

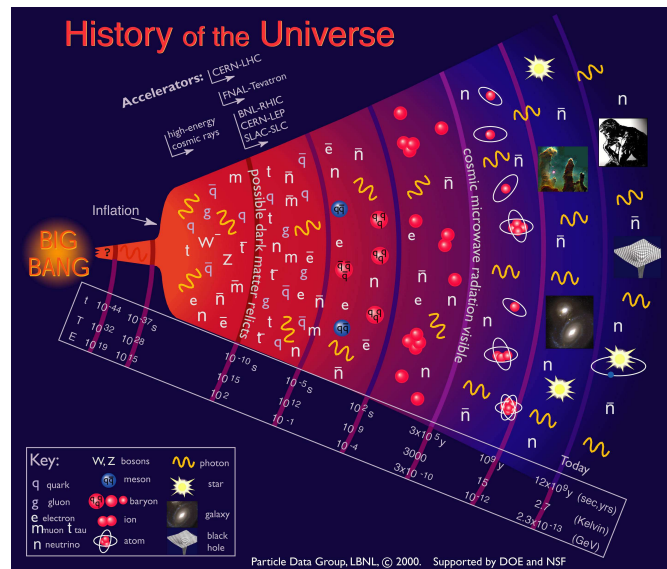


Figure A.1

The evolution of the universe, starting with the Big Bang 13.7 billion years ago and illustrating the period from the formation of the building blocks of matter to the creation of galaxies.

ated. Since the interaction of the photons with these neutral atoms was very weak, the universe got transparent. Then, due to the expansion of the universe, the wavelength of the disconnected background radiation increased, resulting in a redshift that corresponds to a temperature of 2.73 K which is measurable today. This decoupling of radiation caused the gravity to gain more influence and because of spatial density fluctuations, spacious structures like galaxies were created roughly 1 million years after the Big Bang. For a synopsis see Fig. A.1.

Appendix B

Glauber Model

The Glauber Model [121] provides initial conditions for the transverse plane in a heavy-ion collision that can be used by models describing the expansion of a hot and dense medium (like hydrodynamic applications). It describes a nucleus-nucleus collision in terms of multiple nucleon-nucleon interactions. The underlying geometry is shown in Fig. B.1). It leads to the number of wounded (or participating) nucleons in a heavy-ion collision which can be used to specify the centrality class of a collision (see Fig. B.2) and to determine the initial distribution of energy density. The latter one is mandatory in the hydrodynamical framework.

Since the model is based on nucleon-nucleon collisions, it requires the knowledge of the inelastic cross section σ_{NN} and a density profile of the nucleus which is specified to be the Woods–Saxon distribution,

$$\rho_A(\vec{x}) = \frac{\rho_0}{1 + \exp[(|\vec{x}| - R_A)/d]} . \quad (\text{B.1})$$

The mean radius of the nucleus R_A can be calculated via

$$R_A = \left(1.12A^{1/3} - 0.86A^{-1/3} \right) \text{ fm} , \quad (\text{B.2})$$

where d is the skin depth and ρ_0 has to be chosen such that an integration over the Woods–Saxon distribution leads to the number of nucleons A .

Though it is possible to calculate this profile analytically, Monte Carlo simulation are often used to sample ρ_A as probability distribution for nucleons within a nucleus. The model distinguishes:

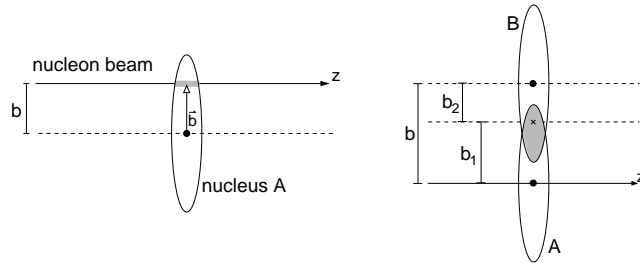


Figure B.1

Schematic representation of the Glauber Model geometry for a nucleon-nucleus collision (left panel) and for a nucleus-nucleus collision (right panel) [297].

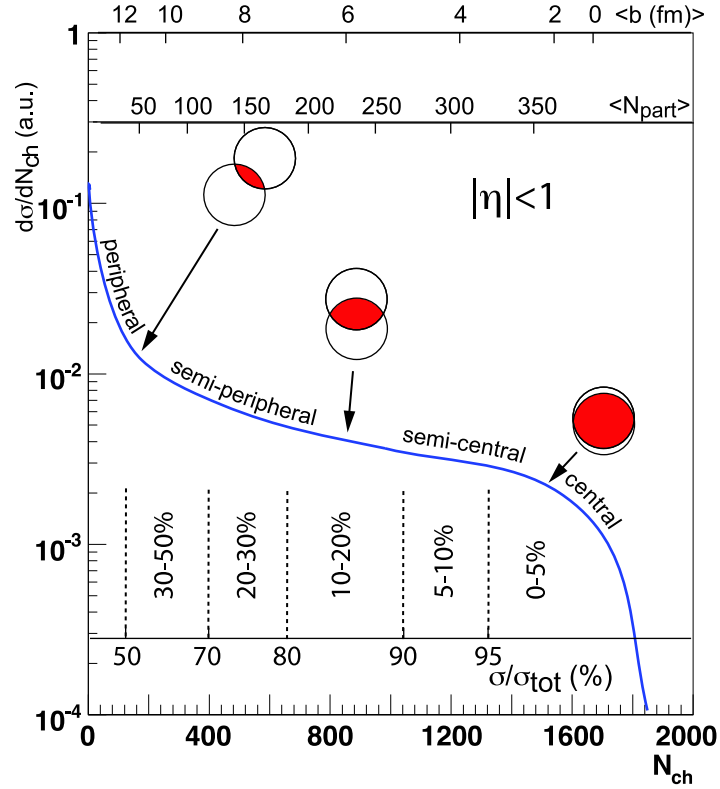


Figure B.2

The correlation between the number of participating nucleons in a heavy-ion collision, their cross section and the impact parameter b , defining the centrality classes [298].

- **Nucleon-nucleus collision:** The nuclear thickness function, describing that part of the nucleus A with which the nucleon passing through may interact (see Fig. B.1), is given by

$$T_A(x, y) = \int_{-\infty}^{+\infty} dz \rho_A(\vec{x}). \quad (\text{B.3})$$

The probability that two nucleons collide is $T_A(x, y, b)\sigma_{NN}$. From this, the number density of binary collisions in a nucleon-nucleus collision can be calculated using the probability of n binary collisions

$$P(n; A, b) = \binom{A}{n} [T_A(x + b, y)\sigma_{NN}]^n \times [1 - T_A(x + b, y)\sigma_{NN}]^{A-n} \quad (\text{B.4})$$

which leads to

$$n_{BC}(x, y, b) = \sum_{n=1}^A n P(n; A, b) = A T_A(x + b, y) \sigma_{NN}. \quad (\text{B.5})$$

- **Nucleus-nucleus collision:** In analogy to the nucleon-nucleus collision, a density distribution $T_{AB}(x, y, b)$ is defined, called nuclear overlap function,

$$T_{AB}(x, y, b) = \int dx dy T_A\left(x + \frac{b}{2}, y\right) T_B\left(x - \frac{b}{2}, y\right). \quad (\text{B.6})$$

Again, a binomial distribution

$$P(n; AB, b) = \binom{AB}{n} [T_{AB}(x, y, b)\sigma_{NN}]^n \times [1 - T_{AB}(x, y, b)\sigma_{NN}]^{AB-n} \quad (\text{B.7})$$

characterizes the probability for n binary collisions from which the mean number density of binary collisions is determined to be

$$n_{BC}(x, y, b) = AB T_{AB}(x, y, b)\sigma_{NN}. \quad (\text{B.8})$$

In a similar way, the number density of wounded (i.e. participating) nucleons can be derived:

$$n_{WN}(x, y, b) = T_A\left(x + \frac{b}{2}, y\right) \left[1 - \left(1 - \frac{\sigma_{NN} T_B\left(x - \frac{b}{2}, y\right)}{B}\right)^B\right] + T_B\left(x - \frac{b}{2}, y\right) \left[1 - \left(1 - \frac{\sigma_{NN} T_A\left(x + \frac{b}{2}, y\right)}{A}\right)^A\right]. \quad (\text{B.9})$$

The number of binary collisions N_{BC} and wounded nucleons N_{WN} is eventually obtained by integration

$$\begin{aligned} N_{BC}(b) &= \int dx dy n_{BC}(x, y), \\ N_{WN}(b) &= \int dx dy n_{WN}(x, y). \end{aligned} \quad (\text{B.10})$$

Appendix C

The EoS for an Ideal Gas

A gas of massless particles with a degeneracy factor g can be described using the grand-canonical partition function

$$Z^{\text{gr}}(T, V, \mu) = \sum_{N=0}^{\infty} \left[\left(e^{\beta\mu} \right)^N Z^{\text{can}}(T, V, N) \right] \quad (\text{C.1})$$

with $\beta = 1/T$ and the canonical partition function $Z^{\text{can}}(T, V, N)$. For non-interacting systems (for simplicity the Maxwell–Boltzmann limit is assumed, i.e., there will be no distinction between bosons and fermions), this expression simplifies since

$$Z^{\text{can}}(T, V, N) = \frac{1}{N!} [Z^{\text{can}}(T, V, 1)]^N. \quad (\text{C.2})$$

Thus, the grand-canonical partition function can be rewritten as

$$\begin{aligned} Z^{\text{gr}}(T, V, \mu) &= \sum_{N=0}^{\infty} \frac{1}{N!} \left[e^{\beta\mu} Z^{\text{can}}(T, V, 1) \right]^N \\ &= \exp \left[\exp(\beta\mu) Z^{\text{can}}(T, V, 1) \right]. \end{aligned} \quad (\text{C.3})$$

This expression can also be formulated in terms of the fugacity $z = e^{\beta\mu}$

$$Z^{\text{gr}}(T, V, z) = \exp \left[z Z^{\text{can}}(T, V, 1) \right]. \quad (\text{C.4})$$

$Z^{\text{can}}(T, V, 1)$ describes the canonical partition function for one particle given by

$$\begin{aligned} Z^{\text{can}}(T, V, 1) &= gV \int \frac{d^3k}{(2\pi)^3} e^{-\beta k} \\ &= g \frac{V}{\pi^2 \beta^3} = g \frac{VT^3}{\pi^2}, \end{aligned} \quad (\text{C.5})$$

which eventually leads for a gas with vanishing chemical potential $\mu = 0$ to a grand-canonical partition function of

$$Z^{\text{gr}}(T, V, z) = \exp \left(g \frac{VT^3}{\pi^2} \right). \quad (\text{C.6})$$

The particle density as well as the energy density can now be computed via

$$\begin{aligned} n &= \frac{\langle N \rangle}{V} = \frac{1}{V} \left[z \frac{\partial}{\partial z} \ln Z^{\text{gr}}(T, V, z) \right] \Big|_{z=1} = g \frac{T^3}{\pi^2}, \\ \varepsilon &= \frac{1}{V} \left[-\frac{\partial}{\partial \beta} \ln Z^{\text{gr}}(T, V, z=1) \right] = g \frac{3T^4}{\pi^2}. \end{aligned} \quad (\text{C.7})$$

Using the grand canonical potential $\Omega = -T \ln Z^{\text{gr}} = -pV$ and Eq. (C.6), the pressure is determined to be

$$p = g \frac{T^4}{\pi^2}, \quad (\text{C.8})$$

and a comparison of this expression with Eq. (C.7) yields the EoS for an ideal gas of massless, non-interacting particles

$$\varepsilon = \frac{1}{3}p. \quad (\text{C.9})$$

For a gas of massless bosons (like gluons), however, the energy density and pressure can be calculated in the Stefan–Boltzmann limit for $m/T \ll 1$ (see e.g. Ref. [299]) and are given by

$$\varepsilon = \frac{g}{30} \pi^2 T^4, \quad p = \frac{g}{90} \pi^2 T^4. \quad (\text{C.10})$$

Appendix D

A Microscopic Derivation of Relativistic Fluid Dynamics

It has been proven at RHIC that the medium created in a heavy-ion collision can be described as a “nearly perfect liquid” [15, 16], i.e., dissipative effects seem to be small, but nevertheless important for a quantitative description of the measured data.

The equations of relativistic fluid dynamics, in particular the transport equations for the bulk viscous pressure Π , the heat flux current q^μ , and the shear stress tensor $\pi^{\mu\nu}$, entering the energy-momentum tensor

$$T^{\mu\nu} = \varepsilon u^\mu u^\nu - (p + \Pi) \Delta^{\mu\nu} + q^\mu u^\nu + q^\nu u^\mu + \pi^{\mu\nu}, \quad (\text{D.1})$$

which is propagated (in time) using numerical applications, have been discussed vividly [122, 138, 139, 140, 141, 142, 143, 144, 145, 146, 147, 148].

This section discusses the derivation of the fluid-dynamical equations including dissipative effects up second order in gradients from kinetic theory, using the Boltzmann equation and Grad’s 14-momentum [152].

D.1 The Boltzmann Equation

The Boltzmann equation [109] applies for a sufficiently dilute gas,

$$k^\mu \partial_\mu f(k, x) = C[f]. \quad (\text{D.2})$$

Choosing the units to be $k_B = c = 1$ and $\hbar^3 = g/(2\pi)^3$ (with the degeneracy factor g), the two-particle collision term reads

$$\begin{aligned} C[f] = & \frac{1}{2} \int \frac{d^3 \vec{k}_1}{E_1} \frac{d^3 \vec{k}'}{E'} \frac{d^3 \vec{k}'_1}{E'_1} \sigma(s, \theta) s \delta^{(4)}(k + k_1 - k' - k'_1) \\ & \times \{ f(k', x) f(k'_1, x) [1 - af(k, x)] [1 - af(k_1, x)] \\ & - f(k, x) f(k_1, x) [1 - af(k', x)] [1 - af(k'_1, x)] \}, \end{aligned} \quad (\text{D.3})$$

where $a = \pm 1$ for fermions and bosons, respectively, and $a = 0$ for classical particles. The differential cross section of the two-particle collision, $\sigma(s, \theta)$, only depends on the Mandelstam variable $s = (k + k_1)^2$ and the scattering angle θ

in the center-of-mass system. The Boltzmann equation is a complicated integro-differential expression in phase space, which however can be solved by an expansion in terms of its *moments*. These moments are obtained by multiplying the Boltzmann equation with the factors $(1, k^\alpha, k^\alpha k^\beta, \dots)$ and subsequent integration over momentum, leading to different conservation equations (for details see Ref. [300]):

- **First moment:** The conservation of a 4-current N^μ

$$\partial_\mu N^\mu = 0. \quad (\text{D.4})$$

Integration of Eq. (D.2) over momentum space leads to

$$\int \frac{d^3 \vec{k}}{E} k^\mu \partial_\mu f(k, x) = \partial_\mu \int \frac{d^3 \vec{k}}{E} k^\mu f(k, x) = \int \frac{d^3 \vec{k}}{E} C[f]. \quad (\text{D.5})$$

The r.h.s. vanishes due to the δ -function in Eq. (D.3) and the (net) charge current is given by

$$N^\mu = \int \frac{d^3 \vec{k}}{E} k^\mu f(k, x). \quad (\text{D.6})$$

- **Second moment:** The conservation of the energy-momentum tensor

$$\partial_\mu T^{\mu\nu} = 0, \quad (\text{D.7})$$

which can be deduced from

$$\int \frac{d^3 \vec{k}}{E} k^\nu k^\mu \partial_\mu f(k, x) = \partial_\mu \int \frac{d^3 \vec{k}}{E} k^\nu k^\mu f(k, x) = \int \frac{d^3 \vec{k}}{E} k^\nu C[f], \quad (\text{D.8})$$

since the r.h.s. again vanishes due to the δ -function in Eq. (D.3) and the definition for the energy-momentum tensor is given by

$$T^{\mu\nu} = \int \frac{d^3 \vec{k}}{E} k^\mu k^\nu f(k, x). \quad (\text{D.9})$$

- **Third moment:** An Equation of Motion of

$$\partial_\mu S^{\mu\nu\lambda} = C^{\nu\lambda}, \quad (\text{D.10})$$

with

$$S^{\mu\nu\lambda} = \int \frac{d^3 \vec{k}}{E} k^\mu k^\nu k^\lambda f(k, x) \text{ and } C^{\nu\lambda} = \int \frac{d^3 \vec{k}}{E} k^\mu k^\lambda C[f]. \quad (\text{D.11})$$

D.2 Ideal Hydrodynamics from Kinetic Theory

It was already shown in section 3.1 that the tensor decomposition of the charge current N^μ and the energy-momentum tensor $T^{\mu\nu}$ can be derived by applying the expressions from kinetic theory. However, due to the fact that the local equilibrium distribution only depends on Lorentz scalars and the 4-velocity u^μ , the decomposition can also be done via

$$\begin{aligned} N_0^\mu(x) &= \int \frac{d^3\vec{k}}{E} k^\mu f_0(k, x) \equiv I_{10}(x) u^\mu(x), \\ T_0^{\mu\nu}(x) &= \int \frac{d^3\vec{k}}{E} k^\mu k^\nu f_0(k, x) \equiv I_{20}(x) u^\mu(x) u^\nu(x) + I_{21}(x) \Delta_{\mu\nu}(x) \end{aligned} \quad (\text{D.12})$$

The first index of the scalar $I_{nq}(x)$ characterizes the rank of the moment considered and the second one counts how often the projector onto the 3-dimensional subspace

$$\Delta^{\mu\nu}(x) = g^{\mu\nu} - u^\mu(x) u^\nu(x) \quad (\text{D.13})$$

appears in the expression. In particular, applying $u^\mu u_\mu = 1$, $k^\mu u_\mu = E$, $k^\mu k_\mu = m^2$, and $m^2 = E^2 - \vec{k}^2$, one can show that [300]

$$\begin{aligned} I_{10} &= N^\mu u_\mu = \int d^3\vec{k} f_0(k, x) \equiv n_0, \\ I_{20} &= T^{\mu\nu} u_\mu u_\nu = \int d^3\vec{k} E f_0(k, x) \equiv \varepsilon_0, \\ I_{21} &= \frac{1}{3} T^{\mu\nu} \Delta_{\mu\nu} = -\frac{1}{3} \int d^3\vec{k} \frac{\vec{k}^2}{E} f_0(k, x) \equiv -p_0. \end{aligned} \quad (\text{D.14})$$

This decomposition will be important for the following calculation of the dissipative effects.

D.3 Viscous Hydrodynamics from Kinetic Theory

We apply Grad's 14-moment method [152] for the derivation of the relativistic dissipative fluid-dynamical Equations of Motion which parametrizes the deviations of the one-particle distribution function from (local) thermodynamic equilibrium. While for (local) equilibrium this distribution function reads

$$f_0 = (e^{-y_0} + a)^{-1}, \quad (\text{D.15})$$

where a again characterizes the fermion/boson or Boltzmann statistics and

$$y_0 = \alpha_0 - \beta_0 k^\lambda u_\lambda, \quad (\text{D.16})$$

with $\alpha_0 \equiv \mu/T$ as well as $\beta_0 \equiv 1/T$, we assume that the following distribution function

$$f = (e^{-y} + a)^{-1}, \quad (\text{D.17})$$

$$y = \alpha - \beta k^\lambda u_\lambda - k^\lambda v_\lambda + k^\lambda k^\rho \omega_{\lambda\rho}, \quad (\text{D.18})$$

describing the most general ellipsoidal deformation of the equilibrium distribution, is applicable to describe the fluid-dynamical system. Here, v^λ is orthogonal to u^λ , thus $v^\lambda u_\lambda = 0$, and

$$\begin{aligned}\omega_{\lambda\rho} &= \omega u_\lambda u_\rho + \omega_\lambda u_\rho + \omega_\rho u_\lambda + \hat{\omega}_{\lambda\rho}, \\ \omega &\equiv \omega_{\lambda\rho} u^\lambda u^\rho, \\ \omega_\lambda &\equiv \Delta_{\lambda\alpha} \omega^{\alpha\rho} u_\rho, \\ \hat{\omega}_{\lambda\rho} &\equiv \Delta_{\lambda\alpha} \omega^{\alpha\beta} \Delta_{\beta\rho},\end{aligned}\tag{D.19}$$

leading to

$$\begin{aligned}\omega_\lambda u^\lambda &= 0, \\ \hat{\omega}_{\lambda\rho} u^\lambda &= 0, \\ \omega_\lambda^\lambda &= 0, \\ \omega &= -\hat{\omega}_\lambda^\lambda.\end{aligned}\tag{D.20}$$

Inserting these definitions into Eq. (D.18), one obtains

$$y = \alpha - \beta E + \vec{v} \cdot \vec{k} + \omega E^2 - 2 E \vec{\omega} \cdot \vec{k} + \sum_{i,j=x,y,z} k^i \hat{\omega}_{ij} k^j \tag{D.21}$$

in the local rest frame, $u^\mu = (1, \vec{0})$, where \vec{v} denotes the vector component of the 4-vector v^λ .

Hence, Eq. (D.17) is a function of 17 independent parameters (including the constraints for u_λ and $\omega_{\lambda\rho}$). To connect these quantities to the 14 independent parameters of the hydrodynamical equations¹, we assume a small deformation of the equilibrium distribution

$$y - y_0 = (\alpha - \alpha_0) - (\beta - \beta_0) k^\lambda u_\lambda - k^\lambda v_\lambda + k^\lambda k^\rho \omega_{\lambda\rho} \equiv O(\delta), \tag{D.22}$$

allowing for a linearization around equilibrium

$$\begin{aligned}f(y) &= f(y_0) + f'(y_0)(y - y_0) + O(\varepsilon^2) \\ &= f_0 + f_0(1 - a f_0)(y - y_0) + O(\varepsilon^2).\end{aligned}\tag{D.23}$$

Here, the fluid velocity u^λ of the system in (local) thermodynamical equilibrium is supposed to be the same as the velocity of the dissipative system.

Inserting these expressions into Eqs. (D.6) and (D.9), the (net) charge current and the energy-momentum tensor become

$$N^\mu = N_0^\mu + (\alpha - \alpha_0) J_0^\mu - (\beta - \beta_0) J_0^{\mu\lambda} u_\lambda - J_0^{\mu\lambda} v_\lambda + J_0^{\mu\lambda\rho} \omega_{\lambda\rho}, \tag{D.24}$$

$$T^{\mu\nu} = T_0^{\mu\nu} + (\alpha - \alpha_0) J_0^{\mu\nu} - (\beta - \beta_0) J_0^{\mu\nu\lambda} u_\lambda - J_0^{\mu\nu\lambda} v_\lambda + J_0^{\mu\nu\lambda\rho} \omega_{\lambda\rho}, \tag{D.25}$$

with the equilibrium distribution function for the (net) charge current N_0^μ and the energy-momentum tensor $T_0^{\mu\nu}$. The tensors

$$J_0^{\alpha_1 \dots \alpha_n} \equiv \int \frac{d^3 \vec{k}}{E} k^{\alpha_1} \dots k^{\alpha_n} f_0(1 - a f_0) \tag{D.26}$$

¹The 14 independent parameters are ε (1 Eq.), n (1 Eq.), Π (1 Eq.), V^μ (3 Eqs.), q^μ (3 Eqs.), and $\pi^{\mu\nu}$ (5 Eqs.), see also chapter 4.

can be decomposed into invariant subspaces according to

$$J_0^\mu = J_{10}u^\mu, \quad (D.27)$$

$$J_0^{\mu\lambda} = J_{20}u^\mu u^\lambda + J_{21}\Delta^{\mu\lambda}, \quad (D.28)$$

$$J_0^{\mu\lambda\rho} = J_{30}u^\mu u^\lambda u^\rho + 3J_{31}u^{(\mu}\Delta^{\lambda\rho)}, \quad (D.29)$$

$$J_0^{\mu\nu\lambda\rho} = J_{40}u^\mu u^\nu u^\lambda u^\rho + 6J_{41}u^{(\mu}u^\nu\Delta^{\lambda\rho)} + 3J_{42}\Delta^{\mu(\nu}\Delta^{\lambda\rho)}, \quad (D.30)$$

with the following abbreviations characterizing symmetry properties

$$3u^{(\mu}\Delta^{\lambda\rho)} = u^\mu\Delta^{\lambda\rho} + u^\lambda\Delta^{\rho\mu} + u^\rho\Delta^{\mu\lambda}, \quad (D.31)$$

$$6u^{(\mu}u^\nu\Delta^{\lambda\rho)} = u^\mu u^\nu\Delta^{\lambda\rho} + u^\nu u^\lambda\Delta^{\rho\mu} + u^\lambda u^\rho\Delta^{\mu\nu} \\ + u^\mu u^\lambda\Delta^{\nu\rho} + u^\mu u^\rho\Delta^{\nu\lambda} + u^\nu u^\rho\Delta^{\mu\lambda}. \quad (D.32)$$

These expressions are a generalization of

$$2u^{(\mu}u^{\nu)} \equiv u^\mu u^\nu + u^\nu u^\mu. \quad (D.33)$$

The functions J_{nq} again denote the projections onto the corresponding subspaces (see section D.2). They only depend on the fluid velocity u^λ and equilibrium quantities T and μ .

Applying the above tensor decompositions together with the expressions for N_0^μ , $T_0^{\mu\nu}$, and $\omega_{\lambda\rho}$, it follows that the (net) charge current N^μ and the energy-momentum tensor $T^{\mu\nu}$ [Eqs. (D.24) and (D.25)] are given by

$$N^\mu = [n_0 + (\alpha - \alpha_0)J_{10} - (\beta - \beta_0)J_{20} + \omega(J_{30} - J_{31})]u^\mu \\ - J_{21}v^\mu + 2J_{31}\omega^\mu, \quad (D.34)$$

$$T^{\mu\nu} = [\varepsilon_0 + (\alpha - \alpha_0)J_{20} - (\beta - \beta_0)J_{30} + \omega(J_{40} - J_{41})]u^\mu u^\nu \\ + [-p_0 + (\alpha - \alpha_0)J_{21} - (\beta - \beta_0)J_{31} + \omega(J_{41} - J_{42})]\Delta^{\mu\nu} \\ - 2\left(J_{31}v^{(\mu} - 2J_{41}\omega^{(\mu)}\right)u^{\nu)} + 2J_{42}\hat{\omega}^{\mu\nu}. \quad (D.35)$$

These equations contain 19 unknown quantities, the 17 originating from the above parametrization of the distribution function as well as α_0 and β_0 . The latter ones are normally determined by assuming that the charge density n and the energy density ε characterize a system in thermodynamic equilibrium,

$$\varepsilon = T^{\mu\nu}u_\mu u_\nu \equiv \varepsilon_0 \quad (D.36)$$

$$n = N^\mu u_\mu \equiv n_0. \quad (D.37)$$

Then, the extra terms in the first lines of Eqs. (D.34) and (D.35) have to vanish, leading via

$$(\alpha - \alpha_0)J_{10} - (\beta - \beta_0)J_{20} + \omega(J_{30} - J_{31}) = 0, \quad (D.38)$$

$$(\alpha - \alpha_0)J_{20} - (\beta - \beta_0)J_{30} + \omega(J_{40} - J_{41}) = 0, \quad (D.39)$$

to the expressions for $(\alpha - \alpha_0)$ and $(\beta - \beta_0)$,

$$\alpha - \alpha_0 = -\omega \left[m^2 - 4 \frac{J_{30}J_{31} - J_{20}J_{41}}{J_{30}J_{10} - (J_{20})^2} \right], \quad (D.40)$$

$$\beta - \beta_0 = -4\omega \frac{J_{10}J_{41} - J_{20}J_{31}}{J_{30}J_{10} - (J_{20})^2}. \quad (D.41)$$

Here, the relation [300]

$$J_{n+2,q} = m^2 J_{nq} - (2q + 3)J_{n+2,q+1} \quad (\text{D.42})$$

needs to be applied. In order to proceed, one has to determine the fluid velocity which we will first consider in the Eckart frame.

D.3.1 Transport Equations in the Eckart Frame

In the Eckart system, u^μ defines the velocity of charge transport. Thus, the (net) charge density n is equivalent to the one in thermodynamic equilibrium, $n = n_0$, resulting in

$$N^\mu = nu^\mu \quad (\text{D.43})$$

and [cf. Eq. (D.34)] a condition for v^μ

$$v^\mu = 2 \frac{J_{31}}{J_{21}} \omega^\mu, \quad (\text{D.44})$$

defining three of the 17 free parameters. The remaining 14 quantities, that are determined below, can be connected to the unknowns of the hydrodynamic equations. Inserting $(\alpha - \alpha_0)$ [Eq. (D.40)], $(\beta - \beta_0)$ [Eq. (D.41)], and v^μ [Eq. (D.44)] into the energy-momentum tensor $T^{\mu\nu}$ [Eq. (D.35)], the dissipative quantities can be defined as

$$\Pi = 4\omega \left[J_{21} \frac{J_{20}J_{41} - J_{30}J_{31}}{J_{30}J_{10} - (J_{20})^2} + J_{31} \frac{J_{20}J_{31} - J_{10}J_{41}}{J_{30}J_{10} - (J_{20})^2} + \frac{5}{3}J_{42} \right], \quad (\text{D.45})$$

$$q^\mu = 2 \frac{J_{41}J_{21} - (J_{31})^2}{J_{21}} \omega^\mu, \quad (\text{D.46})$$

$$\pi^{\mu\nu} = 2J_{42}\tilde{\omega}^{\mu\nu}, \quad (\text{D.47})$$

having in mind that

$$T^{\mu\nu} = \varepsilon u^\mu u^\nu - p \Delta^{\mu\nu} + 2q^{(\mu} u^{\nu)} + \pi^{\mu\nu}, \quad (\text{D.48})$$

$$p \equiv -\frac{1}{3}T^{\mu\nu}\Delta_{\mu\nu} \equiv p_0 + \Pi, \quad (\text{D.49})$$

$$q^\mu \equiv \Delta^{\mu\alpha}T_{\alpha\beta}u^\beta, \quad (\text{D.50})$$

$$\pi^{\mu\nu} \equiv T^{\langle\mu\nu\rangle} \equiv \left(\Delta_\alpha^{(\mu} \Delta^{\nu)}_\beta - \frac{1}{3}\Delta_{\alpha\beta}\Delta^{\mu\nu} \right) T^{\alpha\beta}, \quad (\text{D.51})$$

and using the relations

$$\tilde{\omega}^{\mu\nu} = \hat{\omega}^{\mu\nu} + \frac{\omega}{3}\Delta^{\mu\nu}, \quad (\text{D.52})$$

$$\tilde{\omega}^{\lambda\rho} = \hat{\omega}^{\langle\lambda\rho\rangle}. \quad (\text{D.53})$$

Consequently, there is a direct connection between the nine free parameters of ω , ω^λ , and $\tilde{\omega}^{\lambda\rho}$ as well as the hydrodynamic variables Π , q^μ , and $\pi^{\mu\nu}$ which are defined by nine equations. α , β , and u^λ have already been determined via the charge density, the energy density, and the fluid velocity.

Therefore, one has to derive nine additional equations for those undefined parameters. This is done by calculating the second moment of the Boltzmann equation that can be written in terms of

$$\begin{aligned} S^{\mu\nu\lambda} &= S_0^{\mu\nu\lambda} + (\alpha - \alpha_0)J_0^{\mu\nu\lambda} - (\beta - \beta_0)J_0^{\mu\nu\lambda\rho}u_\rho \\ &\quad - J_0^{\mu\nu\lambda\rho}v_\rho + J_0^{\mu\nu\lambda\alpha\beta}\omega_{\alpha\beta}, \end{aligned} \quad (\text{D.54})$$

applying the linearization of Eq. (D.23), where $J_0^{\mu\nu\lambda\alpha\beta}$ denotes the decomposition

$$\begin{aligned} J_0^{\mu\nu\lambda\alpha\beta} &= J_{50}u^\mu u^\nu u^\lambda u^\alpha u^\beta + 10J_{51}u^{(\mu}u^\nu u^\lambda \Delta^{\alpha\beta)} \\ &\quad + 15J_{52}u^{(\mu}\Delta^{\nu\lambda}\Delta^{\alpha\beta)}. \end{aligned} \quad (\text{D.55})$$

Using again the expressions for $(\alpha - \alpha_0)$ [Eq. (D.40)], $(\beta - \beta_0)$ [Eq. (D.41)], Eqs. (D.45) – (D.47) as well as the relation

$$S_0^{\mu\nu\lambda} = I_{30}u^\mu u^\nu u^\lambda + 3I_{31}u^{(\mu}\Delta^{\nu\lambda)}, \quad (\text{D.56})$$

one obtains

$$\begin{aligned} S^{\mu\nu\lambda} &= S_1u^\mu u^\nu u^\lambda + 3S_2u^{(\mu}\Delta^{\nu\lambda)} + 3\psi_1q^{(\mu}\left[u^{\nu}u^{\lambda)} - \frac{1}{5}\Delta^{\nu\lambda)}\right] \\ &\quad + 3\psi_2\pi^{(\mu\nu}u^{\lambda)}, \end{aligned} \quad (\text{D.57})$$

$$S_1 = I_{30} + \phi_1\Pi, \quad (\text{D.58})$$

$$S_2 = I_{31} + \phi_2\Pi, \quad (\text{D.59})$$

$$\begin{aligned} \phi_1 &= \frac{J_{30}(J_{30}J_{31} - J_{20}J_{41}) + J_{40}(J_{10}J_{41} - J_{20}J_{31}) - J_{51}(J_{30}J_{10} - (J_{20})^2)}{J_{21}(J_{20}J_{41} - J_{30}J_{31}) + J_{31}(J_{20}J_{31} - J_{10}J_{41}) + \frac{5}{3}J_{42}(J_{30}J_{10} - (J_{20})^2)}, \end{aligned} \quad (\text{D.60})$$

$$\phi_2 = -\frac{\phi_1}{3}, \quad (\text{D.61})$$

$$\psi_1 = \frac{J_{21}J_{51} - J_{31}J_{41}}{J_{41}J_{21} - (J_{31})^2}, \quad (\text{D.62})$$

$$\psi_2 = \frac{J_{52}}{J_{42}}. \quad (\text{D.63})$$

Now, the nine requested equations can be derived by evaluating $\partial_\mu S^{\mu\nu\lambda}$

$$\begin{aligned} \partial_\mu S^{\mu\nu\lambda} &= u^\nu u^\lambda \left[\left(\dot{S}_1 - 2\dot{S}_2 \right) + (S_1 - 2S_2)\theta + \partial_\mu (\psi_1 q^\mu) \right] \\ &\quad + \Delta^{\nu\lambda} \left[\dot{S}_2 + S_2\theta - \frac{1}{5}\partial_\mu (\psi_1 q^\mu) \right] \\ &\quad + 2(S_1 - 3S_2)\dot{u}^{(\nu}u^{\lambda)} + 2u^{(\nu}\partial^{\lambda)}S_2 + 2S_2\partial^{(\nu}u^{\lambda)} \\ &\quad + \frac{6}{5}\psi_1 q^\mu \partial_\mu (u^\nu u^\lambda) \\ &\quad + \frac{12}{5} \left\{ q^{(\nu}u^{\lambda)} \left[\dot{\psi}_1 + \psi_1\theta \right] + \psi_1 \left[\dot{u}^{(\lambda}q^{\nu)} + u^{(\lambda}\dot{q}^{\nu)} \right] \right\} \\ &\quad - \frac{2}{5} \left[q^{(\nu}\partial^{\lambda)}\psi_1 + \psi_1\partial^{(\lambda}q^{\nu)} \right] + \dot{\psi}_2\pi^{\nu\lambda} + \psi_2 \left(\dot{\pi}^{\nu\lambda} + \pi^{\nu\lambda}\theta \right) \\ &\quad + 2\pi^{\mu(\nu}u^{\lambda)}\partial_\mu\psi_2 + 2\psi_2\pi^{\mu(\nu}\partial_\mu u^{\lambda)} + 2\psi_2u^{(\nu}\partial_\mu\pi^{\lambda)\mu} \\ &\equiv C^{\nu\lambda}, \end{aligned} \quad (\text{D.64})$$

with $\dot{S} = u^\mu \partial_\mu S$ and $\theta = \partial_\mu u^\mu$. In principle, these are 10 equations, but the trace

$$\partial_\mu S^{\mu\nu} = m^2 \partial_\mu N^\mu = C^\nu = m^2 \int \frac{d^3 \vec{k}}{E} C[f] = 0 \quad (\text{D.65})$$

leads to the equation of charge conservation.

Projecting $\partial_\mu S^{\mu\nu\lambda}$ onto the invariant subspaces results in the following Equations of Motions:

$$\begin{aligned} C^{\nu\lambda} u_\nu u_\lambda &= \dot{I}_{30} + \phi_1 \dot{\Pi} + \dot{\phi}_1 \Pi + \left(I_{30} - 2I_{31} + \frac{5}{3} \phi_1 \Pi \right) \theta \\ &\quad + \partial_\mu (\psi_1 q^\mu) - 2\psi_1 q_\mu \dot{u}^\mu - 2\psi_2 \pi^{\lambda\mu} \partial_\mu u_\lambda, \end{aligned} \quad (\text{D.66})$$

$$\begin{aligned} u_\nu \Delta^\mu_\lambda C^{\nu\lambda} &= \left(I_{30} - 2I_{31} + \frac{5}{3} \phi_1 \Pi \right) \dot{u}^\mu + q^\mu \left(\dot{\psi}_1 + \frac{6}{5} \psi_1 \theta \right) \\ &\quad + \Delta^\mu_\lambda \left[\partial^\lambda (I_{31} + \phi_2 \Pi) + \frac{1}{5} \psi_1 q^\nu \partial^\lambda u_\nu + \psi \dot{q}^\lambda + \psi_2 \partial_\nu \pi^{\lambda\nu} \right] \\ &\quad + \frac{6}{5} \psi_1 q^\nu \partial_\nu u^\mu + (-\psi_2 \dot{u}_\nu + \partial_\nu \psi_2) \pi^{\mu\nu}, \end{aligned} \quad (\text{D.67})$$

$$\begin{aligned} C^{\langle\nu\lambda\rangle} &= 2(I_{31} + \phi_2 \Pi) \partial^{\langle\nu} u^{\lambda\rangle} + \frac{12}{5} \psi_1 \dot{u}^{\langle\nu} q^{\lambda\rangle} \\ &\quad - \frac{2}{5} \left(q^{\langle\nu} \partial^{\lambda\rangle} \psi_1 + \psi_1 \partial^{\langle\lambda} q^{\nu\rangle} \right) + \dot{\psi}_2 \pi^{\nu\lambda} \\ &\quad + \psi_2 \left(\dot{\pi}^{\langle\nu\lambda\rangle} + \pi^{\nu\lambda} \theta \right) + 2\psi_2 \pi^{\mu\langle\nu} \partial_\mu u^{\lambda\rangle}. \end{aligned} \quad (\text{D.68})$$

For the evaluation of the l.h.s., the collision term $C^{\nu\lambda}$ has to be linearized

$$\begin{aligned} C^{\nu\lambda} &= \frac{1}{2} \int \frac{d^3 \vec{k}}{E} \int \frac{d^3 \vec{k}_1}{E_1} \int \frac{d^3 \vec{k}'}{E'} \int \frac{d^3 \vec{k}'_1}{E'_1} \sigma(s, \theta) s \\ &\quad \times \delta^{(4)}(k + k_1 - k' - k'_1) k^\nu k^\lambda \\ &\quad \times \{ f'(k, x) f'_1(k, x) [1 - af(k, x)] [1 - af_1(k, x)] \\ &\quad - f(k, x) f_1(k, x) [1 - af'(k, x)] [1 - af'_1(k, x)] \} \\ &\equiv \omega_{\alpha\beta} C^{\nu\lambda\alpha\beta} + O(\varepsilon^2). \end{aligned} \quad (\text{D.69})$$

The most general decomposition of $C^{\nu\lambda\alpha\beta}$ is given by

$$\begin{aligned} C^{\nu\lambda\alpha\beta} &= \frac{A}{3} \left(3u^\nu u^\lambda u^\alpha u^\beta - u^\nu u^\lambda \Delta^{\alpha\beta} - u^\alpha u^\beta \Delta^{\nu\lambda} + \frac{1}{3} \Delta^{\nu\lambda} \Delta^{\alpha\beta} \right) \\ &\quad + \frac{B}{5} \Delta^{\alpha\langle\lambda} \Delta^{\nu\rangle\beta} + 4C u^{(\nu} \Delta^{\lambda)(\alpha} u^{\beta)}, \end{aligned} \quad (\text{D.70})$$

allowing for the calculation of $C^{\nu\lambda}$

$$\begin{aligned} C^{\nu\lambda} &= \omega_{\alpha\beta} C^{\nu\lambda\alpha\beta} \\ &= \frac{4}{3} A \omega \left(u^\nu u^\lambda - \frac{1}{3} \Delta^{\nu\lambda} \right) + \frac{B}{5} \tilde{\omega}^{\nu\lambda} + 4C u^{(\nu} \omega^{\lambda)}. \end{aligned} \quad (\text{D.71})$$

Thus, the left-hand sides give

$$u_\nu u_\lambda C^{\nu\lambda} = \frac{4}{3} A \omega \equiv A' \Pi, \quad (\text{D.72})$$

$$u_\nu \Delta^\mu_\lambda C^{\nu\lambda} = 2C \omega^\mu \equiv C' q^\mu, \quad (\text{D.73})$$

$$C^{\langle\nu\lambda\rangle} = \frac{B}{5} \tilde{\omega}^{\nu\lambda} \equiv B' \pi^{\nu\lambda}, \quad (\text{D.74})$$

resulting in

$$A' = \frac{A}{3} [J_{31}J_{10} - (J_{20})^2] \times \quad (\text{D.75})$$

$$\left\{ J_{21}(J_{20}J_{41} - J_{30}J_{31}) + J_{31}(J_{20}J_{31} - J_{10}J_{41}) + \frac{5}{3}J_{42}[J_{30}J_{10} - (J_{20})^2] \right\}^{-1},$$

$$C' = C \frac{J_{21}}{J_{41}J_{21} - (J_{31})^2}, \quad (\text{D.76})$$

$$B' = \frac{B}{10J_{42}}. \quad (\text{D.77})$$

Therefore, the *Equations of Motions for the dissipative variables* Π , q^μ , and $\pi^{\mu\nu}$ are

$$A'\Pi = \dot{I}_{30} + \phi_1\dot{\Pi} + \dot{\phi}_1\Pi + \left(I_{30} - 2I_{31} + \frac{5}{3}\phi_1\Pi \right) \theta + \partial_\mu (\psi_1 q^\mu) - 2\psi_1 q_\mu \dot{u}^\mu - 2\psi_2 \pi^{\lambda\mu} \partial_\mu u_\lambda, \quad (\text{D.78})$$

$$C'q^\mu = \left(I_{30} - 2I_{31} + \frac{5}{3}\phi_1\Pi \right) \dot{u}^\mu + q^\mu \left(\dot{\psi}_1 + \frac{6}{5}\psi_1\theta \right) + \Delta_\lambda^\mu \left[\partial^\lambda (I_{31} + \phi_2\Pi) + \frac{1}{5}\psi_1 q^\nu \partial^\lambda u_\nu + \psi_1 \dot{q}^\lambda + \psi_2 \partial_\nu \pi^{\lambda\nu} \right] + \frac{6}{5}\psi_1 q^\nu \partial_\nu u^\mu + (-\psi_2 \dot{u}_\nu + \partial_\nu \psi_2) \pi^{\mu\nu}, \quad (\text{D.79})$$

$$B'\pi^{\mu\nu} = 2(I_{31} + \phi_2\Pi) \partial^{\langle\mu} u^{\nu\rangle} + \frac{12}{5}\psi_1 \dot{u}^{\langle\mu} q^{\nu\rangle} - \frac{2}{5} \left(q^{\langle\mu} \partial^{\nu\rangle} \psi_1 + \psi_1 \partial^{\langle\mu} q^{\nu\rangle} \right) + \dot{\psi}_2 \pi^{\mu\nu} + \psi_2 \left(\dot{\pi}^{\langle\mu\nu\rangle} + \pi^{\mu\nu} \theta \right) + 2\psi_2 \pi_\lambda^{\langle\mu} \partial^{\lambda} u^{\nu\rangle}. \quad (\text{D.80})$$

To rewrite these equations into a more common form containing the relaxation times $(\tau_\Pi, \tau_q, \tau_\pi)$, the coupling lengths coefficients $(l_{\Pi q}, l_{\pi q}, l_{\Pi\pi}, \dots)$ as well as the thermodynamic quantities bulk viscosity ζ , thermal conductivity κ , and shear viscosity η , several mathematical operations are necessary.

A crucial step is to rewrite the scalar functions $I_{nq}(x)$. Following Israel and Stewart [150], their derivatives are connected to the J_{nq} via

$$dI_{nk} = J_{nk}d\alpha - J_{n+1,k}d\beta. \quad (\text{D.81})$$

The expressions for $d\alpha$ and $d\beta$ can be determined using the equations for the (net) charge as well as energy and momentum conservation, Eqs. (4.21) to (4.23), since [150]

$$dn = J_{10}d\alpha - J_{20}d\beta, \quad (\text{D.82})$$

$$d\varepsilon = J_{20}d\alpha - J_{30}d\beta. \quad (\text{D.83})$$

Applying the definition [150]

$$D_{nq} = J_{n+1,q}J_{n-1,q} - (J_{nq})^2 \quad (\text{D.84})$$

it follows that

$$d\beta = \frac{1}{D_{20}} (J_{20}dn - J_{10}d\varepsilon), \quad (\text{D.85})$$

$$d\alpha = \frac{1}{D_{20}} (J_{30}dn - J_{20}d\varepsilon). \quad (\text{D.86})$$

Making use of the relations

$$\pi_\lambda^{\langle\mu} \partial^\lambda u^{\nu\rangle} = -2\pi_\lambda^{\langle\mu} \omega^{\nu\rangle\lambda} + \pi_\lambda^{\langle\mu} \sigma^{\nu\rangle\lambda}, \quad (\text{D.87})$$

$$\sigma^{\mu\nu} = \nabla^{\langle\mu} u^{\nu\rangle}, \quad (\text{D.88})$$

the equation for the vorticity,

$$\omega^{\mu\nu} = \frac{1}{2} \Delta^{\mu\alpha} \Delta^{\nu\beta} (\partial_\alpha u_\beta - \partial_\beta u_\alpha), \quad (\text{D.89})$$

and the fact that the relaxation times as well as coupling lengths are connected to the bulk viscosity ζ , the thermal conductivity κ , and the shear viscosity η [154], the **transport equations for the bulk viscous pressure Π , for the heat flux current q^μ , and the shear stress tensor $\pi^{\mu\nu}$** are given by

$$\begin{aligned} \Pi = & -\zeta\theta - \tau_\Pi \dot{\Pi} + \tau_{\Pi q} q_\mu \dot{u}^\mu - l_{\Pi q} \nabla_\mu q^\mu - \zeta \hat{\delta}_0 \Pi \theta \\ & + \lambda_{\Pi q} q^\mu \nabla_\mu \alpha + \lambda_{\Pi\pi} \pi_{\mu\nu} \sigma^{\mu\nu}, \end{aligned} \quad (\text{D.90})$$

$$\begin{aligned} q^\mu = & \frac{\kappa}{\beta} \frac{n}{\beta(\varepsilon + p)} \nabla^\mu \alpha - \tau_q \Delta^{\mu\nu} \dot{q}_\nu \\ & - \tau_{q\Pi} \Pi \dot{u}^\mu - \tau_{q\pi} \pi^{\mu\nu} \dot{u}_\nu + l_{q\Pi} \nabla^\mu \Pi - l_{q\pi} \Delta^{\mu\nu} \partial^\lambda \pi_{\nu\lambda} + \tau_q \omega^{\mu\nu} q_\nu \\ & - \frac{\kappa}{\beta} \hat{\delta}_1 q^\mu \theta - \lambda_{qq} \sigma^{\mu\nu} q_\nu + \lambda_{q\Pi} \Pi \nabla^\mu \alpha + \lambda_{q\pi} \pi^{\mu\nu} \nabla_\nu \alpha, \end{aligned} \quad (\text{D.91})$$

$$\begin{aligned} \pi^{\mu\nu} = & 2\eta \sigma^{\mu\nu} - \tau_\pi \dot{\pi}^{\langle\mu\nu\rangle} \\ & + 2\tau_{\pi q} q^{\langle\mu} \dot{u}^{\nu\rangle} + 2l_{\pi q} \nabla^{\langle\mu} q^{\nu\rangle} + 4\tau_\pi \pi_\lambda^{\langle\mu} \omega^{\nu\rangle\lambda} - 2\eta \hat{\delta}_2 \theta \pi^{\mu\nu} \\ & - 2\tau_\pi \pi_\lambda^{\langle\mu} \sigma^{\nu\rangle\lambda} - 2\lambda_{\pi q} q^{\langle\mu} \nabla^{\nu\rangle} \alpha + 2\lambda_{\pi\Pi} \Pi \sigma^{\mu\nu}. \end{aligned} \quad (\text{D.92})$$

The transport coefficients ζ, κ, η , the relaxation times $\tau_\Pi, \tau_q, \tau_\pi$, and the coefficients $\tau_{\Pi q}, \tau_{q\Pi}, \tau_{q\pi}, \tau_{\pi q}, \ell_{\Pi q}, \ell_{q\Pi}, \ell_{q\pi}, \ell_{\pi q}, \lambda_{\Pi q}, \lambda_{\Pi\pi}, \lambda_{qq}, \lambda_{q\Pi}, \lambda_{q\pi}, \lambda_{\pi q}, \lambda_{\pi\Pi}, \hat{\delta}_0, \hat{\delta}_1, \hat{\delta}_2$ are (complicated) functions of α, β and will be presented in detail in Ref. [156].

It can indeed be shown that using [see Eq. (4.34)]

$$\frac{\ell_{\text{mfp}}}{\lambda_{\text{th}}} \sim \ell_{\text{mfp}} \partial_\mu \sim \delta \ll 1, \quad (\text{D.93})$$

and [cf. Eq. (4.36)]

$$\frac{\Pi}{\varepsilon} \sim \frac{q^\mu}{\varepsilon} \sim \frac{\pi^{\mu\nu}}{\varepsilon} \sim K \sim \delta \ll 1, \quad (\text{D.94})$$

where the Knudsen number K is defined via Eq. (4.35), all terms in the above equations are at most of order δ^2 . Therefore, the set of equations (D.90) to (D.92) is of **second order in the Knudsen number**.

D.3.2 The Tsumura-Kunihiro-Ohnishi Matching Condition

The above mentioned transport equations for the bulk viscous pressure Π , the heat flux current q^μ , and the shear stress tensor $\pi^{\mu\nu}$ were derived by assuming [see Eqs. (D.36) and (D.37)] that the actual charge density n and the energy density ε are equivalent to the respective quantities in (local) thermodynamic equilibrium. However, Tsumura, Kunihiro, and Ohnishi [301] proposed that

$$\varepsilon = T^{\mu\nu} u_\mu u_\nu + 3\Pi, \quad (\text{D.95})$$

leading to a matching condition of

$$\varepsilon = \varepsilon_0 - 3\Pi. \quad (\text{D.96})$$

In that case, $(\alpha - \alpha_0)$ and $(\beta - \beta_0)$ are not given by Eqs. (D.40) and (D.41), but can be calculated to be

$$\alpha - \alpha_0 = -\omega \left[m^2 - 4 \frac{J_{30}J_{31} - J_{20}J_{41}}{J_{30}J_{10} - (J_{20})^2} \right] + \frac{J_{20}}{J_{30}J_{10} - (J_{20})^2} 3\Pi, \quad (\text{D.97})$$

$$\beta - \beta_0 = -4\omega \frac{J_{10}J_{41} - J_{20}J_{31}}{J_{30}J_{10} - (J_{20})^2} + \frac{J_{10}}{J_{30}J_{10} - (J_{20})^2} 3\Pi, \quad (\text{D.98})$$

resulting in a bulk viscous pressure of

$$\Pi = 4\omega \left\{ \frac{J_{21}(J_{20}J_{41} - J_{30}J_{31}) + J_{31}(J_{20}J_{31} - J_{10}J_{41}) + \frac{5}{3}J_{42}[J_{30}J_{10} - (J_{20})^2]}{J_{10}J_{30} - (J_{20})^2 + 3J_{20}J_{21} - 3J_{10}J_{31}} \right\} \quad (\text{D.99})$$

However, Eqs. (D.46) and (D.47) for the heat flux current q^μ and shear stress tensor $\pi^{\mu\nu}$ still apply. Nevertheless, as one can easily prove, the second moment of the Boltzmann equation, Eq. (D.57), as well as all those ones derived from this expression, in particular the transport equations Eqs. (D.90) – (D.92), are still valid using the above definition for the bulk viscous pressure Π . Of course, ϕ_1 [see Eq. (D.60)] and A' [see Eq. (D.75)] have to be adjusted accordingly.

D.3.3 Transport Equations in the Landau Frame

So far, we considered u^λ as the charge flow velocity, i.e., we worked in the Eckart frame. Choosing u^λ to be the energy flow velocity, the heat flux current vanishes ($q^\mu = 0$ since the spectator moves with the energy flow), while the (net) charge flow will be $V^\mu \neq 0$. Therefore the conservation equations change to

$$N^\mu = nu^\mu + V^\mu \quad (\text{D.100})$$

$$T^{\mu\nu} = \varepsilon u^\mu u^\nu - (p + \Pi)\Delta^{\mu\nu} + \pi^{\mu\nu}. \quad (\text{D.101})$$

Thus, it follows from Eq. (D.35) that

$$0 = q^\mu = J_{31}v^\mu - 2J_{41}\omega^\mu, \quad (\text{D.102})$$

leading to a different condition for v^μ

$$v^\mu = \frac{2J_{41}}{J_{31}}\omega^\mu. \quad (\text{D.103})$$

Using the same procedure as explained above, one obtains the transport equations for the bulk viscous pressure Π , the heat flux current q^μ , and the shear stress tensor $\pi^{\mu\nu}$ the form of which is the same as in Eqs. (D.90) – (D.92) with $q^\mu \rightarrow -V^\mu(\varepsilon + p)/n$.

However, the values of the dissipative quantities are frame-dependent and will be given in Ref. [156].

D.3.4 The Israel–Stewart Equations

It is possible to show that the expressions

$$A'\Pi = \dot{I}_{30} + \phi_1 \dot{\Pi} + (I_{30} - 2I_{31})\theta + \psi_1 \partial_\mu q^\mu, \quad (\text{D.104})$$

$$C'q^\mu = (I_{30} - 2I_{31})\dot{u}^\mu + \Delta_\lambda^\mu \left[\partial^\lambda I_{31} + \psi_1 \dot{q}^\lambda + \phi_2 \partial^\lambda \Pi + \psi_2 \partial_\nu \pi^{\lambda\nu} \right], \quad (\text{D.105})$$

$$B'\pi^{\mu\nu} = 2I_{31}\partial^{\langle\mu} u^{\nu\rangle} - \frac{2}{5}\psi_1 \partial^{\langle\mu} q^{\nu\rangle} + \psi_2 \dot{\pi}^{\mu\nu}, \quad (\text{D.106})$$

[cf. Eqs. (D.78) – (D.80)], which contain terms partially of first and second order in the Knudsen number, are equivalent to the equations derived by Israel and Stewart [Eq. (2.41) of [150]]

$$\Pi = -\frac{1}{3}\zeta_V \left(\partial_\mu u^\mu + \beta_0 \dot{\Pi} - \bar{\alpha}_0 \partial_\mu q^\mu \right) \quad (\text{D.107})$$

$$q^\lambda = -\kappa T \Delta^{\lambda\mu} \left(T^{-1} \partial_\mu T - \dot{u}_\mu + \bar{\beta}_1 \dot{q}_\mu - \bar{\alpha}_0 \partial_\mu \Pi - \bar{\alpha}_1 \partial_\nu \pi_\mu^\nu \right) \quad (\text{D.108})$$

$$\pi^{\mu\nu} = -2\zeta_S \left(\partial^{\langle\mu} u^{\nu\rangle} + \beta_2 \dot{\pi}_{\lambda\mu} - \bar{\alpha}_1 \partial^{\langle\mu} q^{\nu\rangle} \right), \quad (\text{D.109})$$

which however, differ in metric. To prove this, one has to use the conservation equations for (net) charge density, energy and momentum, as well the relation (D.42) and the definitions

$$\bar{\alpha}_0 - \alpha_0 = \bar{\alpha}_1 - \alpha_1 = -(\bar{\beta}_1 - \beta_1) = -[\beta J_{31}]^{-1}, \quad (\text{D.110})$$

$$\alpha_0 = \frac{D_{41} D_{20} - D_{31} D_{30}}{\Lambda \zeta \Omega J_{21} J_{31} D_{20}}, \quad (\text{D.111})$$

$$\alpha_1 = \frac{J_{41} J_{42} - J_{31} J_{52}}{\Lambda \zeta J_{21} J_{31}}, \quad (\text{D.112})$$

$$\beta_0 = \frac{3\beta \{ 5J_{52} - (3/D_{20}) [J_{31} (J_{31} J_{30} - J_{41} J_{20}) + J_{41} (J_{41} J_{10} - J_{31} J_{20})] \}}{\zeta^2 \Omega^2}, \quad (\text{D.113})$$

$$\beta_1 = \frac{D_{41}}{\Lambda^2 \beta J_{21}^2 J_{31}}, \quad (\text{D.114})$$

$$\beta_2 = \frac{1}{2} \beta \frac{J_{52}}{\zeta^2}, \quad (\text{D.115})$$

$$\zeta_V = 3 \frac{(\zeta \Omega)^2}{\beta A}, \quad \zeta_S = 10 \frac{\zeta^2}{\beta B}, \quad \kappa = \frac{(\Lambda \beta J_{21})^2}{C}, \quad (\text{D.116})$$

$$\zeta = \beta J_{42} = I_{31}, \quad I_{10} = \beta J_{21}, \quad \Lambda = \frac{D_{31}}{(J_{21})^2}, \quad (\text{D.117})$$

$$\Omega = \frac{3J_{21}(J_{30}J_{31} - J_{20}J_{41}) + 3J_{31}(J_{10}J_{41} - J_{20}J_{31}) - 5J_{42}D_{20}}{J_{42}D_{20}}. \quad (\text{D.118})$$

Appendix E

Energy and Momentum Deposition in the Bethe–Bloch Formalism

The Bethe–Bloch formalism [239, 240, 241, 242] assumes that [see Eq. (8.7)]

$$\frac{dE(t)}{dt} = a \frac{1}{v_{\text{jet}}(t)}. \quad (\text{E.1})$$

In order to determine the location $x_{\text{jet}}(t)$ as well as the time dependence of the velocity $v_{\text{jet}}(t)$, from which one can calculate the energy loss using the above formula, we start by proving the general expression

$$\frac{dE}{dt} = v_{\text{jet}} \frac{dM}{dt}. \quad (\text{E.2})$$

Applying the relativistic equations ($\beta = v_{\text{jet}}/c$) $E = \gamma m$ and $M = \beta \gamma m = \beta E$, where m denotes the mass of the jet, the momentum deposition can be rewritten as

$$\frac{dM}{dt} = \frac{dM}{dx} \frac{dx}{dt} = \beta \frac{dM}{dx} = \beta \left(\frac{dE}{dx} \beta + E \frac{d\beta}{dx} \right). \quad (\text{E.3})$$

The last term can be further evaluated since $\beta^2 = 1 - 1/\gamma^2$ which leads (taking the derivative w.r.t. x and taking into account that $m = \text{const.}$) to the relation

$$\frac{d\beta}{dx} = \frac{1}{\beta \gamma^3} \frac{dE}{dx} \frac{1}{m}. \quad (\text{E.4})$$

Therefore, the momentum deposition is given by

$$\begin{aligned} \frac{dM}{dt} &= \beta^2 \frac{dE}{dx} \left(1 + \frac{1}{\gamma^2 \beta^2} \right) = \beta^2 \frac{dE}{dx} \left(1 + \frac{1}{\gamma^2 - 1} \right) \\ &= \frac{dE}{dx} = \frac{dE}{dt} \frac{1}{v_{\text{jet}}}. \end{aligned} \quad \square \quad (\text{E.5})$$

This expression can now be used to calculate the time as a function of the jet's rapidity y_{jet} , using $dM/dy_{\text{jet}} = m \cosh y_{\text{jet}}$ and $v_{\text{jet}} = \tanh y_{\text{jet}}$:

$$\begin{aligned} \frac{dE}{dt} &= v_{\text{jet}} \frac{dM}{dt} = \frac{a}{v_{\text{jet}}} \\ \Rightarrow \frac{m}{a} \int_{y_0}^{y_{\text{jet}}} \cosh y'_{\text{jet}} \tanh^2 y'_{\text{jet}} dy'_{\text{jet}} &= t(y_{\text{jet}}) \end{aligned} \quad (\text{E.6})$$

where y_0 is the jet's initial rapidity. This relation is equivalent to

$$\frac{m}{a} \int_{y_0}^{y_{\text{jet}}} \frac{\sinh^2 y'_{\text{jet}}}{\cosh y'_{\text{jet}}} dy'_{\text{jet}} = t(y_{\text{jet}}). \quad (\text{E.7})$$

The integral expression can be solved analytically [302],

$$\int \frac{\sinh^2 y_{\text{jet}}}{\cosh y_{\text{jet}}} dy_{\text{jet}} = \sinh y_{\text{jet}} - \arccos \frac{1}{\cosh y_{\text{jet}}}, \quad (\text{E.8})$$

thus, one obtains for $t(y_{\text{jet}})$ [see Eq. (8.8)]

$$\begin{aligned} t(y_{\text{jet}}) &= \frac{m}{a} \left[\sinh y_{\text{jet}} - \sinh y_0 \right. \\ &\quad \left. - \arccos \frac{1}{\cosh y_{\text{jet}}} + \arccos \frac{1}{\cosh y_0} \right], \end{aligned} \quad (\text{E.9})$$

which can then be applied to calculate the time dependence of the velocity $v_{\text{jet}}(t)$. The location $x_{\text{jet}}(t)$, however, is given by

$$x_{\text{jet}}(t) = x_{\text{jet}}(0) + \int_0^t v_{\text{jet}}(t) dt \quad (\text{E.10})$$

which is, because of $v_{\text{jet}}(t) = \tanh y_{\text{jet}}$, equivalent to

$$x_{\text{jet}}(t) = x_{\text{jet}}(0) + \int_{y_0}^{y_{\text{jet}}} \tanh y'_{\text{jet}} \frac{dt}{dy} dy. \quad (\text{E.11})$$

Using Eq. (E.7) as well as the substitution $dy_{\text{jet}} \cosh y_{\text{jet}} = d \sinh y_{\text{jet}}$, one obtains

$$x_{\text{jet}}(t) = x_{\text{jet}}(0) + \frac{m}{a} \int_{\sinh y_0}^{\sinh y_{\text{jet}}} \frac{\sinh^3 y'_{\text{jet}}}{\cosh^3 y'_{\text{jet}}} d \sinh y'_{\text{jet}}. \quad (\text{E.12})$$

With the substitution $x = \sinh y_{\text{jet}}$, the integral is

$$\int \frac{x^3}{(1+x^2)^{3/2}} dx = \frac{1 + \cosh^2 y_{\text{jet}}}{\cosh y_{\text{jet}}}, \quad (\text{E.13})$$

which can be rewritten using $\cosh y_{\text{jet}} = \gamma_{\text{jet}}$ and $\sinh y_{\text{jet}} = \gamma_{\text{jet}} v_{\text{jet}}$, leading to [cf. Eq. (8.9)]

$$x_{\text{jet}}(t) = x_{\text{jet}}(0) + \frac{m}{a} \left[(2 - v_{\text{jet}}^2) \gamma_{\text{jet}} - (2 - v_0^2) \gamma_0 \right]. \quad (\text{E.14})$$

Appendix F

Joule Heating

This appendix discusses the connection between a source term and the process of Joule heating. Starting with the Boltzmann equation, omitting the collision term,

$$\frac{\partial}{\partial t}f + \vec{v} \cdot \vec{\nabla}f + \vec{F} \cdot \frac{\partial}{\partial \vec{p}}f + \vec{F} \cdot \vec{v} \frac{\partial}{\partial p_0}f = 0, \quad (\text{F.1})$$

where f is a distribution function, $\vec{v} = \vec{p}/E$ the velocity and \vec{F} an external force, one obtains the manifestly covariant expression of the Boltzmann–Vlasov equation by multiplying the above equation with $p_0 = E = \sqrt{p^2 + m^2}$

$$p^\mu \partial_\mu f - ep^\mu F_{\mu\nu} \frac{\partial}{\partial p_\nu} f = 0. \quad (\text{F.2})$$

Here, $F^{\mu\nu}$ is the antisymmetric field tensor. The energy-momentum tensor is given by

$$T^{\mu\nu} = \int \frac{d^3p}{(2\pi)^3 E} p^\mu p^\nu f(x, p) = \int d\Gamma p^\mu p^\nu f(x, p), \quad (\text{F.3})$$

implying

$$\partial_\mu T^{\mu\nu} = \int d\Gamma p^\mu p^\nu \partial_\mu f. \quad (\text{F.4})$$

Inserting the above Boltzmann equation [Eq. (F.2)] results in

$$\partial_\mu T^{\mu\nu} = e \int d\Gamma p^\mu p^\nu F_\mu^\alpha \frac{\partial f}{\partial p^\alpha}. \quad (\text{F.5})$$

After integration by parts (leading to a vanishing surface integral) and applying that $F_\mu^\mu = 0$, the expression can be rewritten as

$$\partial_\mu T^{\mu\nu} = -F_\mu^\nu e \int d\Gamma p^\mu f. \quad (\text{F.6})$$

Defining the current $J^\mu = -e \int d\Gamma p^\mu f$ [303], one ends up with the general expression [303]

$$\partial_\mu T^{\mu\nu} = J^\mu F_\mu^\nu. \quad (\text{F.7})$$

According to Ohm's law, this current is given by

$$\vec{J} = \sigma \vec{E}, \quad (\text{F.8})$$

which reads in covariant generalization

$$\mathcal{J}^\nu = F_{\alpha\beta} \sigma^{\alpha\beta\nu}. \quad (\text{F.9})$$

The heat produced during this process is called *Joule heating*. Thus, Eq. (F.7) becomes

$$\partial_\mu T^{\mu\nu} = F_\mu{}^\nu \sigma^{\mu\alpha\beta} F_{\alpha\beta}. \quad (\text{F.10})$$

Therefore, the source term \mathcal{J}^ν is given by [see Eq. (10.3)]

$$\partial_\mu T^{\mu\nu} = \mathcal{J}^\nu = F^{\nu\alpha a} J_\alpha^a = (F^{\nu\alpha a} \sigma_{\alpha\beta\gamma} * F^{\beta\gamma a}). \quad (\text{F.11})$$

Appendix G

Isochronous and Isothermal Freeze-out

A Mach-cone signal, like any observable from heavy-ion collisions sensitive to hydrodynamics, suffers from the problem that the “fluid” cannot directly be accessed experimentally, but has to be studied from final many-particle correlations which are sensitive to all stages of the hydrodynamic evolution, including the late (and presumably non-thermalized) stages of freeze-out.

A rough approximation assumes that the mean-free path goes from zero to infinity at a certain locus in space-time $\Sigma^\mu = (t, \vec{x})$. This locus can be defined in terms of a local criterion (e.g. a freeze-out temperature T_c), or using a simple global geometry (like an isochronous freeze-out, see section 3.7).

Then, applying the Cooper–Frye formula [Eq. (3.34)],

$$E \frac{dN}{d^3\vec{p}} = \int_{\Sigma} d\Sigma_{\mu} p^{\mu} f(u \cdot p/T), \quad (\text{G.1})$$

which is an ansatz based on energy-momentum and entropy conservation that is repeated here for convenience, the fluid fields of momentum p^μ , velocity u^μ and

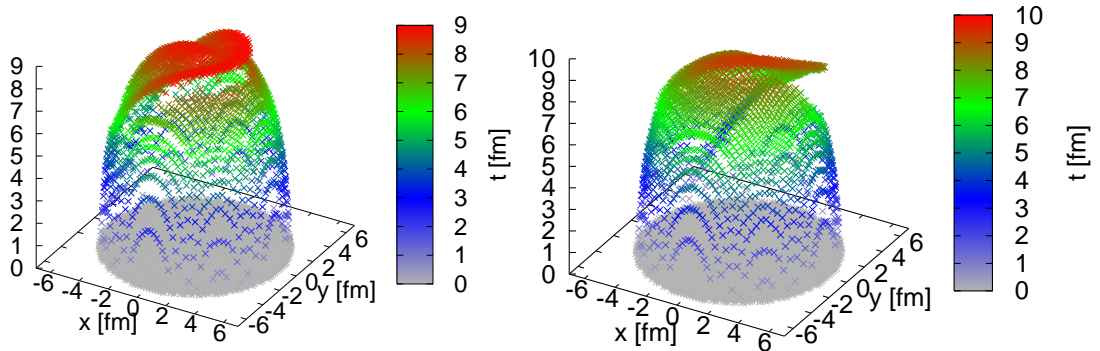
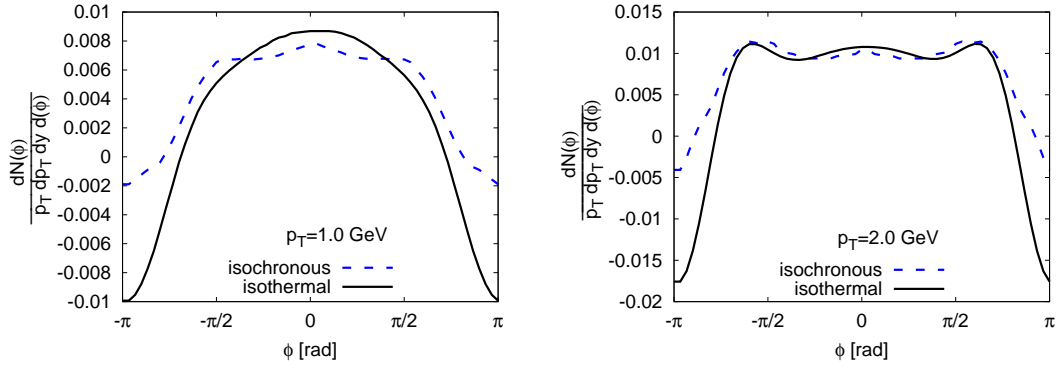
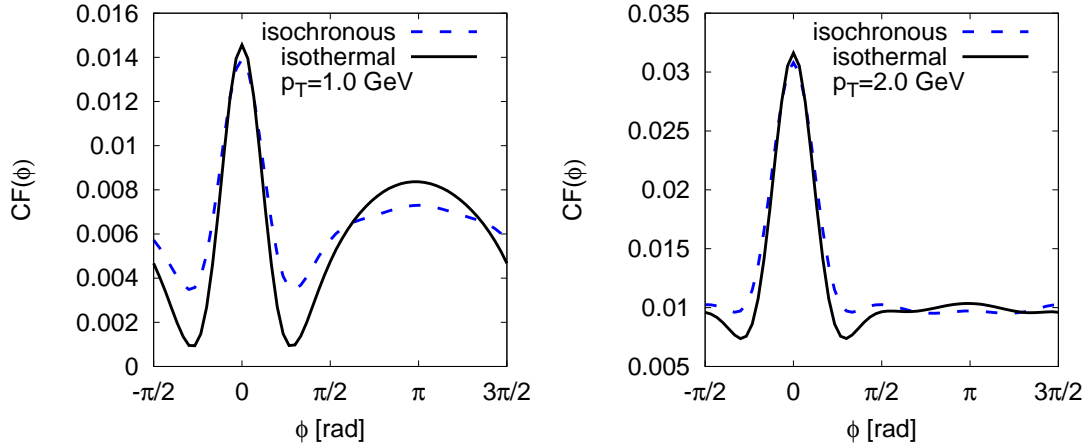


Figure G.1

The freeze-out hypersurface ($T_c = 130$ MeV) for a jet moving through the middle of the medium (left panel, Jet 180 according to Fig. 11.1) and a non-central jet (right panel, Jet 150). In the right panel a beak-like deformation of the hypersurface due to jet heating is clearly visible.

**Figure G.2**

Background subtracted and normalized azimuthal particle correlations obtained from an isochronous (dashed blue line) and an isothermal (solid black line) Cooper–Frye freeze-out for $p_T = 1$ GeV (left panel) and $p_T = 2$ GeV (right panel).

**Figure G.3**

Background subtracted and normalized azimuthal particle correlations obtained from an isochronous (dashed blue line) and an isothermal (solid black line) Cooper–Frye freeze-out for $p_T = 1$ GeV (left panel) and $p_T = 2$ GeV (right panel) after convolution with a trigger jet according to Eq. (11.8).

temperature T are transformed into particles according to a distribution function f . However, the freeze-out hypersurface Σ entering the above equation is severely deformed by a jet propagating through an expanding medium as shown in Fig. G.1. A very characteristic, beak-like elongation occurs for non-central jets (see right panel of Fig. G.1) putting constraints on an isothermal freeze-out which requires the derivative of time w.r.t. spatial coordinates (cf. section 3.7).

Nevertheless, the freeze-out results applying an isochronous and an isothermal freeze-out are rather similar for a central jet (i.e., for jets moving through the middle of the medium) as Fig. G.2 reveals. Here, the particle distribution is obtained according to the above Cooper–Frye formula. Fig. G.3, however, displays the distribution after convoluting with a trigger jet according to Eq. (11.8).

While there is an excellent agreement for $p_T = 2$ GeV, a discrepancy occurs for $p_T = 1$ GeV which could be an effect of larger thermal smearing.

Surprisingly enough, these results suggest that applying an isochronous freeze-out, which is a very strong model assumption, does not drastically alter the results compared to an isothermal conversion (at least for the very central jets).

Appendix H

Distortion of Conical Structures due to Background Flow

Satarov et al. [170] predicted that a Mach cone is deformed in an expanding medium due to the interaction of the jet and background flow patterns. Since a straightforward analytical solution can only be derived if the background flow is parallel (or antiparallel) to the direction of jet propagation (which is not the case for a radially expanding medium), we may just qualitatively investigate such an effect here.

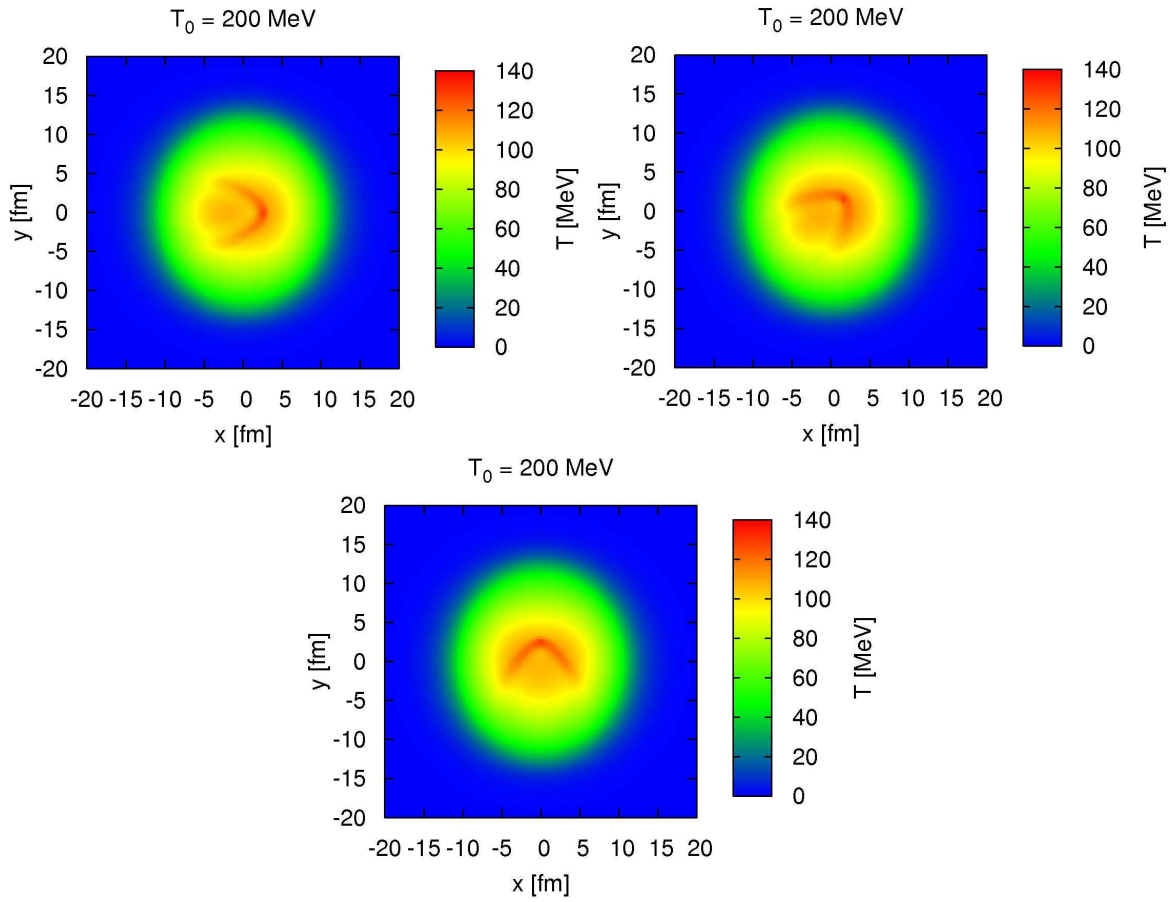
Fig. H.1 displays the temperature patterns at the moment of freeze-out (i.e., when the temperature of all cells has dropped below $T_c = 130$ MeV, see chapter 11) for jets that deposit energy and momentum according to Eq. (11.2) with $dE/dt|_0 = v dM/dt|_0 = 1$ GeV/fm into an expanding $b = 6$ fm medium along trajectories having different angles w.r.t. the x -axis.

As can be seen, the opening angle of the conical structure produced differs for jets propagating along the short (upper left panel of Fig. H.1) or the long axis (lower panel of Fig. H.1), with a larger opening angle for jets encountering a larger background flow gradient.

Moreover, for a jet propagating at an angle of $\phi = 45$ degrees w.r.t. the x -axis (upper right panel of Fig. H.1), the conical structure is distorted in a way that the opening angle in direction of the larger background flow gradient becomes larger than the opening angle in direction of the smaller background flow gradient. This effect, however, remains small for an impact parameter of $b = 6$ fm.

This is in accord with the prediction of Ref. [170] (see also Fig. 5.4). There the opening angles for the outer wings of the Mach-cone angles gets larger since the flow points radially outwards.

Though a detailed study about the distortion of Mach cones remains to be done, the conical structure clearly depends on the centrality of the considered medium.

**Figure H.1**

The temperature pattern of three different jets depositing energy and momentum along trajectories for varying angles w.r.t. the x -axis at the moment of freeze-out. The distortion of the conical shape is clearly visible.

Bibliography

Chapter 1: Introduction

- [1] S. L. Glashow, “Partial Symmetries Of Weak Interactions,” Nucl. Phys. **22**, 579 (1961).
- [2] S. Weinberg, “A Model Of Leptons,” Phys. Rev. Lett. **19**, 1264 (1967).
- [3] D. J. Gross and F. Wilczek, “Ultraviolet Behavior of Non-Abelian Gauge Theories,” Phys. Rev. Lett. **30**, 1343 (1973).
- [4] H. D. Politzer, “Reliable Perturbative Results for Strong Interactions?,” Phys. Rev. Lett. **30**, 1346 (1973).
- [5] J. C. Collins and M. J. Perry, “Superdense Matter: Neutrons Or Asymptotically Free Quarks?,” Phys. Rev. Lett. **34**, 1353 (1975).
- [6] B. A. Freedman and L. D. McLerran, “Fermions And Gauge Vector Mesons At Finite Temperature And Density. 3. The Ground State Energy Of A Relativistic Quark Gas,” Phys. Rev. D **16**, 1169 (1977).
- [7] E. V. Shuryak, “Theory Of Hadronic Plasma,” Sov. Phys. JETP **47**, 212 (1978) [Zh. Eksp. Teor. Fiz. **74**, 408 (1978)].
- [8] *Report of the Workshop on BeV/nucleon Collisions of Heavy Ions: How and Why*, Bear Mountain, New York, 29 Nov - 1 Dec 1974.
- [9] U. W. Heinz and M. Jacob, “Evidence for a new state of matter: An assessment of the results from the CERN lead beam programme,” arXiv:nucl-th/0002042.
- [10] I. Arsene *et al.* [BRAHMS Collaboration], “Quark Gluon Plasma an Color Glass Condensate at RHIC? The perspective from the BRAHMS experiment,” Nucl. Phys. A **757**, 1 (2005) [arXiv:nucl-ex/0410020].
- [11] K. Adcox *et al.* [PHENIX Collaboration], “Formation of dense partonic matter in relativistic nucleus nucleus collisions at RHIC: Experimental evaluation by the PHENIX collaboration,” Nucl. Phys. A **757**, 184 (2005) [arXiv:nucl-ex/0410003].
- [12] B. B. Back *et al.*, “The PHOBOS perspective on discoveries at RHIC,” Nucl. Phys. A **757**, 28 (2005) [arXiv:nucl-ex/0410022].
- [13] J. Adams *et al.* [STAR Collaboration], “Experimental and theoretical challenges in the search for the quark gluon plasma: The STAR collaboration’s critical assessment of the evidence from RHIC collisions,” Nucl. Phys. A **757**, 102 (2005) [arXiv:nucl-ex/0501009].
- [14] E. Shuryak, “Why does the quark gluon plasma at RHIC behave as a nearly ideal fluid?,” Prog. Part. Nucl. Phys. **53**, 273 (2004) [arXiv:hep-ph/0312227].
- [15] P. F. Kolb and U. W. Heinz, “Hydrodynamic description of ultrarelativistic heavy-ion collisions,” arXiv:nucl-th/0305084.
- [16] P. Romatschke and U. Romatschke, “Viscosity Information from Relativistic Nuclear Collisions: How Perfect is the Fluid Observed at RHIC?,” Phys. Rev. Lett. **99**, 172301 (2007) [arXiv:0706.1522 [nucl-th]].
- [17] P. Huovinen, “Hydrodynamical description of collective flow,” arXiv:nucl-th/0305064.

- [18] A. Muronga, "Shear Viscosity Coefficient from Microscopic Models," *Phys. Rev. C* **69**, 044901 (2004) [arXiv:nucl-th/0309056].
- [19] E. Shuryak, "A strongly coupled quark-gluon plasma," *J. Phys. G* **30**, S1221 (2004).
- [20] G. S. Bali and K. Schilling, "Static quark - anti-quark potential: Scaling behavior and finite size effects in SU(3) lattice gauge theory," *Phys. Rev. D* **46**, 2636 (1992).
- [21] S. Bethke, "Experimental tests of asymptotic freedom," *Prog. Part. Nucl. Phys.* **58**, 351 (2007) [arXiv:hep-ex/0606035].
- [22] M. Gyulassy and L. McLerran, "New forms of QCD matter discovered at RHIC," *Nucl. Phys. A* **750**, 30 (2005) [arXiv:nucl-th/0405013].
- [23] M. A. Stephanov, "QCD phase diagram and the critical point," *Prog. Theor. Phys. Suppl.* **153**, 139 (2004) [*Int. J. Mod. Phys. A* **20**, 4387 (2005)] [arXiv:hep-ph/0402115].
- [24] Z. Fodor and S. D. Katz, "Lattice determination of the critical point of QCD at finite T and mu," *JHEP* **0203**, 014 (2002) [arXiv:hep-lat/0106002].
- [25] Z. Fodor and S. D. Katz, "Finite T/mu lattice QCD and the critical point," *Prog. Theor. Phys. Suppl.* **153**, 86 (2004) [arXiv:hep-lat/0401023].
- [26] F. Karsch and E. Laermann, "Thermodynamics and in-medium hadron properties from lattice QCD," arXiv:hep-lat/0305025.
- [27] F. Karsch, C. R. Allton, S. Ejiri, S. J. Hands, O. Kaczmarek, E. Laermann and C. Schmidt, "Where is the chiral critical point in 3-flavor QCD?," *Nucl. Phys. Proc. Suppl.* **129**, 614 (2004) [arXiv:hep-lat/0309116].
- [28] Z. Fodor and S. D. Katz, "Critical point of QCD at finite T and mu, lattice results for physical quark masses," *JHEP* **0404**, 050 (2004) [arXiv:hep-lat/0402006].
- [29] D. H. Rischke, "The quark-gluon plasma in equilibrium," *Prog. Part. Nucl. Phys.* **52**, 197 (2004) [arXiv:nucl-th/0305030].
- [30] D. Bailin and A. Love, "Superfluidity And Superconductivity In Relativistic Fermion Systems," *Phys. Rept.* **107**, 325 (1984).
- [31] S. B. Rüster, V. Werth, M. Buballa, I. A. Shovkovy and D. H. Rischke, "The phase diagram of neutral quark matter: Self-consistent treatment of quark masses," *Phys. Rev. D* **72**, 034004 (2005) [arXiv:hep-ph/0503184].
- [32] D. H. Rischke, M. I. Gorenstein, A. Schäfer, H. Stöcker and W. Greiner, "Nonperturbative effects in the SU(3) gluon plasma," *Phys. Lett. B* **278**, 19 (1992).
- [33] S. L. Glashow and S. Weinberg, "Breaking Chiral Symmetry," *Phys. Rev. Lett.* **20**, 224 (1968).
- [34] D. J. Schwarz, "The first second of the universe," *Annalen Phys.* **12**, 220 (2003) [arXiv:astro-ph/0303574].
- [35] S. A. Bass, "Microscopic Reaction Dynamics at SPS and RHIC," Talk at the Quark Matter Conference 2001, Stony Book, USA (2001).
- [36] S. Soff, S. A. Bass, M. Bleicher, H. Stöcker and W. Greiner, "Directed and elliptic flow," arXiv:nucl-th/9903061.
- [37] R. Rapp and J. Wambach, "Chiral symmetry restoration and dileptons in relativistic heavy-ion collisions," *Adv. Nucl. Phys.* **25**, 1 (2000) [arXiv:hep-ph/9909229].
- [38] J. Rafelski and B. Müller, "Strangeness Production In The Quark - Gluon Plasma," *Phys. Rev. Lett.* **48**, 1066 (1982) [Erratum-ibid. **56**, 2334 (1986)].
- [39] E. Andersen *et al.* [WA97 Collaboration], "Strangeness enhancement at mid-rapidity in Pb Pb collisions at 158-A-GeV/c," *Phys. Lett. B* **449**, 401 (1999).
- [40] T. Matsui and H. Satz, "J/psi Suppression by Quark-Gluon Plasma Formation," *Phys. Lett. B* **178**, 416 (1986).

- [41] A. Andronic, P. Braun-Munzinger, K. Redlich and J. Stachel, “Statistical hadronization of heavy quarks in ultra-relativistic nucleus-nucleus collisions,” Nucl. Phys. A **789**, 334 (2007) [arXiv:nucl-th/0611023].
- [42] S. Jeon and V. Koch, “Event-by-event fluctuations,” arXiv:hep-ph/0304012.
- [43] S. A. Bass, P. Danielewicz and S. Pratt, “Clocking hadronization in relativistic heavy ion collisions with balance functions,” Phys. Rev. Lett. **85**, 2689 (2000) [arXiv:nucl-th/0005044].

Chapter 2: The Experimental Search for the QGP

- [44] A. M. Poskanzer and S. A. Voloshin, “Methods for analyzing anisotropic flow in relativistic nuclear collisions,” Phys. Rev. C **58**, 1671 (1998) [arXiv:nucl-ex/9805001].
- [45] U. W. Heinz, “Thermalization at RHIC,” AIP Conf. Proc. **739**, 163 (2005) [arXiv:nucl-th/0407067].
- [46] Z. Xu, C. Greiner and H. Stöcker, “QCD plasma thermalization, collective flow and extraction of shear viscosity,” J. Phys. G **35**, 104016 (2008) [arXiv:0807.2986 [hep-ph]].
- [47] B. Alver *et al.* [PHOBOS Collaboration], “Elliptic flow fluctuations in Au+Au collisions at $\sqrt{s_{NN}} = 200$ GeV,” arXiv:nucl-ex/0702036.
- [48] P. Arnold, J. Lenaghan, G. D. Moore and L. G. Yaffe, “Apparent thermalization due to plasma instabilities in quark gluon plasma,” Phys. Rev. Lett. **94**, 072302 (2005) [arXiv:nucl-th/0409068].
- [49] V. N. Gribov and L. N. Lipatov, “Deep Inelastic E P Scattering In Perturbation Theory,” Sov. J. Nucl. Phys. **15**, 438 (1972) [Yad. Fiz. **15**, 781 (1972)].
- [50] G. Altarelli and G. Parisi, “Asymptotic Freedom In Parton Language,” Nucl. Phys. B **126**, 298 (1977).
- [51] Y. L. Dokshitzer, “Calculation Of The Structure Functions For Deep Inelastic Scattering And E+ E- Annihilation By Perturbation Theory In Quantum Chromodynamics. (In Russian),” Sov. Phys. JETP **46**, 641 (1977) [Zh. Eksp. Teor. Fiz. **73**, 1216 (1977)].
- [52] A. Accardi *et al.*, “Hard probes in heavy ion collisions at the LHC: Jet physics,” arXiv:hep-ph/0310274.
- [53] J. W. Cronin, H. J. Frisch, M. J. Shochet, J. P. Boymond, R. Mermoud, P. A. Piroué and R. L. Sumner, “Production Of Hadrons With Large Transverse Momentum At 200-GeV, 300-GeV, And 400-GeV,” Phys. Rev. D **11**, 3105 (1975).
- [54] D. Antreasyan, J. W. Cronin, H. J. Frisch, M. J. Shochet, L. Kluberg, P. A. Piroué and R. L. Sumner, “Production Of Hadrons At Large Transverse Momentum In 200-GeV, 300-GeV And 400-GeV P P And P N Collisions,” Phys. Rev. D **19**, 764 (1979).
- [55] D. d’Enterria and B. Betz, “High- p_T hadron suppression and jet quenching”, to be published as Springer Lecture Notes in Physics (LNP) for the QGP Winter School 2008, Springer, Berlin Heidelberg New York (2009); D. d’Enterria, “Jet quenching,” arXiv:0902.2011 [nucl-ex].
- [56] S. S. Adler *et al.* [PHENIX Collaboration], “Centrality dependence of direct photon production in $s(NN)^{1/2} = 200$ -GeV Au + Au collisions,” Phys. Rev. Lett. **94**, 232301 (2005) [arXiv:nucl-ex/0503003].
- [57] S. S. Adler *et al.* [PHENIX Collaboration], “Mid-rapidity neutral pion production in proton proton collisions at $\sqrt{s} = 200$ -GeV,” Phys. Rev. Lett. **91**, 241803 (2003) [arXiv:hep-ex/0304038].
- [58] S. S. Adler *et al.* [PHENIX Collaboration], “Common suppression pattern of eta and π^0 mesons at high transverse momentum in Au + Au collisions at $s(NN)^{1/2} = 200$ -GeV,” Phys. Rev. Lett. **96**, 202301 (2006) [arXiv:nucl-ex/0601037].

- [59] J. Adams *et al.* [STAR Collaboration], “Transverse momentum and collision energy dependence of high p_T hadron suppression in Au + Au collisions at ultrarelativistic energies,” Phys. Rev. Lett. **91**, 172302 (2003) [arXiv:nucl-ex/0305015].
- [60] S. S. Adler *et al.* [PHENIX Collaboration], “High p_T charged hadron suppression in Au + Au collisions at $\sqrt{s_{NN}} = 200$ GeV,” Phys. Rev. C **69**, 034910 (2004) [arXiv:nucl-ex/0308006].
- [61] I. Vitev and M. Gyulassy, “High p_T tomography of $d + Au$ and Au+Au at SPS, RHIC, and LHC,” Phys. Rev. Lett. **89**, 252301 (2002) [arXiv:hep-ph/0209161].
- [62] I. Vitev, “Jet tomography,” J. Phys. G **30**, S791 (2004) [arXiv:hep-ph/0403089].
- [63] B. Müller, “Phenomenology of jet quenching in heavy ion collisions,” Phys. Rev. C **67**, 061901 (2003) [arXiv:nucl-th/0208038].
- [64] J. D. Bjorken, “Highly Relativistic Nucleus-Nucleus Collisions: The Central Rapidity Region,” Phys. Rev. D **27**, 140 (1983).
- [65] M. Gyulassy and M. Plumer, “Jet Quenching In Dense Matter,” Phys. Lett. B **243**, 432 (1990).
- [66] X. N. Wang and M. Gyulassy, “Gluon shadowing and jet quenching in A + A collisions at $s^{1/2} = 200$ -GeV,” Phys. Rev. Lett. **68**, 1480 (1992).
- [67] J. Adams *et al.* [STAR Collaboration], “Experimental and theoretical challenges in the search for the quark gluon plasma: The STAR collaboration’s critical assessment of the evidence from RHIC collisions,” Nucl. Phys. A **757**, 102 (2005) [arXiv:nucl-ex/0501009].
- [68] K. Adcox *et al.* [PHENIX Collaboration], “Suppression of hadrons with large transverse momentum in central Au+Au collisions at $\sqrt{s_{NN}} = 130$ -GeV,” Phys. Rev. Lett. **88**, 022301 (2002) [arXiv:nucl-ex/0109003].
- [69] F. Wang [STAR Collaboration], “Soft physics from STAR,” Nucl. Phys. A **774**, 129 (2006) [arXiv:nucl-ex/0510068].
- [70] A. Adare *et al.* [PHENIX Collaboration], “Dihadron azimuthal correlations in Au+Au collisions at $\sqrt{s_{NN}} = 200$ GeV,” Phys. Rev. C **78**, 014901 (2008) [arXiv:0801.4545 [nucl-ex]].
- [71] J. Adams *et al.* [STAR Collaboration], “Direct observation of dijets in central Au + Au collisions at $s(NN)^{1/2} = 200$ -GeV,” Phys. Rev. Lett. **97**, 162301 (2006) [arXiv:nucl-ex/0604018].
- [72] J. G. Ulery [STAR Collaboration], “Two- and three-particle jet correlations from STAR,” Nucl. Phys. A **774**, 581 (2006) [arXiv:nucl-ex/0510055].
- [73] S. S. Adler *et al.* [PHENIX Collaboration], “Modifications to di-jet hadron pair correlations in Au + Au collisions at $s(NN)^{1/2} = 200$ -GeV,” Phys. Rev. Lett. **97**, 052301 (2006) [arXiv:nucl-ex/0507004].
- [74] J. Y. Jia, “How to Make Sense of the Jet Correlations Results at RHIC?,” arXiv:0810.0051 [nucl-ex].
- [75] M. Ploskon [CERES Collaboration], “Two particle azimuthal correlations at high transverse momentum in Pb-Au at 158 AGeV/c,” Nucl. Phys. A **783**, 527 (2007) [arXiv:nucl-ex/0701023];
- [76] S. Kniese, PhD Thesis, University Frankfurt am Main, Germany (2009).
- [77] M. van Leeuwen [STAR collaboration], “Recent high-pt results from STAR,” arXiv:0808.4096 [nucl-ex].
- [78] C. Vale, “Highlights from PHENIX II - Exploring the QCD medium,” Talk at the Quark Matter Conference 2009, Knoxville, USA (2009)
- [79] W. G. Holzmann, “Using Two and Three-Particle Correlations in PHENIX to Probe the Response of Strongly Interacting Partonic Matter to High-pT Partons,” Talk at the Quark Matter Conference 2009, Knoxville, USA (2009).

- [80] J. W. Qiu and I. Vitev, “Coherent multiple scattering and dihadron correlations in heavy ion collisions,” arXiv:hep-ph/0410218.
- [81] I. Vitev, “Large Angle Hadron Correlations from Medium-Induced Gluon Radiation,” Phys. Lett. B **630**, 78 (2005) [arXiv:hep-ph/0501255].
- [82] H. Stöcker, “Collective Flow signals the Quark Gluon Plasma,” Nucl. Phys. A **750**, 121 (2005) [arXiv:nucl-th/0406018].
- [83] J. Casalderrey-Solana, E. V. Shuryak and D. Teaney, “Conical flow induced by quenched QCD jets,” J. Phys. Conf. Ser. **27**, 22 (2005) [Nucl. Phys. A **774**, 577 (2006)] [arXiv:hep-ph/0411315].
- [84] I. M. Dremin, “Ring-like events: Cherenkov gluons or Mach waves?,” Nucl. Phys. A **767**, 233 (2006) [arXiv:hep-ph/0507167].
- [85] A. Majumder and X. N. Wang, “LPM interference and Cherenkov-like gluon bremsstrahlung in dense matter,” Phys. Rev. C **73**, 051901 (2006) [arXiv:nucl-th/0507062].
- [86] V. Koch, A. Majumder and X. N. Wang, “Cherenkov Radiation from Jets in Heavy-ion Collisions,” Phys. Rev. Lett. **96**, 172302 (2006) [arXiv:nucl-th/0507063].
- [87] C. Adler *et al.* [STAR Collaboration], “Disappearance of back-to-back high p_T hadron correlations in central Au+Au collisions at $\sqrt{s_{NN}} = 200$ -GeV,” Phys. Rev. Lett. **90**, 082302 (2003) [arXiv:nucl-ex/0210033].
- [88] J. Adams *et al.* [STAR Collaboration], “Distributions of charged hadrons associated with high transverse momentum particles in p p and Au + Au collisions at $s(NN)^{1/2} = 200$ -GeV,” Phys. Rev. Lett. **95**, 152301 (2005) [arXiv:nucl-ex/0501016].
- [89] N. N. Ajitanand *et al.*, “Decomposition of harmonic and jet contributions to particle-pair correlations at ultra-relativistic energies,” Phys. Rev. C **72**, 011902 (2005) [arXiv:nucl-ex/0501025].
- [90] J. G. Ulery, “Three-Particle Azimuthal Correlations,” PoS(LHC07), 036 (2007) [arXiv:0709.1633 [nucl-ex]].
- [91] B. I. Abelev *et al.* [STAR Collaboration], “Indications of Conical Emission of Charged Hadrons at RHIC,” Phys. Rev. Lett. **102**, 052302 (2009) [arXiv:0805.0622 [nucl-ex]].
- [92] C. A. Pruneau, “Methods for jet studies with three-particle correlations,” Phys. Rev. C **74**, 064910 (2006) [arXiv:nucl-ex/0608002].
- [93] N. N. Ajitanand [PHENIX Collaboration], “Extraction of jet topology using three particle correlations,” Nucl. Phys. A **783**, 519 (2007) [arXiv:nucl-ex/0609038].
- [94] J. G. Ulery [STAR Collaboration], “Are There Mach Cones in Heavy Ion Collisions? Three-Particle Correlations from STAR,” Int. J. Mod. Phys. E **16**, 2005 (2007) [arXiv:0704.0224 [nucl-ex]].
- [95] B. Alver *et al.* [PHOBOS Collaboration], “High p_T Triggered Delta-eta, Delta-phi Correlations over a Broad Range in Delta-eta,” J. Phys. G **35**, 104080 (2008) [arXiv:0804.3038 [nucl-ex]].
- [96] J. Adams *et al.* [STAR Collaboration], “Transverse-momentum $p(t)$ correlations on (η, Φ) from mean- $p(t)$ fluctuations in Au - Au collisions at $s(NN)^{1/2} = 200$ -GeV,” J. Phys. G **32**, L37 (2006) [arXiv:nucl-ex/0509030].
- [97] J. Putschke, “Intra-jet correlations of high- p_t hadrons from STAR,” J. Phys. G **34**, S679 (2007) [arXiv:nucl-ex/0701074].
- [98] B. Schenke, “Collective Phenomena in the Non-Equilibrium Quark-Gluon Plasma,” PhD Thesis, University Frankfurt, Germany (2008), arXiv:0810.4306 [hep-ph].
- [99] A. Dumitru, F. Gelis, L. McLerran and R. Venugopalan, “Glasma flux tubes and the near side ridge phenomenon at RHIC,” Nucl. Phys. A **810**, 91 (2008) [arXiv:0804.3858 [hep-ph]].
- [100] C. A. Pruneau, S. Gavin and S. A. Voloshin, “Transverse Radial Flow Effects on Two- and Three-Particle Angular Correlations,” Nucl. Phys. A **802**, 107 (2008) [arXiv:0711.1991 [nucl-ex]].

Chapter 3: Ideal Hydrodynamics

- [101] L. D. Landau, "On the multiparticle production in high-energy collisions," *Izv. Akad. Nauk Ser. Fiz.* **17**, 51 (1953).
- [102] H. Stöcker and W. Greiner, "High-Energy Heavy Ion Collisions: Probing The Equation Of State Of Highly Excited Hadronic Matter," *Phys. Rept.* **137** (1986) 277.
- [103] R. B. Clare and D. Strottman, "Relativistic Hydrodynamics and heavy ion reactions," *Phys. Rept.* **141**, 177 (1986).
- [104] L. P. Csernai, "Introduction To Relativistic Heavy Ion Collisions," John Wiley & Sons Ltd, Chichester (1994).
- [105] M. Bleicher *et al.*, "Relativistic hadron hadron collisions in the ultra-relativistic quantum molecular dynamics model," *J. Phys. G* **25**, 1859 (1999) [arXiv:hep-ph/9909407].
- [106] Z. Xu and C. Greiner, "Thermalization of gluons in ultrarelativistic heavy ion collisions by including three-body interactions in a parton cascade," *Phys. Rev. C* **71**, 064901 (2005) [arXiv:hep-ph/0406278].
- [107] H. H. Gutbrod, B. W. Kolb, H. R. Schmidt, A. M. Poskanzer, H. G. Ritter and K. H. Kampert, "A New Component Of The Collective Flow In Relativistic Heavy Ion Collisions," *Phys. Lett. B* **216**, 267 (1989).
- [108] L. D. Landau and E. M. Lifshitz, "Fluid Mechanics, Volume 6 (Course of Theoretical Physics) ", Pergamon Press, New York, (1987).
- [109] S. R. deGroot, W. A. van Leeuwen, and Ch. G. van Weert, "Relativistic Kinetic Theory ", North-Holland, Amsterdam, (1980).
- [110] D. H. Rischke, S. Bernard and J. A. Maruhn, "Relativistic hydrodynamics for heavy ion collisions. 1. General aspects and expansion into vacuum," *Nucl. Phys. A* **595**, 346 (1995) [arXiv:nucl-th/9504018].
- [111] J. Boris and D. Book, "Flux corrected transport I: SHASTA a fluid algorithm that works", *J. Comp. Phys.* **11**, 38 (1973).
- [112] D. L. Book, J. P. Boris, and K. Hain, "Flux-Corrected Transport II - Generalizations of the method", *J. Comp. Phys.* **18**, 248 (1975).
- [113] D. H. Rischke, Y. Pürsün and J. A. Maruhn, "Relativistic hydrodynamics for heavy ion collisions. 2. Compression of nuclear matter and the phase transition to the quark - gluon plasma," *Nucl. Phys. A* **595**, 383 (1995) [Erratum-ibid. A **596**, 717 (1996)] [arXiv:nucl-th/9504021].
- [114] D. H. Rischke, Y. Pürsün, J. A. Maruhn, H. Stöcker and W. Greiner, "The phase transition to the quark-gluon plasma and its effects on hydrodynamic flow," *Heavy Ion Phys.* **1**, 309 (1995).
- [115] V. Schneider, U. Katscher, D. H. Rischke, B. Waldhauser, J. A. Maruhn and C. D. Munz, "New algorithms for ultrarelativistic numerical hydrodynamics," *J. Comput. Phys.* **105**, 92 (1993).
- [116] D. H. Rischke, "Fluid dynamics for relativistic nuclear collisions," arXiv:nucl-th/9809044.
- [117] R. Courant, K. O. Friedrichs, and H. Lewy, "Über die partiellen Differenzengleichungen der mathematischen Physik," *Math. Ann.* **100**, 92 (1928).
- [118] L. D. Landau and S. Z. Belenkii, "Гидродинамическая теория множественного образования частиц", *Uspekhi Fizicheskikh Nauk* **56**, 309 (1955).
- [119] F. Cooper, G. Frye and E. Schonberg, "Landau's Hydrodynamic Model Of Particle Production And Electron Positron Annihilation Into Hadrons," *Phys. Rev. D* **11**, 192 (1975).
- [120] I. Mishustin, Lectures on "Dynamical models of relativistic heavy-ion collisions", University Frankfurt (2005).

- [121] P. F. Kolb, U. W. Heinz, P. Huovinen, K. J. Eskola and K. Tuominen, “Centrality dependence of multiplicity, transverse energy, and elliptic flow from hydrodynamics,” Nucl. Phys. A **696**, 197 (2001) [arXiv:hep-ph/0103234].
- [122] M. Luzum and P. Romatschke, “Conformal Relativistic Viscous Hydrodynamics: Applications to RHIC results at $\sqrt{s_{NN}} = 200$ GeV,” Phys. Rev. C **78**, 034915 (2008) [arXiv:0804.4015 [nucl-th]].
- [123] P. Arnold, J. Lenaghan and G. D. Moore, “QCD plasma instabilities and bottom-up thermalization,” JHEP **0308**, 002 (2003) [arXiv:hep-ph/0307325].
- [124] E. Iancu, A. Leonidov and L. McLerran, “The colour glass condensate: An introduction,” arXiv:hep-ph/0202270.
- [125] A. Chodos, R. L. Jaffe, K. Johnson, C. B. Thorn and V. F. Weisskopf, “A New Extended Model Of Hadrons,” Phys. Rev. D **9**, 3471 (1974).
- [126] B. D. Serot and J. D. Walecka, “The Relativistic Nuclear Many Body Problem,” Adv. Nucl. Phys. **16**, 1 (1986).
- [127] J. Steinheimer, M. Bleicher, H. Petersen, S. Schramm, H. Stöcker and D. Zschesche, “(3+1)-Dimensional Hydrodynamic Expansion with a Critical Point from Realistic Initial Conditions,” Phys. Rev. C **77**, 034901 (2008) [arXiv:0710.0332 [nucl-th]].
- [128] J. Noronha-Hostler, J. Noronha and C. Greiner, “Transport Coefficients of Hadronic Matter near T_c ,” arXiv:0811.1571 [nucl-th].
- [129] F. Cooper and G. Frye, “Comment On The Single Particle Distribution In The Hydrodynamic And Statistical Thermodynamic Models Of Multiparticle Production,” Phys. Rev. D **10**, 186 (1974).
- [130] The figure is taken from <http://www-rnc.lbl.gov/ssalur/www/Research3.html>.
- [131] P. F. Kolb, “Early Thermalization and Hydrodynamic Expansion in Nuclear Collisions at RHIC,” PhD Thesis, University Regensburg, Germany (2002).
- [132] C. Nonaka and S. A. Bass, “3-D hydro + cascade model at RHIC,” Nucl. Phys. A **774**, 873 (2006) [arXiv:nucl-th/0510038].
- [133] H. Petersen, J. Steinheimer, G. Burau, M. Bleicher and H. Stöcker, “A Fully Integrated Transport Approach to Heavy Ion Reactions with an Intermediate Hydrodynamic Stage,” Phys. Rev. C **78**, 044901 (2008) [arXiv:0806.1695 [nucl-th]].
- [134] R. J. Fries, B. Müller, C. Nonaka and S. A. Bass, “Hadronization in heavy ion collisions: Recombination and fragmentation of partons,” Phys. Rev. Lett. **90**, 202303 (2003) [arXiv:nucl-th/0301087].
- [135] V. Greco, C. M. Ko and P. Levai, “Parton coalescence and antiproton/pion anomaly at RHIC,” Phys. Rev. Lett. **90**, 202302 (2003) [arXiv:nucl-th/0301093].
- [136] B. Betz, M. Gyulassy, J. Noronha and G. Torrieri, “Anomalous Conical Di-jet Correlations in pQCD vs AdS/CFT,” Phys. Lett. B **675**, 340 (2009) [arXiv:0807.4526 [hep-ph]].
- [137] B. Betz, J. Noronha, G. Torrieri, M. Gyulassy, I. Mishustin and D. H. Rischke, “Universality of the Diffusion Wake from Stopped and Punch-Through Jets in Heavy-Ion Collisions,” Phys. Rev. C **79**, 034902 (2009) [arXiv:0812.4401 [nucl-th]].

Chapter 4: Viscous Hydrodynamics

- [138] A. Muronga, “Second order dissipative fluid dynamics for ultra-relativistic nuclear collisions,” Phys. Rev. Lett. **88**, 062302 (2002) [Erratum-ibid. **89**, 159901 (2002)] [arXiv:nucl-th/0104064].
- [139] A. Muronga and D. H. Rischke, “Evolution of hot, dissipative quark matter in relativistic nuclear collisions,” arXiv:nucl-th/0407114.

- [140] U. W. Heinz, H. Song and A. K. Chaudhuri, “Dissipative hydrodynamics for viscous relativistic fluids,” *Phys. Rev. C* **73**, 034904 (2006) [arXiv:nucl-th/0510014].
- [141] R. Baier, P. Romatschke and U. A. Wiedemann, “Dissipative hydrodynamics and heavy ion collisions,” *Phys. Rev. C* **73**, 064903 (2006) [arXiv:hep-ph/0602249].
- [142] A. K. Chaudhuri, “Dissipative hydrodynamics in 2+1 dimension,” *Phys. Rev. C* **74**, 044904 (2006) [arXiv:nucl-th/0604014].
- [143] R. Baier and P. Romatschke, “Causal viscous hydrodynamics for central heavy-ion collisions,” *Eur. Phys. J. C* **51**, 677 (2007) [arXiv:nucl-th/0610108].
- [144] A. Muronga, “Relativistic Dynamics of Non-ideal Fluids: Viscous and heat-conducting fluids I. General Aspects and 3+1 Formulation for Nuclear Collisions,” *Phys. Rev. C* **76**, 014909 (2007) [arXiv:nucl-th/0611090].
- [145] A. Muronga, “Relativistic Dynamics of Non-ideal Fluids: Viscous and heat-conducting fluids II. Transport properties and microscopic description of relativistic nuclear matter,” *Phys. Rev. C* **76**, 014910 (2007) [arXiv:nucl-th/0611091].
- [146] K. Dusling and D. Teaney, “Simulating elliptic flow with viscous hydrodynamics,” *Phys. Rev. C* **77**, 034905 (2008) [arXiv:0710.5932 [nucl-th]].
- [147] D. Molnar and P. Huovinen, “Dissipative effects from transport and viscous hydrodynamics,” *J. Phys. G* **35**, 104125 (2008) [arXiv:0806.1367 [nucl-th]].
- [148] A. El, A. Muronga, Z. Xu and C. Greiner, “Shear viscosity and out of equilibrium dissipative hydrodynamics,” arXiv:0812.2762 [hep-ph].
- [149] W. A. Hiscock and L. Lindblom, “Generic instabilities in first-order dissipative relativistic fluid theories,” *Phys. Rev. D* **31**, 725 (1985).
- [150] W. Israel and J. M. Stewart, “Transient relativistic thermodynamics and kinetic theory,” *Annals Phys.* **118**, 341 (1979).
- [151] W. A. Hiscock and L. Lindblom, “Stability and causality in dissipative relativistic fluids,” *Annals Phys.* **151**, 466 (1983).
- [152] H. Grad, “Statistical mechanics, thermodynamics, and fluid dynamics of systems with an arbitrary number of integrals,” *Commun. Pure App. Math.* **2**, 381 (1949).
- [153] I. Müller, “Zum Paradoxon der Wärmeleitungstheorie,” *Z. Phys.* **198**, 329 (1967).
- [154] A. Muronga, “Causal Theories of Dissipative Relativistic Fluid Dynamics for Nuclear Collisions,” *Phys. Rev. C* **69**, 034903 (2004) [arXiv:nucl-th/0309055].
- [155] B. Betz, D. Henkel and D. H. Rischke, “From kinetic theory to dissipative fluid dynamics,” *Prog. Part. Nucl. Phys.* **62**, 556 (2009) [arXiv:0812.1440 [nucl-th]].
- [156] B. Betz, D. Henkel, H. Niemi, and D. H. Rischke, in preparation.
- [157] H. Song and U. W. Heinz, “Multiplicity scaling in ideal and viscous hydrodynamics,” *Phys. Rev. C* **78**, 024902 (2008) [arXiv:0805.1756 [nucl-th]].
- [158] R. Baier, P. Romatschke, D. T. Son, A. O. Starinets and M. A. Stephanov, “Relativistic viscous hydrodynamics, conformal invariance, and holography,” *JHEP* **0804**, 100 (2008) [arXiv:0712.2451 [hep-th]].
- [159] M. A. York and G. D. Moore, “Second order hydrodynamic coefficients from kinetic theory,” arXiv:0811.0729 [hep-ph].
- [160] M. Prakash, M. Prakash, R. Venugopalan and G. Welke, “Nonequilibrium properties of hadronic mixtures,” *Phys. Rept.* **227**, 321 (1993).
- [161] P. Danielewicz and M. Gyulassy, “Dissipative Phenomena In Quark Gluon Plasmas,” *Phys. Rev. D* **31**, 53 (1985).
- [162] U. W. Heinz and P. F. Kolb, “Early thermalization at RHIC,” *Nucl. Phys. A* **702**, 269 (2002) [arXiv:hep-ph/0111075].
- [163] H. Song and U. W. Heinz, “Suppression of elliptic flow in a minimally viscous quark-gluon plasma,” *Phys. Lett. B* **658**, 279 (2008) [arXiv:0709.0742 [nucl-th]].

Chapter 5: Shock Wave Phenomena

- [164] A. H. Taub, "Relativistic Rankine-Hugoniot Equations," *Phys. Rev.* **74**, 328 (1948).
- [165] W. Scheid, H. Müller and W. Greiner, "Nuclear Shock Waves in Heavy-Ion Collisions," *Phys. Rev. Lett.* **32**, 741 (1974).
- [166] H. G. Baumgardt *et al.*, "Shock Waves And Mach Cones In Fast Nucleus-Nucleus Collisions," *Z. Phys. A* **273**, 359 (1975).
- [167] J. Hofmann, H. Stöcker, U. W. Heinz, W. Scheid and W. Greiner, "Possibility Of Detecting Density Isomers In High Density Nuclear Mach Shock Waves," *Phys. Rev. Lett.* **36** (1976) 88.
- [168] H. H. Gutbrod, A. M. Poskanzer and H. G. Ritter, "Plastic Ball Experiments," *Rept. Prog. Phys.* **52**, 1267 (1989).
- [169] P. Rau, J. Steinheimer, B. Betz, H. Petersen, M. Bleicher and H. Stocker, to be published.
- [170] L. M. Satarov, H. Stöcker and I. N. Mishustin, "Mach shocks induced by partonic jets in expanding quark-gluon plasma," *Phys. Lett. B* **627**, 64 (2005) [arXiv:hep-ph/0505245].
- [171] J. Casalderrey-Solana, E. V. Shuryak and D. Teaney, "Hydrodynamic flow from fast particles," arXiv:hep-ph/0602183.
- [172] T. Renk and J. Ruppert, "Mach cones in an evolving medium," *Phys. Rev. C* **73**, 011901 (2006) [arXiv:hep-ph/0509036].
- [173] B. Betz, M. Bleicher, U. Harbach, T. Humanic, B. Koch and H. Stöcker, "Mini black holes at the LHC: Discovery through di-jet suppression, mono-jet emission and a supersonic boom in the quark-gluon plasma in ALICE, ATLAS and CMS," arXiv:hep-ph/0606193.
- [174] I. Bouras *et al.*, "Relativistic shock waves in viscous gluon matter," arXiv:0902.1927 [hep-ph].
- [175] D. H. Rischke, H. Stöcker and W. Greiner, "Flow In Conical Shock Waves: A Signal For The Deconfinement Transition?," *Phys. Rev. D* **42**, 2283 (1990).
- [176] R. Courant and K. O. Friedrichs, "Supersonic Flow and Shock Waves ", Interscience, New York, (1948).
- [177] G. I. Taylor and J. W. Maccoll, "The Air Pressure on a Cone Moving at High Speeds. I ", *Proc. R. Soc.* **A139**, 278 (1933).
- [178] G. I. Taylor and J. W. Maccoll, "The Air Pressure on a Cone Moving at High Speeds. II ", *Proc. R. Soc.* **A139**, 298 (1933).

Chapter 6: Jet Energy Loss

- [179] A. B. Migdal, "Bremsstrahlung and Pair Production in Condensed Media at High Energies", *Phys. Rev.* **103**, 1811 (1956).
- [180] W. M. Yao *et al.* [Particle Data Group], "Review of particle physics," *J. Phys. G* **33**, 1 (2006).
- [181] S. Wicks, W. Horowitz, M. Djordjevic and M. Gyulassy, "Heavy quark jet quenching with collisional plus radiative energy loss and path length fluctuations," *Nucl. Phys. A* **783**, 493 (2007) [arXiv:nucl-th/0701063].
- [182] G. Y. Qin, J. Ruppert, C. Gale, S. Jeon, G. D. Moore and M. G. Mustafa, "Radiative and Collisional Jet Energy Loss in the Quark-Gluon Plasma at RHIC," *Phys. Rev. Lett.* **100**, 072301 (2008) [arXiv:0710.0605 [hep-ph]].
- [183] K. J. Eskola, H. Honkanen, C. A. Salgado and U. A. Wiedemann, "The fragility of high-p(T) hadron spectra as a hard probe," *Nucl. Phys. A* **747**, 511 (2005) [arXiv:hep-ph/0406319].
- [184] C. Loizides, "High transverse momentum suppression and surface effects in nucleus nucleus collisions within the parton quenching model," *Eur. Phys. J. C* **49**, 339 (2007) [arXiv:hep-ph/0608133].

- [185] A. Adare *et al.* [PHENIX Collaboration], “Quantitative Constraints on the Opacity of Hot Partonic Matter from Semi-Inclusive Single High Transverse Momentum Pion Suppression in Au+Au collisions at $\sqrt{s_{NN}} = 200$ GeV,” *Phys. Rev. C* **77**, 064907 (2008) [arXiv:0801.1665 [nucl-ex]].
- [186] TECHQM, Theory-Experiment Collaboration for Hot QCD Matter, https://wiki.bnl.gov/TECHQM/index.php/Main_Page.
- [187] M. Gyulassy, P. Levai and I. Vitev, “Jet quenching in thin quark-gluon plasmas. I: Formalism,” *Nucl. Phys. B* **571**, 197 (2000) [arXiv:hep-ph/9907461].
- [188] M. Djordjevic and M. Gyulassy, “Heavy quark radiative energy loss in QCD matter,” *Nucl. Phys. A* **733**, 265 (2004) [arXiv:nucl-th/0310076].
- [189] R. Baier, Y. L. Dokshitzer, A. H. Mueller, S. Peigne and D. Schiff, “Radiative energy loss of high energy quarks and gluons in a finite-volume quark-gluon plasma,” *Nucl. Phys. B* **483**, 291 (1997) [arXiv:hep-ph/9607355].
- [190] R. Baier, Y. L. Dokshitzer, A. H. Mueller, S. Peigne and D. Schiff, “Radiative energy loss and $p(T)$ -broadening of high energy partons in nuclei,” *Nucl. Phys. B* **484**, 265 (1997) [arXiv:hep-ph/9608322].
- [191] B. G. Zakharov, “Fully quantum treatment of the Landau-Pomeranchuk-Migdal effect in QED and QCD,” *JETP Lett.* **63**, 952 (1996) [arXiv:hep-ph/9607440].
- [192] U. A. Wiedemann, “Gluon radiation off hard quarks in a nuclear environment: Opacity expansion,” *Nucl. Phys. B* **588**, 303 (2000) [arXiv:hep-ph/0005129].
- [193] J. W. Qiu and G. Sterman, “Power corrections in hadronic scattering. 1. Leading $1/Q^{*2}$ corrections to the Drell-Yan cross-section,” *Nucl. Phys. B* **353**, 105 (1991).
- [194] J. W. Qiu and G. Sterman, “Power corrections to hadronic scattering. 2. Factorization,” *Nucl. Phys. B* **353**, 137 (1991).
- [195] P. Arnold, G. D. Moore and L. G. Yaffe, “Photon emission from ultrarelativistic plasmas,” *JHEP* **0111**, 057 (2001) [arXiv:hep-ph/0109064].
- [196] A. Majumder, “A comparative study of jet-quenching schemes,” *J. Phys. G* **34**, S377 (2007) [arXiv:nucl-th/0702066].
- [197] S. A. Bass, C. Gale, A. Majumder, C. Nonaka, G. Y. Qin, T. Renk and J. Ruppert, “Systematic Comparison of Jet Energy-Loss Schemes in a 3D hydrodynamic medium,” *J. Phys. G* **35**, 104064 (2008) [arXiv:0805.3271 [nucl-th]].
- [198] O. Fochler, Z. Xu and C. Greiner, “Towards a unified understanding of jet-quenching and elliptic flow within perturbative QCD parton transport,” arXiv:0806.1169 [hep-ph].
- [199] R. B. Neufeld, B. Müller and J. Ruppert, “Sonic Mach Cones Induced by Fast Partons in a Perturbative Quark-Gluon Plasma,” *Phys. Rev. C* **78**, 041901 (2008) [arXiv:0802.2254 [hep-ph]].
- [200] J. Casalderrey-Solana, “Mach cones in quark gluon plasma,” *J. Phys. G* **34**, S345 (2007) [arXiv:hep-ph/0701257].
- [201] A. K. Chaudhuri and U. Heinz, “Effect of jet quenching on the hydrodynamical evolution of QGP,” *Phys. Rev. Lett.* **97**, 062301 (2006) [arXiv:nucl-th/0503028].
- [202] T. Renk and J. Ruppert, “The rapidity structure of Mach cones and other large angle correlations in heavy-ion collisions,” *Phys. Lett. B* **646**, 19 (2007) [arXiv:hep-ph/0605330].
- [203] R. B. Neufeld, “Fast Partons as a Source of Energy and Momentum in a Perturbative Quark-Gluon Plasma,” *Phys. Rev. D* **78**, 085015 (2008) [arXiv:0805.0385 [hep-ph]].
- [204] M. Asakawa, S. A. Bass and B. Müller, “Anomalous transport processes in anisotropically expanding quark-gluon plasmas,” *Prog. Theor. Phys.* **116**, 725 (2007) [arXiv:hep-ph/0608270].
- [205] R. B. Neufeld, “Propagating Mach Cones in a Viscous Quark-Gluon Plasma,” arXiv:0807.2996 [nucl-th].
- [206] G. Y. Qin, A. Majumder, H. Song and U. Heinz, “Energy and momentum deposited into a QCD medium by a jet shower,” arXiv:0903.2255 [nucl-th].

Chapter 7: From String to Field Theory: The AdS/CFT Correspondence

- [207] M. B. Green, J. H. Schwarz, and E. Witten, “Superstring Theory”, Cambridge University Press, Cambridge, (1987).
- [208] O. Aharony, S. S. Gubser, J. M. Maldacena, H. Ooguri and Y. Oz, “Large N field theories, string theory and gravity,” *Phys. Rept.* **323**, 183 (2000) [arXiv:hep-th/9905111].
- [209] G. 't Hooft, “A Planar Diagram Theory For Strong Interactions,” *Nucl. Phys. B* **72**, 461 (1974).
- [210] J. M. Maldacena, “The large N limit of superconformal field theories and supergravity,” *Adv. Theor. Math. Phys.* **2**, 231 (1998) [*Int. J. Theor. Phys.* **38**, 1113 (1999)] [arXiv:hep-th/9711200].
- [211] E. Witten, “Anti-de Sitter space and holography,” *Adv. Theor. Math. Phys.* **2**, 253 (1998) [arXiv:hep-th/9802150].
- [212] E. Witten, “Anti-de Sitter space, thermal phase transition, and confinement in gauge theories,” *Adv. Theor. Math. Phys.* **2**, 505 (1998) [arXiv:hep-th/9803131].
- [213] I. R. Klebanov, “TASI lectures: Introduction to the AdS/CFT correspondence,” arXiv:hep-th/0009139.
- [214] P. M. Chesler, K. Jensen, A. Karch and L. G. Yaffe, “Light quark energy loss in strongly-coupled N = 4 supersymmetric Yang-Mills plasma,” arXiv:0810.1985 [hep-th].
- [215] C. P. Herzog, A. Karch, P. Kovtun, C. Kozcaz and L. G. Yaffe, “Energy loss of a heavy quark moving through N = 4 supersymmetric Yang-Mills plasma,” *JHEP* **0607**, 013 (2006) [arXiv:hep-th/0605158].
- [216] J. Casalderrey-Solana and D. Teaney, “Transverse momentum broadening of a fast quark in a N = 4 Yang Mills plasma,” *JHEP* **0704**, 039 (2007) [arXiv:hep-th/0701123].
- [217] S. S. Gubser, “Drag force in AdS/CFT,” *Phys. Rev. D* **74**, 126005 (2006) [arXiv:hep-th/0605182].
- [218] J. J. Friess, S. S. Gubser, G. Michalogiorgakis and S. S. Pufu, “The stress tensor of a quark moving through N = 4 thermal plasma,” *Phys. Rev. D* **75**, 106003 (2007) [arXiv:hep-th/0607022].
- [219] A. Yarom, “On the energy deposited by a quark moving in an N=4 SYM plasma,” *Phys. Rev. D* **75**, 105023 (2007) [arXiv:hep-th/0703095].
- [220] S. S. Gubser and S. S. Pufu, “Master field treatment of metric perturbations sourced by the trailing string,” *Nucl. Phys. B* **790**, 42 (2008) [arXiv:hep-th/0703090].
- [221] S. S. Gubser, I. R. Klebanov and A. W. Peet, “Entropy and Temperature of Black 3-Branes,” *Phys. Rev. D* **54**, 3915 (1996) [arXiv:hep-th/9602135].
- [222] G. Torrieri, B. Betz, J. Noronha and M. Gyulassy, “Mach cones in heavy ion collisions,” *Acta Phys. Polon. B* **39**, 3281 (2008) [arXiv:0901.0230 [nucl-th]].
- [223] G. Policastro, D. T. Son and A. O. Starinets, “The shear viscosity of strongly coupled N = 4 supersymmetric Yang-Mills plasma,” *Phys. Rev. Lett.* **87**, 081601 (2001) [arXiv:hep-th/0104066].
- [224] A. Buchel and J. T. Liu, “Universality of the shear viscosity in supergravity,” *Phys. Rev. Lett.* **93**, 090602 (2004) [arXiv:hep-th/0311175].
- [225] P. Kovtun, D. T. Son and A. O. Starinets, “Viscosity in strongly interacting quantum field theories from black hole physics,” *Phys. Rev. Lett.* **94**, 111601 (2005) [arXiv:hep-th/0405231].
- [226] Y. Kats and P. Petrov, “Effect of curvature squared corrections in AdS on the viscosity of the dual gauge theory,” *JHEP* **0901**, 044 (2009) [arXiv:0712.0743 [hep-th]].
- [227] M. Brigante, H. Liu, R. C. Myers, S. Shenker and S. Yaida, “Viscosity Bound Violation in Higher Derivative Gravity,” *Phys. Rev. D* **77**, 126006 (2008) [arXiv:0712.0805 [hep-th]].

- [228] M. Brigante, H. Liu, R. C. Myers, S. Shenker and S. Yaida, “The Viscosity Bound and Causality Violation,” *Phys. Rev. Lett.* **100**, 191601 (2008) [arXiv:0802.3318 [hep-th]].
- [229] J. Noronha, G. Torrieri and M. Gyulassy, “Near Zone Navier-Stokes Analysis of Heavy Quark Jet Quenching in an $\mathcal{N}=4$ SYM Plasma,” *Phys. Rev. C* **78**, 024903 (2008) [arXiv:0712.1053 [hep-ph]].
- [230] M. Gyulassy, J. Noronha and G. Torrieri, “Conical Di-jet Correlations from a Chromo-Viscous Neck in AdS/CFT,” arXiv:0807.2235 [hep-ph].
- [231] J. Noronha, M. Gyulassy and G. Torrieri, “Di-Jet Conical Correlations Associated with Heavy Quark Jets in anti-de Sitter Space/Conformal Field Theory Correspondence,” *Phys. Rev. Lett.* **102**, 102301 (2009) [arXiv:0807.1038 [hep-ph]].
- [232] P. M. Chesler and L. G. Yaffe, “The stress-energy tensor of a quark moving through a strongly-coupled $\mathcal{N}=4$ supersymmetric Yang-Mills plasma: comparing hydrodynamics and AdS/CFT,” *Phys. Rev. D* **78**, 045013 (2008) [arXiv:0712.0050 [hep-th]].
- [233] S. S. Gubser, S. S. Pufu and A. Yarom, “Sonic booms and diffusion wakes generated by a heavy quark in thermal AdS/CFT,” *Phys. Rev. Lett.* **100**, 012301 (2008) [arXiv:0706.4307 [hep-th]].
- [234] F. Dominguez, C. Marquet, A. H. Mueller, B. Wu and B. W. Xiao, “Comparing energy loss and p_{\perp} -broadening in perturbative QCD with strong coupling $\mathcal{N}=4$ SYM theory,” *Nucl. Phys. A* **811**, 197 (2008) [arXiv:0803.3234 [nucl-th]].

Chapter 8: The Diffusion Wake

- [235] R. B. Neufeld, “Comparing different freeze-out scenarios in azimuthal hadron correlations induced by fast partons,” arXiv:0810.3185 [hep-ph].
- [236] A. K. Chaudhuri, “Conical flow due to partonic jets in central Au+Au collisions,” *Phys. Rev. C* **75**, 057902 (2007) [arXiv:nucl-th/0610121].
- [237] A. K. Chaudhuri, “Di-jet hadron pair correlation in a hydrodynamical model with a quenching jet,” *Phys. Rev. C* **77**, 027901 (2008) [arXiv:0706.3958 [nucl-th]].
- [238] H. Bethe, “On the theory of passage of fast particles through matter,” *Annalen der Physik* **397**, 325 (1930).
- [239] W. H. Bragg and R. Kleemann, “On the α particles of radium, and their loss of range in passing through various atoms and molecules”, *Philos. Mag.* **10**, 318 (1905).
- [240] G. T. Y. Chen, J. R. Castro and J. M. Quivey, “Heavy charged particle radiotherapy”, *Ann. Rev. Biohys. Bioeng.* **10**, 499 (1981).
- [241] L. Sihver, D. Schardt and T. Kanai, “Depth dose distributions of high-energy carbon, oxygen and neon beams in water”, *Jpn. J. Med. Phys.* **18**, 1 (1998).
- [242] U. Amaldi and G. Kraft, “Radiotherapy with beams of carbon ions”, *Rep. Prog. Phys.* **68**, 1861 (2005).
- [243] R. R. Wilson, “Range, Straggling, and Multiple Scattering of Fast Protons”, *Phys. Rev.* **71**, 385 (1947).
- [244] I. Pshenichnov, I. Mishustin and W. Greiner, “Neutrons from fragmentation of light nuclei in tissue-like media: a study with the GEANT4 toolkit”, *Phys. Med. and Biol.* **50**, 5493 (2005).
- [245] I. Pshenichnov, I. Mishustin and W. Greiner, “Comparative study of depth-dose distributions from beams of light and heavy nuclei in tissue-like media”, *Nucl. Inst. Meth.* **B 226**, 1094 (2008).
- [246] B. Betz, M. Gyulassy, D. H. Rischke, H. Stöcker and G. Torrieri, “Jet Propagation and Mach Cones in (3+1)d Ideal Hydrodynamics,” *J. Phys. G* **35**, 104106 (2008) [arXiv:0804.4408 [hep-ph]].

- [247] R. J. Fries, B. Müller, C. Nonaka and S. A. Bass, “Hadron production in heavy ion collisions: Fragmentation and recombination from a dense parton phase,” *Phys. Rev. C* **68**, 044902 (2003) [arXiv:nucl-th/0306027].
- [248] R. J. Fries, S. A. Bass and B. Müller, “Correlated emission of hadrons from recombination of correlated partons,” *Phys. Rev. Lett.* **94**, 122301 (2005) [arXiv:nucl-th/0407102].
- [249] V. Greco, C. M. Ko and P. Levai, “Parton coalescence at RHIC,” *Phys. Rev. C* **68**, 034904 (2003) [arXiv:nucl-th/0305024].
- [250] B. Betz, M. Gyulassy and G. Torrieri, “Polarization probes of vorticity in heavy ion collisions,” *Phys. Rev. C* **76**, 044901 (2007) [arXiv:0708.0035 [nucl-th]].
- [251] M. Gyulassy and X. N. Wang, “Multiple collisions and induced gluon Bremsstrahlung in QCD,” *Nucl. Phys. B* **420**, 583 (1994) [arXiv:nucl-th/9306003].
- [252] X. N. Wang, M. Gyulassy and M. Plumer, “The LPM effect in QCD and radiative energy loss in a quark gluon plasma,” *Phys. Rev. D* **51**, 3436 (1995) [arXiv:hep-ph/9408344].
- [253] X. N. Wang and X. F. Guo, “Multiple parton scattering in nuclei: Parton energy loss,” *Nucl. Phys. A* **696**, 788 (2001). [arXiv:hep-ph/0102230].
- [254] P. Arnold, G. D. Moore and L. G. Yaffe, “Photon emission from quark gluon plasma: Complete leading order results,” *JHEP* **0112**, 009 (2001) [arXiv:hep-ph/0111107].
- [255] P. Arnold, G. D. Moore and L. G. Yaffe, “Photon and Gluon Emission in Relativistic Plasmas,” *JHEP* **0206**, 030 (2002) [arXiv:hep-ph/0204343].
- [256] H. Liu, K. Rajagopal and U. A. Wiedemann, “Calculating the jet quenching parameter from AdS/CFT,” *Phys. Rev. Lett.* **97**, 182301 (2006) [arXiv:hep-ph/0605178].
- [257] A. Majumder, B. Müller and X. N. Wang, “Small Shear Viscosity of a Quark-Gluon Plasma Implies Strong Jet Quenching,” *Phys. Rev. Lett.* **99**, 192301 (2007) [arXiv:hep-ph/0703082].

Chapter 9: Polarization Probes of Vorticity

- [258] G. Bunce *et al.*, “Lambda0 Hyperon Polarization In Inclusive Production By 300-Gev Protons On Beryllium,” *Phys. Rev. Lett.* **36**, 1113 (1976).
- [259] P. Hoyer, “Particle Polarization As A Signal Of Plasma Formation,” *Phys. Lett. B* **187**, 162 (1987).
- [260] A. D. Panagiotou, “Lambda0 Nonpolarization: Possible Signature Of Quark Matter,” *Phys. Rev. C* **33**, 1999 (1986).
- [261] B. Andersson, G. Gustafson and G. Ingelman, “A Semiclassical Model For The Polarization Of Inclusively Produced Lambda 0 Particles At High-Energies,” *Phys. Lett. B* **85**, 417 (1979).
- [262] J. Bensinger *et al.*, “Inclusive Lambda Production And Polarization In 16-Gev/C Pi- P Interactions,” *Phys. Rev. Lett.* **50**, 313 (1983).
- [263] Z. T. Liang and X. N. Wang, “Globally polarized quark gluon plasma in non-central A + A collisions,” *Phys. Rev. Lett.* **94**, 102301 (2005) [arXiv:nucl-th/0410079].
- [264] M. Jacob and J. Rafelski, “Longitudinal Anti-Lambda Polarization, Anti-Xi Abundance And Quark Gluon Plasma Formation,” *Phys. Lett. B* **190**, 173 (1987).
- [265] Z. T. Liang and X. N. Wang, “Spin alignment of vector mesons in non-central A + A collisions,” *Phys. Lett. B* **629**, 20 (2005) [arXiv:nucl-th/0411101].
- [266] F. Becattini and L. Ferroni, “The microcanonical ensemble of the ideal relativistic quantum gas with angular momentum conservation,” *Eur. Phys. J. C* **52**, 597 (2007) [arXiv:0707.0793 [nucl-th]].
- [267] Z. T. Liang, “Global polarization of QGP in non-central heavy ion collisions at high energies,” *J. Phys. G* **34**, S323 (2007) [arXiv:0705.2852 [nucl-th]].

- [268] A. Bravar [Spin Muon Collaboration], “Hadron azimuthal distributions and transverse spin asymmetries in DIS of leptons off transversely polarized targets from SMC,” Nucl. Phys. Proc. Suppl. **79**, 520 (1999).
- [269] Z. F. Liang and C. Boros, “Hyperon polarization and single spin left-right asymmetry in inclusive production processes at high energies,” Phys. Rev. Lett. **79**, 3608 (1997) [arXiv:hep-ph/9708488].
- [270] B. I. Abelev *et al.* [STAR Collaboration], “Global polarization measurement in Au+Au collisions,” Phys. Rev. C **76**, 024915 (2007) [arXiv:0705.1691 [nucl-ex]].
- [271] M. Jacob and G. C. Wick, “On the general theory of collisions for particles with spin,” Annals Phys. **7**, 404 (1959).
- [272] A. Milov [PHENIX Collaboration], “Centrality and $s(NN)^{1/2}$ dependence of the $dE(T)/d\eta$ and $dN(ch)/d\eta$ in heavy ion collisions at mid-rapidity,” J. Phys. Conf. Ser. **5**, 17 (2005) [arXiv:nucl-ex/0409023].
- [273] S. J. Brodsky, J. F. Gunion and J. H. Kuhn, “Hadron Production In Nuclear Collisions: A New Parton Model Approach,” Phys. Rev. Lett. **39**, 1120 (1977).
- [274] A. Adil and M. Gyulassy, “3D jet tomography of twisted strongly coupled quark gluon plasmas,” Phys. Rev. C **72**, 034907 (2005) [arXiv:nucl-th/0505004].
- [275] W. Busza, “Structure and fine structure in multiparticle production data at high energies,” Acta Phys. Polon. B **35**, 2873 (2004) [arXiv:nucl-ex/0410035].
- [276] G. Torrieri, “Scaling of $v(2)$ in heavy ion collisions,” Phys. Rev. C **76**, 024903 (2007) [arXiv:nucl-th/0702013].
- [277] A. H. Taub, “On circulation in relativistic hydrodynamics,” Arch. Rational Mech. Anal. **3**, 312 (1959).
- [278] W. Florkowski, B. L. Friman, G. Baym and P. V. Ruuskanen, “Convective stability of hot matter in ultrarelativistic heavy ion collisions,” Nucl. Phys. A **540**, 659 (1992).
- [279] N. Armesto *et al.*, “Heavy Ion Collisions at the LHC - Last Call for Predictions,” J. Phys. G **35**, 054001 (2008) [arXiv:0711.0974 [hep-ph]].
- [280] C. d. C. Barros and Y. Hama, “Antihyperon polarization in high-energy inclusive reactions,” Int. J. Mod. Phys. E **17**, 371 (2008) [arXiv:hep-ph/0507013].
- [281] B. I. Abelev *et al.* [the STAR Collaboration], “Mass, quark-number, and $s(NN)^{1/2}$ dependence of the second and fourth flow harmonics in ultra-relativistic nucleus nucleus collisions,” Phys. Rev. C **75**, 054906 (2007) [arXiv:nucl-ex/0701010].
- [282] A. Baran, W. Broniowski and W. Florkowski, “Description of the particle ratios and transverse-momentum spectra for various centralities at RHIC in a single-freeze-out model,” Acta Phys. Polon. B **35**, 779 (2004) [arXiv:nucl-th/0305075].
- [283] G. Torrieri and J. Rafelski, “Search for QGP and thermal freeze-out of strange hadrons,” New J. Phys. **3**, 12 (2001) [arXiv:hep-ph/0012102].

Chapter 10: Di-Jet Correlations in pQCD vs. AdS/CFT

- [284] S. S. Gubser and A. Yarom, “Universality of the diffusion wake in the gauge-string duality,” Phys. Rev. D **77**, 066007 (2008) [arXiv:0709.1089 [hep-th]].
- [285] S. S. Gubser and A. Yarom, “Linearized hydrodynamics from probe-sources in the gauge-string duality,” Nucl. Phys. B **813**, 188 (2009) [arXiv:0803.0081 [hep-th]].
- [286] U. W. Heinz, “Quark - Gluon Transport Theory. Part 2. Color Response And Color Correlations In A Quark - Gluon Plasma,” Annals Phys. **168**, 148 (1986).
- [287] A. H. Mueller, “Separating hard and soft scales in hard processes in a QCD plasma,” Phys. Lett. B **668**, 11 (2008) [arXiv:0805.3140 [hep-ph]].

- [288] A. Selikhov and M. Gyulassy, “Color diffusion and conductivity in a quark - gluon plasma,” *Phys. Lett. B* **316**, 373 (1993) [arXiv:nucl-th/9307007].
- [289] A. V. Selikhov and M. Gyulassy, “QCD Fokker-Planck equations with color diffusion,” *Phys. Rev. C* **49**, 1726 (1994).
- [290] K. J. Eskola and M. Gyulassy, “Color conductivity and the evolution of the mini - jet plasma at RHIC,” *Phys. Rev. C* **47**, 2329 (1993).
- [291] S. S. Gubser, “Comparing the drag force on heavy quarks in $N = 4$ super-Yang-Mills theory and QCD,” *Phys. Rev. D* **76**, 126003 (2007) [arXiv:hep-th/0611272].
- [292] W. Fleischer and G. Soff, “Bound State Solutions Of The Klein-Gordon Equation For Strong Potentials,” *Z. Naturforsch.* **39A**, 703 (1984).

Chapter 11: Conical Correlations in an Expanding Medium

- [293] B. Tomasik, “The contribution of hard processes to elliptic flow,” arXiv:0812.4071 [nucl-th].
- [294] E. Schnedermann, J. Sollfrank and U. W. Heinz, “Thermal phenomenology of hadrons from 200-A/GeV S+S collisions,” *Phys. Rev. C* **48**, 2462 (1993) [arXiv:nucl-th/9307020].
- [295] J. Putschke, “Full Jet-Reconstruction in STAR,” Talk at the RHIC & AGS Annual Users’ Meeting 2009, Brookhaven National Laboratory, USA (2009).
- [296] Y. S. Lai, “Direct jet reconstruction in p+p and Cu+Cu with PHENIX,” Talk at the RHIC & AGS Annual Users’ Meeting 2009, Brookhaven National Laboratory, USA (2009).

Appendices

- [297] O. Fochler, “Energy loss of high- p_T partons in transport simulations of heavy-ion collisions,” Diploma Thesis, University Frankfurt, Germany (2006).
- [298] M. L. Miller, K. Reygers, S. J. Sanders and P. Steinberg, “Glauber modeling in high energy nuclear collisions,” *Ann. Rev. Nucl. Part. Sci.* **57**, 205 (2007) [arXiv:nucl-ex/0701025].
- [299] M. Le Bellac, “Thermal Field Theory,” Cambridge Monographs on Mathematical Physics, Cambridge (1996).
- [300] D. H. Rischke, “Ultrarelativistische Schwerionenphysik - Untersuchungen zur Zustandsgleichung heißer und dichter Kernmaterie,” PhD Thesis, University Frankfurt, Germany (1992).
- [301] T. Tsumura, T. Kunihiro and K. Ohnishi, “Derivation Of Covariant Dissipative Fluid Dynamics In The Renormalization-Group Method,” *Phys. Lett. B* **646**, 134 (2007).
- [302] I. S. Gradshteyn and I. W. Ryzhik, “Table of Integrals Series and Products,” Adademic Press Inc. New York San Francisco London (1965).
- [303] G. Gattoff, A. K. Kerman and T. Matsui, “The Flux Tube Model For Ultrarelativistic Heavy Ion Collisions: Electrohydrodynamics Of A Quark Gluon Plasma,” *Phys. Rev. D* **36**, 114 (1987).

Acknowledgements

I would like to thank all those who helped and supported me while I did my PhD. First of all, I thank my supervisor Prof. Dr. Dirk Rischke for his advice, help, and continuous interest in my work, but also for giving me freedom which is essential in research.

Likewise, I thank Prof. Dr. Miklos Gyulassy for the great collaboration, the enlightening discussions, his many new ideas, and his hospitality during my stays at Columbia University.

Moreover, I thank Prof. Dr. Horst Stöcker, Prof. Dr. Carsten Greiner, and Prof. Dr. Peter Braun-Munzinger for their interest and strong support of my work as well as Prof. Dr. Igor Mishustin and Prof. Dr. Laszlo Csernai for helpful discussions.

Furthermore, I thank Dr. Jorge Noronha and Dr. Giorgio Torrieri for the stimulating, inspiring, and extremely fruitful collaboration. I especially thank Dr. Jorge Noronha for being always reachable and for his advice in many different situations. I also thank Daniel Henkel and Andrej El for many useful discussions about viscous hydrodynamics.

A special thank goes to my office mate Dr. Joachim Reinhardt for his companionship during the last 6 years since I started my diploma thesis and for his help in many different issues. There has always been a great working environment and his dry humor often helped to lighten up the atmosphere.

I thank Astrid Steidl, Denise Meixler, and Gabriela Meyer for the distractions during lunchtime as well as Daniela Radulescu and Veronika Palade for their assistance.

I'm especially thankful for the help of Astrid Steidl with many different plots and sketches.

In addition, I thank the Helmholtz Research School H-QM for financial support, but especially for bringing together a group of experimental and theoretical physicists, stimulating discussions, and offering advanced training. In particular, I thank Dr. Henner Büsching for his continuous enthusiasm, the excellent organization of the many different events, and for creating a team spirit.

I especially thank Prof. Dr. Dirk Rischke, Prof. Dr. Peter Braun-Munzinger, and Prof. Dr. Miklos Gyulassy for their contribution in my H-QM PhD-Committee.

I also thank Prof. Dr. Azwinndini Muronga, Michael Hauer, Prof. Dr. Charles Gale, and Dr. Björn Schenke for their hospitality during my stays at Cape Town and Montreal.

Besides that I thank the computer administration for the help with all the technical problems, Dr. Stefan Scherer for providing me with the layout for this thesis, and

Oliver Fochler, Mauricio Martinez, Irina Sagert, and Sascha Vogel for some helpful discussions and explanations.

Last but not least I thank my parents for their continuous encouragement and for their support that made my studies possible.

This work was supported by the Bundesministerium für Bildung und Forschung BMBF.

Frankfurt am Main, July 2009

Barbara Betz